THE UNIVERSITY
of LIVERPOOL

JET IMPINGEMENT ONTO A CIRCULAR CYLINDER

Thesis submitted in accordance with the requirements of the University of Liverpool for the degree of Doctor in philosophy by:

Seyed Parviz Alavi Tabrizi

August 1996

ABSTRACT

An experimental and numerical study has been made of the characteristics of a turbulent compressible jet impinging onto a circular cylinder with a view of obtaining a better understanding of the behaviour of an air jet used to clean the fouled surfaces of cylindrical tubes in a heat exchanger.

An experimental study of the impingement of an axisymmetric jet as well as two-dimensional slot jet with a circular cylinder are considered. The effect of different nozzle inlet pressures, different spacing between nozzle and cylinder and different offsets between cylinder and jet axis are investigated. Pressure distribution on the cylinder surface indicated an independence from nozzle inlet pressure or jet exit velocity in the range of experiments. It has been found that the Coanda effect is more effective on the offset side.

For the case of a slot jet, velocity measurements behind the cylinder were carried out by using a LDA system. The velocity profiles behind the cylinder indicated the Coanda effect influenced the flow field. These sets of experiments show the flow behaviour as the jet interacts with the cylinder and provides test data for assessing the accuracy of the numerical calculations. Flow Visualisation by the Schlieren method and by oil-film on the surface of cylinder were also carried out.

In the computational study a hybrid finite difference method obtained from TEACH-2E code, based on the SIMPLE algorithm has been used to solve the full Navier-Stokes equations for a turbulent, compressible and two-dimensional jet with the high Reynolds version of the k~ε turbulence model. The computations allow for slot to cylinder distances ranging from 1.8 to 3.5 cylinder diameters and for offsets ranging from 0 to 0.4 cylinder diameters. The jet exit velocity was fixed at 120 m/sec. and $R_{ej}=1.05\times10^5$. The results show that the Coanda effect is more effective at higher spacings between the slot and the cylinder and for higher offsets between the cylinder and the jet axis. The flow pattern includes an enclosed wake region behind the cylinder which was not readily detectable in the experimental case due to the unsteady flow.

Increasing the offset decreased the minimum pressure coefficient on the offset side and increased the shear stress coefficient at the same position, which is important from the cleaning point of view.

The overall results of the experimental and theoretical calculations are similar but the numerical data show some differences when compared with experiment, and this may be due to the shortcomings of the high-Reynolds version of the k~ε model. The main effect appears to associated with the prediction of the separation points which in turn alter the velocity profiles downstream of the cylinder.

By considering that shear stress is the more probable controlling parameter of surface cleaning, the overall results of the study show the slot jet is more effective for cleaning than a round jet. The model for the slot jet indicates that there is an optimum distance between slot and cylinder which maximises the cleaning area. By moving the jet axis from the top to bottom of the cylinder approximately 70% of cylinder surface may be cleaned.

ACKNOWLEDGEMENTS

My special gratitude goes to my supervisors, Dr. I. Owen and Dr. J. W. Cleaver for their valuable advice and encouragement throughout this research project. I am grateful for the great patience and graciousness they have shown me and I can offer here only inadequate acknowledgment of my appreciation.

I would like to express my thanks to Dr. M.W. Johnson for letting me use his grid generation program.

I would like to thank Mr. D. Smith for his photographic expertise, and Mr. S. Bode for his assistance with the LDA measurements.

I gratefully acknowledge the main financial support for my studies by the Ministry of Culture and Higher Education, and Tabriz University, The Islamic Republic of Iran.

Finally thanks to my family for all their support, encouragement and great patience throughout my study.

CONTENTS

NOMENCLATURE

A^+	van Driest' s constant.
A	Area.
C^*	Constant value.
C_1	Constant value.
C_D	Constant value.
C_μ'	Constant of turbulent viscosity equation.
C_μ	Constant of turbulent viscosity equation.
C_{s1}	Constant in algebraic stress model.
D	Cylinder diameter.
D_e	Dffusion conductance.
D_n	Diffusion conductance.
D_s	Diffusion conductance.
D_w	Diffusion conductance.
D_N	Nozzle diameter.
DXEP(I)	Distance, as shown in fig.(5-5).
DXPW(I)	Distance, as shown in fig.(5-5).
DYNP(J)	Distance, as shown in fig.(5-5).
DYPS(J)	Distance, as shown in fig.(5-5).
E	Integration constant.
F	Strength of convection=ρu
F_e, F_n, F_s, F_w	Mass flow rate through the faces of control volume.
G	Generation of turbulence kinetic energy.
H	Nozzle to plate distance.

K_1	Constant value.
L_D	Length scale of turbulence dissipation.
L_μ	Length scale of turbulence.
M_P	Mass source.
P	Peclet number.
P, N, S, E, W	Node points.
R_e	Reynolds number.
R_{ej}	Jet Reynolds number.
R_{eT}	Turbulence Reynolds number.
S_u	Source term.
S_v	Source term.
S_Φ	Generation per unit volume.
SEW(I)	Distance, as shown In fig.(5-5), =0.5*(DXEP(I) + DXPW(I)).
SNS(J)	Distance, as shown in fig.(5-5), =0.5*(DYPS(J) + DYNP(J)).
S_1, S_2	Separation points on cylinder surface.
T	Temperature

***

a	Coefficient representing convection and diffusion.
b	Half width of jet.
b_0	Half of the slot width.
c_p	Pressure coefficient.
d_e	Coefficient of pressure difference relation(eq:5-35).

d_n	Coefficient of pressure difference relation(eq:5-35).
d_s	Coefficient of pressure difference relation(eq:5-35).
d_w	Coefficient of pressure difference relation(eq:5-35).
e	Offset, (eccentricity).
h	Distance between slot and cylinder centre.
i, j	Subscripts denoting cartesian coordinate directions.
k	Turbulent kinetic energy.
l_m	Turbulence length scale (mixing length).
n, s, e, w	Cell boundaries.
p	Pressure.
p_s	Static pressure.
p_{st}	Stagnation point pressure.
p^*	Guessed pressure.
p'	Pressure correction.
$q^\bullet$	Total (convective + diffusive) fluxes.
r	Radial distance.
r_N	Nozzle exit radius.
t	Time.
u	Axial velocity.
u_j	Axial velocity of jet at exit from nozzle or slot.
u_m	Jet centre line velocity.
u_0	Mean velocity of jet at exit from slot.
$\bar{u}$	Time averaged axial velocity.
u'	Fluctuation component of axial velocity,

u'	Velocity correction.
u_τ	Friction velocity.
u^+	The ratio of velocity to friction velocity.
u^*	Guessed axial velocity.
v_m	Maximum radial velocity.
v	Radial velocity.
$\bar{v}$	Time averaged radial velocity.
v'	Fluctuation component of radial velocity,
v'	Velocity correction.
v^*	Guessed radial velocity.
w	Time average square of vorticity fluctuations.
x	Axial distance.
x'	Axial distance from rear stagnation point of cylinder.
y	Radial distance. Distance from the wall.
y_1	$=\lvert y_{s.c.} - y \rvert$
y_2	$=\lvert y_{c.c.} - y \rvert$
y_p^+	Local Reynolds number.
z	Distance from impingement plate.

Greek

α	Constant. Constant in algebraic stress model.
Γ_Φ	Exchange coefficient.
ε	Dissipation rate of turbulence kinetic energy.
η	Under-relaxation factor.

θ	Angular position.
κ	von Karman constant.
μ	Laminar viscosity.
μ_t	Turbulent viscosity.
μ_{eff}	Effective viscosity.
ν	Kinematic viscosity.
ϱ	Density.
σ	Standard deviation.
τ	Shear stress.
τ_w	Wall shear stress.
Φ	Transport quantity.

Subscripts

c. c.	Cylinder centre line.
cl.	Centre line.
max.	Maximum.
min.	Minimum.
n, s, e, w	Cell boundaries.
ref.	Reference.
s. c.	Slot centre line.

CHAPTER

1

INTRODUCTION

Heat exchangers are devices which have been designed to improve or facilitate the flow of heat between two or more streams of fluid. According to the requirements of the second law of thermodynamics, a temperature difference between the fluids is necessary for transferring energy from hot fluid to cold fluid.

For fluids flowing through the heat exchanger, energy will always be used, and so, there is always pressure difference at inlet and outlet of two fluids. Due to frictional reduction of pressure energy during the flow, the fluid pressure at outlet is less than that at inlet. In general the thermal performance of a heat exchanger is related to the frictional pressure drop. Improvement in thermal performance will likely be accompanied by increased pressure drop.

Heat exchangers are usually designed on the basis of specified design operating conditions. The design of heat exchangers take place in two stages: thermal design and mechanical design. Thermal design is concerned with those aspects of heat transfer and fluid mechanics related to requirements of acceptable surface area and flow guidance to ensure that the heat exchanger is capable of the required thermal duty with an acceptable fluid pumping power. Mechanical design is concerned with all matters necessary to ensure the integrity and durability of the heat exchanger as a pressure vessel. For new and unfamiliar systems it is rarely possible to predict the performance closer than ±20 percent. After a period of service the heat

transfer surface of a heat exchanger will become coated with deposits originating in the flow system, or the surface may become corroded as a result of the interaction between the fluids and the material used for construction. In any case the fouling represents an additional resistance to heat flow across the heat exchanger. Due to the increased thermal resistance of the deposit layer, the thermal performance of a heat exchanger may progressively fall off to less than half of its original value. In these cases the ease of cleaning the surfaces to restore the performance is an important selection criterion.

In thermal design, fouling factors are used to account for deposits on heat exchanger surfaces. However the use of high fouling factors may give rise to excessive economic penalties and significantly alter the performance of heat exchanger under clean conditions. Thus it is important at the start of the design to assess whether either side of heat exchanging parts will require mechanical cleaning during its lifetime. If a fluid has a fouling tendency and the effect of other parameters are ignored, this fluid should be placed on tube side where high velocities and smooth surfaces minimize the rate of build up of fouling layer, and in this case if mechanical cleaning is required it can be carried out by water jets and mechanical tube cleaners. If other factors require that the fouling fluid be placed on the shell side, then mechanical surface cleaning techniques are required for removal of fouling deposits.

The present study deals with surface cleaning of fouled tubes of heat exchangers using a high velocity impinging air jet onto its cylindrical tubes.

The material of chapter 2 aims at describing the fouling and fouling mechanisms. Different types of fouling mechanisms are defined and the affecting

parameters on fouling resistance are discussed. The general categories of fouling prevention, mitigation and accommodation techniques with emphasis on surface cleaning techniques are included. At the end of this chapter a brief comparison between jet flow used for surface cleaning of cylindrical tubes and parallel flow is made.

In chapter 3, a literature review is carried out. The structure of a turbulent free jet in subsonic, moderately underexpanded and highly underexpanded cases are reviewed. The flow characteristics of an impinging jet and its different regions are discussed. For better understanding of flow separation on cylindrical surface, a brief review related to separation of parallel flow from cylindrical surface and also the Coanda effect on such a surface is carried out. Finally in order to obtain an understanding of how a turbulent jet impinges onto a flat plate a survey of experimental and theoretical work on impinging jet flows onto flat surfaces is presented.

Numerical modelling is the subject of chapter 4. In this chapter the governing equations of a turbulent two-dimensional impinging jet are discussed. The different kinds of turbulence modelling including one-equation models, two-equation models and algebraic stress model are gathered. Boundary conditions for jet interaction with a flat plate as well as a cylindrical surface are discussed. Finally in relation to the high Reynolds version of the standard k~ε model of turbulence which has been used in present study, the near wall modelling is considered.

Finite difference approximations of the differential equations are derived in chapter 5. The construction of control volumes, the finite difference form of conservation equations, general solution procedure of these equations by using

SIMPLE algorithm are the main subjects discussed in this chapter. At the end of this chapter the overall structure of the **TEACH-T** computer program is represented.

The numerical study of an axisymmetric jet as well as slot jet impingement onto a flat plate are carried out in chapters 6 and 7 respectively. The implications of these two studies show that the model described in chapter 4 is satisfactory and should be valid at least for the impingement region of jet interaction with a circular cylinder.

Chapter 8 describes the experimental work. Flow visualisation techniques used in present study are presented. The experimental work for the axisymmetric jet case considers the effect of different jet velocities at nozzle exit, different spacings between nozzle and cylinder and different offsets between cylinder and nozzle horizontal symmetry planes are discussed. For the case of a slot jet the velocity profiles behind the cylinder, measured by LDA at different offsets as well as non offset condition are discussed. Pressure distribution around the cylinder for different offset conditions are also considered.

Chapter 9 discusses the results obtained from a numerical study of the turbulent slot jet interaction with a circular cylinder at different spacings between cylinder and slot and also at different offsets.

In chapter 10, the overall results are discussed and finally in chapter 11, the achievements of this study are concluded.

CHAPTER

2

FOULING IN HEAT EXCHANGERS

2-1 Fouling and fouling mechanisms

Fouling can be defined as the formation of any undesirable deposit as an insulating layer of material on heat transfer surfaces which increases resistance to both heat transfer and fluid flow. A few examples illustrating the variety of fouling include: biofouling in a condenser using seawater as the coolant, coking in heat exchangers used in the petrochemical industry and ash deposits in a coal-fired boiler.

There are at least five different types of fouling mechanisms that are currently recognized. They are individually complex and often occur simultaneously. Hassan (1980) classifies them according to their controlling driving force. The same classification was developed by Epstein (1978, 1981) and also reported by Chenoweth (1990):

Precipitation fouling due to crystallization . This relates to the precipitation of dissolved substances onto a heat transfer surface. When dissolved substances, such as calcium sulphate, magnesium silicate and lithium carbonate, for instance, have inverse rather than normal solubility versus temperature characteristics, the precipitation occurs on superheated rather than sub-cooled surfaces. This process is often referred to as ***scaling***.

Particulate fouling. This occurs when finely divided solids (rust, dust, sand, etc.) suspended in the process fluid accumulate on the heat transfer surfaces. In a

minority of instances settling by gravity predominates, and the process is then referred to as ***sedimentation fouling***.

Chemical reaction fouling. Deposits formed by heat induced surface reactions at the heat transfer surface, where the surface material itself is not a reactant, describe this category. Polymerisation, cracking and coking of hydrocarbons are typical examples.

Corrosion fouling. The material of construction of the heat transfer surface participates in the reaction, and produces adherent corrosion products. These products which thermally insulate (foul) the surface may in turn promote the attachment of other fouling materials.

Biological fouling. This type of fouling is due to the presence of macro or micro organisms, which adhere to the heat transfer surface. Adherent slimes may also be generated.

Epstein (1978, 1981) and Somerscales (1981) identify a sixth category of thermal fouling as:

Freezing fouling. This occurs as a result of solidification of a liquid or some of its higher melting components in a gas stream onto a sub-cooled heat transfer surface.

Often a combination of two or more fouling processes is present and in some cases they may exert a synergistic effect. For example fouling in a condenser using seawater as the cooling medium is generally caused by the combined effects of biological and corrosion fouling. Similarly, fouling of a suspension preheater in a cement industry may involve the simultaneous action of particulate, chemical reaction and freezing fouling.

2-2 Parameters that affect fouling resistance

Fouling is a complex, transient process involving the simultaneous transport of heat, mass and momentum, and there are many factors that need to be considered when specifying fouling resistances for the design of heat exchangers. These factors include:

Fluid characterization. The most important consideration is the fluid and its thermodynamic and transport properties such as specific heat, density, thermal conductivity, viscosity, diffusion coefficients and the conditions when it produces fouling. If the fluid contains suspended particles, the particle concentration, composition and size distribution are also important parameters as are condensable components and their related dew-point temperatures. In some cases the chemical species in the fluid stream can react to produce new components, and it is important to know if and when such processes might take place.

The various thermodynamic and transport properties of a fluid are functions of temperature, which itself can affect the transport processes taking place. For example, according to Eckert and Drake (1959), the diffusion coefficients for gases are very strong functions of the temperature and vary as the absolute temperature raised to the power 1.8.

$$\frac{D}{D_{ref}}=(\frac{T}{T_{ref}})^{1.8} \tag{2-1}$$

Surface and bulk temperature. For many kinds of fouling, the amount of fouling increases with increasing temperature. Lower temperatures produce slower fouling build up, and, often deposits that are easier to remove.

The surface temperature is the controlling parameter where the formation of

deposits onto heat transfer surfaces are due to condensation, crystallization or sublimation of the species. In such cases the fluid temperature plays a very minor role in the deposition process which take place (e.g.Brown, 1966).

Fluid velocity and shear stress. The fluid velocity is an important parameter governing the transport of material to the surface as well as removing material from the surface. Normally, keeping the velocities high reduces the tendency to foul. Velocities on the tube side are limited by pressure drop and erosion, and on the shell side by flow induced vibration. Although the fluid velocity is frequently used as a characterising parameter in the assessing of removal processes, it is more probable that the controlling parameter is the shear stress. The distinction between velocity and fluid shear stress depends on the geometry of the heat transfer surface, fluid properties and Reynolds number. For example, for a given average velocity the shear stress at the surface will be much higher for a plate heat exchanger than for a shell-and-tube heat exchanger. Also in a double-pipe heat exchanger for an identical average velocity of the fluid, the shear stress at the outer surface of the annulus is not the same as that at the inner surface. Thus the removal forces generated by the shear stresses at the two surfaces will also be different. Another important parameter in the removal process is the mechanical strength of the fouling deposit, which depends on the material transported to the surface, chemical reactions within the deposit and removal of material from the deposit surface.

Surface material and surface finish. The selection of surface material is significant and is critical in situations where corrosion fouling takes place. Corrosion arising from an incorrect choice of material not only reduces the equipment life, but also blockage of the exchanger passages due to deposition of corrosion products may

result in frequent, costly shutdowns for cleaning. In such cases the interaction between surface material and fouling deposit, with consideration of surface and fluid temperature, is very important. Materials also should be selected on the basis of minimising overall costs within the expected life-time of the heat exchanger. A different method of surface coating (e.g. galvanizing) has been used in an attempt to overcome corrosion fouling. Some kinds of biological fouling also can be lessened by copper-bearing tube materials.

Rough surfaces are an important parameter for the adhesion of deposits. When deposits begin to build up, the rough fouling layer encourages more growth, and so on. Surface finish has been shown to influence the delay of fouling and the ease of cleaning, Hassan (1980), but, it is especially important during the initial stages of fouling and plays a significant role in determining the duration of the developing period. Heat exchangers with smooth surfaces are preferred. However, once a deposit covers a surface, the surface finish no longer plays an important role.

Heat exchanger geometry and orientation. The geometry of a particular shell-and-tube heat exchanger can influence the uniformity of the flows both on the tube side and shell side. The ease of cleaning can be greatly influenced by the orientation of the heat exchanger.

Heat transfer process. Heat transfer processes have considerable effect on fouling resistance. For the same fluid, fouling resistance can be different depending upon whether heat is transferred through sensible heating or cooling, boiling or condensing.

Fluid purity and freedom from contamination. Most fluids have some contamination and fluids seldom have high purity. This contamination can either

deposit as a fouling layer or act as a catalyst to the fouling processes. It is often economically attractive to remove these fouling constituents by filters.

Fluid treatment. Fluid treatment is commonly carried out to prevent corrosion and biological growth. If treatment is neglected, rapid fouling can occur.

2-3 Surface cleaning techniques

Fouling deposits reduce the effectiveness of a heat exchanger by reducing the heat transfer and by affecting the pressure drop of the exchanger. A decrease in the performance of a heat exchanger beyond the acceptable levels require it to be cleaned. A number of prevention, mitigation and accommodation techniques are used to deal with gas-side fouling. Referring to Marner and Suitor (1983), these techniques may be grouped under general categories of: (1) fluid cleaning techniques, (2) control of combustion conditions, (3) fuel and gas additives, (4) surface cleaning techniques, (5) quenching, (6) control of operating conditions, and (7) gas cleaning techniques.

A number of surface cleaning techniques have been developed to remove gas-side fouling deposits, including steam and air sootblowing, sonic sootblowing, and water washing. Other procedures which are used to some extent include chemical, mechanical, and thermal cleaning.

The accepted and most widely used on-line technique of cleaning gas-side fouled surfaces is sootblowing. A high pressure jet of air or dry steam as the blowing medium is forced through the heat exchanger matrix to remove the deposit. The location and spacing of the sootblowers within the heat exchanger are very important, and the frequency of sootblower operation depends on the type of fuel, amount of excess air, and operating conditions. Two major types of sootblowers, rotary and long retractable types has been presented by Di Carlo (1972). The rotary sootblower is

permanently located in the tube bank to be cleaned, but because this type of sootblower is exposed to the flue gases at all times, it is limited to flue gas temperatures below 811K (Di Carlo, 1972). In contrast, the long retractable sootblowers can be used at virtually any temperature. However there is little knowledge of the fundamental principles of how the jet behaves within the often complex passage of the heat exchanger and how the jet actually removes the deposit. The result is that the heat exchangers often becomes so heavily fouled that the sootblowing system needs to operate continuously and eventually the heat exchanger has to be closed down for manual cleaning.

Surface cleaning by using a high pressure jet of air relies on an understanding of the aerodynamic removal of real deposits and knowledge of the complex fluid dynamics involved when a jet interacts with a heat exchanger. In this thesis, work is focused on clarifying the fluid dynamic aspects of the problem by means of experimental and numerical analysis. In particular, the interaction of a two-dimensional slot jet with a circular cylinder situated in crossflow with respect to the jet is considered. The interaction of round jet and slot jet with flat surfaces has been covered by several authors, but for cylindrical surfaces only a few experimental works have been reported, for example, Brahma *et al.* (1991) and Tsuchiya *et al.* (1993).

The turbulent jet impinging normally onto surfaces with different shapes may cause a large amount of heat and mass transfer in the vicinity of the stagnation point. Thus it is a flow configuration which is extensively used in the process industries for rapid heating, cooling or drying, cleaning and as a boosting force for the transport of small solids. The overall heat or mass transfer performance of an impinging jet

has been examined in many experiments for example by Goldstein & Franchett (1988), and Jambunathan *et al.* (1992).

The impinging turbulent jet is also an interesting flow from another, rather different, point of view. Models of momentum and heat transport in turbulent shear flows are invariably developed by reference to flows parallel to walls. Yet turbulence modelling for separated and recirculating flows is by no means in a generally satisfactory state. A wide range in the predicted heat transfer coefficient in the vicinity of reattachment point arises, in large measure, from unsuitable assumptions in their turbulence models for turbulent transport processes in the immediate vicinity of the wall.

The turbulent impinging jet is noticeable as an excellent test case for validation of turbulence models for recirculating flows. While relatively simple, it differs in several important respects from flows parallel to walls, Cooper *et al.* (1993), for example:

-In the vicinity of the axis of symmetry, turbulence energy is created by normal straining, while, in parallel flow the turbulence energy generation is by shear;

-The r.m.s. fluctuating velocity normal to the wall is larger than that parallel to the wall, but in a parallel flow, fluctuations normal to the wall are much smaller than other components;

-The local turbulent length scales near the wall are strongly affected by the length scales of the jet turbulence, while in a parallel flow length scales are usually determined by the distance from the wall alone;

-Convective transport of turbulence energy towards the stagnation point is important, but in parallel flow, convective effects are usually negligible, and an

approximate balance exists between generation and dissipation processes. In addition, it should be mentioned that just beyond the impingement region the flow structure will be significantly affected by the strong curvature of the stream lines, while at greater radii, the flow turns into a radial wall jet.

In the design of an impinging jet system, the designer is immediately faced with the task of specifying a rather large number of geometric and flow parameters including, jet type, jet configuration (array geometry), nozzle-to-target surface spacing, location of exhaust ports, effects of induced or imposed cross flow, surface motion, angle of impingement, nozzle design, large temperature differences between the jet and impinging surface and cylinder deviation from the jet axis (offset).

In this research emphasis is placed on the effect of the offsets and nozzle-to-cylinder surface spacing, on pressure distributions and flow field around a circular cylinder.

CHAPTER

3

REVIEW OF LITERATURE

Surface cleaning techniques for removing gas side fouling deposit in heat exchangers are discussed in chapter 2. One of the effective techniques in this area is using a high pressure jet of air impinging upon the cylindrical tubes of the heat exchanger. The flow field of an impinging jet on a cylindrical surface can be subdivided into five regions: the potential core region, the free jet region, the impingement region, the wall jet region and the wake region behind the cylinder. These regions, as well as the structure of turbulent free jet, are discussed in this chapter. Due to lack of data about the interaction of a turbulent jet with a cylindrical surface and in order to obtain a reference for assessing the numerical calculations, a brief review about the theoretical and experimental works related to jet impingement onto a flat plate has been carried out.

3-1 Structure of turbulent free jet

The general structure of a turbulent free jet is well known and has been reviewed extensively by Abramovich (1963), Rajaratnam (1976) and Pai (1954). The turbulent free jet has also been investigated experimentally by different experimenters at various levels. Much of the experimental results in certain areas are in conflict with each other owing to both the variety of inlet and boundary conditions employed, many of which are reported unsatisfactorily, and the level of experimental error

essential in hot-wire anemometry by which most of the experimental data has been obtained. The former problem is well illustrated by the results obtained by Kotsovinos (1976) who reported a non-linear spreading rate which varies from $db/dx=0.0913$ at $x<60b_0$ to $db/dx=0.14$ at $x>600b_0$,where, b_0 is the nozzle half width, b is half width of jet ($b\equiv y$ at $u=0.5u_m$) and u_m is centreline jet velocity. Bradbury (1965) showed that the increased spreading rate may be due to the fall in the mean velocity and turbulence intensity of the jet to the same order of magnitude as that of the fluctuating draughts in the room caused by recirculation of the fluid. He showed that the reported increase in spreading rate corresponds to a background turbulence level of 0.5% of the inlet velocity.

By considering a flow issuing from a nozzle or slot, depending on the pressure ratio through the nozzle or slot, three forms of flow pattern are possible. These are known as the subsonic jet, the moderately under-expanded jet and the highly underexpanded jet.

3-1-1 Subsonic jet

The main features of a subsonic turbulent free jet are shown in fig.(3-1). When a turbulent jet issues from a nozzle, the velocity profile at the nozzle exit is affected by the nozzle design such as length-to-diameter ratio, nozzle shape and presence or absence of a transition section upstream of the nozzle. Two possible nozzle velocity profiles are a uniform velocity profile and a 5.5 power velocity profile. When the velocity profile at the nozzle exit is uniform

$$u=u_j \tag{3-1}$$

but for the 5.5 power velocity profile:

$$u=u_{max}[1-0.3412(\frac{r}{r_N})^{5.5}] \quad (3\text{-}2)$$

this profile is a result of experimental measurements of Bradshaw and Love (1959).

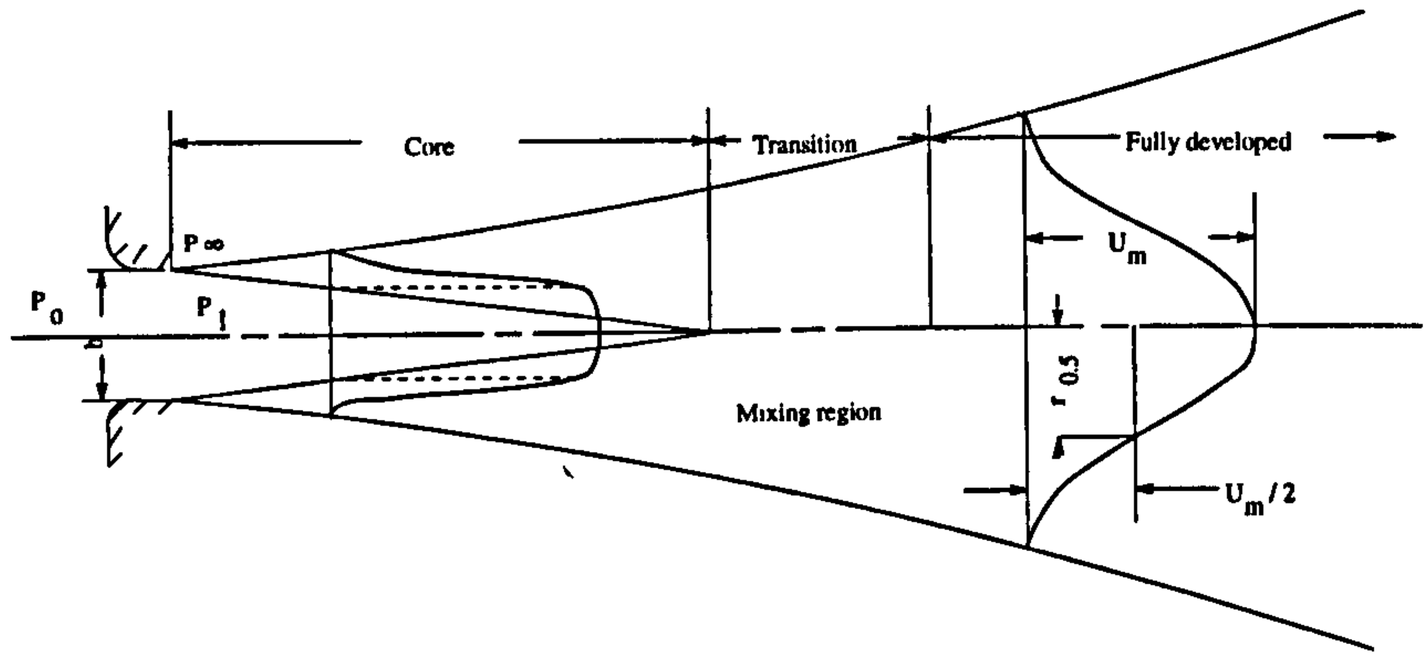

Fig.(3-1) Subsonic jet

The subsonic jet is characterized by a potential core surrounded by a region in which mixing between jet and ambient fluid takes place. The width of the free jet grows in the downstream direction of the jet. According to Schlichting (1968), the half width b of a free jet is directly proportional to the distance along the jet centreline,

$$b=constant\cdot x \quad (3\text{-}3)$$

The potential core is the main characteristic of the flow development region, wherein fluid properties and velocity are relatively constant. Finally the potential core is dissipated as a result of mixing action between the core and jet boundary. According to Abramovich (1963), in the flow development region the pressure is virtually constant and equal to the ambient (surrounding fluid) pressure.

The tangential shear within the mixing zone causes the deceleration of the jet and acceleration of the surrounding fluid and consequently the momentum flux must

be constant at every normal section. By neglecting the influence of viscous action on the mixing process, the mean flow should be dynamically similar under all conditions. It has been experimentally found that the velocity distribution could be represented satisfactorily by a Gaussian curve

$$\frac{u}{u_m}=\exp(-\frac{y^2}{2\sigma^2}) \qquad (3\text{-}4)$$

where y is the transverse distance from the jet centreline or axis and σ is the standard or root-mean-square deviation, that is the value of y for which $u=0.606u_m$, fig.(3-2). The equation (3-4) is a result of curve fit and does not have any theoretical basis. By considering dynamic similarity at all cross sections, neglecting efflux velocity, for the slot jet we have:

$$\frac{\sigma}{x}=K_1 \qquad (3\text{-}5)$$

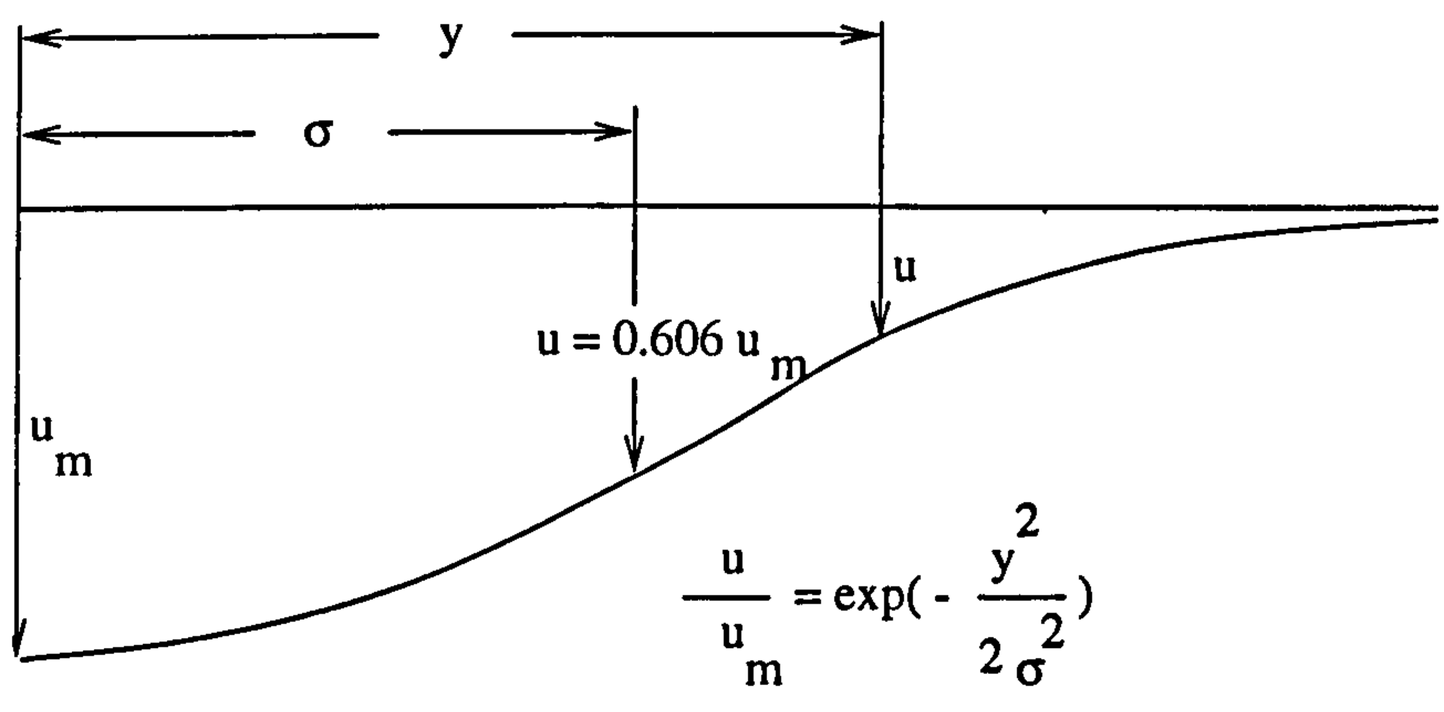

Fig.(3-2):Characteristic of normal probability curve

which means that the angle of jet diffusion is constant. The value of K_1 must be determined experimentally. In a real jet the angle of jet diffusion is not necessarily

constant and according to Albertson *et al.* (1950) its value is different for developed and developing jets.

To determine the potential core length a knowledge of centreline velocity decay in the developed flow region is required. Unfortunately the values of potential core lengths differ for investigations carried out by different experimenters. For a slot jet, according to Albertso*n et al.* (1950), the potential core extends 5.2 slot widths. His experiments were for an air jet issued through slots of width 1/4, 1/6 and 1/32 inch and for a range of Reynolds numbers of

$$1.5\times10^{3}<R_{e}<7.2\times10^{4}$$

Trentacoste *et al.* (1966) reported a core length of about 7 slot widths for various size and shape of slots through a Reynolds number range of

$$3.6\times10^{3}<R_{e}<8.8\times10^{4}$$

according to Rajaratnam (1976) for a plane jet the length of the potential core is about 6 slot widths. To summarize, it has been noted that for a turbulent jet, potential core lengths varying from about 4.7-7.7 slot widths, have been obtained by different investigators. Some of them state that the potential core length is dependent on Reynolds number, while others state that core length is independent of Reynolds number.

According to Abramovich (1963) by considering Trüpel's (1915) experiments there is similarity among velocity profiles in all sections of principal area of a round jet. Thus at corresponding points of any two cross sections of the main part of the jet, the non dimensional velocities are the same. This conclusion is valid for other types of jet including the two dimensional slot jet. This has been shown by many

observers and authors including Schlichting (1968), Gauntner *et al.* (1970), Rajaratnam (1976) and Pai (1954). The same results are obtained experimentally in the present study.

According to Tollmien (1945) the solution in the developed flow region, referring to fig.(3-3), is

$$\frac{u_m}{u_0}=\frac{1.21}{\sqrt{\alpha}}\cdot\frac{1}{\sqrt{x/b_0}} \tag{3-6}$$

where b_0 is the half of the width of slot. Using the experimental results of Forthman (1936) and others Abramovich (1963) found that the experimental coefficient α varied from 0.09-0.12 and adopted a simple average value of 0.10. With this value of α

$$\frac{u_m}{u_0}=\frac{3.78}{\sqrt{x/b_0}}\cdot \tag{3-7}$$

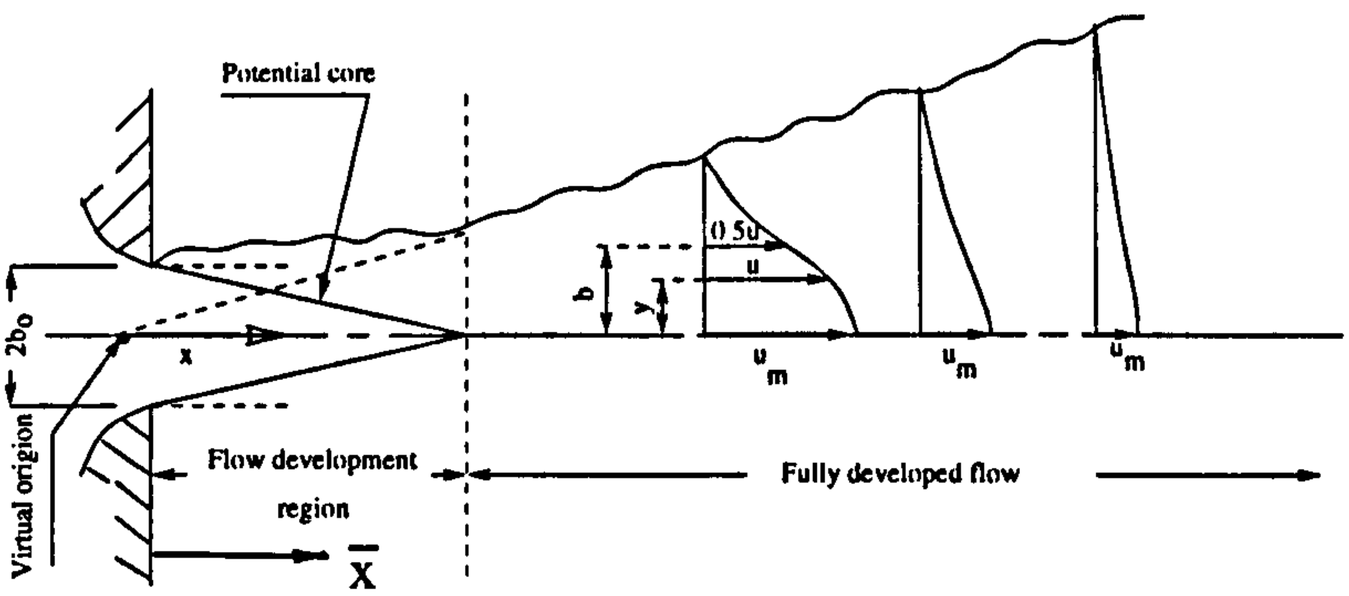

Fig.(3-3): definition sketch of plane turbulent free jet

According to Goertler (1942)

$$\frac{u_m}{u_0}=1-\tanh^2(\sigma\frac{y}{x})\cdot \tag{3-8}$$

By using the experimental results of Reichardt (1951), Goertler (1942) found that $\sigma=7.67$ which gives

$$\frac{u_m}{u_0}=\frac{3.39}{\sqrt{x/b_0}}\cdot \tag{3-9}$$

According to Zijnen (1958) for a 0.5 ×10 cm slot assuming $\bar{x}$ as the distance from nozzle exit :

$$\frac{u_m}{u_0}=\frac{3.52}{\sqrt{x/b_0}}=\frac{3.52}{\sqrt{(\bar{x}+1.2b_0)/b_0}} \tag{3-10}$$

and for a 1cm×25cm slot

$$\frac{u_m}{u_0}=\frac{3.12}{\sqrt{x/b_0}}=\frac{3.12}{\sqrt{(\bar{x}+2.40b_0)/b_0}}\cdot \tag{3-11}$$

The experiments of Albertson *et al.* (1950) showed that

$$\frac{u_m}{u_0}=\frac{3.24}{\sqrt{x/b_0}} \tag{3-12}$$

and that in general all these equations could be represented by

$$\frac{u_m}{u_0}=\frac{c1}{\sqrt{(\bar{x}+c^*b_0)/b_0}} \tag{3-13}$$

where c1 varies from 3.12 to 3.78 and c^* from 0 to 2.40. According to Rajaratnam

(1976) for all practical purposes c1 could be given an average value of 3.5 and c^* a value of zero, thereby giving

$$\frac{u_m}{u_0} = \frac{3.50}{\sqrt{\bar{x}/b_c}}. \qquad (3\text{-}14)$$

In all the above equations, x is the axial distance from a virtual origin (located from a geometrical consideration), fig.(3-3), and $\bar{x}$ is the distance from the nozzle exit. For practical purposes the virtual origin could be located at the nozzle exit itself and $\bar{x}$ becomes identical with x.

3-1-2 Moderately underexpanded jet

When, for the flow of a jet issuing from a slot, the sonic or critical pressure ratio is reached, a very weak normal shock forms at the exit of the slot. With increasing pressure ratio, this shock changes rapidly and at $p_l/p_\infty \approx 1.1$ the familiar pattern of shock diamonds or cells due to intersecting oblique shocks is established in the core. For a sonic exit this structure remains until $p_l/p_\infty \approx 2$, and this is why, for this range of pressure ratio ($1.1 \leq p_l/p_\infty \leq 2$), the term "moderately underexpanded jet" is used. By the additional expansion of the jet flow beyond the nozzle or slot, the

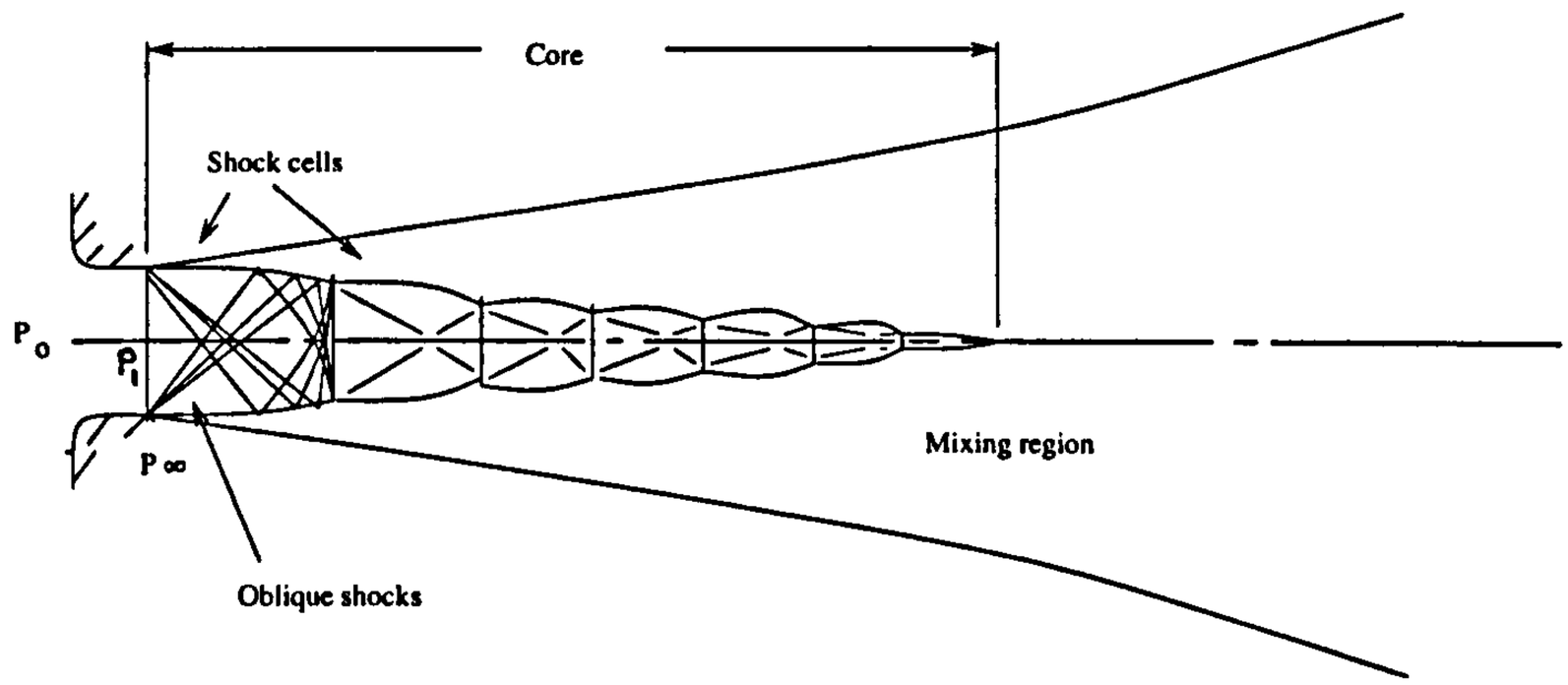

Fig.(3-4): Moderately underexpanded jet

boundaries of the potential core in the subsonic case are now determined by the requirement of pressure equilibrium between the outermost portion of the flow within the shock structure and the surrounding ambient air. By continuing the diffusion of jet flow, the core region finally dissipates and downstream of the core the jet has become subsonic and its behaviour is similar to a subsonic jet, Donaldson & Snedeker (1971), fig.(3-4).

3-1-3 Highly underexpanded jet

For a sonic exit of jet flow from the nozzle and at a pressure ratio $p_j/p_\infty \approx 2$, the form of the shock structure in the first cell changes. On the centreline, where the expansion is maximum, the pressure becomes very low relative to ambient pressure and recompression in the remainder of the cell reaches the limiting value for conical shocks and the required compression takes place through a normal shock disk. By increasing the pressure ratio p_j/p_∞ the strength and diameter of the shock disk increases. Immediately downstream of the disk the flow is subsonic. Since the surrounding flow in the oblique shock region remains supersonic, a slip line exists

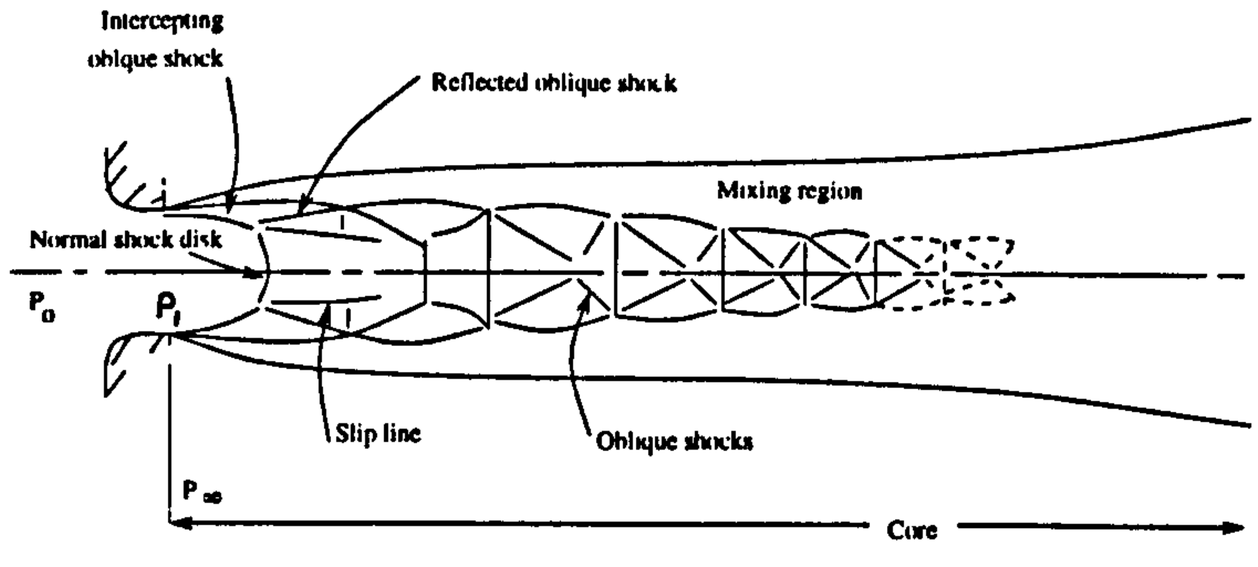

Fig.(3-5): Highly underexpanded jet

at the boundary of the two concentric regions. For quite a high degree of underexpansion, this subsonic core region is rapidly accelerated and becomes supersonic once again near the beginning of the second cell. For very high pressure ratios the structure downstream of the first cell is dominated for a great distance by a very strong normal shock in the first cell, and no other normal shocks are present. The flow then decays through a structure of oblique shocks. The mixing region surrounds the core as usual, with the result that the core of a highly underexpanded jet can be extremely long. Far downstream, the usual subsonic decay takes place, Donaldson & Snedeker (1971), fig.(3-5).

3-2: Flow characteristics of impinging jets

As shown by Polat *et al.* (1989), Gauntner *et al.* (1970), Martin (1977) , Beltaos and Rajaratnam (1973) and Kang *et al.* (1992), the flow pattern of impinging jets from single round nozzle and slots (slot nozzles) onto a surface can be subdivided into four characteristic regions: the flow establishment or "potential core" region, the free jet region, the impingement or "stagnation" region and the wall jet region. The velocity field of an impinging jet is shown schematically in fig.(3-6).

3-2-1: Flow establishment or "potential core" region

This region is the central portion of the flow and extends from nozzle exit to the apex of the nozzle core, where the axial velocity remains almost constant and equal to the velocity at the nozzle exit.

3-2-2: Established flow or "free jet "region

In this region, in the direction of the jet beyond the apex of the potential core, the centreline axial velocity starts to decay and the flow spreads to the surroundings in the transverse direction. The structure of this region depends on the nozzle-surface

spacing.

According to Vickers (1959), the free jet may be considered to be turbulent

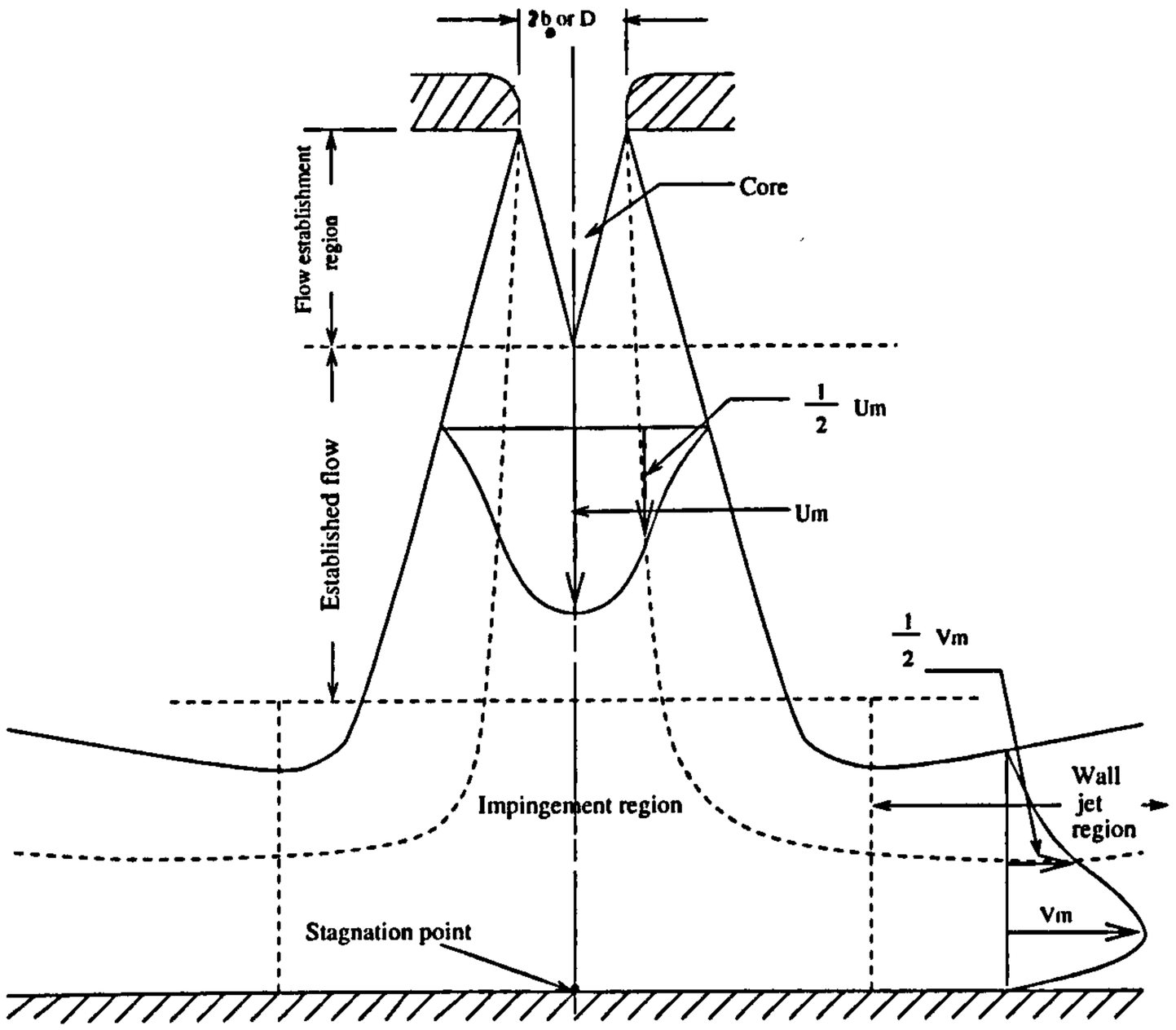

Fig.(3-6):Schematic diagram of velocity field of an impinging jet

when Reynolds number based on nozzle diameter and jet velocity is higher than 1000. However Mc Naughton & Sinclair (1966) report four characteristic jet patterns for free jets:

The dissipated laminar jet, R_{ej}<300, in this case the viscous forces are large compared with the inertial forces, and the jet diffuses rapidly into the surrounding fluid.

Fully laminar jets, 300<R_{ej}<1000, in this case there is no noticeable diffusion of the jet into the surrounding fluid.

Transition or semi-turbulent jet, 1000<R_{ej}<3000.

And finally

Fully turbulent jet, R_{ej}>3000.

These regions are also reported by Polat *et al.* (1989) and Gauntner *et al.* (1970).

3-2-3: Impingement or "stagnation" region

This region is characterized by an increased static pressure as a result of a sharp decrease in the mean axial velocity. At the stagnation point the velocity is zero and the pressure is maximum. According to Gutmark *et al.* (1978), the presence of the impingement plate is not felt beyond one quarter of the distance between the plate and nozzle exit, away from the surface. According to Schauer (1963), the limiting distance for this region is about 1.2 times nozzle diameter from the surface. Exact analytical solutions of the Navier-Stokes equations of motion for the idealized limiting case of the infinitely extended plane are known (see Schlichting, 1968). Those flow patterns are also to be met in the immediate vicinity of the stagnation point of cylinders and spheres in the cross flow. They are typical boundary layer flows with the influence of viscosity being restricted to a thin layer near the solid surface. According to Schlichting (1968), the axial component of the velocity outside this boundary layer may be written as

$$u=-2az \tag{3-16}$$

and the radial component of velocity as

$$v=ar \tag{3-17}$$

where a is a constant. These equations mean that the velocity components are linearly proportional to the distance from stagnation point.

Upon impingement, the jet deflects from the axial direction and starts to

accelerate along the impingement surface. The end of the impingement region is the location where the pressure gradient at the impingement surface becomes zero. Poreh & Cermak (1959) concluded that the stagnation zone could be defined to be the interior of a hemisphere with a centre at the stagnation point and with a radius of 0.05 times the nozzle-to-plate distance for the case of a round jet. According to Saad (1981) this distance is about 0.5 times the nozzle-to-surface spacing for single and noninteracting multiple jets.

3-2-4: Wall jet region

Beyond the stagnation point the flow accelerates in the direction parallel to the wall and develops into a wall jet. The radial (parallel direction to the wall) velocity component, v, initially increases linearly from zero and reaches to a maximum value at a certain distance from the stagnation point and finally tends to zero with r^{-n} in the fully developed wall jet,

$$v_m = \frac{constant}{r^n} \tag{3-18}$$

different values of n have been found by different authors. Glauert (1956) found it as 1.14, according to Poreh *et al.* (1967), n=1.1 and according to Bakke (1957) its value is n=1.12. All of these values gives results very close to experimental values. However for the radial wall jet its value is greater than 1, whereas for a free circular jet in which equation (3-18) acts as centreline velocity decay equation, n is equal to 1; hence the decay of maximum velocity along the plate is faster than that of a free jet. The stabilizing effect of acceleration causes the boundary layer to remain laminar in the stagnation zone, and generally in the decelerating region transition to a turbulent boundary layer take place. The directed flow increases in thickness as the

boundary layer builds up along the solid surface.

3-3: Flow separation and Coanda effect on the cylinder surface

Due to the lack of sufficient information about the behaviour of boundary layer on a cylindrical surface resulting from the impingement of a turbulent jet onto such a surface, and for a better understanding of the flow separation on the cylinder a brief review of flow separation from a cylindrical surface due to parallel flow past a cylinder is carried out in this section.

3-3-1: Flow separation on a cylindrical surface

For the case of parallel flow past a cylinder, by increasing Reynolds number towards 2×10^5 a thin layer gradually appears on the front part of the cylinder, across which the flow velocity changes rapidly. This thin layer is known as the boundary layer. Outside this layer velocity changes rather gently. Inside the boundary layer shear stresses are very large even for fluids with small viscosities, but outside the boundary layer because of less deviation from oncoming flow they are negligible. Thus in the front portion of the cylinder with a large enough Reynolds number, the flow break into two regions: a boundary layer with high shear stresses and an outer flow mainly shearless outside the boundary layer. This front portion is laminar up to $R_e\approx2\times10^5$.

In the rear portion of the cylinder, the laminar boundary layer disconnects from the cylinder. This is known as separation of the boundary layer. After separation the flow forms a rather wide wake filled with vortices. In the wake region, the pressure variation in the transverse direction is rather small, thus the pressure on the rear side of the cylinder is relatively constant from the upper separation point to the lower separation point. This portion is largely turbulent.

As Reynolds number reaches 2×10^5 (critical Reynolds number for this transition), the laminar boundary layer on the cylinder begins to become turbulent. According to actual measurements, the turbulent boundary layer has a much flatter velocity profile across its thickness and therefore carries larger momentum with it. This larger momentum will enable the layer to be carried farther downstream, so that it will penetrate farther into the rear region of the cylinder before it separates from it and due to this later separation, the wake behind the cylinder will become narrower.

Further increasing Reynolds number from the critical value will cause the turbulence in the boundary layer to increase. The turbulent boundary layer must have a laminar sublayer in the immediate vicinity of the cylinder wall, because all the fluid particles at a cylinder wall must assume zero velocity for the case of a stationery cylinder. This sublayer determines the shear stress on the cylinder to be μ times the slope at the wall of the local velocity profile. It is obvious that by changing the boundary layer from laminar to turbulent, the shear stress on the cylinder will increase substantially.

Consider the fluid particles in a band of outer flow adjacent to the top of the cylinder, fig.(3-7). By assuming the same amount of mass flow rate at positions a, b and c, as the flow passage at b is smaller than a and c, so the fluid velocity at b

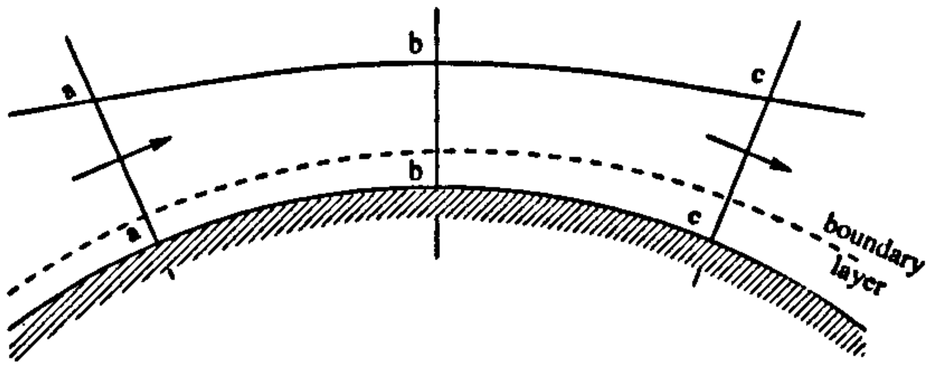

Fig.(3-7): Flow on the top of cylinder

will be larger, therefore flow accelerates from a to b and decelerates from b to c. Accordingly p_b must be smaller than p_a and p_c, so that pressure variation affected on the boundary layer is decreasing from a to b and increasing from b to c. Thus the boundary layer can not separate between a to b but if the adverse pressure gradient is large enough and the momentum of the boundary layer is small enough it may separate from the cylinder surface.

A schematic diagram of velocity profiles in the boundary layer on top of the cylinder beyond the separation point is shown in fig.(3-8). Separation point is characterized by a vertical tangent in the velocity profile indicating that shear stress at the wall ($\mu \partial c/\partial y$) is zero locally and flow close to the wall is going to turn from forward to backward motion. After separation the boundary layer turns backward and this backward region pushes the forward boundary layer from the wall and causes a wide wake further to the rear of the cylinder.

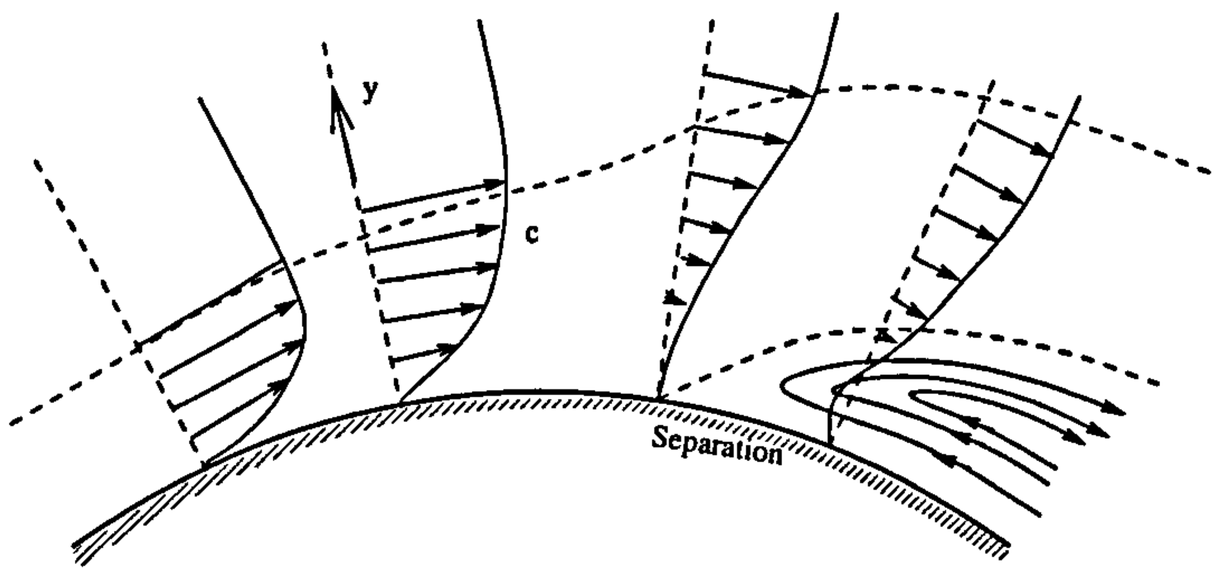

Fig.(3-8): Flow separation on the cylinder

3-3-2: Coanda effect

Jets always drag the surrounding fluid in motion to some degree. If the jet and its environment are of the same fluid, the environment will actually feed the jet continuously with new masses and nearby particles of fluid are dragged along with

the jet. This is a process called entrainment. If however one side of the jet is close enough to a solid surface, the space between the jet and the surface may be partially evacuated because of the constant dragging of the surrounding fluid into the jet. This partial vacuum may be enough to suck the jet to the surface. This is known as the Coanda effect, after the Romanian Engineer Henri Coanda (1885-1972), who made use of it in various aeronautical applications. For the case of fully developed turbulent velocity profile the jet adheres to the cylinder surface due to the Coanda effect. According to Brahma *et al.* (1991), the Coanda effect appears only for large values of H/b, and when the jet has a large turbulent intensity. H is the distance of the cylinder from the slot exit and b is the width of the slot. In such cases the pressure drops to very low values with pressure recovery taking place in the rear of the cylinder. In this region the flow adheres to the cylinder surface, due to the Coanda effect, and without flow separation.

3-4:Previous work on turbulent impinging jet onto flat surfaces:

Work carried out in this section is a review of some of the numerical and experimental studies on turbulent jet impingement. The overall aim of this study is to obtain an understanding of how a turbulent jet impinges onto a flat plate and to obtain a reference condition for assessing the success of numerical simulations. This will also provide an understanding of how a turbulent jet impinges upon a circular cylinder.

3-4-1: Numerical work

Table (1) shows a summary of studies related to (a): plane jet, and (b): axisymmetric jet impingement on flat plates. All these studies for incompressible turbulent impinging jets are performed for two dimensional cases using either a one

equation (k), or a two equation (k-ε) model of turbulence. Among these studies only Looney & Walsh (1984) tested the algebraic stress model (ASM) of turbulence as well as the standard (k-ε) model and found that the results obtained at the stagnation region for the ASM differed markedly from experiments.

The flow at the stagnation region of an impinging jet is pressure driven and therefore good predictions of mean flow and pressure distribution are usually reported. The only way to verify the validity of the results of numerical work in turbulent impinging jets is to compare them with the results of experiments at the same conditions as the numerical study. However, all experimental results are subject to an uncertainty level themselves which is rarely quantified and reported by the authors. Experimental parameters such as turbulence level, jet velocity profile are generally not specified. A flow domain which is assumed to be two dimensional, may have three dimensional effects due to peculiarities of the apparatus.

A majority of studies reported in table (1) use the (k-ε) model of turbulence together with Boussinesq Viscosity Model (BVM). Some studies (Wolfshtein, 1969 and Kotansky *et al.*, 1978) used a one-equation model, which required empirical specification of the turbulence length scale. This is inappropriate in view of the complicated structure of impinging jets. Higher order models, namely (k-ε) and ASM have been used in the most recent studies. Jones & Launder's two-equation turbulence models (1972, 1973) seems to have gained popularity due to their success with the prediction of recirculating flows.These models are relatively easy to understand and economical to use. Since using these models require solving a differential equation for dissipation of turbulent kinetic energy, there is no need to determine the turbulence length scale experimentally.

Table (1): Impinging jet - numerical study

Study	Impinging jet type	Turbulence model	R_{ej}	$H/2b_0$
Wolfshtein (1967)	2D-plane jet	One-equation model	450-22000 11000 43000	8 8 40
Russel & Hatton (1972)	"	"	125000	31
Lampinen (1985)	"	"	-	-
Kotansky & Bower (1978)	"	"	1000, 10000, 100000	2, 4
Looney & Walsh (1984)	"	(k-ε) high Re. model & ASM	22000 30000 42000 50000	43 20 15 30
van Heiningen (1982)	"	(k-ε) high Re. model	5200 8100	6 6
Polat, Mujumdar & Douglas (1985)	"	"	10400 5000 10000 20000	2.6 6 2.6, 6 2.6, 6

Table(1): continued				
Guo & Maxwell (1984)	"	"	5650 25000 43000	67.5 40 40
Huang, Mujumdar & Douglas (1984)	"	"	11000 22000	8, 12, 16 8, 12
Agrawal & Bower (1982)	2D-plane jet	(k-ε) low Re. model	100 10000 130000 158000	2 2 2 2
Amano (1983)	2D-Axisymmetric jet	(k-ε) high Re. model	100000	2-20
Amano & Brandt (1984)	"	"	170000 180000 100000	4, 8, 12 18 2-20
Amano & Sugiyama (1985)	"	"	20000	4, 7, 10

R_{ej} =Jet Reynolds number,

H =spacing between nozzle or slot and flat plate,

b_0 =nozzle or slot half width.

The most detailed study of plane impinging jets was carried out by Wolfshtein (1967). He used Prandtl's one-equation model and solved the equations in stream function-vorticity form for the impingement region only. In comparison with Schauer & Eustis's (1963) experimental data, he found that his predictions for wall shear stress, wall pressure and mean velocity were too low. He attributed the differences to both an inaccurate turbulent viscosity law, and his near wall boundary conditions. Russel & Hatton (1972) repeated aspects of Wolfshtein's work employing similar boundary conditions. Looney and Walsh (1984) solved free and turbulent impinging jets for $8<H/2b_0<43$ and for various Reynolds numbers. In their study a partially or fully developed free jet, depending on $H/2b_0$, was used as an inlet condition at approximately 0.55H above the plate. For the outflow condition they specified the similarity velocity profile of a wall jet at about 0.55H, downstream from the stagnation point. They also tested the modifications to the ($k\sim\varepsilon$) model in the form of Rodi's (1972) suggestion for modelling both strong and week shear flows, and Ljuboja & Rodi's (1979) algebraic stress model for wall-bounded flows, for the case of plane free jets and impinging jets. In the case of a free jet, results improved by using algebraic stress models, but there was not such an improvement for the case of impinging jets. Thus the standard (k-ε) model is preferred because of its relative simplicity. The main effect of algebraic stress models was to lower the peak in k near the stagnation point. van Heiningen *et al.* (1982) carried out some preliminary numerical predictions with the standard (k-ε) model, solving stream function-vorticity equations. They found their stagnation Nusselt number prediction to be too low compared with Gardon and Akfirat's (1965) and as they suggested, the failure was related to their wall functions.

Polat *et al.* (1985) used a high Reynolds number case of the (k-ε) method for multiple jet impingement to predict heat transfer distribution along an impingement plate. They found that for small values of s/H, the stagnation region and separating flow region under the exhaust ports, which were located symmetrically between the jets were close enough to affect the intermediate flow region. Guo and Maxwell (1984) computed the flow in impinging jet configurations by using the high Reynolds number version of the (k-ε) model. Huang *et al.*'s (1982, 1984) results are for a slot jet impinging symmetrically with superimposed cross flow for H/b=8 and R_{ej}=11000. Different inlet conditions were tested by them, but for a fully developed velocity profile, k and ε profiles for a two dimensional channel flow were used. The disagreement between experimental and theoretical results are not more than 25% at any point for no cross flow and a stationery impinging surface. These results indicated that when a small amount of cross flow is introduced to the upstream of the jet at some distance away from the jet centre line, a small recirculation region developed near the impingement surface on that side of the jet where cross flow was introduced. This region disappears at higher cross flows. Agrawal & Bower (1982) in their study of VTOL aircraft design included normal jet impingement in their calculations, employing the low-Reynolds number (k-ε) turbulence model of Jones & Launder (1973), i.e. allowing them to dispense with wall functions. They found an excellent agreement for their ground-plane static pressure results with Schauer & Eustis (1963) and Gardon & Akfirat's (1965) data.

Amano (1983) and Amano & Brandt (1984) made flow predictions for the case of an axisymmetric jet for 2<H/D<40 and 10000<R_{ej}<2000,000. They predicted a secondary peak in the skin friction profiles along the impingement surface for

H/D=2 and R_{ej}>100000. Amano used a modified near-wall treatment in which each dissipation or generation term in the ε-equation is computed in accordance with the k-equation instead of using equilibrium conditions to compute ε near the wall. Amano and Sugiyama (1985) investigated heat transfer under a turbulent axisymmetric jet impinging on a flat plate. They used the high Reynolds number version of (k-ε) model with the wall function method for near-wall treatment. They compared three near-wall models and they claimed an improvement with prediction of stagnation point heat transfer by using their model.

3-4-2: Experimental work

A summary of some of the experimental works which have been carried out on plane turbulent jet impingement onto flat plate are listed in table(2). Nozzle (slot) width, jet Reynolds number and spacing between nozzle and flat plate, normalized by nozzle (slot) width are included. Russell & Hatton's (1972) and Gutmark *et al.*'s (1978) results also present fluctuating velocity measurements. Russell & Hatton, employed a very low nozzle aspect ratio (length/width) of 6 and reported a high initial turbulence intensity due to inadequate plenum-chamber design. The study of Gutmark *et al.* was constrained to centreline measurements at $H/2b_0$=100. In addition Beltaos & Rajaratnam's (1973) and Gardon & Akfirat's (1965) data represent the only extensive measurements for different values of $H/2b_0$.

In comparison with jet impingement onto a flat plate, few studies have been carried out for jet impingement onto a circular cylinder. Sparrow & Alhomoud (1984) studied heat transfer properties of an impinging slot jet onto a circular cylinder in offset and non-offset positions with respect to the jet axis. Brahma *et al.* (1991) experimentally measured the pressure distribution around a circular cylinder

Table (2): Impinging jet - experimental study

Study	$2b_0$ (mm)	R_{ej}	$H/2b_0$
Russel & Hatton (1972)	25.4	125000	31.5
Kotansky & Bower (1978)	38.1	380000	2, 1.5, 1
Beltaos & Rajaratnam (1973)	2.24	5000-10000	14-70
Gutmark, Wolfshtein & Wyananski (1978)	13	30000	100
Gardon & Akfirat (1965)	1.53-6.125	450-22000	2-32

b_0 = Slot half width,

R_{ej}= Jet Reynolds number,

$H/2b_0$ = spacing between slot and flat plate normalized by b_0.

at different eccentricities. They found that the slot jet from a smaller nozzle width spreads in the flow direction at a slower rate compared to a jet of larger nozzle width, and this gives higher stagnation pressure, higher rate of decrease of pressure beyond the stagnation point and lower pressure recovery for the smaller nozzle width. The latter is due to a thinner jet adhering to the cylinder due to the Coanda effect. For offset conditions with the jet axis shifted towards the lower surface they found that the eccentricity shifts the stagnation point to positions lower than the intersection of the jet axis with the cylinder and the pressure distribution becomes unsymmetrical with higher pressure on the upper surface. Kang & Greif (1992) and Chiou & Lee (1993) have studied an air jet impinging with a cylinder from a heat transfer point of view. Finally Tsuchiya *et al.* (1993) have considered a two dimensional turbulent jet impinging with a circular cylinder near a flat plate and placed at different axial distances, offsets between the cylinder and the jet axis, and gaps between the cylinder and flat plate. They found a remarkable increase of separation angle around the cylinder without offset at larger gaps as well as in the region near zero gap, and that the increase of separation angle at larger gaps causes a noticeable decrease for both the base and minimum pressure on the cylinder without offset, resulting in the increase of the drag and drag coefficient.

Only three papers report work concerned with a jet impinging on a circular cylinder. Kang & Greif (1992) only considered low Reynolds number flows and is only relevant in that it provides some indication of numerical procedure used broad indications of the way of pressures and shear stresses may be affected by different jet velocities. No other theoretical studies have been found. Only two experimental papers deal with slot jet impingement onto a circular cylinder. However these have

limited value in that the range of parameters and Reynolds numbers are restricted. For the purpose of cleaning studies these three papers are insufficient to provide parametric evaluations of possible cleaning efficiencies of jets. In consequence the main thrust of the work in this thesis has been to gain a better understanding of the jet interaction with a cylinder by means of a number of experiments and a numerical study.

CHAPTER

4

THEORETICAL MODELLING

4-1 Governing equations

In most practical applications the flow is usually turbulent and therefore time-averaged behaviour of these flows are important. Time-averaged equations for turbulent flow have the same aspect as the equations for laminar flow except the laminar exchange coefficient such as viscosity are replaced by an effective value (laminar plus turbulent)

$$\mu \rightarrow \mu_{eff} = \mu + \mu_t$$

and also

$$p \rightarrow p_s + \frac{2}{3}\varrho k$$

Thus for two dimensional steady turbulent flow of a compressible jet impinging onto a surface, in a rectangular cartesian coordinate system, incorporating the Boussinesq turbulent viscosity concept, the following set of equations describes the velocity field of flow. It is required to mention that the equations related to turbulence parameters will be discussed later in this chapter.

continuity equation:

$$\frac{\partial}{\partial x}(\varrho u) + \frac{\partial}{\partial y}(\varrho v) = 0 \qquad (4\text{-}1)$$

momentum equations:

$$\frac{\partial}{\partial x}(\varrho u^2)+\frac{\partial}{\partial y}(\varrho uv)=\frac{\partial}{\partial x}(\mu_{eff}\frac{\partial u}{\partial x})+\frac{\partial}{\partial y}(\mu_{eff}\frac{\partial u}{\partial y})+S_u \tag{4-2}$$

$$\frac{\partial}{\partial x}(\varrho uv)+\frac{\partial}{\partial y}(\varrho v^2)=\frac{\partial}{\partial x}(\mu_{eff}\frac{\partial v}{\partial x})+\frac{\partial}{\partial y}(\mu_{eff}\frac{\partial v}{\partial y})+S_v \tag{4-3}$$

where u and v are velocities in the horizontal (x) and normal (y) directions, respectively. ϱ is the density and S_u and S_v are the appropriate source terms.

$$S_u=-\frac{\partial p}{\partial x}+\frac{\partial}{\partial x}(\mu_{eff}\frac{\partial u}{\partial x})+\frac{\partial}{\partial y}(\mu_{eff}\frac{\partial v}{\partial x}) \tag{4-4}$$

$$S_v=-\frac{\partial p}{\partial y}+\frac{\partial}{\partial x}(\mu_{eff}\frac{\partial u}{\partial y})+\frac{\partial}{\partial y}(\mu_{eff}\frac{\partial v}{\partial y}) \tag{4-5}$$

where p is the pressure and the effective viscosity μ_{eff} is given by

$$\mu_{eff}=\mu+\mu_t \tag{4-6}$$

In the above equation μ and μ_t are the laminar and the turbulent viscosity, respectively.

By selecting the appropriate generalized transport quantity Φ, and the general exchange coefficient $\Gamma_{\Phi,}$ the Navier-Stokes equations, the continuity equation as well as the energy equation can be represented by the same generalized equation,

$$\nabla\cdot(\varrho u\phi)=\nabla\cdot(\Gamma_\phi\nabla\phi)+S_\phi. \tag{4-7}$$

For the mass conservation or continuity equation, for steady flow,

$$\nabla\cdot(\varrho u)=0. \tag{4-8}$$

In the cartesian-tensor form these equations can be written as

$$\frac{\partial}{\partial x_j}(\varrho u_j \phi)=\frac{\partial}{\partial x_j}(\Gamma_\phi \frac{\partial \phi}{\partial x_j})+S_\phi \qquad (4\text{-}9)$$

$$\frac{\partial}{\partial x_j}(\varrho u_j)=0 \qquad (4\text{-}10)$$

where the subscript j can take the values 1,2 denoting two space coordinates. When a subscript is repeated in a term, a summation of two terms is implied.

4-2 Turbulence Modelling

In turbulent flow the actual velocity at every point is considered to be the sum of the time averaged velocity and the fluctuating component of that velocity.

$$u=\bar{u}+u' \qquad (4\text{-}11)$$

$$v=\bar{v}+v' \qquad (4\text{-}12)$$

By substituting these values to the conservation of momentum equation and dropping the bar sign, for turbulent flow :

$$\frac{\partial}{\partial t}(\varrho u_i)+\frac{\partial}{\partial x_j}(\varrho u_i u_j)=-\frac{\partial p}{\partial x_i}+\frac{\partial}{\partial x_j}[\mu(\frac{\partial u_i}{\partial x_j}+\frac{\partial u_j}{\partial x_i})]-\frac{\partial}{\partial x_j}(\overline{\varrho u_i' u_j'}) \qquad (4\text{-}13)$$

where $\overline{\varrho u'_i u'_j}$ is known as **Reynolds stresses** which require modelling assumptions and are modeled using k- ε or algebraic stress models. Models of varying complexity have been recommended by different authors, but for the case of impinging jets only one-equation, two-equation and algebraic stress models are used and these three cases of modelling are discussed in this chapter.

According to the Bossinesq hypothesis, the Reynolds stress is equal to:

$$\overline{\varrho u_i' u_j'}=\frac{2}{3}\varrho k\delta_{ij}-\mu_t(\frac{\partial u_i}{\partial x_j}+\frac{\partial u_j}{\partial x_i}) \qquad (4\text{-}14)$$

where:

k=turbulent kinetic energy

δ_{ij}= 1 if i=j

δ_{ij}= 0 if i≠j

μ_t=turbulent viscosity.

By analogy to molecular viscosity

$$\mu_t \sim \nu l_m$$

where l_m=turbulence length scale.

In most of the mixing length turbulence models, the velocity is calculated from the mixing length and mean velocity gradient according to:

$$\nu = l_m \sqrt{\frac{1}{2}\left(\frac{\partial u_i}{\partial x_j}+\frac{\partial u_j}{\partial x_i}\right)^2} \qquad (4\text{-}15)$$

and the viscosity becomes:

$$\mu_t = \varrho l_m^2 \sqrt{\frac{1}{2}\left(\frac{\partial u_i}{\partial x_j}+\frac{\partial u_j}{\partial x_i}\right)^2} \qquad (4\text{-}16)$$

Many empirically derived expressions for mixing length and turbulent viscosity for the case of attached wall shear layers have been proposed by different authors, among them the expressions derived by van Driest (1956) from empirical data, and by Patankar and Spalding (1970) based on modification to van Driest's proposal are important. In these cases:

$$l_m = ky\left[1-\exp\left(-\sqrt{\left(\frac{\tau}{\varrho}\right)}y/\nu A^+\right)\right] \qquad (4\text{-}17)$$

In this equation A^+ according to van Driest is constant and equal to 26, and y is the

distance from the wall. The velocity scale is then

$$\nu = l_m \left| \frac{\partial u}{\partial y} \right| \tag{4-18}$$

and the resulting expression for μ_t is:

$$\mu_t = \varrho k^2 y^2 [1 - \exp(-\sqrt{\frac{\tau}{\varrho}} y / \nu A^+)]^2 \left| \frac{\partial u}{\partial y} \right| \tag{4-19}$$

The main problem with mixing length models is their lack of generality. Specification of the mixing length is dependent on flow geometry and becomes very difficult for geometries with multiple walls and separated regions. Except for special cases, mixing length models have very limited use in most C.F.D. problems.

4-2-1 One-equation models

The one-equation models are the simplest turbulence models. In this model along with the turbulence kinetic energy equation, a relation for the length scale is required to describe the dissipation rate and to complete the set of governing equations. In most one-equation models the following kinetic energy equation is solved:

$$\frac{\partial k}{\partial t} + u_i \frac{\partial k}{\partial x_i} = \frac{\partial}{\partial x_i} \left(\frac{\nu_t}{\sigma_k} \frac{\partial k}{\partial x_i} \right) + G - \epsilon \tag{4-20}$$

where

$$G = \nu_t \left(\frac{\partial u_i}{\partial x_j} + \frac{\partial u_j}{\partial x_i} \right) \frac{\partial u_i}{\partial x_j} \tag{4-21}$$

and the dissipation rate is determined from:

$$\epsilon = C_D \frac{k^{3/2}}{L_D} \tag{4-22}$$

where L_D is the length scale of turbulence dissipation.

By using the Kolomogorov-Prandtl expression for turbulent viscosity,

$$\nu_t = C_\mu' \sqrt{k} L_\mu \tag{4-23}$$

where L_μ is length scale of turbulence. In one-equation models L_D and L_μ are determined from empirical relations. According to Wolfshtein (1967) and Russell & Hatton (1972)

$$\frac{L_D}{y} = 1 - \exp(-A_D Re_T) \tag{4-24}$$

$$\frac{L_\mu}{y} = 1 - \exp(A_\mu Re_T) \tag{4-25}$$

where A_μ=0.016, A_D=0.263, C_μ'=0.22, C_D=0.416 and σ_k=1.53, for large values of y (distance from the wall)

$$L_D = L_\mu = L \tag{4-26}$$

and for small values of y

$$\frac{L_D}{y} = A_D Re_T \tag{4-27}$$

$$\frac{L_\mu}{y} = A_\mu Re_T \tag{4-28}$$

As already mentioned, the empirical determination of length scale is especially difficult in complex geometries and is the major parameter limiting one-equation models.

4-2-2 Two-equation models

Many attempts have been made to calculate the turbulent length scale by means of a transport equation. Several two-equation turbulence models such as *k~kl*, *k~w* and *k*-ε are recommended, where *k* is the turbulence energy and equal to

$$k \equiv \frac{1}{2}\overline{u_i u_j} \tag{4-29}$$

l is the turbulence length scale which can be described in terms of k, ε and a constant C_D

$$l = C_D \frac{k^{3/2}}{\epsilon} \tag{4-30}$$

w is a time average square of vorticity fluctuations which can also be defined in terms of k, ε and C_D

$$w = (\frac{\epsilon}{C_D k})^2 \tag{4-31}$$

and ε in homogeneous turbulence is equal to:

$$\epsilon = \nu \overline{\frac{\partial u_i}{\partial x_j}\frac{\partial u_i}{\partial x_j}} \tag{4-32}$$

The *k~kl* model has been used in a large number of turbulent flows, with and without the presence of a solid wall, for example by Rodi & Spalding (1970) and Ng and Spalding (1970, 1972). The *k~w* model has been described in different papers by Spalding (1969, 1971, 1972) and Gibson and Spalding (1972). Launder and Spalding (1974), after an investigation on different kinds of two-equation models, namely *k~kl*, *k~w* and *k*~ε model, judged that the various two equation models are different only

in mathematical form and not in content. The k~ε model is the only one which agrees well with the experimental data at locations far from the wall. For this reason the developers of k~kl and k~w models have to suggest that one or more of the constants should vary with y/l and only for the k~ε model is this adjustment unnecessary.

The k-ε model was proposed first by Harlow and Nakayama (1968) and discussed in more detail by Jones and Launder (1972, 1973). In both models a transport equation for the dissipation rate of turbulence energy is solved to obtain the distribution of turbulence length scale. The general approach is the same for both models. The only wall flow considered by Harlow and Nakayama was flow in a pipe. For this case the agreement with experimental data was poor and it was because of their low Reynolds number proposal, which according to Jones and Launder (1972) was chiefly at fault. The k-ε model of Jones and Launder (1972) has been tested widely and agreement with experimental data is satisfactory.

4-2-2-1 The high Reynolds-number form of the model

It is assumed by Jones and Launder (1972) that the turbulent shear stress is equal to:

$$\overline{\varrho u_i u_j} = -\mu_t \frac{\partial u}{\partial y} \tag{4-33}$$

Referring to the work of Emmons (1954), in this model the turbulent viscosity is determined by the local values of density, turbulence kinetic energy k, and turbulence length scale l according to:

$$\mu_t = C_\mu' \varrho k^{\frac{1}{2}} l \tag{4-34}$$

where C_μ' is a constant. In this model an equation for k is solved and as mentioned

already the length scale is determined by solving a transport equation for the dissipation rate of turbulence kinetic energy ε, as:

turbulence energy

$$\frac{\partial}{\partial t}(\varrho k)+\frac{\partial}{\partial x_i}(\varrho u_i k)=\frac{\partial}{\partial x_i}(\frac{\mu_t}{\sigma_k}\cdot\frac{\partial k}{\partial x_i})+G-\varrho\epsilon \qquad (4\text{-}35)$$

energy dissipation

$$\frac{\partial}{\partial t}(\varrho \epsilon)+\frac{\partial}{\partial x_i}(\varrho u_i \epsilon)=\frac{\partial}{\partial x_i}(\frac{\mu_t}{\sigma_\epsilon}\cdot\frac{\partial \epsilon}{\partial x_i})+C_1\frac{\epsilon}{k}G-C_2\varrho\frac{\epsilon^2}{k} \qquad (4\text{-}36)$$

where G is the generation of k and is given by

$$G=\mu_t(\frac{\partial u_j}{\partial x_i}+\frac{\partial u_i}{\partial x_j})\frac{\partial u_j}{\partial x_i} \qquad (4\text{-}37)$$

At high Reynolds numbers, ε may be assumed proportional to $\rho k^{3/2}/l$ so, the turbulent viscosity may be written as:

$$\mu_t=C_\mu\varrho\frac{k^2}{\epsilon} \qquad (4\text{-}38)$$

where C_μ is a constant.

The coefficients C_1, C_2, C_μ, σ_k and σ_ε are empirical constants and according to the recommendations of Launder *et al.* (1972), they take the values given in table(4-1):

Table (4-1): The values of empirical constants in high Reynolds number form of the k-ε model of turbulence.

C_μ	C_1	C_2	σ_k	σ_ε
0.09	1.44	1.92	1.0	1.3

The above constants have been found appropriate to plane jets. For the case of axisymmetric jets, two of the above constants known as C_2 and C_μ need modification. Launder *et al.* (1972) has recommended the following relations for them based on the work of Rodi (1972):

$$C_\mu = 0.09 - 0.04f \tag{4-39}$$

$$C_2 = 1.92 - 0.0667f \tag{4-40}$$

where

$$f = \left| \frac{y}{2\Delta u} \left(\frac{\partial u_{cl}}{\partial x_l} - \left| \frac{\partial u_{cl}}{\partial x_l} \right| \right) \right|^{0.2} \tag{4-41}$$

Here u_{cl} is velocity at and in the direction of the symmetry axis of the jet, y is the radial width of the mixing region and Δu is axial direction velocity difference across the width of the region. σ_k and σ_ε in equations (4-35) and (4-36) represent respectively the diffusion rates of k and ε.

Hanjalic (1970) has found that the equations (4-35) and (4-36) for k and ε may provide satisfactory predictions of a variety of high Reynolds number flow near the wall and away from it.

4-2-2-2 The low Reynolds number form of the model

In the design of many thermal process components it is very important to recognize the behaviour of turbulent motion immediately adjacent to the wall. The presence of a wall gives rise to a finite region of the flow in which the turbulence Reynolds number is low. In the case of high turbulence Reynolds number, near the wall, special wall functions are required to link the wall to the main flow, but in the case of low Reynolds number versions of the model, the calculations can be carried

out right to the wall. According to Jones and Launder (1973), the introduction of the flow within the viscous layer adjacent to the wall requires that the high Reynolds number version of the model be expanded in three ways:

(i) viscous diffusion of k and ε must be included,

(ii) the terms containing constant values, C, in equations (4-36) and (4-38) will become dependent upon the Reynolds number of the turbulence,

(iii) additional terms allowing for the fact that dissipation processes are not isotropic, must be added.

Under these conditions, the recommended relations by Jones and Launder (1973) are:

turbulence energy:

$$\frac{\partial}{\partial t}(\varrho k)+\frac{\partial}{\partial x_i}(\varrho u_i k)=\frac{\partial}{\partial x_i}[(\frac{\mu_t}{\sigma_k}+\mu)\frac{\partial k}{\partial x_i}]+G-\varrho\epsilon-2\mu(\frac{\partial k^{1/2}}{\partial x_i}) \qquad (4\text{-}42)$$

energy dissipation:

$$\frac{\partial}{\partial t}(\varrho\epsilon)+\frac{\partial}{\partial x_i}(\varrho u_i\epsilon)=\frac{\partial}{\partial x_i}[(\frac{\mu_t}{\sigma_\epsilon}+\mu)\frac{\partial\epsilon}{\partial x_i}]+C_1\frac{\epsilon}{k}\cdot G-C_2\varrho\frac{\epsilon^2}{k}-2\nu\mu_t(\frac{\partial^2 u_i}{\partial x_j\partial x_i})^2 \qquad (4\text{-}43)$$

where again G is a generation function and described in equation (4-37).

The turbulent viscosity is obtained from equation (4-38). In the above equations C_1, σ_k and σ_ϵ have the same values for the case of high Reynolds number, but C_μ and C_2 are varying with turbulence Reynolds number according to:

$$C_\mu=0.09\exp[\frac{-2.5}{1+R_{e_T}/50}] \qquad (4\text{-}44)$$

$$C_2=1.92[1.0-0.3\exp(-R_{e_T}{}^2)] \qquad (4\text{-}45)$$

In the right hand side of equation (4-42), the extra term

$$2\mu(\frac{\partial k^{1/2}}{\partial x_i})$$

has been included for computational rather than physical reasons to let ε go to zero at the wall. The extra term

$$2\nu\mu_t(\frac{\partial^2 u_i}{\partial x_j \partial x_i})^2$$

in equation (4-43) has been included to produce satisfactory variation of k with distance from the wall.

The capabilities of the *k*~ε model have been examined by different authors. Launder *et al.* (1972) in the prediction of free shear flows, have tested the *k*~ε model for the case of the decay of plane jet in a moving stream and they found that the predictions obtained with the *k*~ε model are in satisfactory agreement with experiment throughout the region of measurement. In the other works for the cases of wall jets, flow in the pipes, boundary layer on turbine blades, film cooling, coaxial jets, cavity flow, flow through square-sectioned ducts, etc..... , after a review by Launder and Spalding (1974) they found that the *k*~ε model is the simplest kind of model that permits good prediction of both near-wall and free shear flow phenomena. Sometimes, for example, as in the case of the wall jet examined by Matthews and Whitelaw (1971) turbulence generated away from the wall may cause uncommonly high levels of the length scale near a wall. Amano (1983) found that for the case of a turbulent axisymmetric jet, the use of the *k*~ε model results in good predictions of velocity distribution and pressure within 5 percent of the measured values, but the

near-wall model for kinetic energy and turbulent shear stress at high Reynolds number gives predictions of skin friction coefficient within only 25 percent of measured values. According to Polat *et al.* (1989) the limitations of k~ε models are:

(i) They are based on an eddy viscosity / diffusivity concept which is not valid under all flow conditions,

(ii) in these models the eddy viscosity and diffusivity are assumed to be isotropic, and

(iii) additional effects such as buoyancy, stream line curvature, etc., are not included in these models.

4-2-3 Algebraic stress model

In accordance with a suggestion by Rodi (1972), if the convection and diffusion terms are to be proportional to those of the k equation multiplied by the ratio $u_i u_j/k$, the following equation may result from which, turbulent viscosity can be calculated by using equation (4-14).

$$-\varrho(\overline{u_i u_j}-\frac{2}{3}\delta_{ij}k)=\frac{2}{3}(1-\alpha)[\frac{C_{s1}-1+\alpha G/\epsilon}{(C_{s1}-1+G/\epsilon)^2}]\frac{\varrho k^2}{\epsilon}(\frac{\partial u_i}{\partial x_j}+\frac{\partial u_j}{\partial x_i}) \qquad (4\text{-}46)$$

where α and C_{s1} are constants related to mean strain and turbulence interaction effects of pressure-strain relation. As recommended by Hanjalic and Launder (1972), α=0.06 and C_{s1}=2.486. In deriving equation (4-46), according to Rodi (1972) the surface integral (and hence wall effects) in the pressure-strain correlation is neglected and the stress redistribution part of the pressure-strain correlation which is important in the stagnation region of an impinging jet is included . In equation (4-46) if G/ε=1 then the turbulent viscosity reduces to:

$$\mu_t = C_\mu \frac{\varrho k^2}{\epsilon}$$

here, for the standard k~ε model C_μ=0.09.

According to Ljuboja and Rodi (1979) if the surface integral (and hence wall effects) in the pressure-strain correlation term of the Reynolds stress equation is included, the following turbulent viscosity expression results:

$$\mu_t = F_D G_1 G_2 \frac{\varrho k^2}{\epsilon} \qquad (4\text{-}47)$$

where

$$G_1 = \frac{1+1.5\alpha C_2' f/(1-\alpha)}{1+1.5\alpha C_1' f/C_{s1}}$$

$$G_2 = \frac{1-2\alpha C_2 G f/(C_{s1}\epsilon-\epsilon+\alpha G)}{1+2C_1' f/(C_{s1}-1+G/\epsilon)}$$

$$F_D = \frac{2(1-\alpha)(C_{s1}-1+\alpha G/\epsilon)}{3C_{s1}(C_{s1}-1+G/\epsilon)}$$

$$f = \min(1.0, \frac{k^{3/2}}{C_w y \epsilon})$$

where, y=distance from the wall and

C_{s1}=2.2 α=0.55 C_1'=0.75 C_2'=0.45 C_w=4.4

The algebraic expressions (4-46) or (4-47) together with k and ε equations of k~ε model has been applied by Looney and Walsh (1984) to a single turbulent impinging jet, and they found that the results obtained by using the algebraic stress model at the

stagnation point differed markedly from experiments.

4-3 Boundary conditions

After selecting the required model of turbulence, which is the high Reynolds number form of the k~ε model of turbulence for the present study, a careful choice of boundary conditions is the final step to complete the statement of the problem. It is required for the numerical solution to produce results of physical significance without making excessive demands of computing time. The size and shape of the mesh also has a significant influence on the capability of the numerical calculation. For the case of the jet impinging onto a flat plate, a contracting grid system is used in the x-direction and an expanding grid system is adopted in the y-direction; in this way, finer grids near the wall and within the jet are obtained. For the case of the jet impinging onto a circular cylinder a uniform grid is used in both directions by fixing grid points on internal lines using linear interpolation.

The boundary conditions, referring to Fig (4-1) are:

4-3-1 Boundary I - nozzle exit

The velocity profile at the nozzle exit is under the influence of the nozzle design. In the present study a 5.5 power velocity profile at the nozzle exit is considered. For this case the boundary conditions at nozzle exit are:

$$u=u_j[1-0.3412(\frac{\Delta Y}{b_0})^{5.5}]$$

$$k=k_j=iu_j$$

$$\varepsilon=\varepsilon_j=\frac{k_j^{3/2}}{\lambda b_0} \qquad (4\text{-}48)$$

where i is turbulence intensity (i=0.005), λ is length scale constant, b_0 is the half width of the slot and ΔY is the distance from slot centre.

4-3-2 Boundary II - entrainment boundary

Fluid enters the solution domain at an unknown rate along this boundary. Without any confinement this boundary can only be approximated. The usual boundary condition here is zero gradients for all variables in the direction normal to the boundary. For the case of jet impingement onto a cylindrical surface, the constant pressure boundary is assumed in addition to the above mentioned conditions.

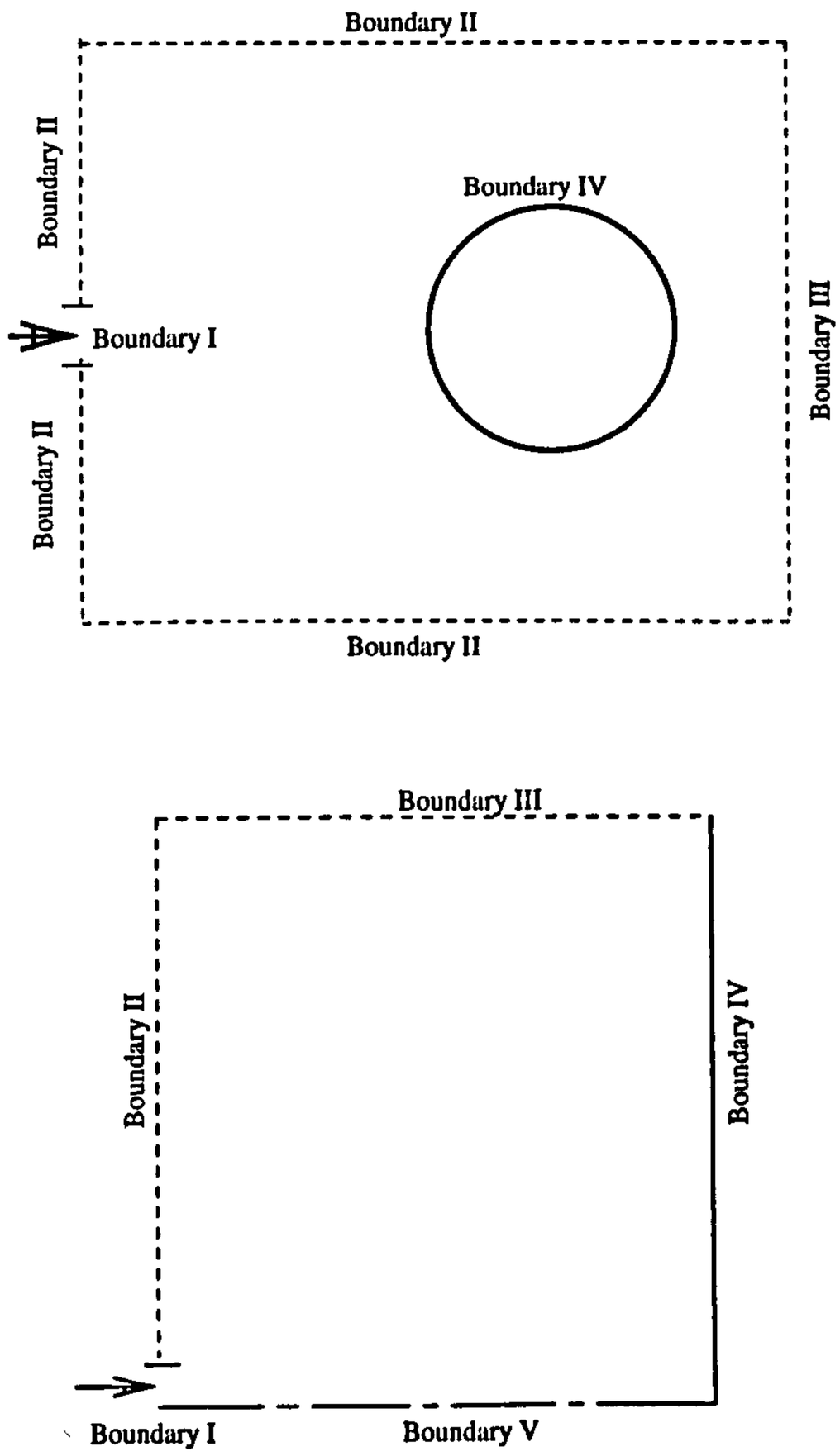

Fig(4-1): boundary definitions for jet impinging onto a)flat plate, b)circular cylinder

4-3-3 Boundary III - outflow

For the case of jet interaction with a flat plate, the usual approach for this boundary is to assume a developing flow parallel to the impingement plate, which means that axial velocity is equal to zero, and the gradient of all the other variables in the direction normal to the boundary are set to zero. In both cases velocities at the outlet plane are obtained by requiring overall mass balance for the entire flow domain in addition to the above conditions for the flat plate.

4-3-4 Boundary IV - impingement surface

The no slip conditions are imposed at this boundary, the gradients of k and ε may be set to zero.

4-3-5 boundary V - axis of symmetry (for the case of flat plate only)

At the axis of symmetry, the velocity v is set to zero and the gradients of all other variables are set to zero.

4-4 Near-wall modelling

The high Reynolds number form of turbulence modelling is used in the present study. This model is valid only for fully turbulent flows. Near the solid wall there are unavoidable regions where the local Reynolds number of turbulence is too small and the high Reynolds version of the turbulence model can not handle these regions. Therefore a bridging technique in the form of suitable wall functions is required.

Wall functions have been suggested and used by many authors including Spalding (1967), Wolfshtein (1969) and Patankar and Spalding (1970). Chieng and Launder (1980) proposed an improved version of wall functions which evaluates the mean generation rate and mean dissipation rate in the k equation, in a numerical cell

adjacent to the wall. This method has been applied to an axisymmetric impinging jet problem by Amano (1983) and Amano *et al.* (1982, 1984, 1985).

In the region close to the wall the local Reynolds number changes considerably and the accepted approach is dependent upon the local Reynolds number y_p^+

$$y_p^+ = \frac{u_\tau y_p}{\nu} \tag{4-49}$$

based on distance y_p from the wall, fig.(4-2), and the friction velocity u_τ is:

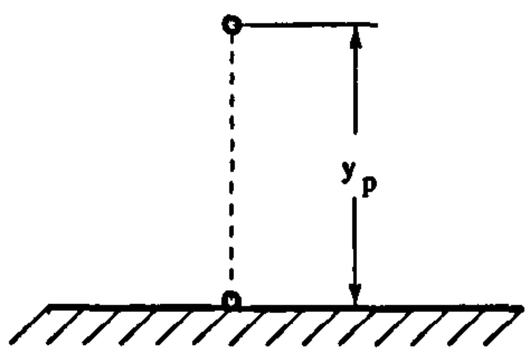

Fig(4-2): The near wall nodes

$$u_\tau = \sqrt{\frac{\tau_w}{\varrho}} \tag{4-50}$$

The wall region itself is made up of three zones:

(i) the *viscous sublayer,* where the viscous effects are dominant

$$0 < y^+ < 5$$

(ii) the *inertial layer,* where the flow is assumed to be completely turbulent

but $\tau = \tau_w$

$$30 < y^+ < 400$$

(iii) the *transition or buffer zone*, where the flow is neither completely dominated by viscous effects, nor completely turbulent.

$$5<y^+<30$$

In this approach, as in many engineering calculations, the buffer layer is discarded by defining a poin*t* $y^+=11.63$, the intersection of the linear velocity profile in the viscous sublayer with the logarithmic velocity profile in the inertial layer. Below this point the flow is assumed to be purely viscous and above it, the flow is purely turbulent. So, by defining

$$u^+=\frac{u}{u_\tau}$$

for $y^+\leq 11.63$

$$\frac{\mu_t}{\mu}\ll 1 \qquad \tau\cong\tau_w \qquad u^+=y^+$$

and for $y^+> 11.63$

$$\frac{\mu_t}{\mu}\gg 1 \qquad \tau\cong\tau_w \qquad u^+=\frac{1}{\kappa}\ln(Ey^+)$$

where κ = von Karman constant =0.4187,

and E is the integration constant which depends on the magnitude of variation of shear stress across the layer and the roughness of the wall. Normally its value is taken as : E=9.793 .

The commonly used wall function is known as "the logarithmic law of the wall". According to this law the shear stress is assumed to be constant near the wall up to the turbulent region of the flow. By considering node P, which is the first node next to the wall and y_p is its distance to the wall, Fig(4-2). The wall shear stress is

equal to:

$$\tau_w=\varrho\kappa C_\mu^{1/4}k_p^{1/2}\frac{u_p}{\ln(Ey_p^+)} \tag{4-51}$$

where

$$y_p^+=\frac{y_p(\tau_w/\varrho)^{1/2}}{\nu}\approx y_p\varrho C_\mu^{1/4}k_p^{1/2}/\mu \tag{4-52}$$

Assuming local equilibrium

$$k_p=(\frac{\tau_w}{\varrho})C_\mu^{-1/2} \tag{4-53}$$

and for extension to the buffer and viscous sublayer in k-balance, ε *is* modified as

$$\int_v \epsilon dv\approx C_\mu^{3/4}k^{3/2}u^+\delta v/y \tag{4-54}$$

with

$$u^+=y^+$$

for $y^+\leq 11.63$ and

$$u^+=\frac{1}{\kappa}\ln(Ey^+)$$

for $y^+>11.63$.

According to Chieng and Launder (1980), the near-wall flow is composed of two layers, laminar inside the viscous sublayer and fully turbulent beyond this point. It is assumed that the turbulent kinetic energy has a parabolic distribution inside the viscous sublayer and a linear variation beyond this region. Within the viscous sublayer the turbulent shear stress is zero and at the edge of sublayer it has an abrupt

increase, beyond this it varies linearly. This model is summarized in Fig(4-3). In the numerical calculation the grid is so arranged that the near-wall cell is large enough for the node P to be always outside the viscous sublayer. The viscous sublayer thickness is determined such that the Reynolds number y^+>11.5, and according to Amano (1983) taken equal to 20.

In Chieng and Launder's (1980) model, the treatment illustrated in Fig(4-3) was applied only for the k equation. In the model developed by Amano and Jensen (1982) the treatment for evaluating the mean generation and destruction rates are incorporated into the ε equation. The present study is carried out by using this version of near wall modelling. Finally the mean rate of generation of turbulent

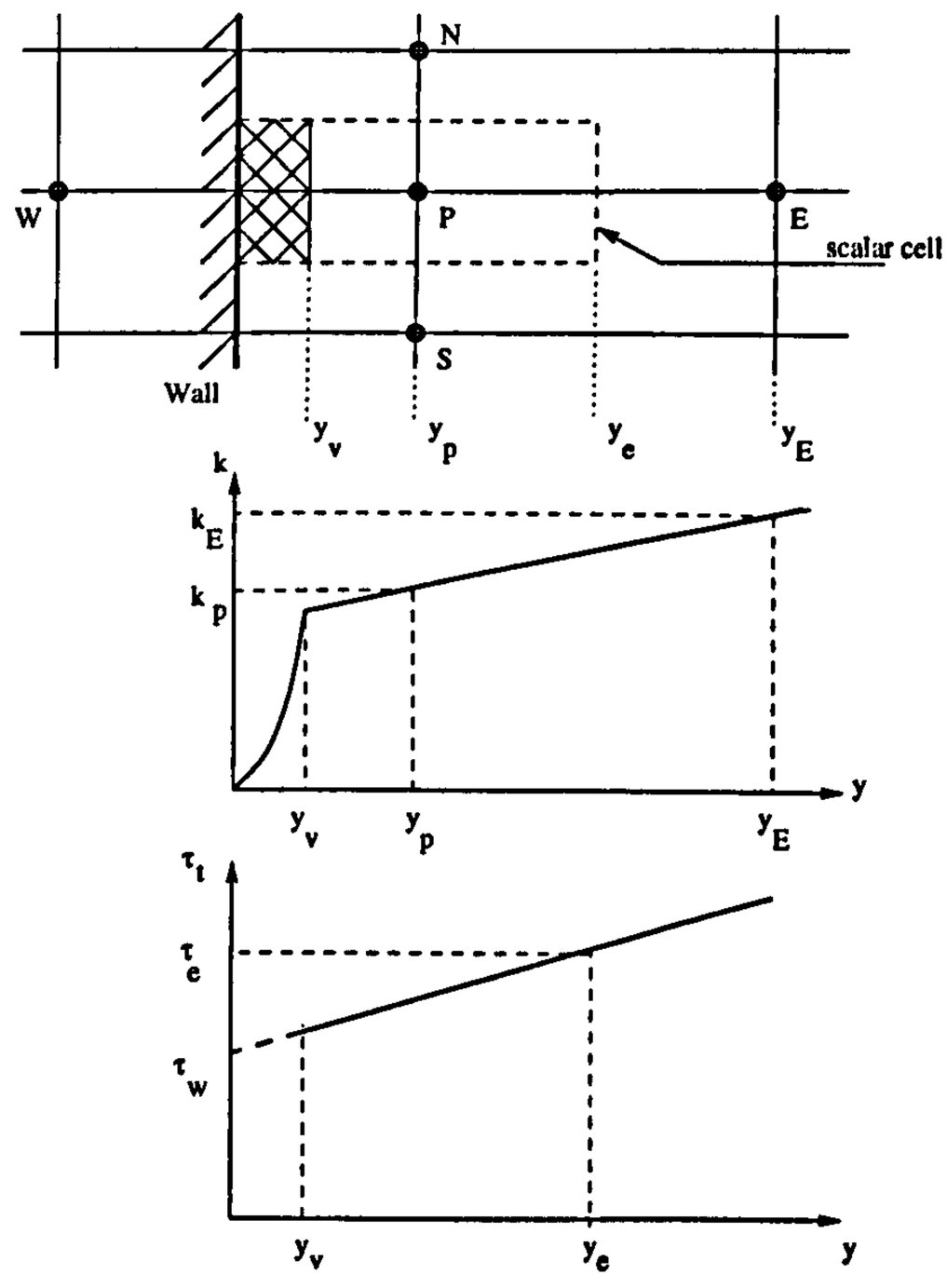

Fig(4-3): Physical model for near wall condition

kinetic energy near a wall from Amano (1983) is equal to:

$$\overline{G}=\frac{\tau_w(u_e-u_v)}{y_e}+\frac{\tau_w(\tau_e-\tau_w)}{\varrho C_\mu^{1/4}k_v^{1/2}y_e}(1-\frac{y_v}{y_e}) \tag{4-55}$$

4-5 Mathematical formulation used in the present study

The equations used for defining the mean velocity field in turbulent flow of a compressible jet impinging onto a cylindrical surface may be given in general form as

$$\frac{\partial}{\partial x_j}(\varrho u_j\phi)=\frac{\partial}{\partial x_j}(\Gamma_\phi\frac{\partial\phi}{\partial x_j})+S_\phi \tag{4-3}$$

where Φ stands for dependent variables u, v, k and ε, and S_Φ is the corresponding source term. These equations are tabulated in Table(4-2).

Table(4-2): Summary of equations solved

Equation	Φ	Γ_Φ	S_Φ
Continuity	1	0	**0**
x-Momentum	u	μ_{eff}	$-\frac{\partial p}{\partial x}+\frac{\partial}{\partial x}(\mu_{eff}\frac{\partial u}{\partial x})+\frac{\partial}{\partial y}(\mu_{eff}\frac{\partial v}{\partial x})$
y-momentum	v	μ_{eff}	$-\frac{\partial p}{\partial y}+\frac{\partial}{\partial x}(\mu_{eff}\frac{\partial u}{\partial y})+\frac{\partial}{\partial y}(\mu_{eff}\frac{\partial v}{\partial y})$
Turbulence energy	k	μ_t/σ_k	**G-ρε**
Energy dissipation	ε	μ_t/σ_ε	$C_1\frac{\epsilon}{k}G-C_2\varrho\frac{\epsilon^2}{k}$

where

$$\mu = C_\mu \varrho \frac{k^2}{\epsilon}$$

$$\mu_{eff} = \mu + \mu_t$$

and

$$G = \mu_t \left(\frac{\partial u_j}{\partial x_i} + \frac{\partial u_i}{\partial x_j} \right) \frac{\partial u_j}{\partial x_i}$$

C_μ	C_1	C_2	σ_k	σ_ε
0.09	1.44	1.92	1.0	1.3

The system of equation is completed with the equation of state:

$$P = \varrho RT$$

where P and T are absolute pressure and temperature, and R is the gas constant of air.

This set of equations, as well as boundary conditions mentioned in section 4-3, are employed for numerical calculation of the present problem. The details of numerical solution is the subject of next chapter.

CHAPTER

5

NUMERICAL METHOD OF SOLUTION

5-1: Construction of control volumes

The forms of differential equations for determining the flow field around a circular cylinder or on a flat plate due to a compressible turbulent jet impinging onto these surfaces were introduced in the previous chapter. The aim of this chapter is to introduce the numerical solution method of these equations by derivation of finite difference equations. The first step in deriving the finite difference equations is the establishment of a suitable grid and storage locations for the variables. The solution domain is discretized into a regular and rectangular mesh with arbitrary spacing. The finite difference equations for each variable are derived by approximate integration of parent differential equations over each control volume. The typical control volume is shown in fig.(5-1). The variables are stored at different locations of the grid, pressure p and other scalar variables are located at the intersections of grid and surrounded by scalar cell. The velocities are located at the boundaries of scalar cells midway between the pressures which drive them, and so the pressure gradients driving velocities u and v are easy to evaluate. This is the main advantage of staggered grid system.

5-2: Conservation equations and their finite difference form

The control volume of a cell in two dimensional form is shown in fig.(5-2), in which the points n, s, w, e, denotes cell boundaries. The conservation law for

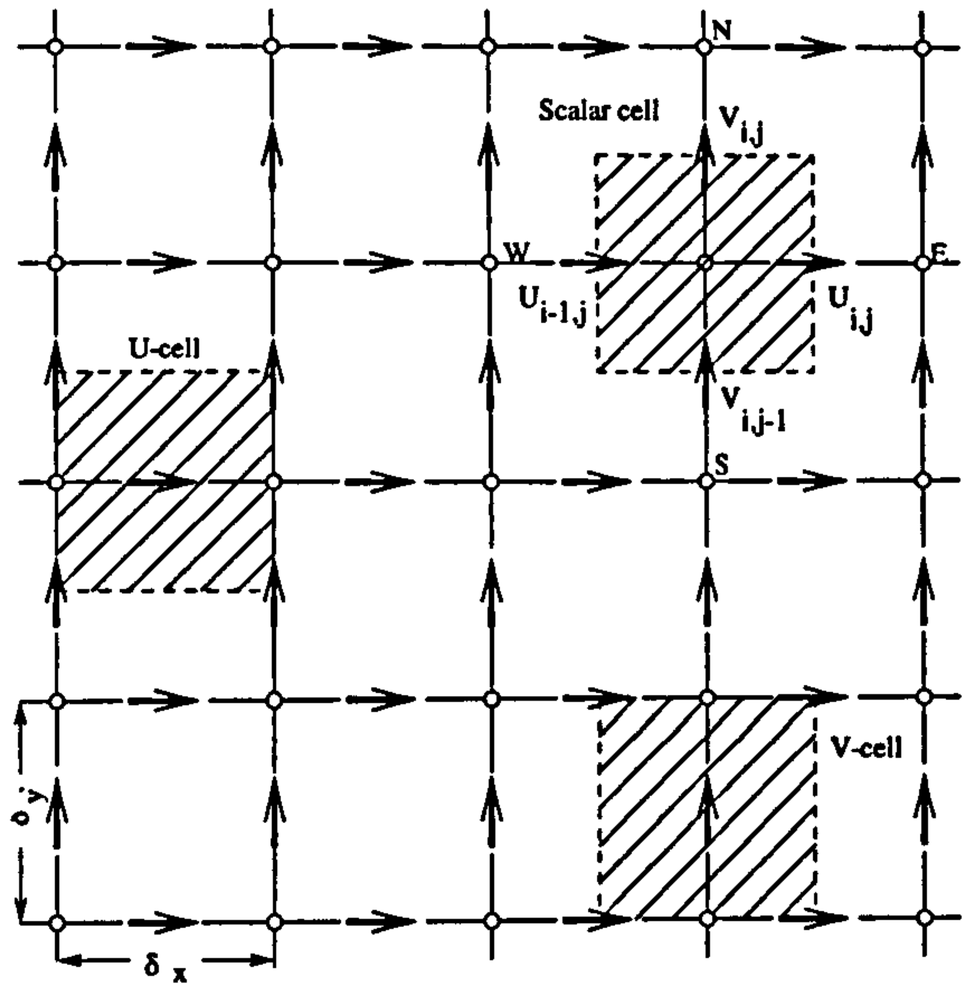

location	variable stored
+	P, T, m_j, K, E
→	U
↑	V

Fig.(5-1):Staggered rectangular mesh illustrating different control volumes.

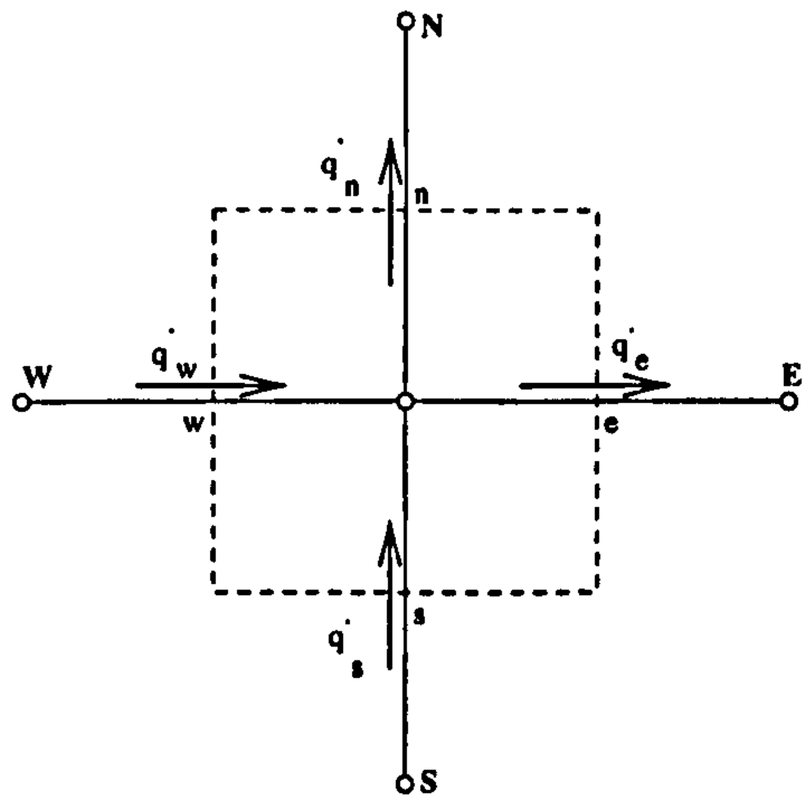

Fig.(5-2): Control volume of a cell.

transport of any extensive property Φ(mass, momentum, energy, etc.) may be expressed as:

rate of increase of Φ in a cell = (net rate of inflow of Φ to the cell by convective fluxes) + (net rate of inflow of Φ to the cell by diffusive fluxes) + (rate of generation of Φ within the cell).

This expression may be shown mathematically as:

$$\frac{\Delta(\varrho\phi)}{\Delta t}dv = q^{\cdot}_{w} - q^{\cdot}_{e} + q^{\cdot}_{s} - q^{\cdot}_{n} + \oint_{v} S_{\phi}\,dv$$

where

Φ= u, v, T, m_j, k, e (or unity for Φ=mass),

$q^{\cdot}$= total (convective + diffusive) fluxes,

S_{Φ}= generation per unit volume.

For steady flow

$$\frac{\Delta(\varrho\phi)}{\Delta t} = 0.$$

The convective and diffusive fluxes are derived by considering steady one-dimensional transport across the cell boundaries, since it is required that in one-dimensional limit the fluxes must be exactly calculated. By referring to Patankar (1980), and fig.(5-3), the governing differential equations are:

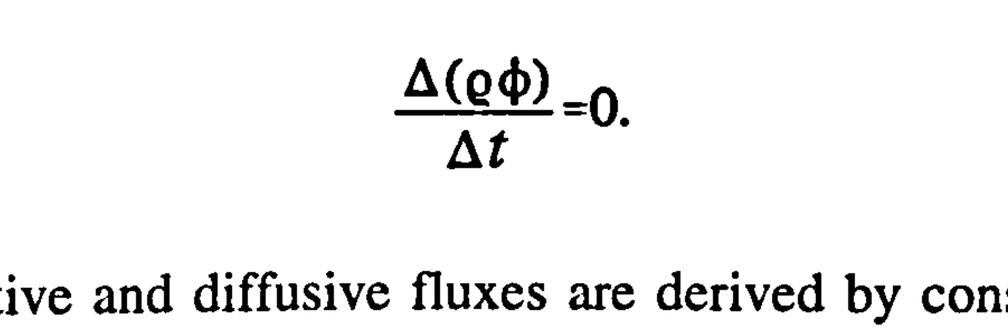

Fig.(5-3): 1-D transport across the cell boundaries.

$$\frac{d}{dx}(\varrho u\phi)=\frac{d}{dx}(\Gamma\frac{d\phi}{dx}) \tag{5-1}$$

where u is the velocity in x direction. The continuity equation is:

$$\frac{d}{dx}(\varrho u)=0$$

The exact solution of equation (5-1) for a domain $0\leq x\leq L$ by considering constant Γ, and boundary conditions, is:

$$\frac{\phi-\phi_o}{\phi_L-\phi_o}=\frac{\exp(Px/L)-1}{\exp(P)-1} \tag{5-2}$$

where, for:

$$x=0 \qquad \phi=\phi_o$$

$$x=L \qquad \phi=\phi_L$$

and

$$P=\frac{\varrho uL}{\Gamma}$$

is the **Peclet number.**

The combined convective and diffusive fluxes are given by

$$q^{\cdot}=\varrho u\phi-\Gamma\frac{d\phi}{dx}\ . \tag{5-3}$$

By considering equation (5-1)

$$\frac{dq^{\cdot}}{dx}=0 \tag{5-4}$$

the solution of which, referring to fig.(5-3), is

$$q_e^{\bullet}-q_w^{\bullet}=0 \tag{5-5}$$

By substitution of the exact solution of (5-2) into (5-3)

$$q^{\bullet}_e=F_e\ (\phi_P+\frac{\phi_P-\phi_E}{\exp(P_e)-1}) \tag{5-6}$$

where

$$P_e=\frac{(\varrho u)_e(\delta x)_e}{\Gamma_e}=\frac{F_e}{D_e}$$

$$F=\varrho u$$

$$D=\frac{\Gamma}{\delta x}$$

by substitution of equation (5-6) in (5-5) and by considering similar relation for $q^{\bullet}_w$

$$F_e\ (\phi_P+\frac{\phi_P-\phi_E}{\exp(P_e)-1})-F_w\ (\phi_P+\frac{\phi_W-\phi_P}{\exp(P_W)-1})=0 \tag{5-7}$$

This relation can be written in the standard form of a finite difference equation as:

$$a_P\phi_P=a_E\phi_E+a_W\phi_W \tag{5-8}$$

where

$$a_E=\frac{F_e}{\exp(F_e/D_e)-1} \tag{5-9}$$

$$a_W=\frac{F_w\ \exp(F_w/D_w)}{\exp(F_w/D_w)-1} \tag{5-10}$$

$$a_P=a_E+a_W+(F_e-F_w) \tag{5-11}$$

These coefficient expressions are known as the **exponential scheme.** For the

case of steady one-dimensional flow this scheme attains an exact solution to be obtained for any value of Peclet number. Exponentials are expensive to compute and in order to avoid expensive calculations of exponentials, a method is used to approximate the exact relation between q^*_e~P_e with little loss of accuracy. From equation (5-9)

$$\frac{a_E}{D_e}=\frac{P_e}{\exp(P_e)-1} \tag{5-12}$$

According to Patankar (1980), by plotting a_E/D_e with respect to P_e the following results are obtained:

i) For $P_e \rightarrow \infty$

$$\frac{a_E}{D_e} \rightarrow 0 \tag{5-13a}$$

ii) For $P_e \rightarrow -\infty$

$$\frac{a_E}{D_e} \rightarrow -P_e \tag{5-13b}$$

iii) At $P_e=0$

$$\frac{a_E}{D_e}=1-\frac{P_e}{2}. \tag{5-13c}$$

By considering the **hybrid scheme** discussed by Spalding (1972) and Patankar (1980), a_E/D_e takes one of the following values according to the magnitude of Peclet number;

i) For $P_e < -2$

$$\frac{a_E}{D_e} = -P_e \tag{5-14a}$$

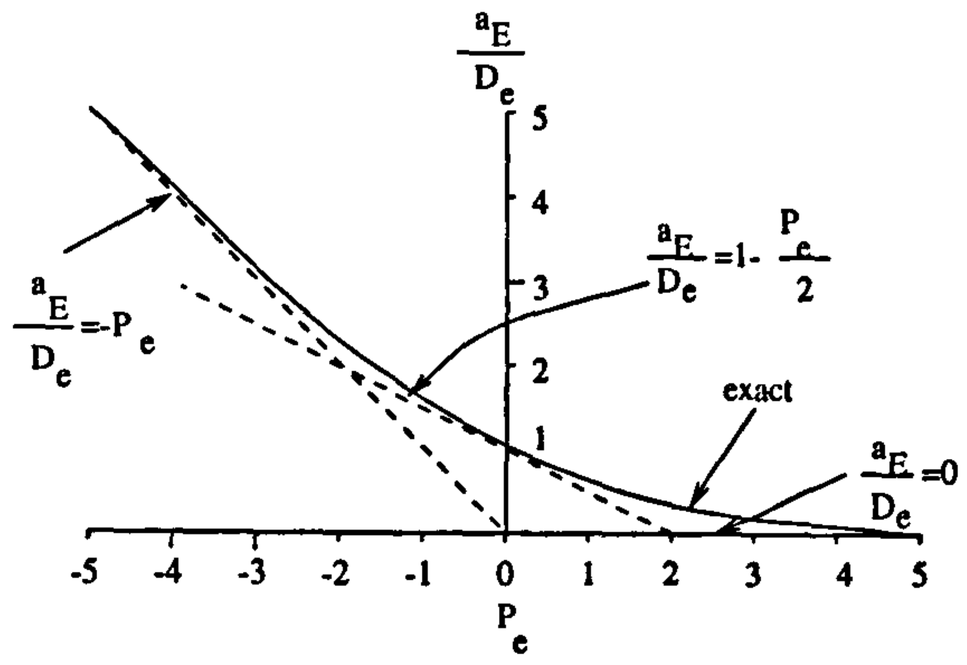

Fig.(5-4) Variation of α_E with Peclet number (from Patankar, 1980).

ii) For $P_e > 2$

$$\frac{a_E}{D_e} = 0 \tag{5-14b}$$

iii) For $-2 \leq P_e \leq 2$

$$\frac{a_E}{D_e} = 1 - \frac{P_e}{2} \tag{5-14c}$$

These equations can be written as

$$a_E = D_e [\![-P_e,\ 1 - \frac{P_e}{2},\ 0]\!]$$

or

$$a_E = [\![-F_e,\ D_e - \frac{F_e}{2},\ 0]\!]$$

where the symbol [[a, b, c]] denotes the choice of maximum value between a, b and

c.

In summary, for one-dimensional flow the total set of convection-diffusion discretization equations in finite difference form for the hybrid scheme can be written as:

$$a_P\phi_P=a_E\phi_E+a_W\phi_W \tag{5-15}$$

$$a_E=[\![-F_e,\ D_e-\frac{F_e}{2},\ 0]\!] \tag{5-16}$$

$$a_W=[\![F_w,\ D_w+\frac{F_w}{2},\ 0]\!] \tag{5-17}$$

$$a_P=a_E+a_W+(F_e-F_w) \tag{5-18}$$

5-3: Finite difference equations for two dimensions

By assuming combined convective - diffusive fluxes $q^{\cdot}_x$ and $q^{\cdot}_y$ as

$$q^{\cdot}_x\equiv\varrho u\phi-\Gamma\frac{\partial\phi}{\partial x} \tag{5-19}$$

and

$$q^{\cdot}_y\equiv\varrho v\phi-\Gamma\frac{\partial\phi}{\partial y} \tag{5-20}$$

the two-dimensional form of the general differential equation in steady flow can be written as:

$$\frac{\partial q^{\cdot}_x}{\partial x}+\frac{\partial q^{\cdot}_y}{\partial y}=S \tag{5-21}$$

where u and v are velocity components in x and y directions. Considering fig.(5-5), this equation can be written as:

$$q^{\cdot}_{e}-q^{\cdot}_{w}+q^{\cdot}_{n}-q^{\cdot}_{s}=(S_c+S_P\phi_P)\ SEW(I)\cdot SNS(J) \qquad (5\text{-}22)$$

in which the linearized form of the source term has been used. Noting that control

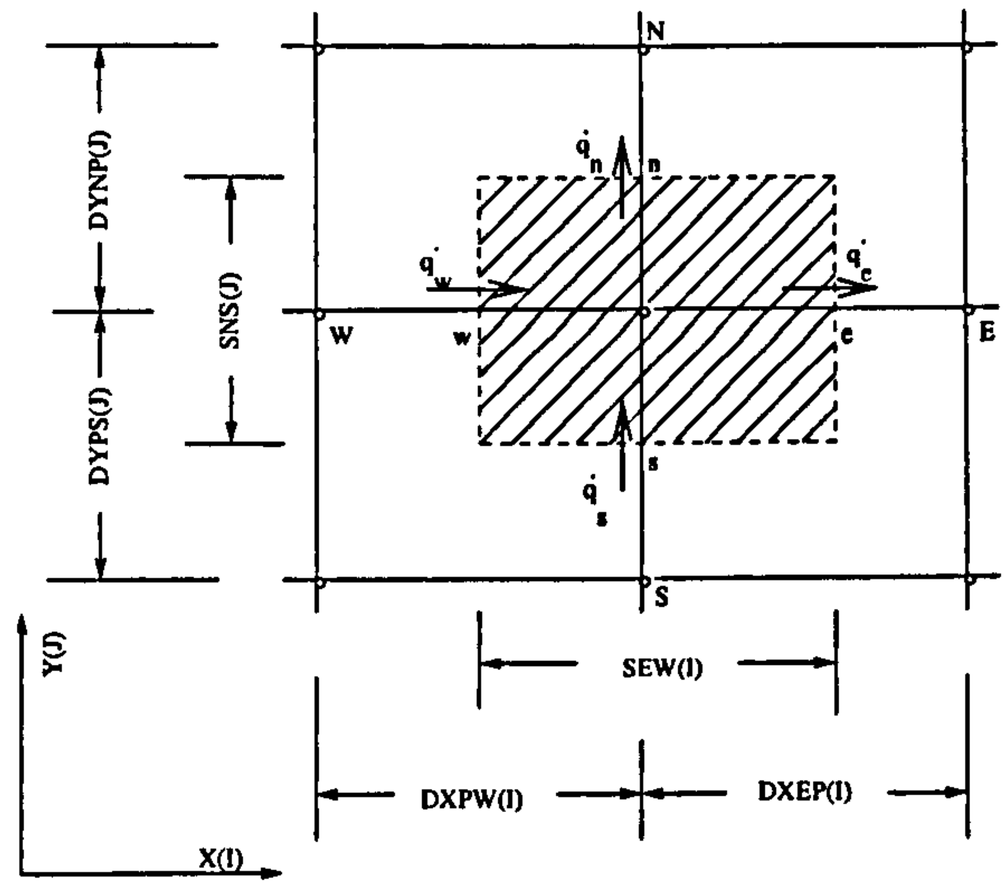

Fig.(5-5): Control volume for two dimensional case.

volume face areas are SEW(I) × 1 and SNS(J) × 1, the continuity equation over the control volume is:

$$F_e-F_w+F_n-F_s=0 \qquad (5\text{-}23)$$

where F_e, F_w, F_n and F_s are mass flow rates through the faces of the control volume and equal to:

$$F_e=(\varrho u)_e\cdot SNS(J) \qquad (5\text{-}24a)$$

$$F_w=(\varrho u)_w\cdot SNS(J) \qquad (5\text{-}24b)$$

$$F_n=(\varrho v)_n\cdot SEW(I) \qquad (5\text{-}24c)$$

$$F_s=(\varrho v)_s \cdot SEW(I) \tag{5-24d}$$

Multiplying equation (5-23) by Φ_P and subtracting it from (5-22) leads to:

$$(q^{\cdot}_e-F_e\phi_P)-(q^{\cdot}_w-F_w\phi_P)+(q^{\cdot}_n-F_n\phi_P)-(q^{\cdot}_s-F_s\phi_P)=(S_c+S_P\phi_P)SEW(I) \cdot SNS(J).$$

By assuming:

$$q^{\cdot}_e-F_e\phi_P=a_E(\phi_P-\phi_E) \tag{5-25a}$$

$$q^{\cdot}_w-F_w\phi_P=a_w(\phi_W-\phi_P) \tag{5-25b}$$

$$q^{\cdot}_n-F_n\phi_P=a_N(\phi_P-\phi_N) \tag{5-25c}$$

$$q^{\cdot}_s-F_s\phi_P=a_s(\phi_S-\phi_P) \tag{5-25d}$$

The resultant two-dimensional finite difference equation connecting each nodal value of the variable Φ to its four nearest neighbours can be written as :

$$a_P\phi_P=a_E\phi_E+a_W\phi_W+a_N\phi_N+a_S\phi_S+b\phi+c \tag{5-26}$$

or

$$(a_p-b)\phi_p=\sum_n a_n\phi_n+c \tag{5-27}$$

where:

$$a_E=D_eA(|P_e|)+[\![-F_e, 0]\!] \tag{5-28a}$$

$$a_W=D_wA(|P_w|)+[\![F_w, 0]\!] \tag{5-28b}$$

$$a_N=D_nA(|P_n|)+[\![-F_n, 0]\!] \tag{5-28c}$$

$$a_S=D_sA(|P_s|)+[\![F_s,\ 0]\!] \tag{5-28d}$$

$$a_p=\sum_n a_n=a_E+a_W+a_S+a_N \tag{5-28e}$$

$$b=S_pSEW(I)\ \cdot\ SNS(J) \tag{5-28f}$$

$$c=S_cSEW(I)\ \cdot\ SNS(J) \tag{5-28g}$$

$\sum_n$=Summation over node P's four neighbours (N, S, E, W).

In the set of equations (5-28) the corresponding conductances are

$$D_e=\frac{\Gamma_e SNS(J)}{DXEP(I)} \tag{5-29a}$$

$$D_w=\frac{\Gamma_w SNS(J)}{DXPW(I)} \tag{5-29b}$$

$$D_n=\frac{\Gamma_n SEW(I)}{DYNP(J)} \tag{5-29c}$$

$$D_s=\frac{\Gamma_s SEW(I)}{DYPS(J)} \tag{5-29d}$$

and Peclet numbers are

$$P_e=\frac{F_e}{D_e},\quad P_w=\frac{F_w}{D_w},\quad P_n=\frac{F_n}{D_n},\quad P_s=\frac{F_s}{D_s} \tag{5-30}$$

and the function A(|P|) can be selected from table (5-1) developed by Patankar (1980).

Table (5-1): The function A(| P |) for different schemes.

Scheme	A(| P |)
Central difference	1-0.5 | P |
Upwind	1
Hybrid	[[0,1-0.5 | P |]]
Power law	[[0,(1-0.1 | P |)^5]]
Exponential (exact)	| P | /[exp(| P |)-1]

5-4: Insertion of boundary conditions

For insertion of boundary conditions, the grid arrangement is such that the boundaries coincide with the cell walls. This is helpful for securing conservation and also for flux calculations. At the boundaries of the calculation domain, the usual flux expression is unsuitable, because for example by referring to fig.(5-6) and considering the west wall coincident with the boundary of the calculation domain, there is no link between Φ_P and Φ_W through the general finite difference equation, hence the usual flux expression is suppressed by setting the relevant coefficient equal

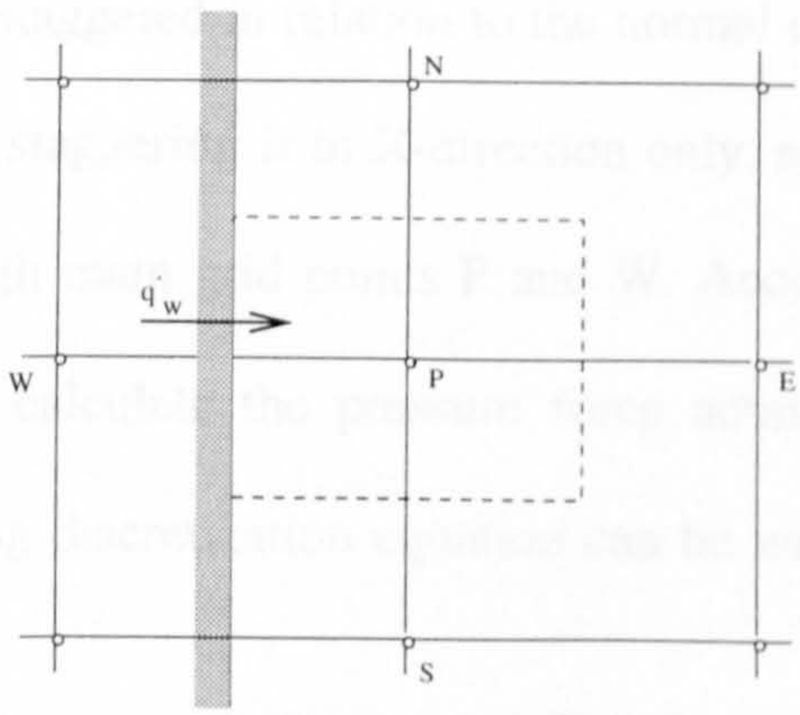

Fig.(5-6): Coincident of west wall with boundary of calculation domain.

to zero (a_W=0), which breaks the normal Φ_P~Φ_W link.

5-5: Finite difference momentum equations

For a given pressure field, the finite difference momentum equations are derived in a similar manner to the general variable Φ. In the momentum equation Φ stands for the relevant velocity component by considering that, in this case, the control volumes are centred around the velocity locations. A staggered control volume for considering x-momentum equation is shown in fig.(5-7). Considering the location of u only, control volume faces lie between point w and corresponding locations for the neighbouring u's.

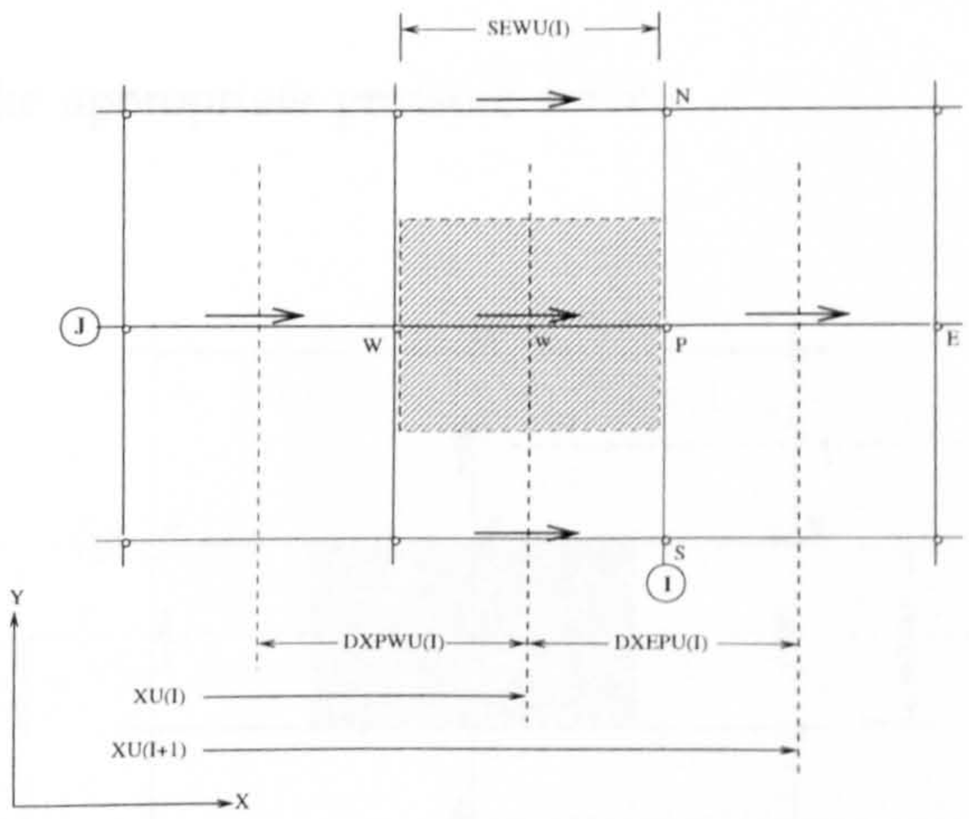

Fig.(5-7): Control volume for u.

The control volume is staggered in relation to the normal control volume around the main grid point P. The staggering is in X-direction only, so that the faces parallel to Y-direction pass through main grid points P and W. According to this assumption, P_W-P_P can be used to calculate the pressure force acting on control volume for velocity u. The resulting discretization equation can be written as:

$$a_w u_w = \Sigma a_{nb} u_{nb} + A_{ew}(P_W - P_P) + c \qquad (5\text{-}31)$$

Here the four neighbours of u are shown outside the control volume in fig.(5-7). The neighbour coefficient a_{nb} accounts for the combined convective-diffusive influence at the control volume faces. All coefficients are defined in the same manner as equation (5-28) but the pressure gradient is not included in source terms S_c and S_p. A_{ew} is the area on which the pressure force acts on the control volume.

The momentum equation for the Y-direction is handled in a similar manner. The control volume for the Y-direction momentum equation is shown in fig.(5-8).The discretization equation for v_s can be written as:

$$a_s v_s = \Sigma a_{nb} v_{nb} + A_s(P_S - P_P) + c \qquad (5\text{-}32)$$

where $(P_S\text{-}P_P)A_s$ is the appropriate pressure force.

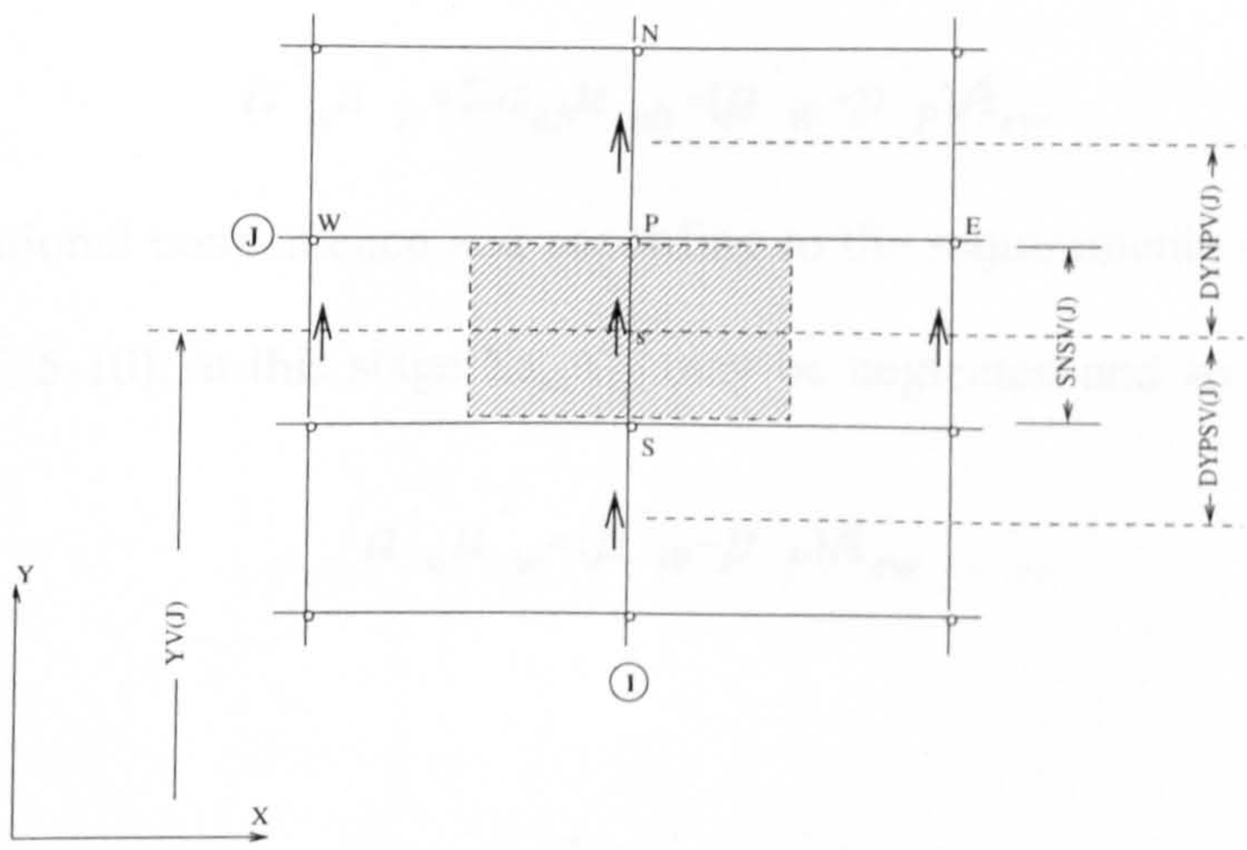

Fig.(5-8): control volume for v.

5-6: Pressure and velocity corrections

The momentum equations (5-31) and (5-32) can be solved only when the pressure field is given or estimated. Unless the correct pressure field is employed, the resulting velocity will not satisfy the continuity equation. Supposing the guessed

values for pressure field and velocities are denoted by p^*, u^* and v^*. The major objective is to improve the guessed pressure p^* such that the resulting velocity field will progressively get closer to satisfying the continuity equation and to eliminate the mass source.

Assuming that p', u', v' are the pressure and velocity corrections, so that the corrected values of pressure p and velocities u and v are :

$$p=p^*+p'$$

$$u=u^*+u'$$

$$v=v^*+v'$$

For velocity u at point w

$$a'_w u'_w=\Sigma a_{nb}u'_{nb}+(p'_W-p'_P)A_{ew} \qquad (5\text{-}34)$$

As a computational convenience and according to the requirements of the **SIMPLE** algorithm (c.f. 5-10), at this stage $\Sigma a_{nb}u'_{nb}$ may be neglected and so

$$a'_w u'_w=(p'_W-p'_P)A_{ew}$$

or

$$u'_w=d_w(p'_W-p'_P)$$

where

$$d_w=\frac{A_{ew}}{a_w}$$

or

$$u_w=u^*_w+d_w(p'_w-p'_P) \tag{5-35a}$$

Equation (5-34), known as velocity correction formula, shows that how u_w^* is corrected by considering pressure correction to produce u_w. The correction equations for other velocities are:

$$u_e=u^*_e+d_e(p'_P-p'_E) \tag{5-35b}$$

$$v_s=v_s^*+d_s(p'_S-p'_P) \tag{5-35c}$$

$$v_n=v_n^*+d_n(p'_P-p'_N) \tag{5-35d}$$

5-7: Pressure correction equation

By assuming two-dimensional steady flow and that the density ϱ does not directly depend on pressure*, the continuity equation is:

$$\frac{\partial(\varrho u)}{\partial x}+\frac{\partial(\varrho v)}{\partial y}=0$$

Referring fig.(5-9) and integrating this equation over the control volume leads to:

$$(\varrho uA)_e-(\varrho uA)_w+(\varrho vA)_n-(\varrho vA)_s=0$$

By substitution of all velocity components from equations (5-35), the following discretization equation is obtained for p′:

---

* This is an approximation in p′ equation. The density ϱ in general to be calculated from equation of state and dependent on temperature and pressure. As long as a convergent solution can be obtained the approximate p′ equation is sufficient.

$$a_P p'_P = a_E p'_E + a_W p'_W + a_N p'_N + a_S p'_S + M_P$$

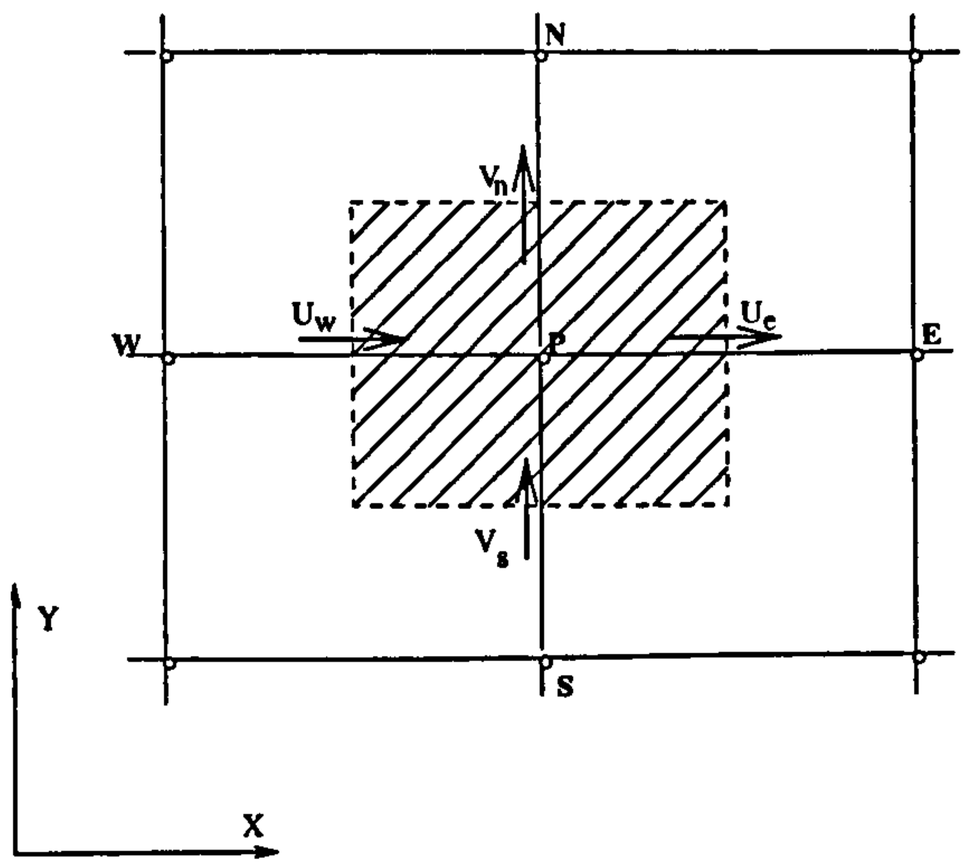

Fig.(5-9): Control volume for continuity equation.

or by considering linearized source term:

$$(a_P - b)p'_P = \sum_{nb} a_{nb} p'_{nb} + M_P + c \qquad (5\text{-}36)$$

where

$$a_P = \sum_{nb} a_{nb}$$

$$a_E = \varrho_e d_e A_e$$

$$a_S = \varrho_s d_s A_s$$

$$a_N = \varrho_n d_n A_n$$

$$a_W = \varrho_w d_w A_w$$

$$M_P = \varrho_e u^*_e A_e - \varrho_w u^*_w A_w + \varrho_n v^*_n - \varrho_s v^*_s A_s$$

The term M_P represents a "mass source" which the pressure correction must

eliminate. If M_p=0 it means that the starred velocities do satisfy the continuity equation and no pressure correction is needed. Solution of p´-equation, as with the other finite difference equations, is carried out by an iterative line-by-line (LBL) method and completes the process of seeking to obtain the desired set of corrections u´, v´ and p´ which are required to make up u^*, v^* and p^*.

5-8: General solution procedure

The solution employed for the algebraic equation resulting from the discretization process is an iterative line-by-line (LBL) method. An initial guess

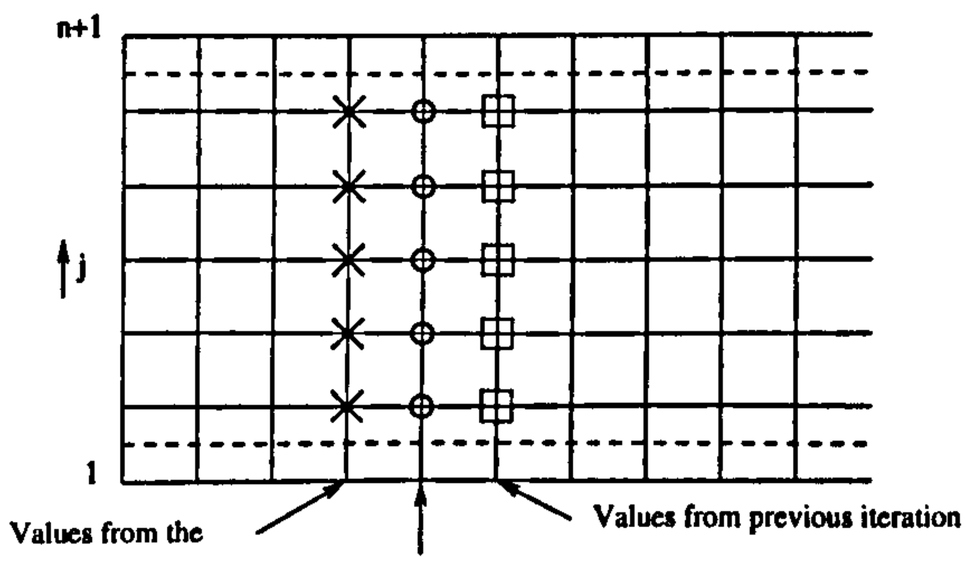

Fig.(5-10): Solution procedure by LBL method.

of values for flow field is made and these are improved upon from one line to the next. For solution of the equation on each N-S line, the values of neighbouring lines are assumed to be known temporarily. So that the equations for each point on the N-S line reduce to one with only three unknown values Φ_P, Φ_N and Φ_S. Φ_1 and Φ_{n+1} generally will be known.

$$a'_P\phi_P=a_N\phi_N+a_S\phi_S+c' \qquad (5\text{-}37)$$

where

$$c' = a_W \phi_W + a_E \phi_E + c(known)$$

and

$$a'_P = a_P - b$$

by assuming $D=a'_P$, $\alpha=a_N$ and $\beta=a_S$, and considering the variation of j=2.....n

$$-\beta_j \phi_{j-1} + D_j \phi_j - \alpha_j \phi_{j+1} = c_j'$$

where referring to fig.(5-10), $\alpha_{n+1}=0$ and $\beta_1=0$.

The set of equations for all points on N-S line takes a particularly simple form in which the coefficient matrix is tridiagonal and the relevant equations can be solved by **Tri-Diagonal Matrix Algorithm (TDMA)**.

$$\begin{bmatrix} -\beta_2 & D_2 & -\alpha_2 & 0 & \cdots & 0 \\ 0 & -\beta_3 & D_3 & -\alpha_3 & 0 & \cdots & 0 \\ \cdots & \cdots & \cdots & \cdots & \cdots & \cdots & \cdots \\ \cdots & \cdots & -\beta_j & D_j & -\alpha_j & \cdots & 0 \\ \cdots & \cdots & \cdots & \cdots & \cdots & \cdots & \cdots \\ \cdots & \cdots & \cdots & \cdots & -\beta_n & D_n & -\alpha_n \end{bmatrix} \begin{bmatrix} \phi_1 \\ \phi_2 \\ \cdots \\ \phi_j \\ \cdots \\ \phi_{n+1} \end{bmatrix} = \begin{bmatrix} c_2' \\ c_3' \\ \cdots \\ \cdots \\ \cdots \\ c_n' \end{bmatrix}$$

5-9: Under-relaxation

In the above mentioned iterative procedure for the solution of algebraic equations, in order to handle non-linearity at each time step, to slow down the changes from iteration to iteration and to avoid divergence and also to accelerate convergence of the solution, under-relaxation is used. Under-relaxation is a very useful device for non-linear problems, especially with the line-by-line method.

Considering the general discretization equation of form:

$$(a_P-b)\phi_P=\Sigma a_{nb}\phi_{nb}+c$$

Φ_P can be written as

$$\phi_P=\phi^*_P+(\frac{\Sigma a_{nb}\phi_{nb}+c}{a_P-b}-\phi^*_P) \qquad (5\text{-}38)$$

where Φ^*_P stands for the value of Φ_P from the previous iteration. The contents of the parentheses in equation (5-38) describe the change of Φ_P in the current iteration. To slow down this change, an underrelaxation factor η ($0<\eta\leq1$) is introduced so that

$$\phi_P=\phi^*_P+\eta(\frac{\Sigma a_{nb}\phi_{nb}+c}{a_P-b}-\phi^*_P)$$

or

$$\frac{a_P-b}{\eta}\phi_P=\Sigma a_{nb}\phi_{nb}+c+(1-\eta)\frac{a_P-b}{\eta}\phi^*_P \qquad (5\text{-}39)$$

When convergence is reached $\Phi_P = \Phi^*_P$. For very small values of η the change in Φ_P becomes very slow.

There is not any general rule for selecting the value of η. The optimum value of η depends on the nature of problem, the number of grid points, the grid spacing, and the iterative procedure used, and usually can be found by experience.

5-10: SIMPLE algorithm

The method of solution for calculating the flow field is presented by Patankar and Spalding (1972), Garetto, Gosman, Patankar and Spalding (1972), and Patankar (1980), and is known as **SIMPLE** which stands for **S**emi-**I**mplicit **M**ethod for **P**ressure-**L**inked **E**quations. The words semi-implicit in the name of **SIMPLE** have been selected to confirm the omission of the term $\Sigma a_{nb}u'_{nb}$ in equation (5-34). This term represents an indirect influence of pressure correction on velocity and as this

influence is not included in the **SIMPLE** algorithm, the work is not totally implicit.

5-11:Sequence of operation

The different stages in the SIMPLE algorithm may now be combined with the solution of the equations for the non-hydrodynamic variables in order to form a general solution procedure. The important operations in the order of their execution, are:

1. Guess the fields of all variables (u, v, p, k and ε).

2. Assemble the coefficients of the momentum equation and solve the momentum equations to obtain improved values of u^* and v^*.

3. Solve the p' equation after calculating the relevant coefficients.

4. Calculate p by adding p' to p^*.

5. Calculate u and v from velocity correction formulas.

6. Solve the discretization equation for all other Φ's which influence the flow field.

7. Treat the corrected values for p, u, v, etc. as new guesses and repeat the procedure from step 2 until a converged solution is obtained.

5-12: The overall structure of TEACH-T computer program

TEACH-T is mainly a general program for steady, two-dimensional, laminar or turbulent flow. It can be made to handle compressible as well as incompressible flow. The program is written for flows which can be represented in cartesian or cylindrical-polar coordinates and uniform or non-uniform grid structure. The programming language used for the present study is FORTRAN 77 and the program has been run on a Sun-Unix system. There are six general subroutines in this program relevant for any particular variable to be solved: CONTRO, INIT, PROPS,

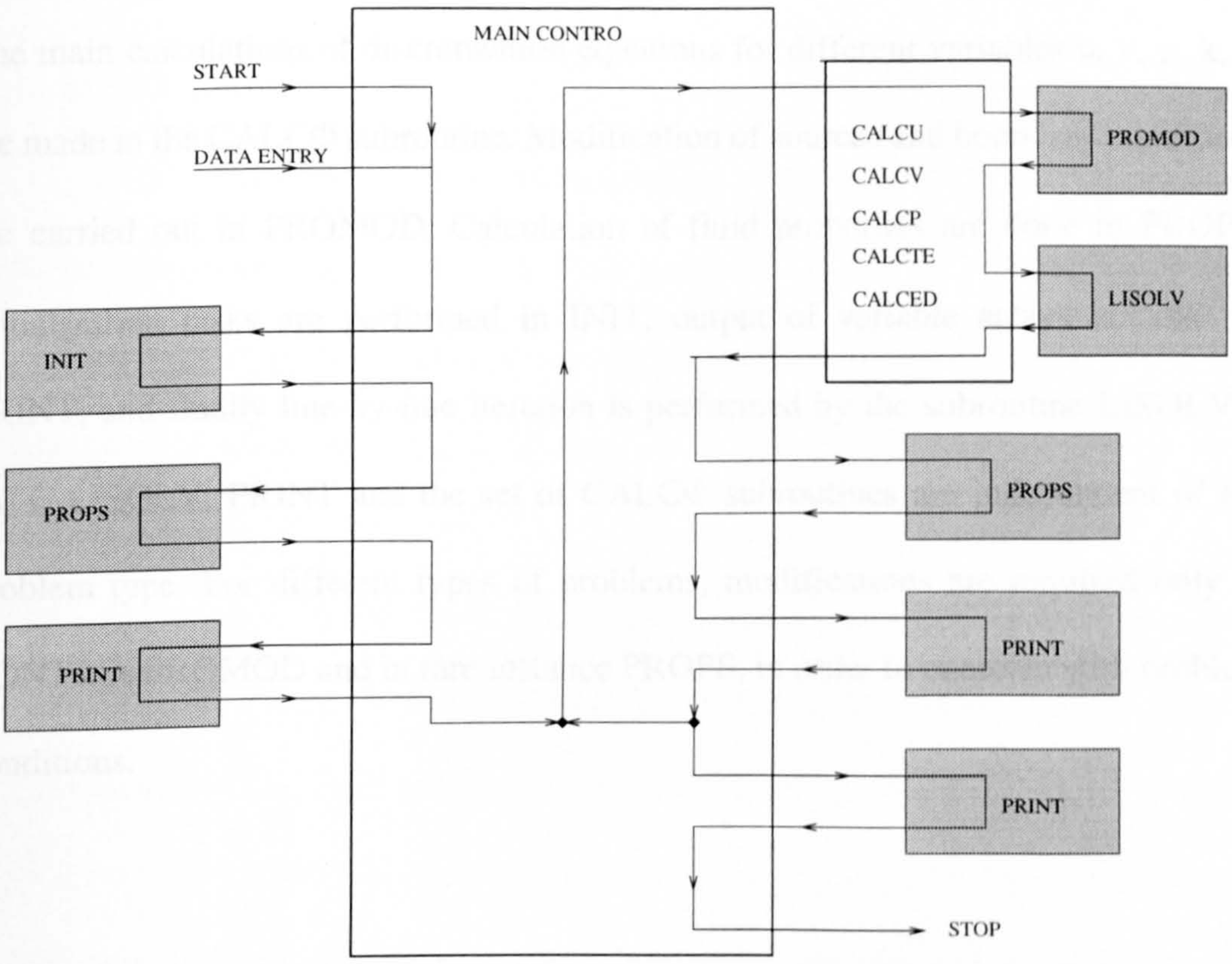

Fig.(5-11) : Structure of TEACH-T program.

PROMOD, LISOLVE, and PRINT. In addition, there are sets of CALCΦ subroutines, where Φ stands for the particular variable being solved. The inter-connection between subroutines is shown in fig.(5-11).

The overall control is carried out in the main subroutine CONTRO. This subroutine performs the initial and final operations and also controls the iterations. The main calculations of discretization equations for different variables u, v, p, k, ε are made in the CALCΦ subroutine. Modification of sources and boundary conditions are carried out in PROMOD. Calculation of fluid properties are done in PROPS. Initialization tasks are performed in INIT, output of variable arrays is done by PRINT, and finally line-by-line iteration is performed by the subroutine LISOLVE. INIT, LISOLV, PRINT and the set of CALCΦ subroutines are independent of the problem type. For different types of problems, modifications are required only in CONTRO, PROMOD and in rare instance PROPS, in order to conform with problem conditions.

CHAPTER

6

AXISYMMETRIC JET IMPINGEMENT ONTO A FLAT PLATE

6-1: Introduction

In order to obtain a better understanding of the behaviour of a turbulent jet, used to remove the foulent deposit from a cylindrical surface, as a first step, the numerical study of an axisymmetric and two-dimensional turbulent impinging jet onto a flat plate is made in this chapter and in chapter 7. This kind of study for a turbulent submerged axisymmetric incompressible jet has been done by Amano (1983), Amano and Brandt (1984) and Amano and Sugiyama (1985). They used a hybrid finite difference method to solve the full Navier-Stokes equations for an incompressible submerged jet with the k~ε turbulence model. They have compared their computed results with the experimental works reported by Tani and Komatsu (1966) and Bradshaw and Love (1959), and they found good agreement and good predictions of the velocity distributions, pressure and skin friction. To confirm the operation and validity of the numerical procedures a similar study has been carried out in the present work as a precursor to studying the impingement of jet onto a circular cylinder.

6-2: Mathematical formulation

The governing equations to define the flow field of a turbulent axisymmetric jet impinging onto a flat plate, in axisymmetric cylindrical coordinates can be written as:

$$\frac{1}{r}[\frac{\partial}{\partial x}(r\varrho u\phi)+\frac{\partial}{\partial r}(r\varrho v\phi)]=\frac{1}{r}[\frac{\partial}{\partial x}(r\Gamma_{\phi}\frac{\partial\phi}{\partial x})+\frac{\partial}{\partial r}(r\Gamma_{\phi}\frac{\partial\phi}{\partial r})]+S_{\phi} \qquad (6\text{-}1)$$

where Φ stands for dependent variables u, v, k and ε, and S_Φ is the related source term. These set of equations are summarized in table(6-1).

Table(6-1): Governing equations in axisymmetric cylindrical coordinates

Equation	Φ	Γ_Φ	S_Φ
Continuity	1	0	0
x-Momentum	u	μ_{eff}	$-\frac{\partial p}{\partial x}+\frac{\partial}{\partial x}(\mu_{eff}\frac{\partial u}{\partial x})+\frac{1}{r}\frac{\partial}{\partial r}(r\mu_{eff}\frac{\partial v}{\partial x})$
r-Momentum	v	μ_{eff}	$-\frac{\partial p}{\partial r}+\frac{\partial}{\partial x}(\mu_{eff}\frac{\partial u}{\partial r})+\frac{1}{r}\frac{\partial}{\partial r}(r\mu_{eff}\frac{\partial v}{\partial r})-2\mu_{eff}\frac{v}{r^2}$
Turbulence Energy	k	$\mu+\mu_t/\sigma_k$	$\varrho G-\varrho\epsilon$
Energy Dissipation	ε	$\mu+\mu_t/\sigma_\varepsilon$	$C_1\frac{\varrho\epsilon}{k}G-C_2\frac{\varrho\epsilon^2}{k}$

where

$$\mu_t=C_\mu\frac{\varrho k^2}{\epsilon}$$

$$\mu_{eff}=\mu+\mu_t$$

and

$$G=\nu_t[(\frac{\partial u}{\partial r}+\frac{\partial v}{\partial x})^2+2(\frac{\partial u}{\partial x})^2+2(\frac{\partial v}{\partial r})^2+2(\frac{v}{r})^2]$$

and constant coefficients are:

C_μ	C_1	C_2	σ_k	σ_ε
0.09	1.44	1.92	1.0	1.3

6-3: Numerical procedure

The boundary conditions for axisymmetric jet impingement onto a flat plate are described in section 3-3. The grid generated for the numerical calculation consists of 30×40 cells with an expanding-contracting ratios of 1.2 and 0.825 respectively in the x-direction, and an expanding ratio of 1.2 in the r-direction. In this system the finer grids are obtained near the wall and nozzle exit. The mathematical and numerical procedure for solving the governing equations are described in chapters 4 and 5.

6-4: Presentation and discussion of results

The axial centreline velocity decay as a function of distance from the nozzle exit is presented in fig.(6-1). The centreline velocity is normalized by the jet velocity at nozzle exit and the distance x, is normalized by the nozzle diameter D_N. The experimental results obtained by Tani and Komatsu (1966) are used to examine the accuracy of the numerical method. By referring to fig.(6-1) agreement between the computed and experimental results is within 7%. Referring to fig.(6-1), for a nozzle-to-plate distance of $H/D_N=4$, the centreline velocity is constant up to about 3 nozzle diameters, which is quite close to the findings of Beltaos and Rajaratnam (1973). According to their findings, the presence of the impingement plate was not felt

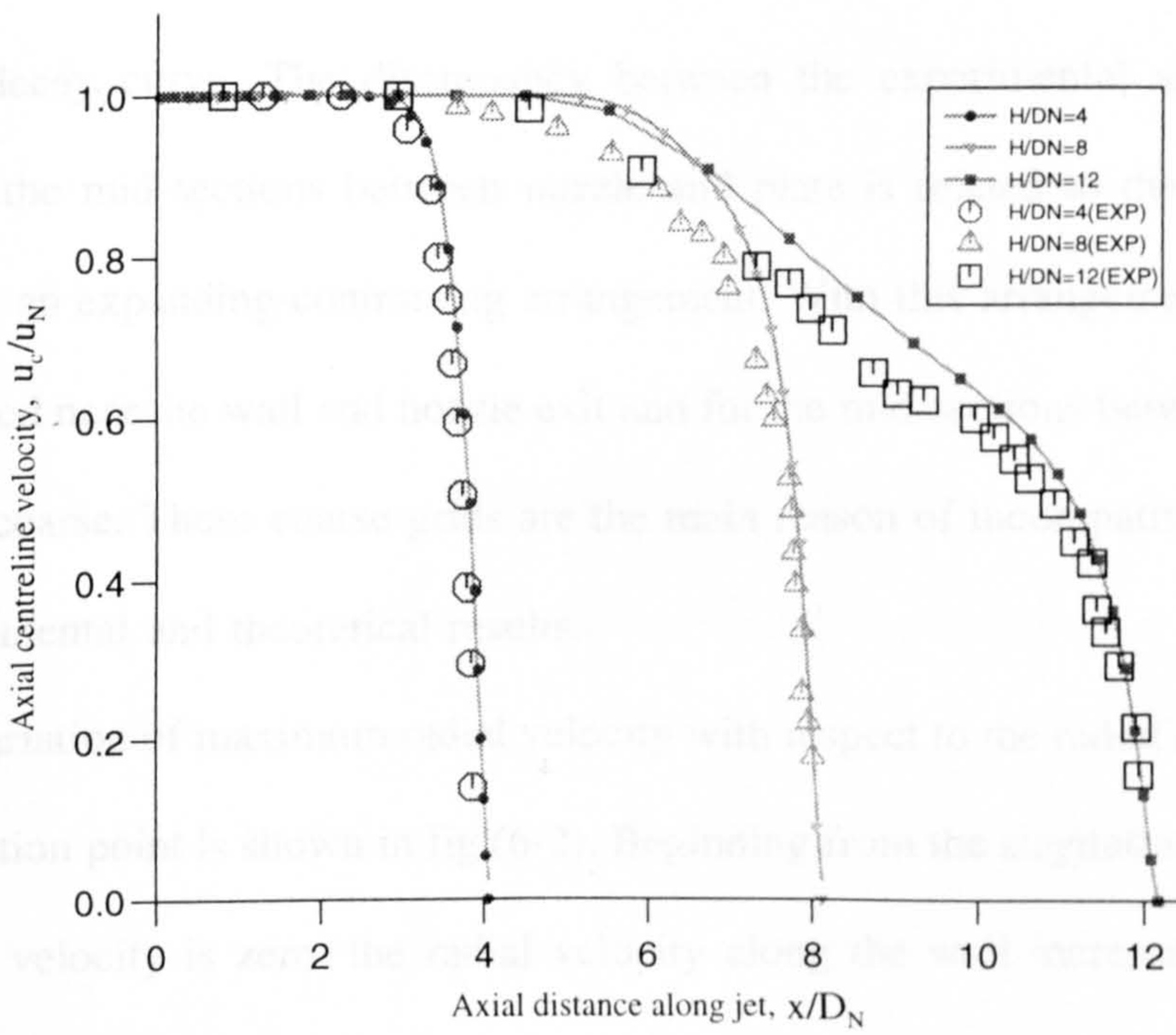

Fig.(6-1): Axial centreline velocity decay of an axisymmetric jet impinging onto a flat plate.

beyond about x/H=0.86 from nozzle exit . This portion of jet is known as the potential core. From the end position of the potential core centreline, the velocity of the jet starts to decrease rapidly towards zero velocity at the stagnation point. For the higher nozzle to plate distance, the jet begins to take the behaviour of a free jet. For the case of H/D_N=8, as shown in fig.(6-1), there is a smooth transition of the axial centreline velocity decay between the potential core and the developed region of the jet. For H/D_N=12, the flow field has the characteristics of both a free jet and an impingement jet. This has been shown by two inflection points on the centreline velocity decay curve. The discrepancy between the experimental and computed results at the mid-sections between nozzle and plate is related to the type of grid which has an expanding-contracting arrangement. With this arrangement finer grids are obtained near the wall and nozzle exit and for the mid-sections between them the grids are coarse. These coarse grids are the main reason of incompatibility between the experimental and theoretical results.

Variation of maximum radial velocity with respect to the radial distance from the stagnation point is shown in fig.(6-2). Beginning from the stagnation point where the radial velocity is zero, the radial velocity along the wall increases with radial distance due to the influence of pressure gradient and this increase is greater for smaller nozzle to plate distances. The maximum radial velocity occurs at a normalized radius of between 1 and 1.8 for nozzle to plate distances of 4 and 12 respectively. The variation of maximum radial velocity as a function of radial distance after reaching to the maximum point falls off due to viscous dissipation. The discrepancy between the experimental and computed results, specially after the maximum point, is related to the uncommonly high levels of length scale near the

wall. Studies by Malin (1988) and Bradshaw (1973) suggest that these high levels of length scale are related to lateral divergence of flow in the radial case. The nature of the wall functions also affects the accuracy of calculations.

Fig.(6-3) shows the distribution of pressure along the wall as a function of radial distance from the stagnation point. The maximum pressure location is at the stagnation point and the pressure decreases to less than 10 percent of its maximum value at a radial distance of 1.03 times of nozzle diameter for the case of H/D_N=4. For the case of H/D_N=12, the pressure reduces to less than 10 percent of its maximum value at a radial distance of 1.85 times of nozzle diameter. Amano (1983) and Amano and Brandt (1984) have reported these radial distances as 1.1 times of nozzle diameter for H/D_N=4, and 1.5 times of nozzle diameter for the case of H/D_N=12. Thus by increasing nozzle-to-plate distance (H/D_N) the impingement region increases. It should be noted that for H/D_N>4 the normalized pressure is less than one, and the reason for this behaviour is that the impingement region is outside the potential core of the jet.

The variation of shear stress coefficient ($C_f=\tau_w/\rho\ u_j^2$) along the wall as a function of radial distance from the stagnation point is shown in fig.(6-4). The shear stress coefficient is zero at the stagnation point and reaches to its maximum value at 1.04 times of nozzle diameter for H/D_N=4 and 1.33 times of nozzle diameter for the case of H/D_N=12. After the maximum position the shear stress coefficient begins to reduce and this reduction is sharper for shorter nozzle-to-plate distances. The reason for a maximum shear stress arises through the rapid increase of the velocity in the shear layer, see for example fig.(6-2), followed by a decreasing velocity due to radial expansion of the jet and boundary layer (or shear layer) growth. For a two

dimensional case the shear stress decay is more slowly after the maximum value has been reached.

Distribution of k_{cl} for H/D_N=4, 8, 12 with respect to the normalized distance from nozzle exit is shown in fig.(6-5). All three cases indicate a sharp increase in k_{cl} beyond 0.94H for H/D_N=4, 0.63H for H/D_N=8 and 3.8H for H/D_N=12 which results in the larger value of skin friction coefficient along the wall. For closer distance between nozzle and plate (H/D_N=4) the relative rise in k_{cl} is at its minimum value and for higher nozzle to plate distances where the jet begins to take the behaviour of free jet, $k_{cl,max}$ increases. For the case of H/D_N=12 the flow field has the characteristics of both free jet and impingement jet, and this affects the distribution of k_{cl} and how its maximum value decreases. In all the cases $k_{cl,max}$ moves away fromthe stagnation point by increasing H/D_N.

Referring to fig.(6-6) the centreline static pressure as a function of axial distance from the nozzle shows that the effect of the wall on the free jet is not significant until 0.64H downstream for H/D_N=4, 0.77H downstream for H/D_N=8 and 0.81H downstream for H/D_N=12. After this point there is firstly a slight and then a rapid rise in static pressure to achieve its maximum value at the stagnation point.

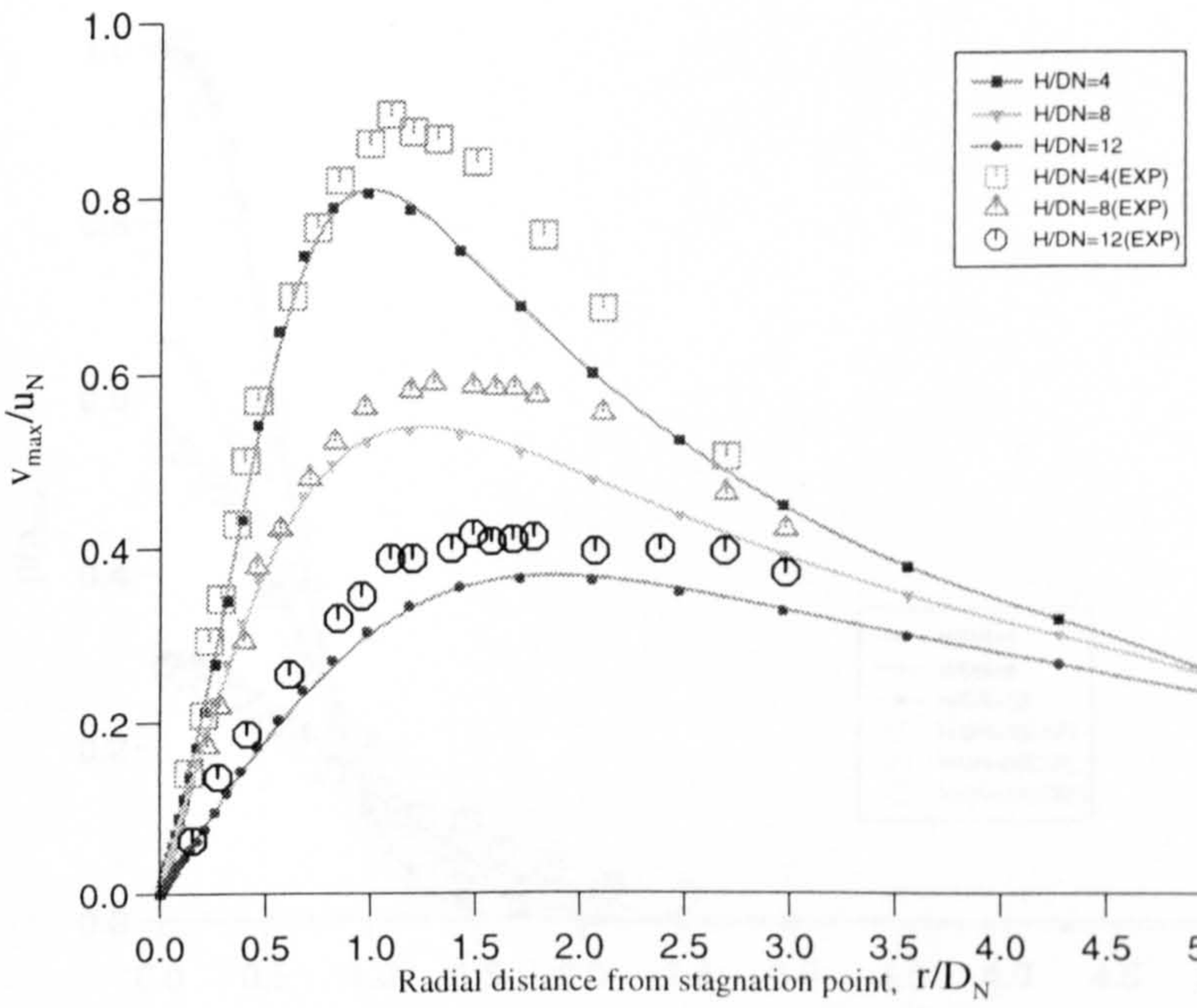

Fig.(6-2): Maximum radial velocity along the wall for an axisymmetric jet impinging onto a flat plate.

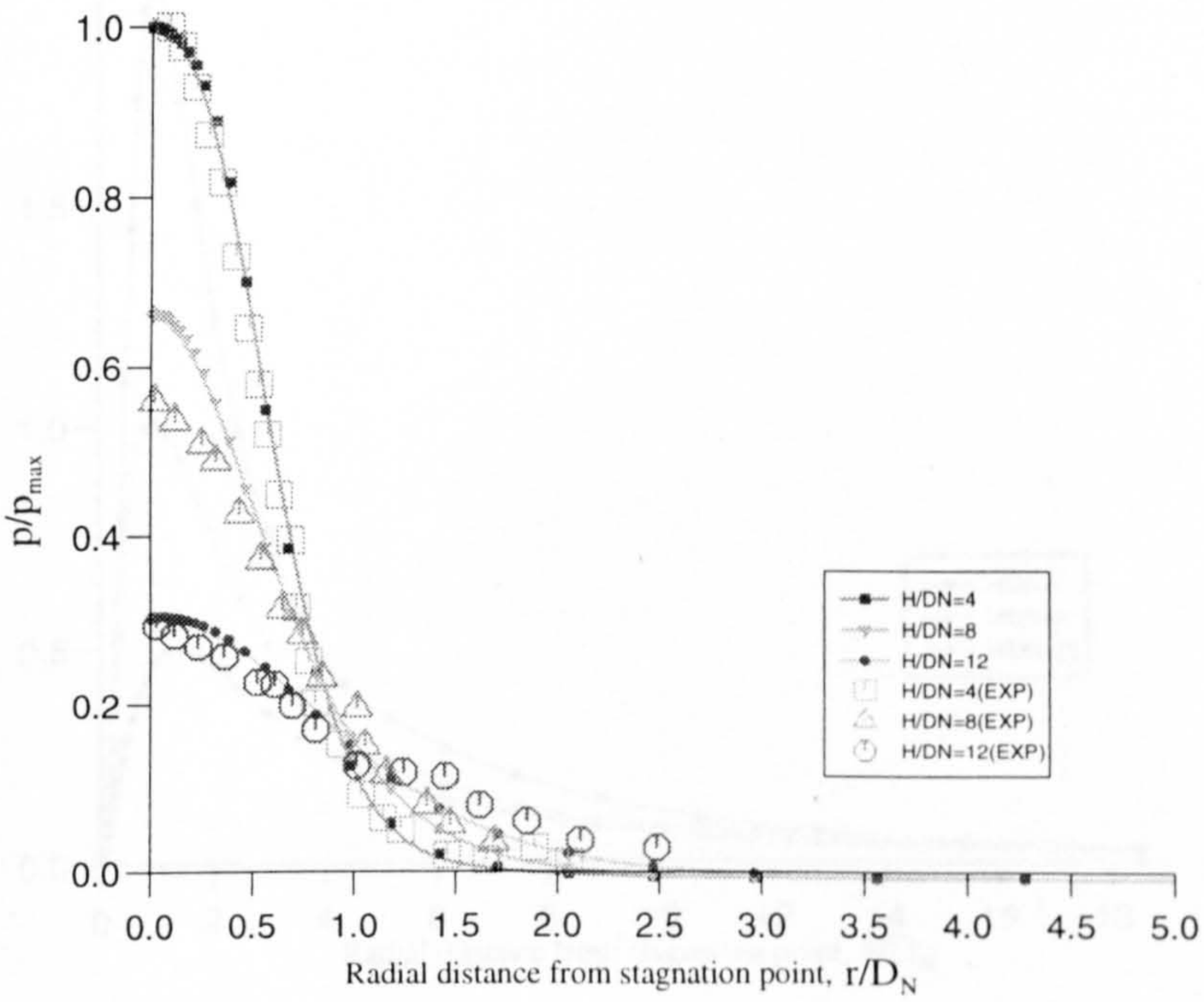

Fig.(6-3): Pressure distribution along the wall for an axisymmetric jet impinging onto a flat plate.

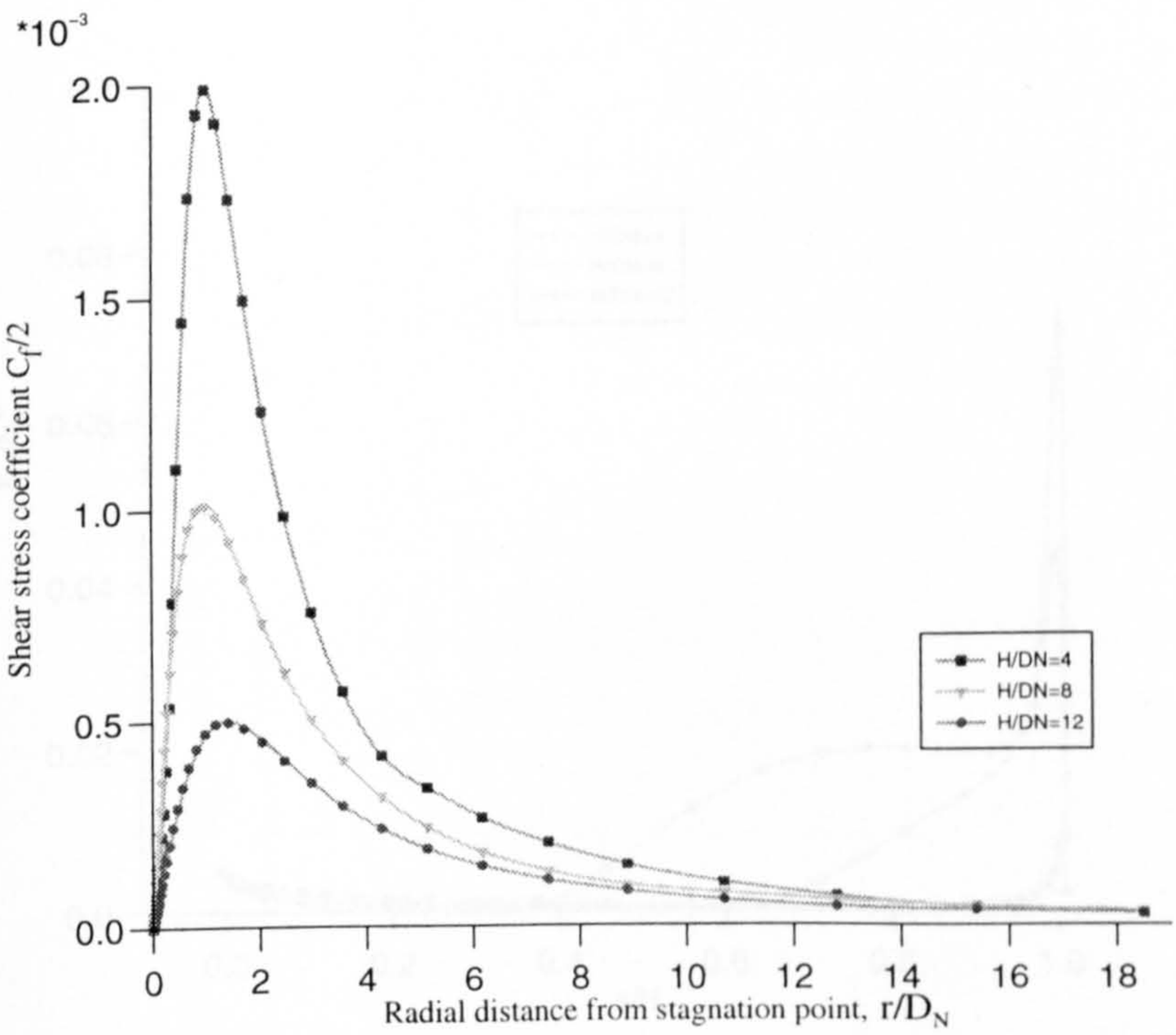

Fig.(6-4): Shear stress coefficient along the wall for an axisymmetric jet impinging onto a flat plate.

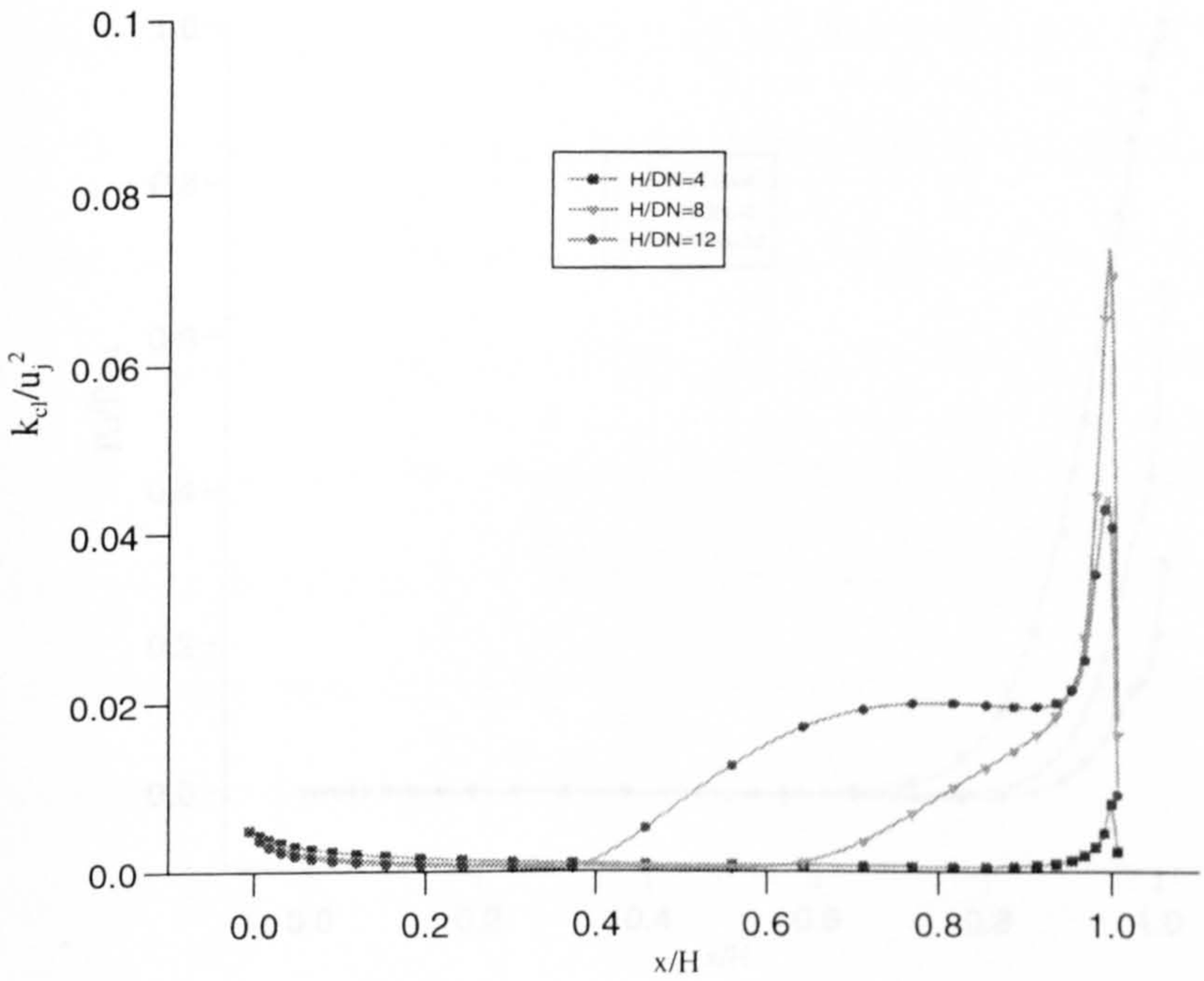

Fig.(6-5): Variation of turbulent kinetic energy on the centreline of an axisymmetric impinging jet onto a flat plate.

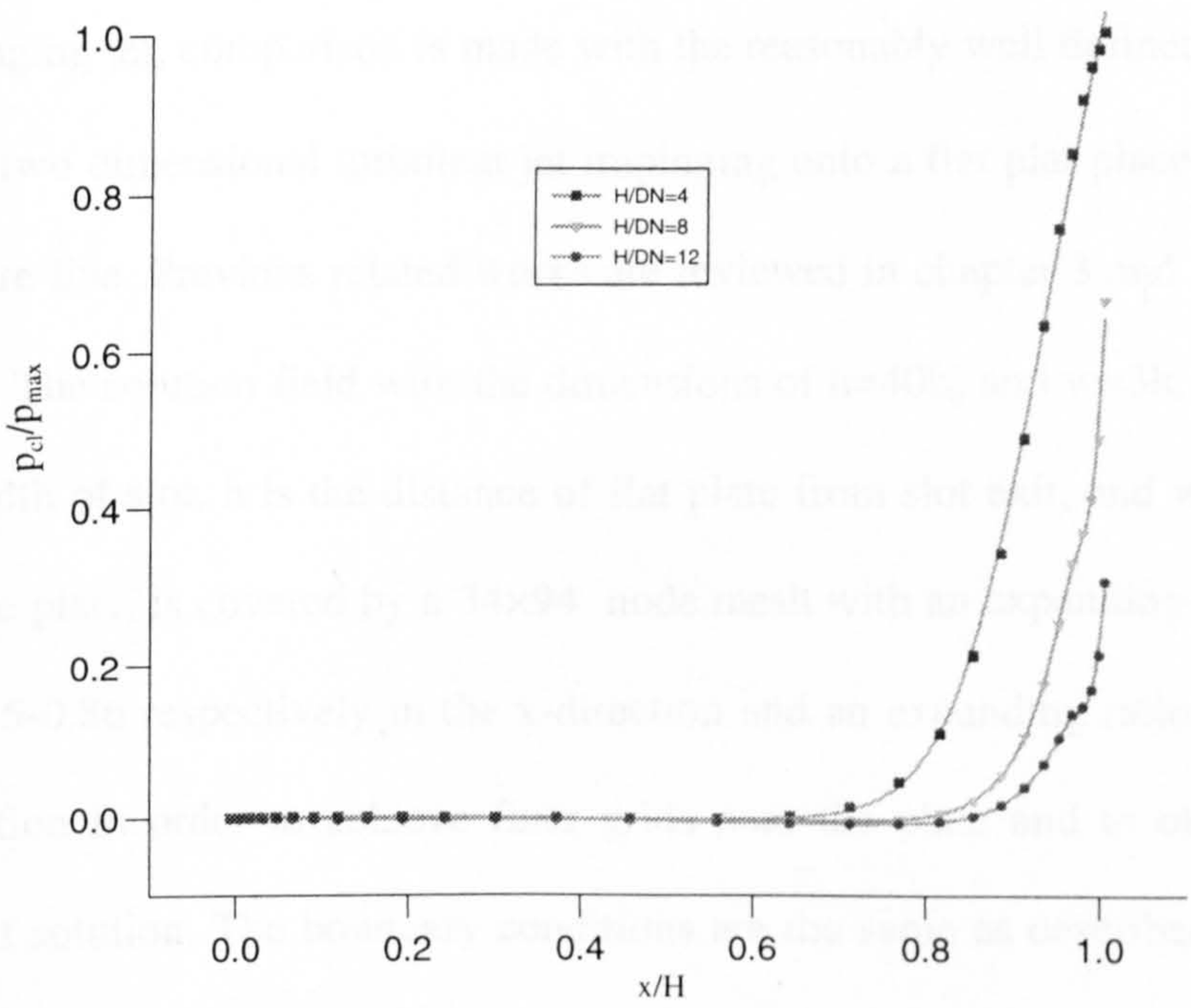

Fig.(6-6): Variation of static pressure on the centreline of an axisymmetric impinging jet onto a flat plate.

CHAPTER

7

SLOT JET IMPINGEMENT ONTO A FLAT PLATE

7-1: Introduction

In order to further verify the computer code and to explore the characteristics of an impinging jet, comparison is made with the reasonably well defined flow of an isothermal two dimensional turbulent jet impinging onto a flat plat placed normal to the jet centre-line. Previous related works are reviewed in chapter 3 and tabulated in Table(3-1). The solution field with the dimensions of $h=40b_0$ and $w=3h$, where b_0 is the half width of slot, h is the distance of flat plate from slot exit, and w is the half width of the plate, is covered by a 34×94 node mesh with an expanding-contracting ratio of 1.15-0.86 respectively in the x-direction and an expanding ratio of 1.05 in the y-direction in order to achieve finer grids near the plate and to obtain a grid independent solution. The boundary conditions are the same as described in section 3-3. The mathematical and numerical procedure for solving the governing equation (4-3) are described previously in chapters 4 and 5.

7-2: Presentation and discussion of results

Fig.(7-1) shows the pressure distribution along the flat plate as a function of distance from the stagnation point. The pressure is a maximum at the stagnation point and then decreases to less than 10 percent of stagnation pressure at a radial distance of y/h=0.24. The computational results have been compared with the experimental data obtained by Gardon and Akfirat (1965), Beltaos and Rajaratnam (1973) and

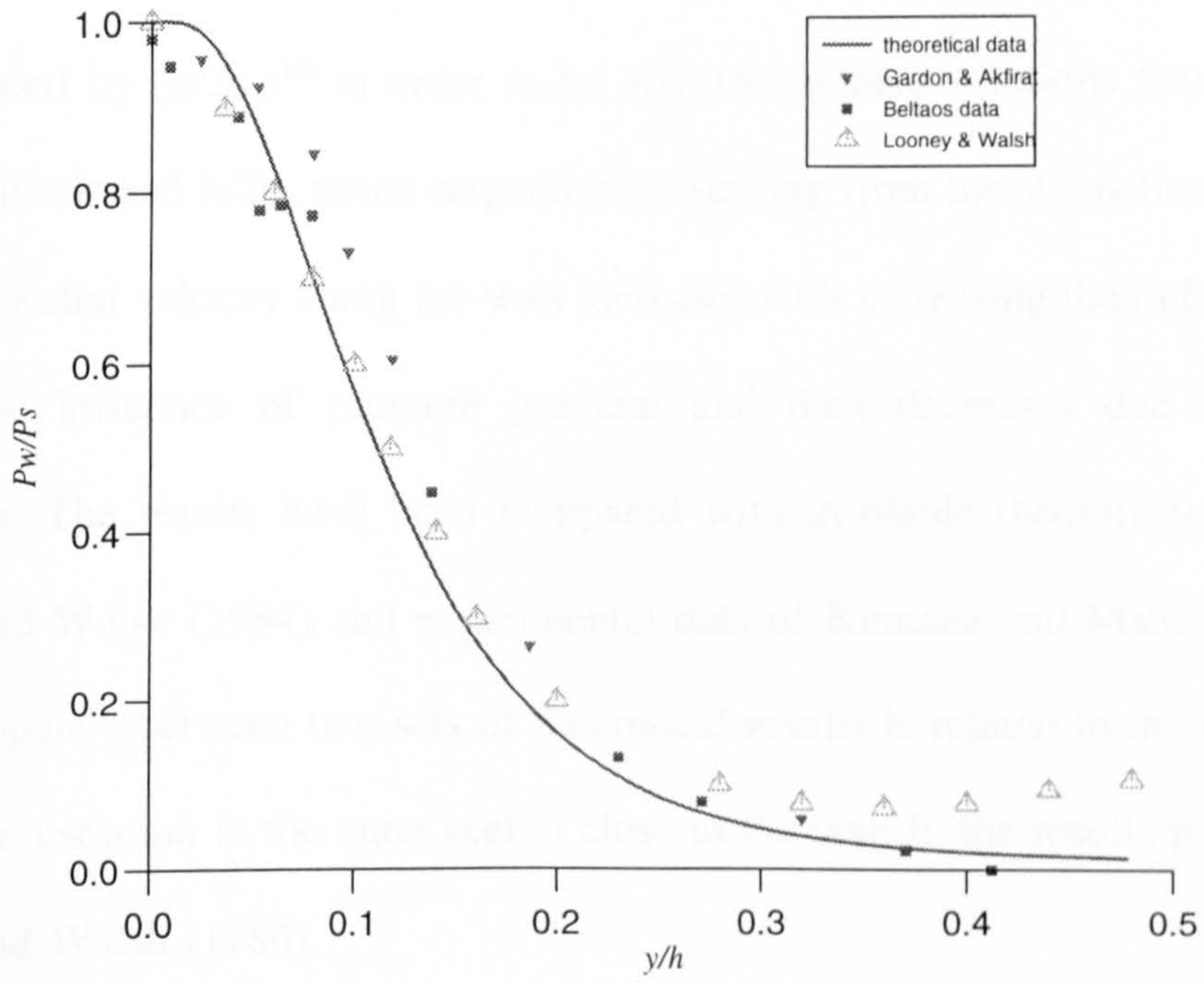

Fig.(7-1) : Wall static pressure profile for slot jet interaction with flat plate compared with theoretical data of Looney and Walsh and experimental data of Gardon and Akfirat, and Beltaos and Rajaratnam.

the theoretical data of Looney and Walsh (1984). In the data of Looney and Walsh (1984) there is a slight rise in the predicted wall profiles in outer region, which according to Looney and Walsh is due to approximate side boundary conditions. In the present calculation by increasing the width of calculation domain (length of the wall) the predicted wall profiles in outer region is in agreement with experimental data of Beltaos and Rajaratnam (1973) and Gardon and Akfirat (1965).

The variation of maximum radial velocity with the radial distance from the stagnation point is shown in fig.(7-2). The maximum velocity v_m is normalized by u_0 and scaled by $(h/2b_0)^{1/2}$ in order to be able to compare solutions from different inlet conditions and $h/2b_0$ ratios respectively. Starting from the stagnation point, the maximum radial velocity along the wall increases with increasing the radial distance due to the influence of pressure gradient and then decreases due to viscous dissipation. The results have been compared with available theoretical data from Looney and Walsh (1984) and experimental data of Kumada and Mabuchi (1970). The discrepancy between two sets of theoretical results is related to the divergence of pressure variation in the outer region close to the wall in the results predicted by Looney and Walsh (1984).

The distribution of centre line kinetic energy, k_{cl}, which is normalized by u_0^2 and scaled by $h/2b_0$, with respect to normalized axial distance from slot exit is shown in fig.(7-3). The results of numerical calculations indicate a sharp increase in k_{cl} beyond 0.85h downstream which results in the larger value of shear stress along the wall and the improved heat transfer characteristics near the stagnation point. The results have been compared with Looney and Walsh (1984) data and there is good agreement between them.

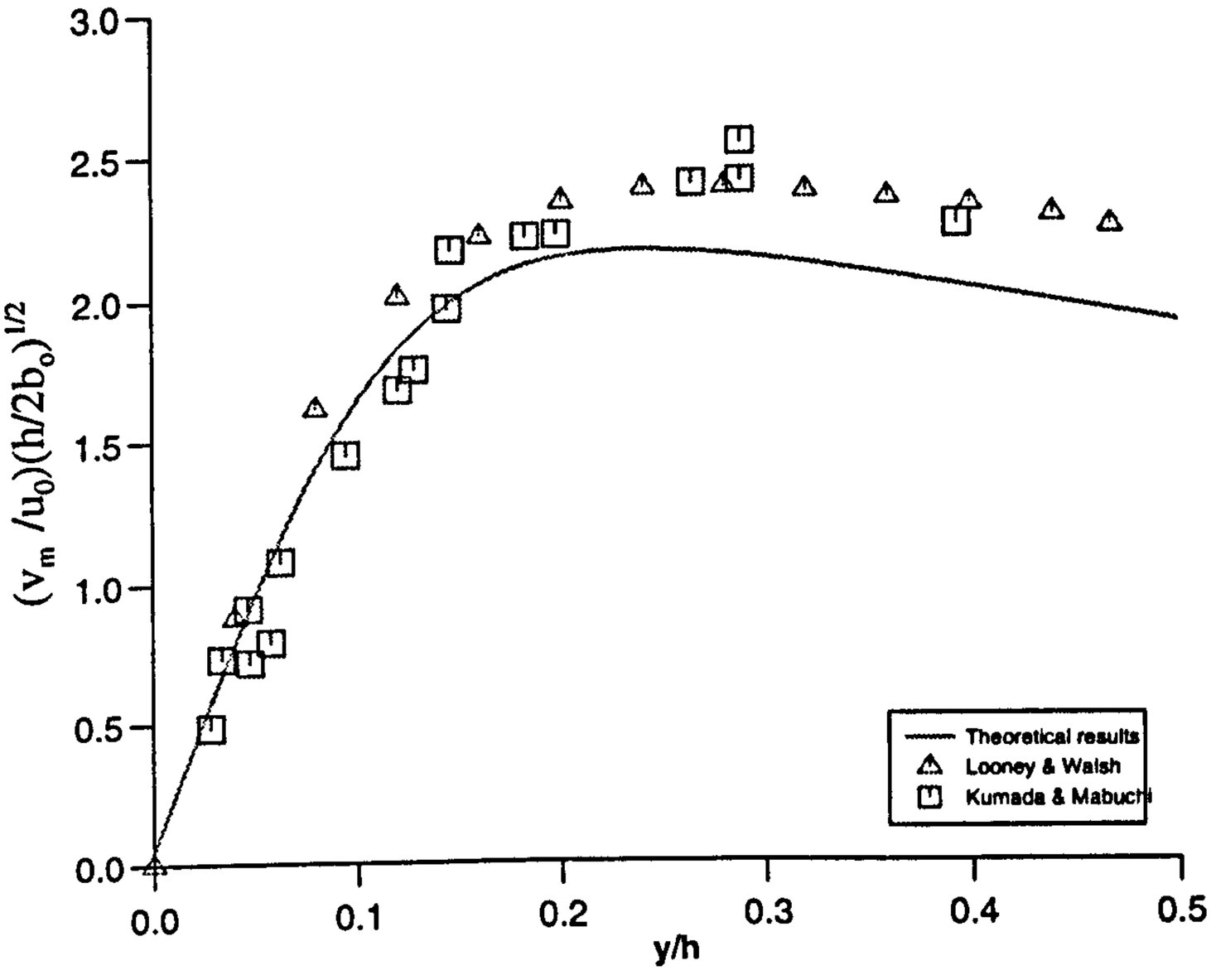

Fig.(7-2): Variation of maximum radial velocity with radial distance from stagnation point.

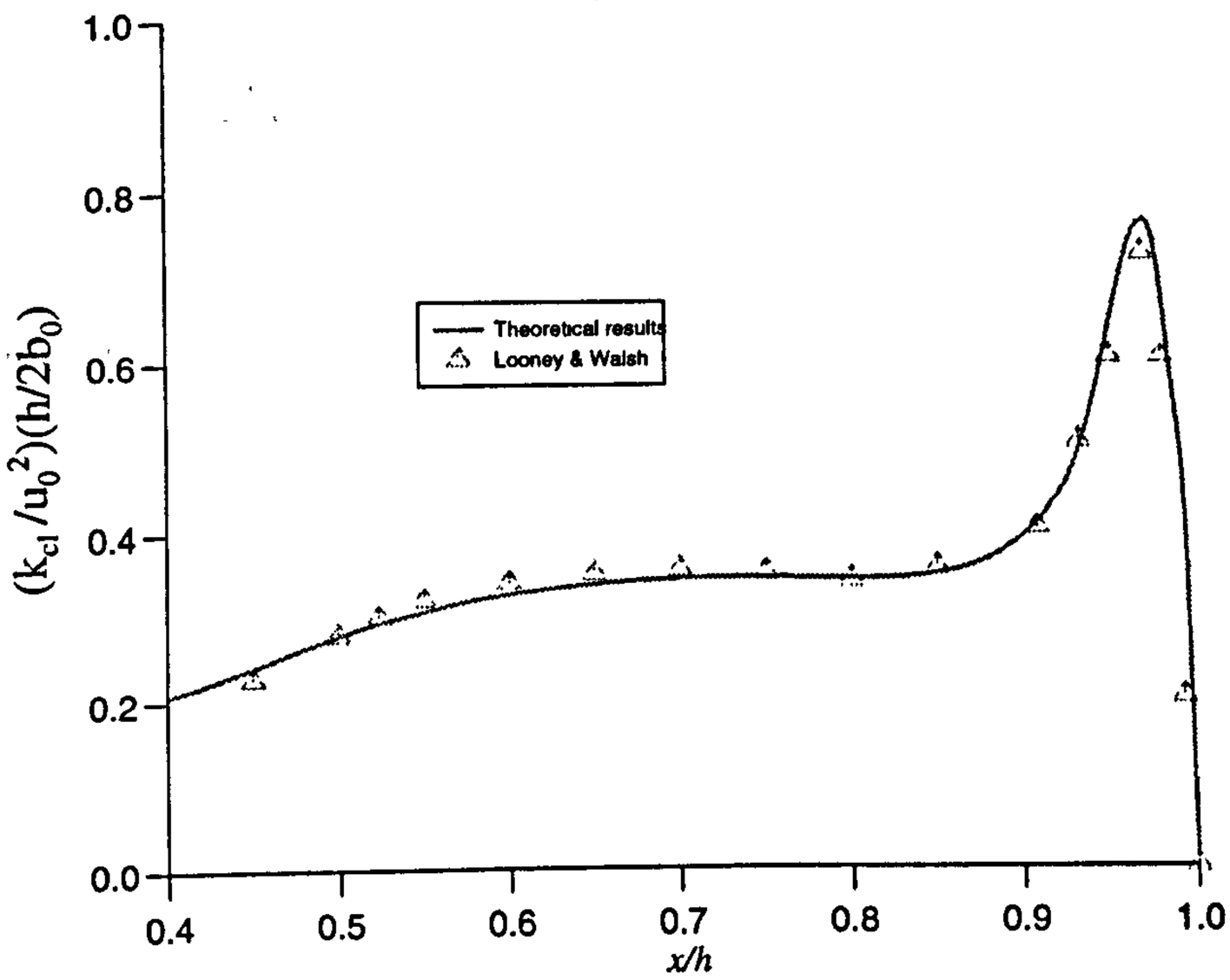

Fig.(7-3): Axial distribution of K_{cl} with axial distance from slot exit.

Fig.(7-4) shows the distribution of normalized centreline pressure with respect to normalized axial distance from the slot exit. The results show that there is not any effect of the wall on the free jet until 0.7h downstream and this is in agreement with the results obtained for both u_{cl} and k_{cl} and also the results obtained by Looney and Walsh (1984).

According to fig.(7-5) the agreement between predictions and the theoretical results of Looney and Walsh (1984) and experimental results of Beltaos and Rajaratnam (1973) for centreline velocity distribution is good. Difference between the calculated and experimental results are due to non-similarity effects of the lower $h/2b_0$ case where the undeveloped free jet enters the impingement region. As shown in fig.(7-5), centreline velocity which is normalized by u_0 and scaled by $(h/2b_0)^{1/2}$ decreases by increasing the axial distance from slot exit and finally reaches zero at the stagnation point.

Mean velocity results in the wall jet region are shown in fig.(7-6) and are in quantitative agreement with Looney and Walsh (1984). The velocity is zero on the wall and increases with distance from the wall and reaches to its maximum value at a close distance to the wall and then decreases by further increasing of distance. The distribution is similar and is well described by the curve of the simple plane turbulent wall jet, Beltaos and Rajaratnam (1973), generally referred to as the classic wall jet.

The variation of wall shear stress coefficient as a function of radial distance from the stagnation point is shown in fig.(7-7). Starting from the stagnation point the shear stress coefficient increases and reaches to its maximum value at a radial distance of y/h=0.13 and then decreases with further increase of radial distance due

to viscous effects.

The implications of the above comparisons show that the model described in chapter 4 is satisfactory, and should be valid at least for the impingement region of jet flow onto a circular cylinder.

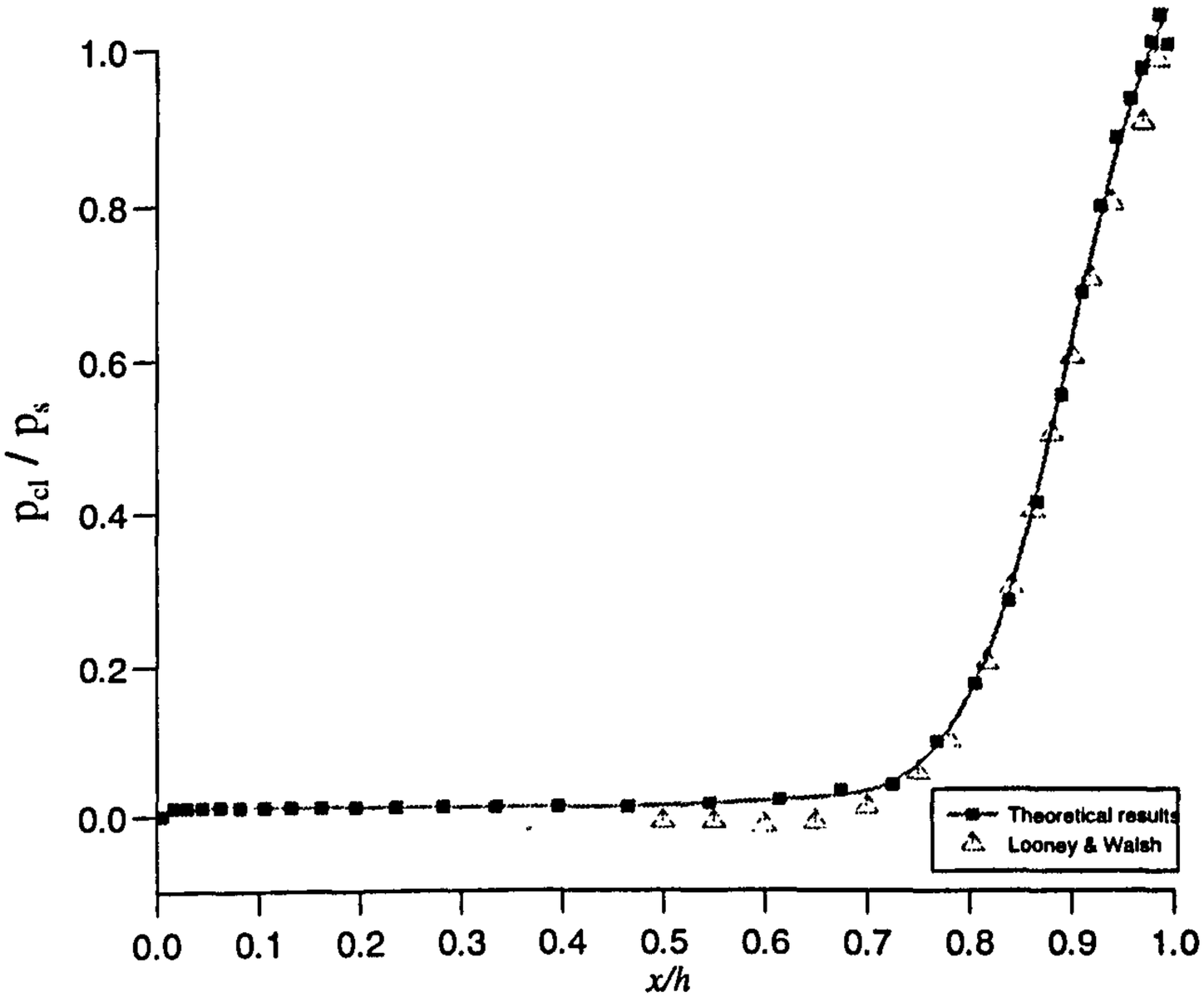

Fig.(7-4): Axial distribution of centreline pressure with axial distance from the slot.

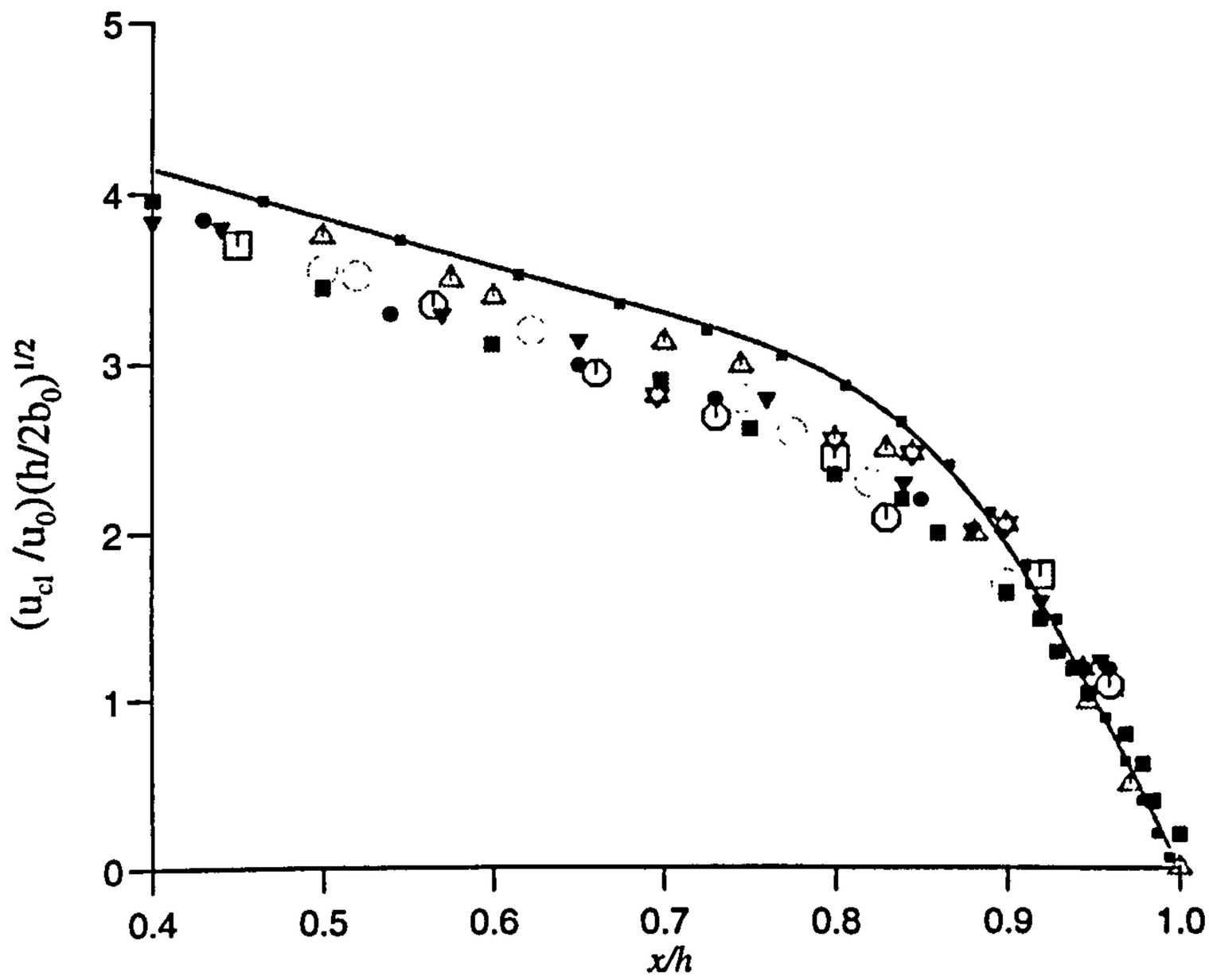

Fig.(7-5) : Axial distribution of centreline velocity with distance from the slot

—■— Present study $h/2b_0=20$, $R_{ej}=2.83\times10^4$; ▵ Looney and Walsh $h/2b_0=20$, $R_{ej}=2.2\times10^4$

■ Gutmark et al. $h/2b_0=100$, $R_{ej}=3\times10^4$; Beltaos and Rajaratnam : ▾ $h/2b_0=67.5$, $R_{ej}=5650$; • $h/2b_0=30.96$, $R_{ej}=6970$; □ $h/2b_0=14.05$, $R_{ej}=5270$; ⏲ $h/2b_0=43.64$, $R_{ej}=7100$; ✡ $h/2b_0=43.64$, $R_{ej}=5270$; o Schauer and Eustis $h/2b_0=40$, $R_{ej}=4.3\times10^4$.

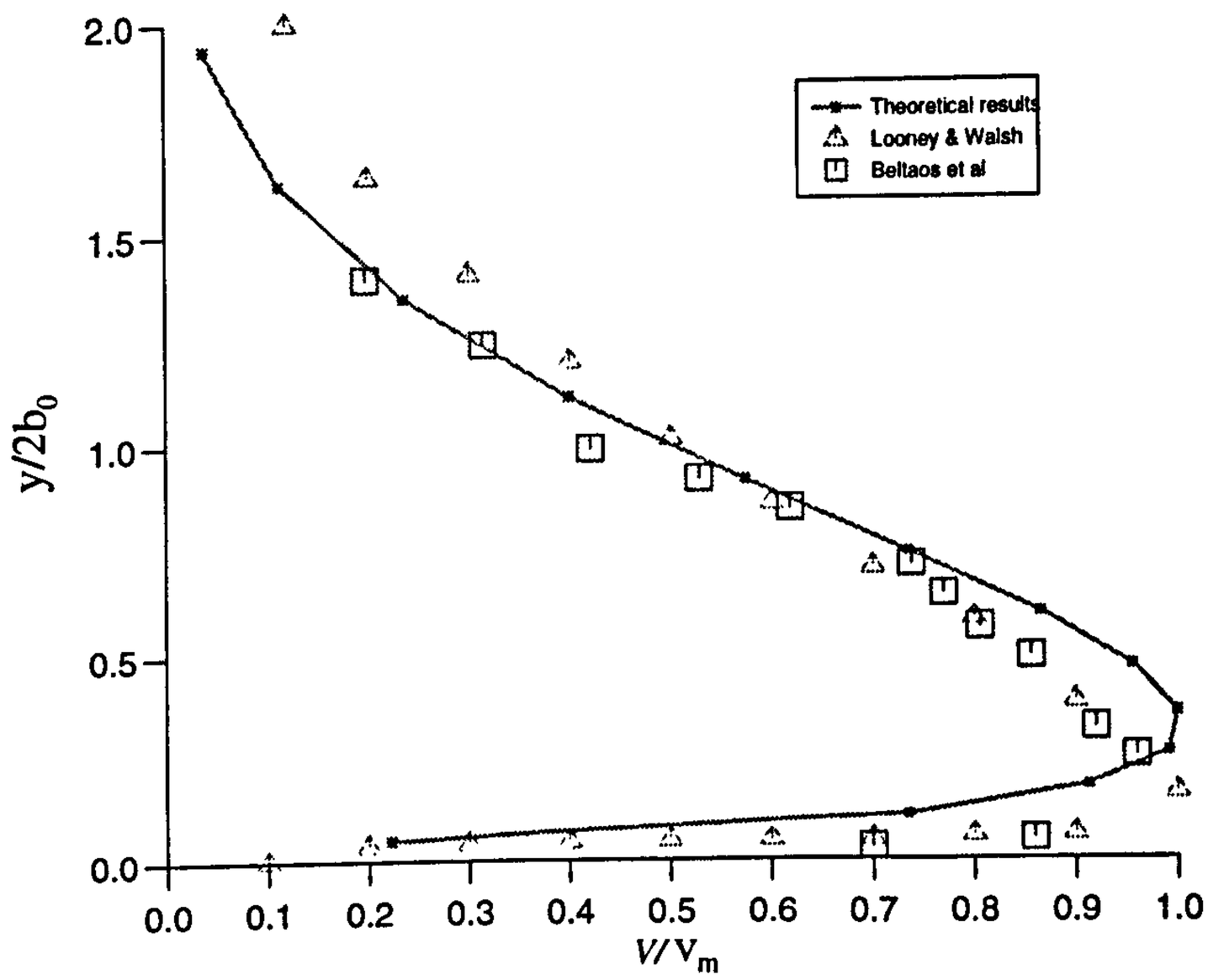

Fig.(7-6):Wall jet velocity profile.

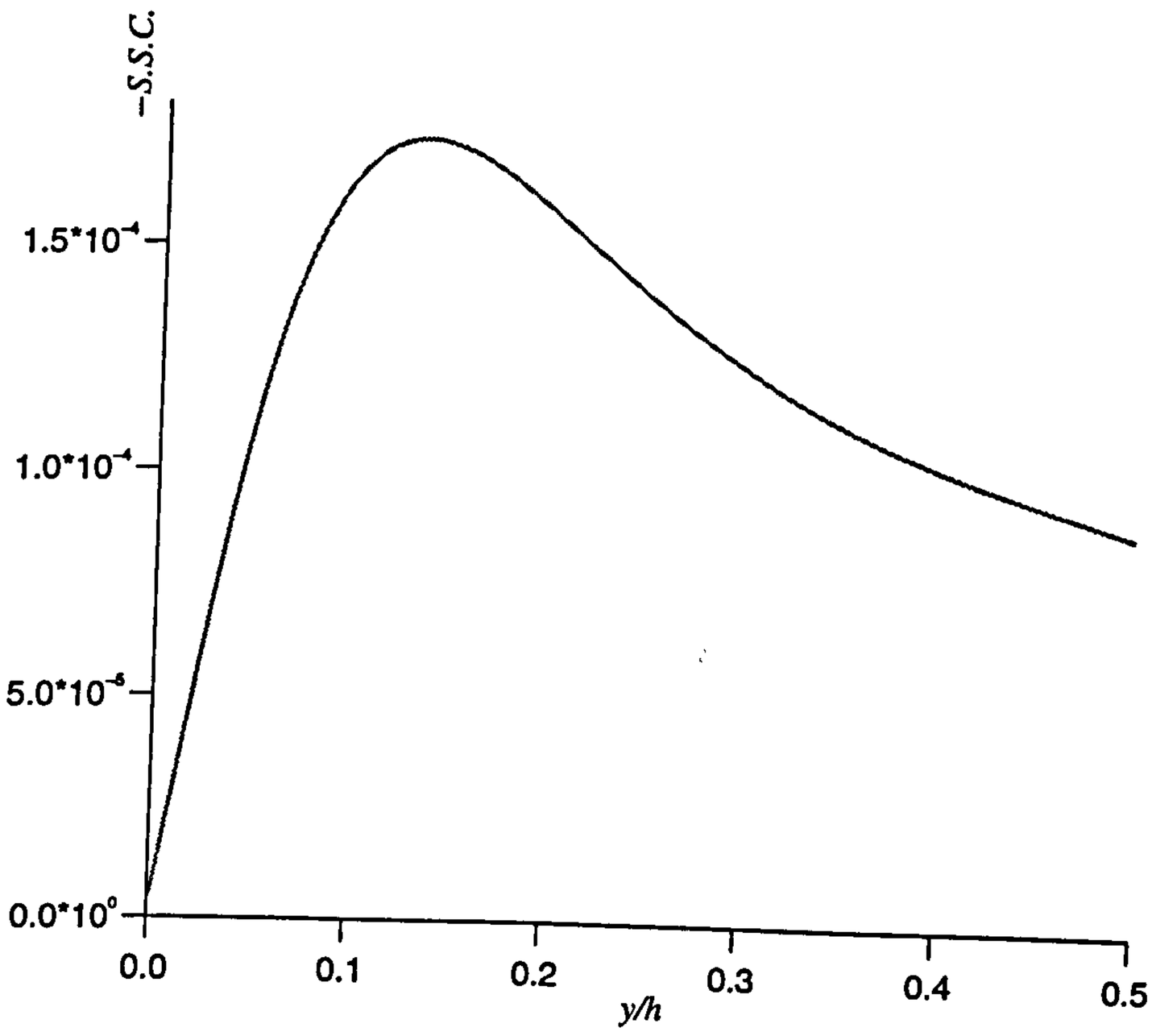

Fig.(7-7): Variation of shear stress coefficient with radial distance from stagnation point.

CHAPTER

8

EXPERIMENTAL STUDY OF JET IMPINGEMENT ONTO A CIRCULAR CYLINDER

8-1: Introduction

The main aim of the experimental study of a turbulent jet interaction with a circular cylinder is to find out how the jet flow behaves under these circumstances, and to provide test data for assessing the accuracy of the numerical calculations.

This part of work is performed in different sections. First, an attempt is made to visualize the flow field, then, a study is carried out for the interaction of an axisymmetric jet with a circular cylinder. This section of work gives some indication of the value of modelling the jet interaction by a slot jet. Finally an experimental study of a slot jet interaction with circular cylinder is carried out.

8-2:Flow visualisation

In many engineering problems, for example air flow past airfoils, jet flows, convection problems, jet impingement problems, etc, flow cannot be viewed directly. In such cases, the frequently interesting phenomena contains the changes of the refractive index across the field to be investigated, which can then be visualised or photographed by using the optical methods that depend on the effects of refractive index changes on the transmission of light. Probably, the most popular available technique for such cases is *Schlieren photography*. Extensive use of this method is made of flow visualisation in aerodynamic research, for studying high speed air flow,

where the change of refractive index that accompany the density changes across the flow field can be easily observed.

In this part of the work flow visualisation was adopted for observing the interaction of a jet flow issued through a convergent nozzle with 12.9 mm exit diameter with a circular cylinder.

8-2-1: Experimental apparatus and procedure for Schlieren photography

The schematic diagram of flow visualisation experimental rig for Schlieren photography is shown in fig.(8-1). Air was supplied at pressures of 30, 40 and 50 psig by a large 4-stage reciprocating compressor. A pressure controlling valve and a pressure gauge are supplied on the pipe line before the nozzle, for regulating the inlet pressure to the nozzle. A convergent nozzle with exit diameter of 12.9 mm was connected to the end of the pipe line. The jet issued from this nozzle and interacted with a cylinder spanned horizontally between two parallel plates and located in cross direction with respect to the jet axis.

The Schlieren apparatus was conventional and consisted of an argon arc spark light source (including condensing lens and knife edge), a condensing lens, a knife edge, two 8" diameter concave mirrors of 6 feet focal length, and a camera.

In setting up the Schlieren apparatus the argon jet light source was placed at the focal point of first mirror. The horizontal knife edge was located at the focus of the first lens. The light passed through the second lens and converged to its focal point and then diverged onto the first mirror. The first mirror was rotated until the parallel light beams formed by the first mirror passed through the cylinder in the direction perpendicular to the jet flow direction. The second mirror was moved laterally and vertically until it received the parallel beams emerging from the test

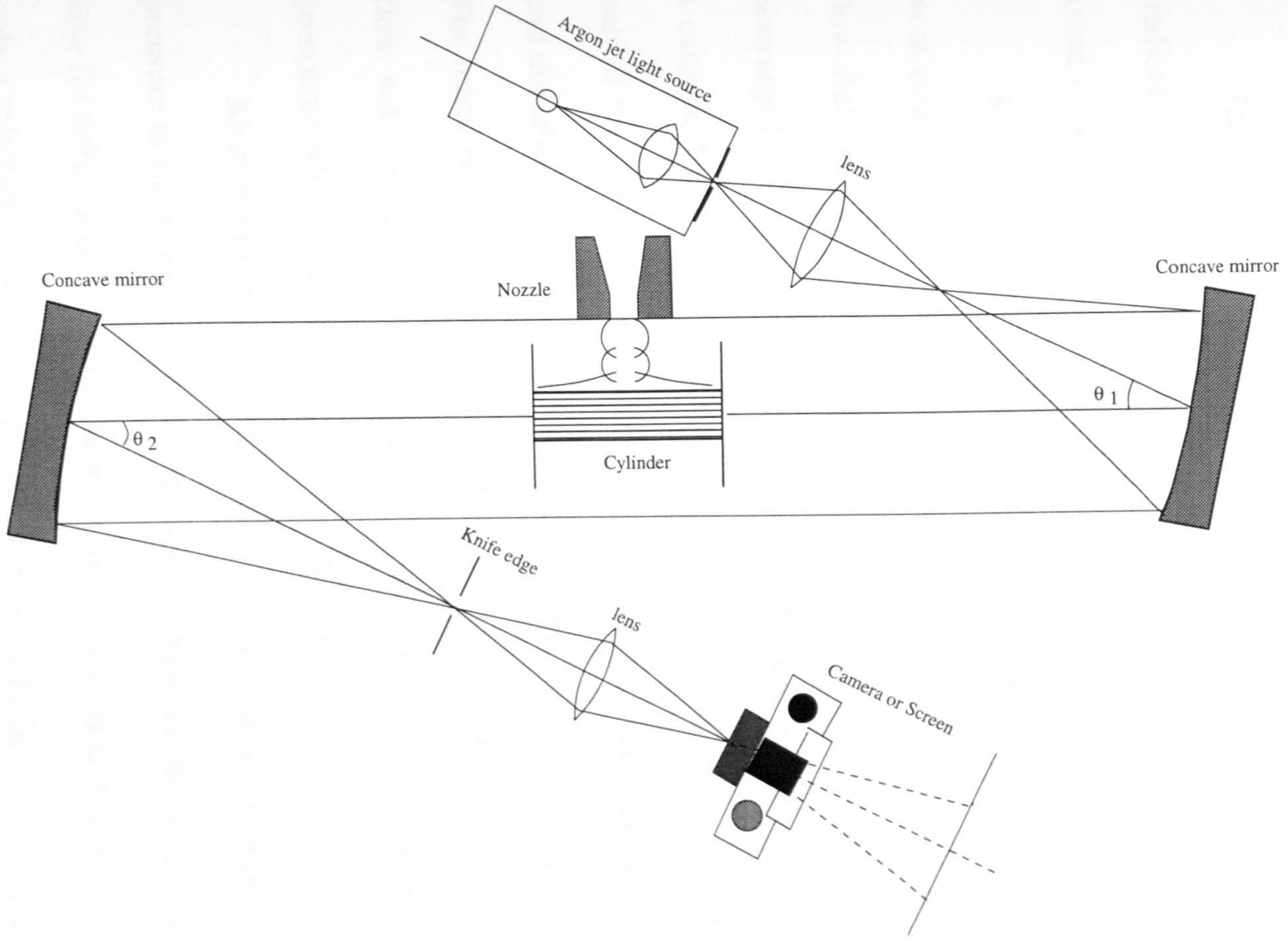

Fig(8-1): Arrangement of Schlieren photography

section and was rotated until the light reflected from it passed through the second knife edge and formed an image of the flow on the viewing screen. The knife edge was set at the focal point of the second mirror. In order to maintain the light beams parallel and to avoid abnormality difficulties, the angle θ_1 was set approximately equal to θ_2 and both angles kept as small as possible, fig.(8-1).

The appearance of the images of the flow in the vicinity of large density gradients were very sensitive to the focusing of the apparatus and the focusing was found to be more accurate for the case of high speed jet flows.

Schlieren images of the high speed jet impingement with circular cylinder were observed by projecting parallel light beams from the light source, across the flow field between concave mirrors. The light beams leaving the second mirror, converged in its focal point, where a knife edge was placed and then diverged onto a camera. The knife edge acts as an optical filter and only allowed approximately half of the light to be transmitted and set up a better contrast between undisturbed and disturbed light beams on passing through the flow containing a density gradient. The refractive index changes in the flow and so the light beams passing through the flow will diverge and regions of the flow will appear relatively dark and bright compared with the average background intensity.

Many photographs were taken during investigation for different values of inlet pressure to the nozzle and different distances between the nozzle and cylinder and also for different eccentricities between the cylindrical section and jet centre line and only a selection of them are represented in fig.(8-2). In all of these photographs, the formation of shock waves in the nozzle exit and also the impingement region due to jet interaction with circular cylinder are clearly visible. This indicates that significant

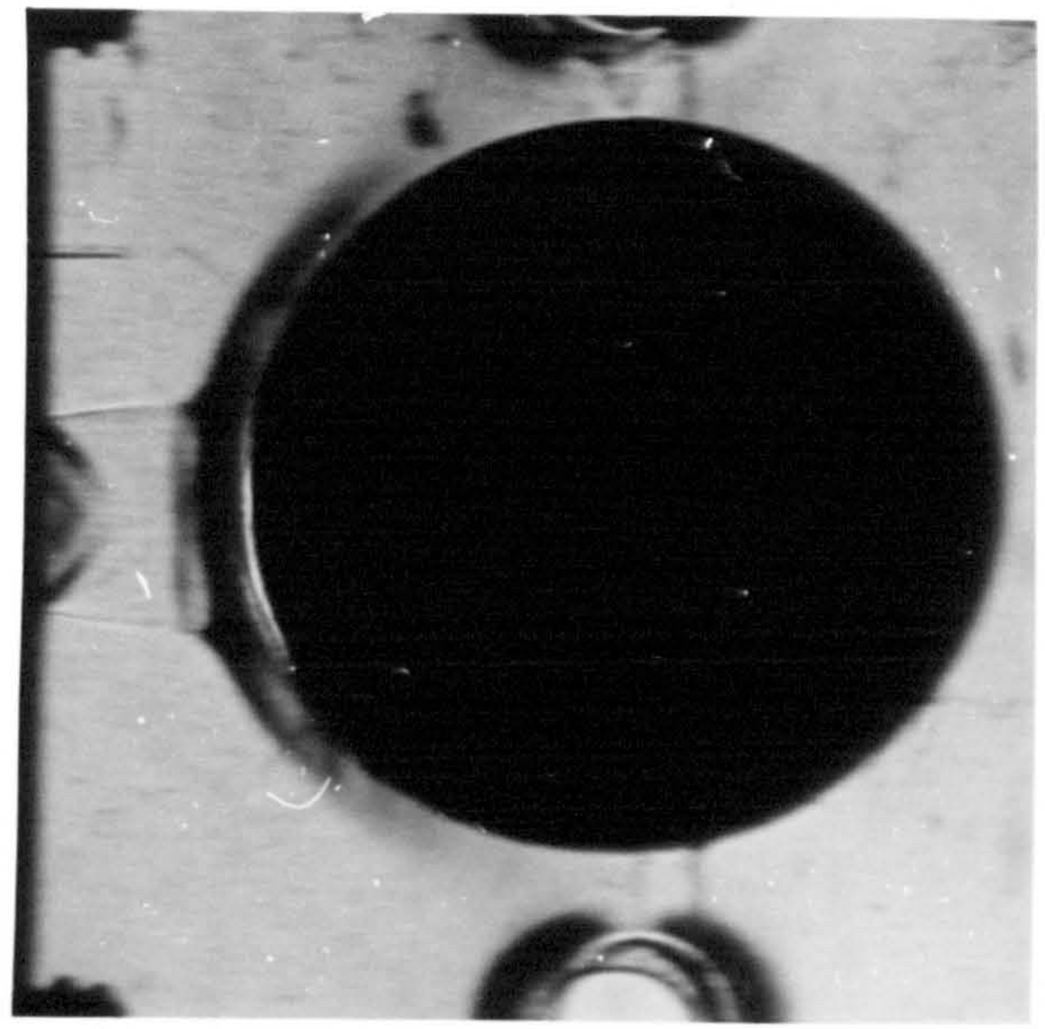

(a)

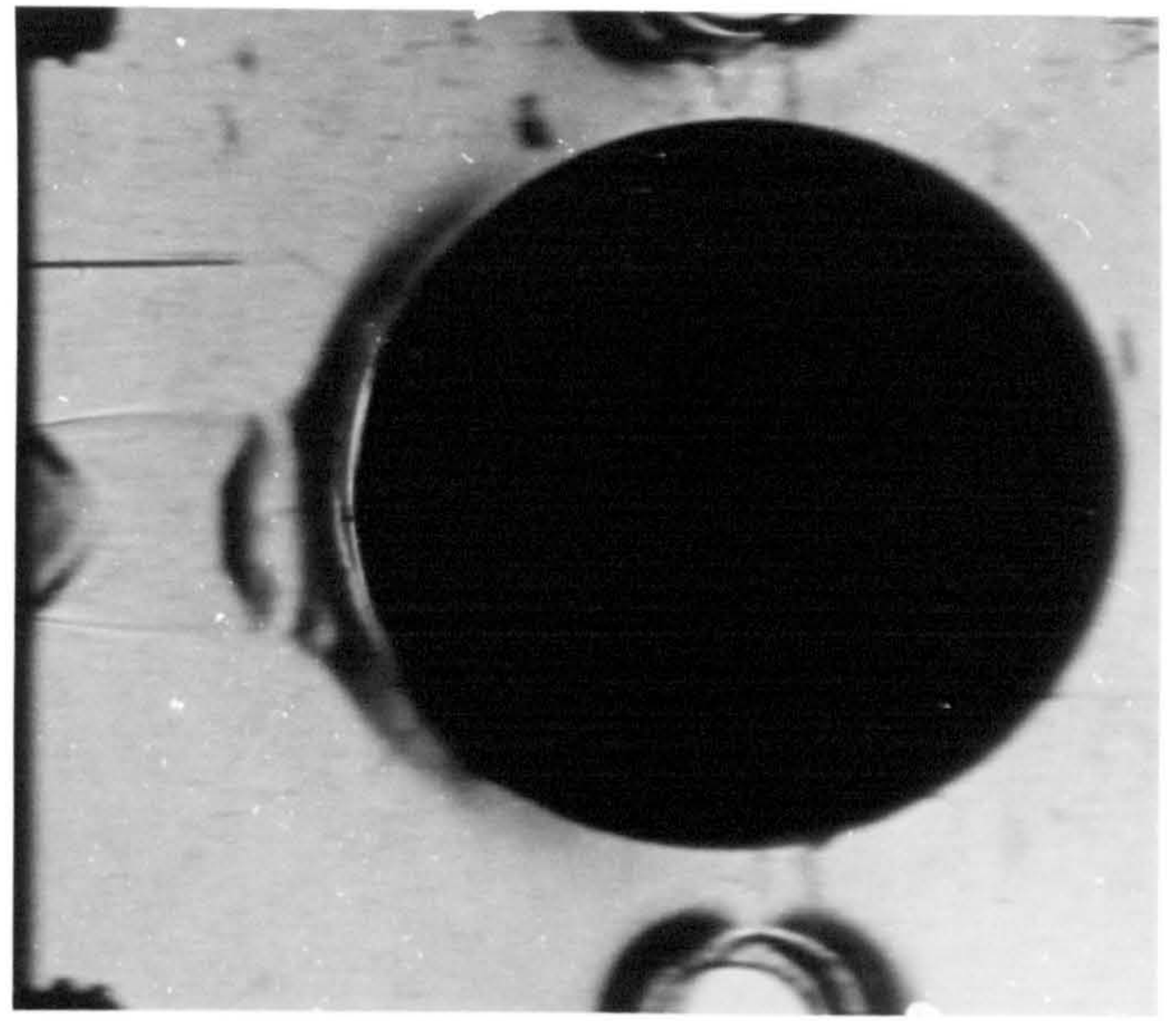

(b)

Fig.(8-2a): Schlieren photographs from jet impingement onto a circular cylinder for nozzle inlet pressure = 50 psig.

(a) H/D=1.0 (b) H/D=1.5

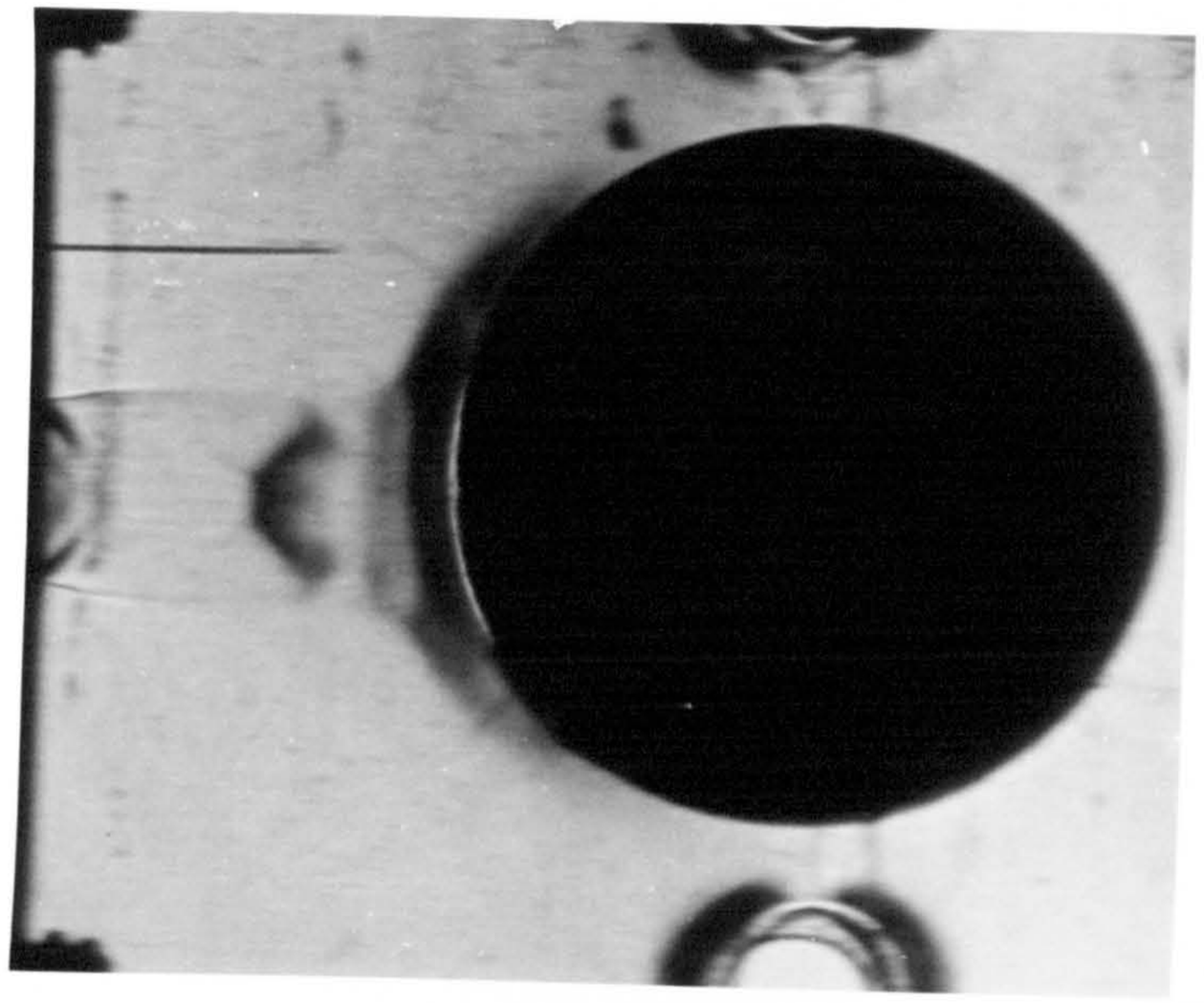

(c)

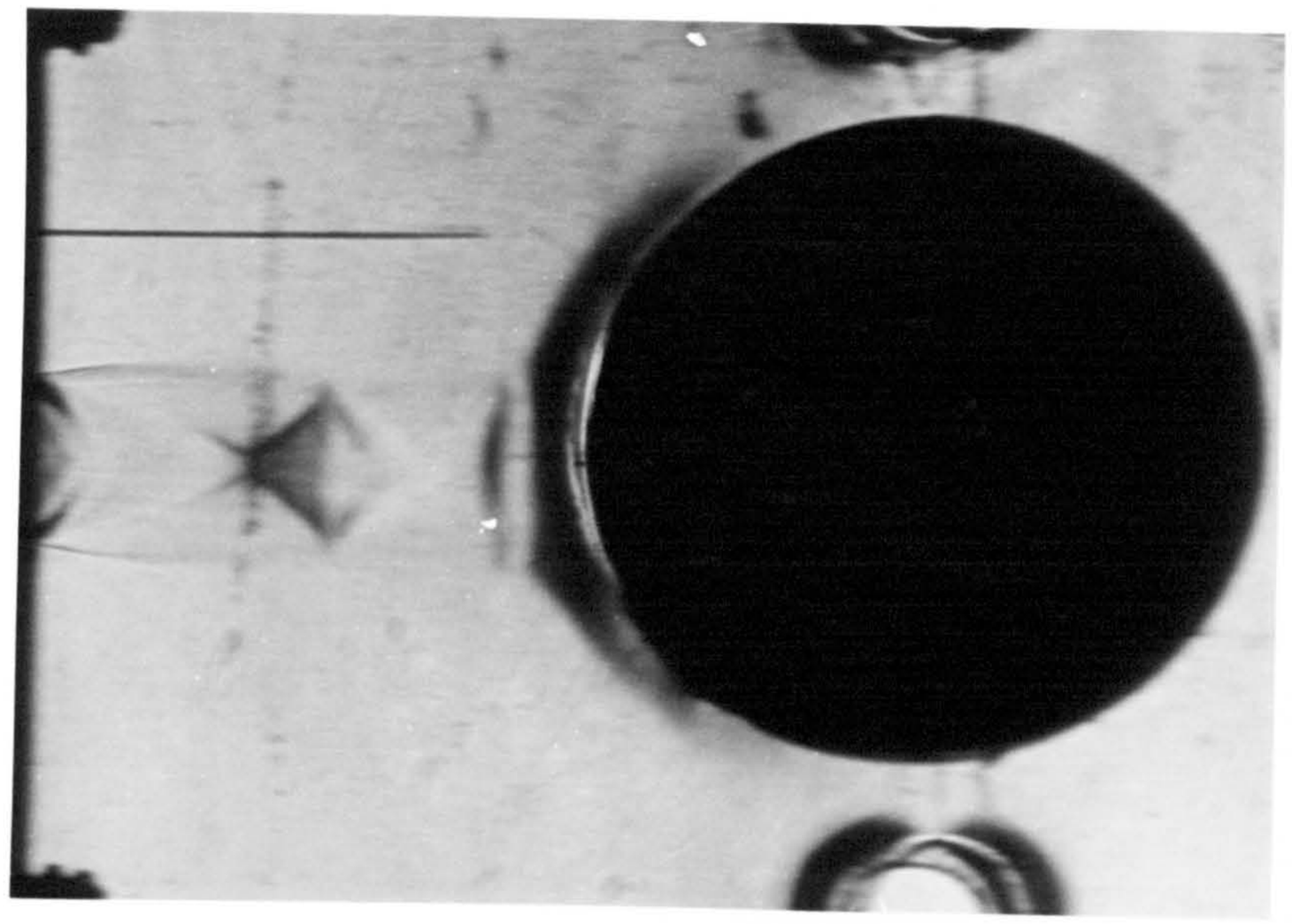

(d)

Fig.(8-2b): Schlieren photographs from jet impingement onto a circular cylinder for nozzle inlet pressure = 50 psig.

(c) H/D=2.0 (d) H/D=3.0

significant air density gradients existed in these regions, but separation points on the cylinder and also wake region behind the cylinder were not detected by using this method.

Referring to fig.(8-2), the flow field of an under-expanded supersonic jet in front of the cylinder may be divided into two different parts, (1) the free jet region, and (2) the impingement region. The impingement region is separated from the free jet by a strong plane-shock wave due to impingement and intersection of the jet shock wave forming a triple point shock structure. The reflected shock strikes the jet

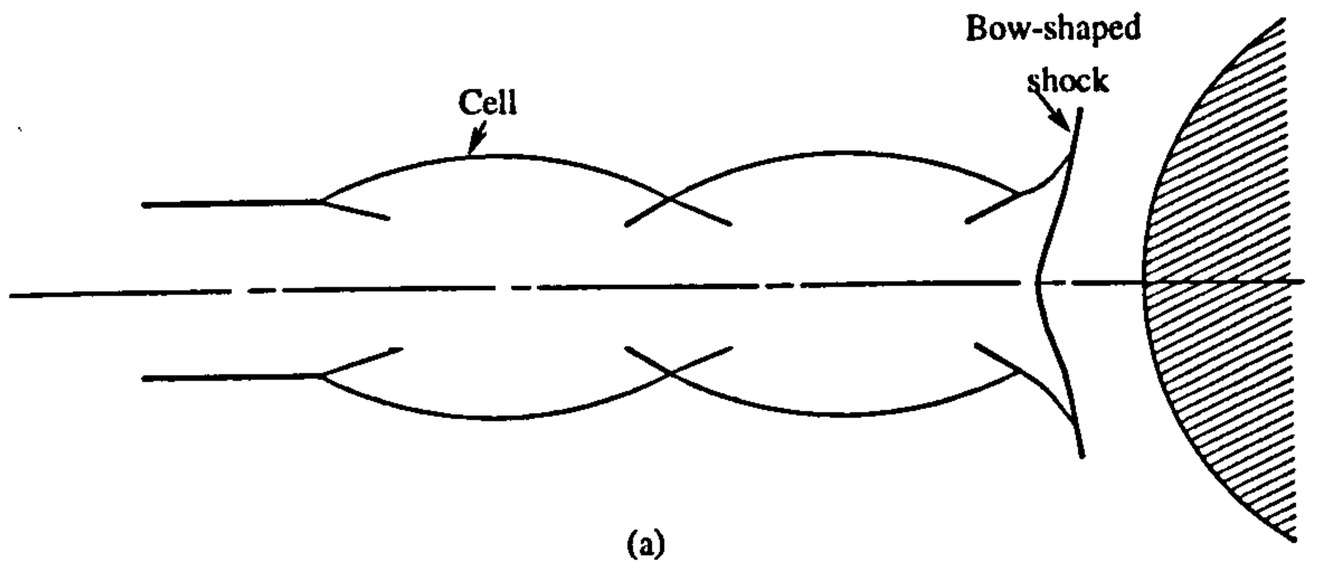

(a)

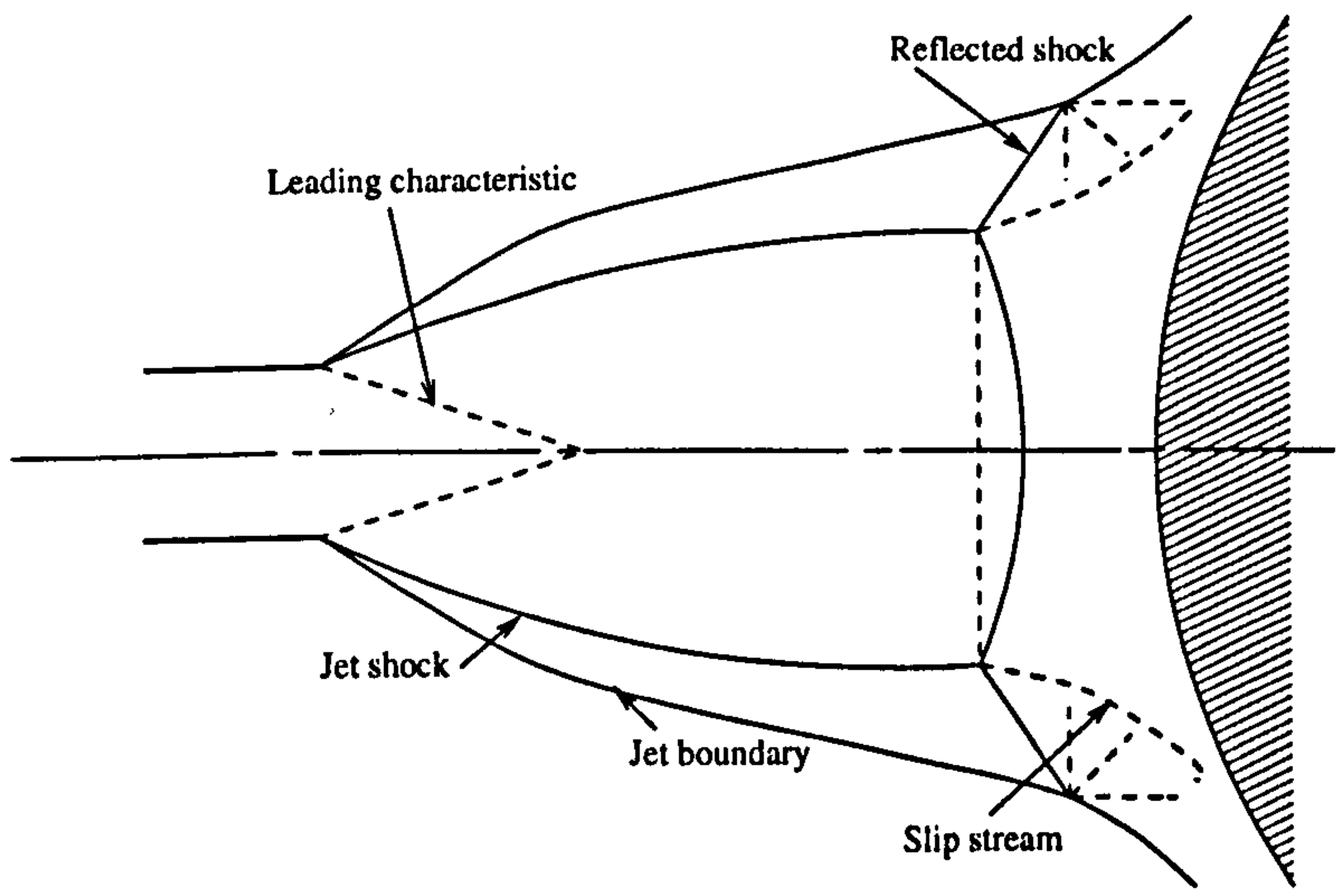

(b)

Fig.(8-3): Schematic sketch of the flow field for (a) moderately under-expanded jet, (b) highly underexpanded jet.

boundary and gets back into the flow as a family of expansion waves. For the case of a moderately under-expanded jet, instead of plate-shock a bow-shaped shock will arise. In any case the flow beneath the impingement shock is subsonic, and for the case of jet interaction with a circular cylinder, the flow over the cylinder will be subsonic flow. For this reason the numerical solution of high speed jet interaction with a cylindrical surface described in chapter 9 is carried out for the case of subsonic flow. The schematic representation of the structure of under-expanded supersonic jet is shown in fig.(8-3). This structure is described in more details by Love *et al.* (1959), Pamadi (1981), and also presented by Birch (1992).

8-2-2: Surface flow visualisation by the aid of oil-lampblack method

The second method of visualisation was carried out with the aid of the oil-lampblack technique. In order to use this method, a mixture of lampblack and oil of suitable viscosity is prepared. The viscosity of the mixture should be such that when the mixture is brushed on the surface of the cylinder, it will not droop under the pull of gravitional force and be able to move over the surface in response to shear stresses exerted by the jet driven fluid flow.

It should be noted that in the region of low velocity areas, such as the stagnation point, the oil-lampblack mixture does not move. Since the whole surface of the cylinder was coated with a uniform layer of black mixture before the interaction with high speed jet, the low velocity regions remains black during the air flow period.

After the completion of the period of exposure of the cylinder to the air flow, the cylinder surface was covered by transparent adhesive tapes, then these tapes were removed and laid on a paper. A representative picture of the visualisation pattern is

presented in fig.(8-4). This figure corresponds to the distance of 10 cm between nozzle exit and cylinder and inlet pressure of 20 psig.

An inspection of fig.(8-4) shows that at the stagnation point of axisymmetric jet interaction with the cylinder, the oil-lampblack mixture is nearly stagnant. Fig.(8-4) includes fine streaklines which originate from the stagnation point and end in the black regions that are not affected by the jet flow. These regions in the circumferential direction indicates the separation of jet flow from cylinder surface and shows a very narrow separation region at the rear of the cylinder in mid-position. For the average results obtained from repeated tests, the separation angle at the rear of the cylinder is about 37°, and so the separation points positions on the cylinder measured from the front stagnation point are $s_1 \approx 161^{\circ}$ and $s_2 \approx 198^{\circ}$. This result is in good agreement with experimental results obtained for pressure distribution around the cylinder at the same conditions. The half length of the cleaned area in the longitudinal direction of the cylinder obtained from surface flow visualisation test is 2.42 times the cylinder diameter (l/D=2.42). This position happens to coincide with the point where the static pressure on the longitudinal direction of the cylinder is atmospheric, fig.(8-5).

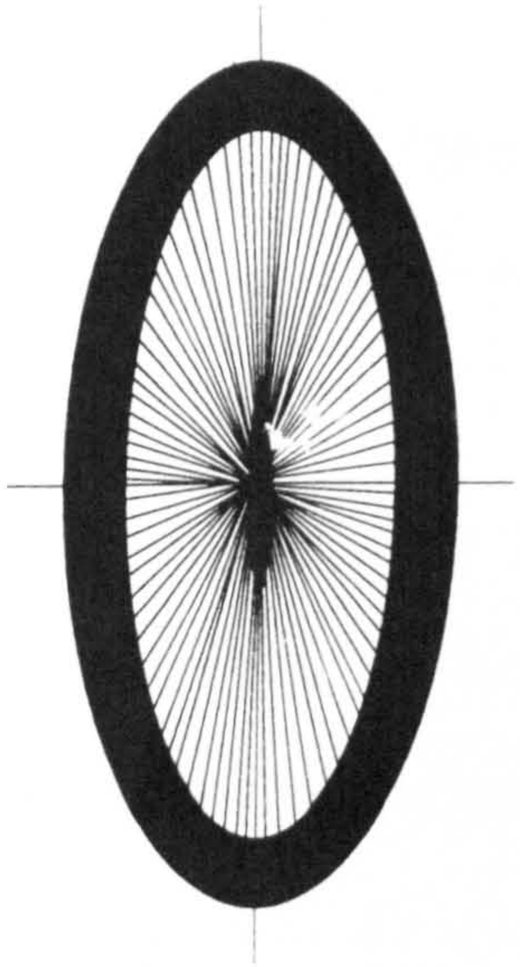

(a)

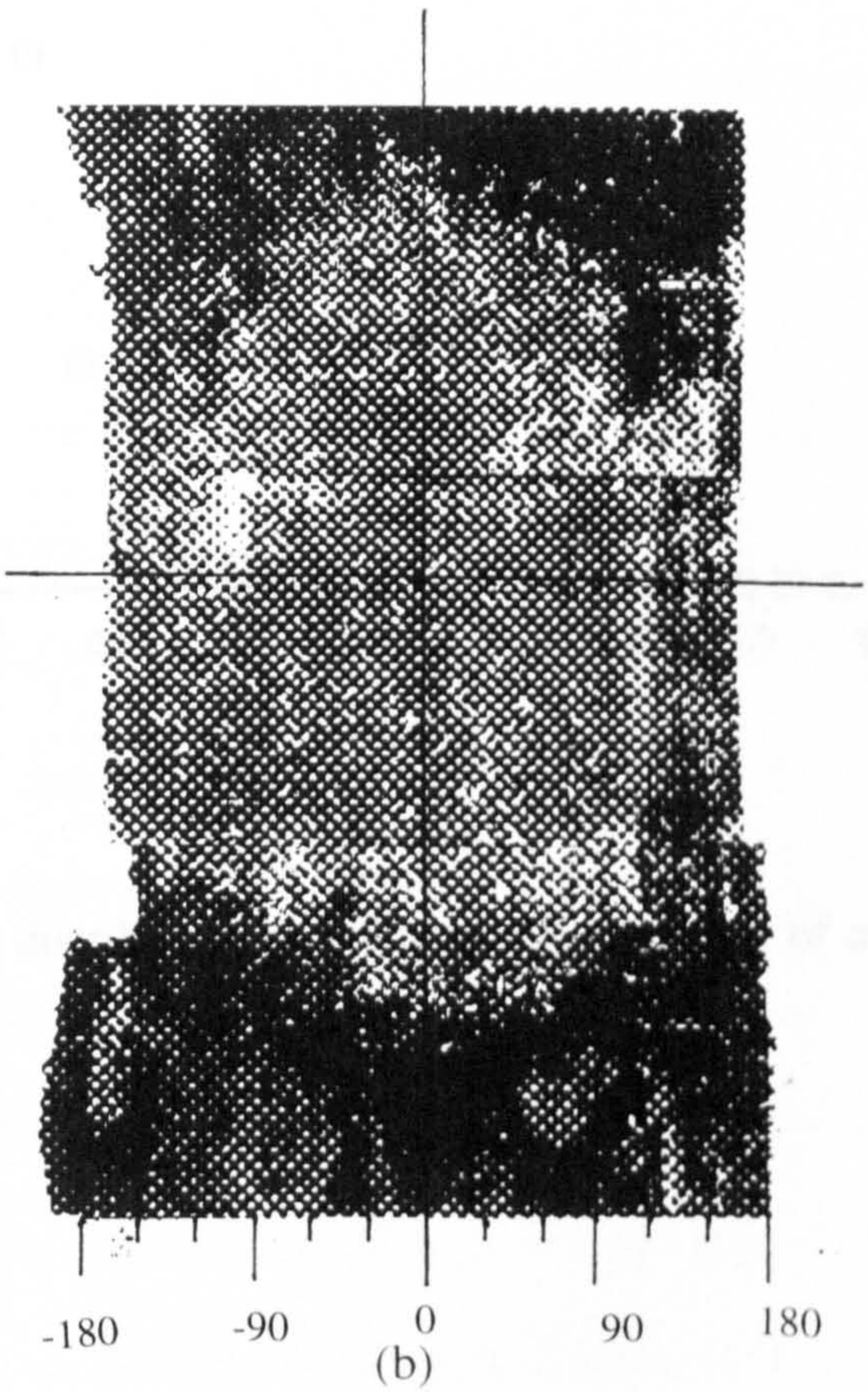

-180 -90 0 90 180

(b)

Fig.(8-4): Schematic representation of cleaned area by the aid of oil-lampblack method, (a) schematic diagram, (b) actual representation.

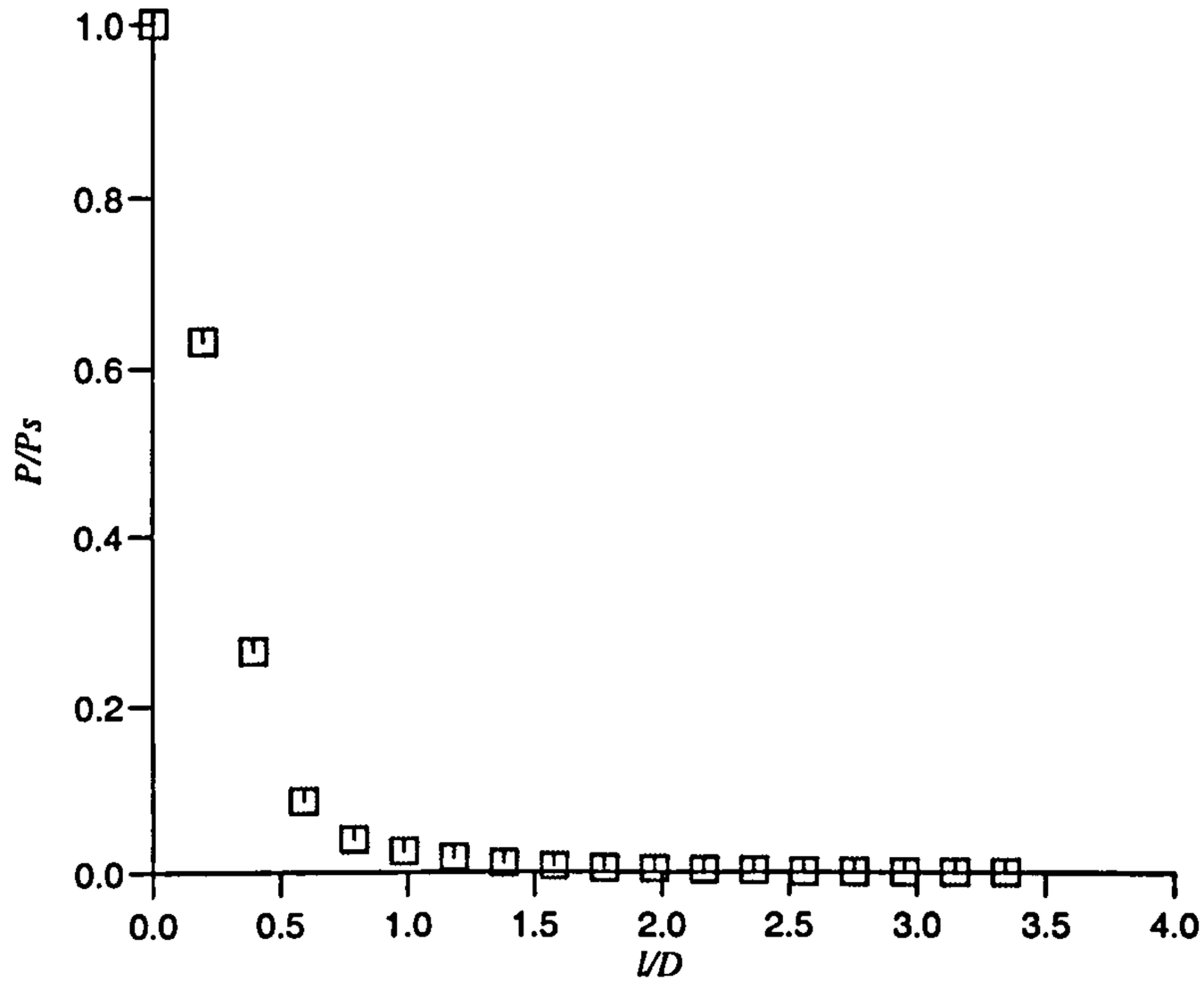

Fig.(8-5): Pressure distribution on longitudinal direction of a cylinder for p_{in}=20 psig, and H/D=4.

8-3: Experimental investigation

8-3-1:Axisymmetric jet impingement onto a circular cylinder

The schematic representation of the experimental set up is shown in fig.(8-6). The figure shows a round nozzle of diameter d_N, into which air is drawn from the main supply of compressed air. The flow at the exit from the nozzle forms an axisymmetric free jet. A circular cylinder of diameter D, spanned horizontally between two parallel plates and positioned in cross flow to the jet serves as the impingement surface. The cylinder is situated at a distance H from the nozzle exit plane. The cylinder centre may be offset by the distance e (eccentricity) from the geometric horizontal symmetry plane of the axisymmetric jet. The cylinder was pressure tapped at the mid-span and by rotating it, pressure measurements could be made at any angular position.

The cylinder diameter was 1" (≈25 mm) and its length-to-diameter ratio was 15.6. It was situated at 4-12 cylinder diameters from the nozzle exit. The eccentricity (offset) between cylinder centre and geometric horizontal symmetry plane of the jet was varied over the range of 0-0.5 of the cylinder diameter. The nozzle exit diameter was 5mm, and the experiments were carried out for a nozzle inlet pressure range of 10-40 psig (≈0.7-2.75 bar). The nozzle choking pressure by calculation, using data obtained from experiments, is nearly equal to 16 psig., so the set of experiments for p≥20 psig., are related to the choked flow conditions (under-expanded jet).

For further clarity, the pressure distributions around the cylinder have been measured for the distances in the range of 0.4-2 cylinder diameter between cylinder and nozzle exit, only for the non-offset condition. In order to determine the length of area of cylinder surface affected by the jet, the pressure changes in a longitudinal

direction of the cylinder from its mid-position have been measured.

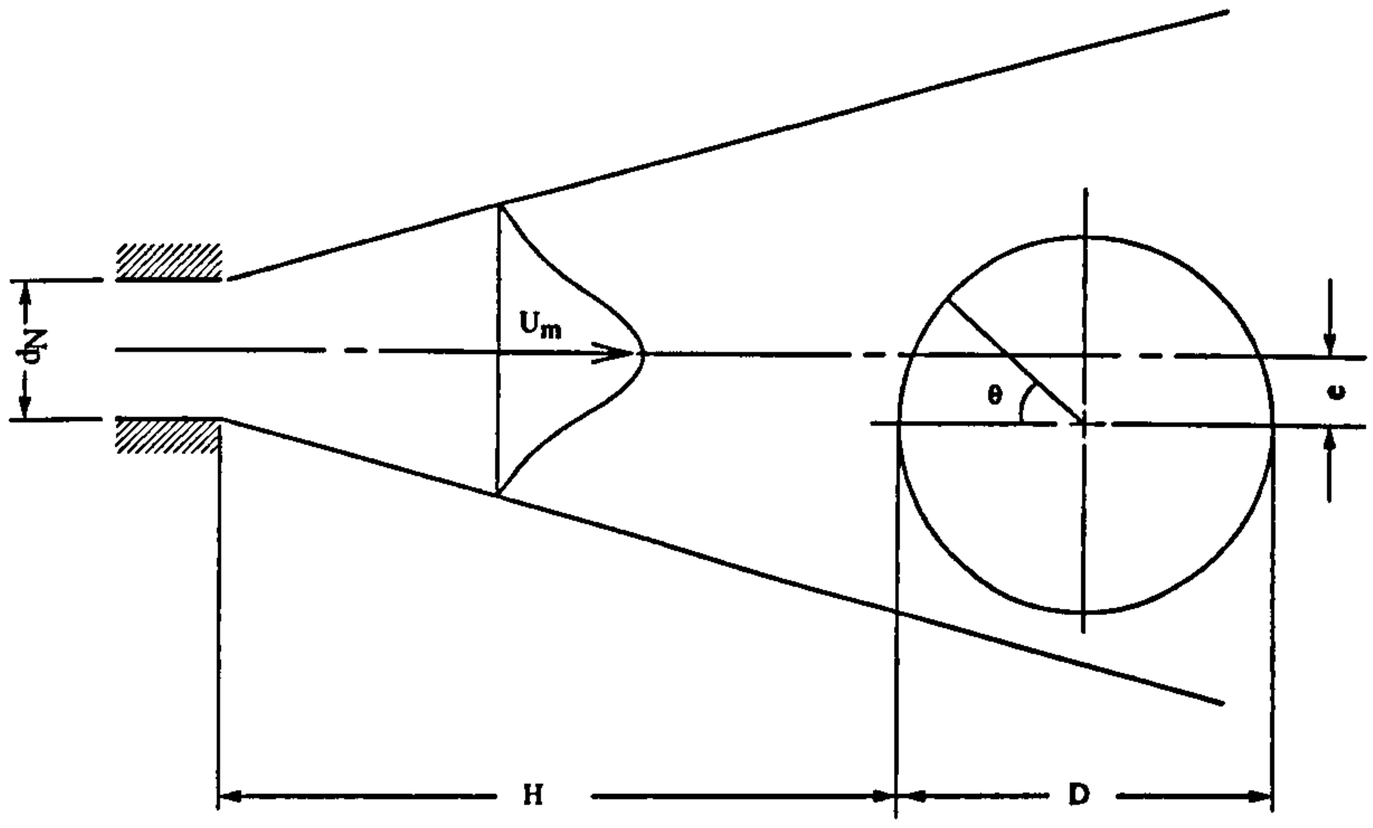

Fig.(8-6): Experimental set up.

8-3-1-1: The effect of nozzle inlet pressure on pressure distribution around the cylinder

The cylinder surface pressure p is measured relative to the atmospheric pressure and is normalized by the stagnation gauge pressure on the cylinder, p_{st}, or the dynamic pressure at the nozzle exit $\varrho u_0^2/2$; each of them is expressed as a pressure coefficient c_p.

The pressure distributions around the cylinder in a non-offset condition for nozzle inlet pressures in the range of 10-40 psig and for constant spacing are shown in figs.(8-7) - (8-8). All the profiles collapse together and are symmetrical for the upper and lower halves of the cylinder and show that the pressure distribution around the cylinder for the non-offset condition is independent of nozzle inlet pressure and therefore nozzle exit velocity in the range of experiments. Separation points are located at the rear of the cylinder and by considering the narrow constant pressure region behind the cylinder they are positioned close together. For H/D=4 their

angular position are ±15° from the rear stagnation point. This is in agreement with the results obtained from flow visualisation.

The pressure distribution around the cylinder for differing offsets, constant spacings between cylinder and nozzle and varying nozzle inlet pressures are shown in figs.(8-9) - (8-13). As illustrated by the figures, offset jet conditions give rise to non-symmetrical pressure distribution on the surface. The position of the frontal stagnation point also changes and its behaviour will be illustrated in the next section. The separation point on the upper semi cylinder moves towards 180°, whereas in the lower semi-cylinder the separation point moves away from 180°. Again all the profiles of pressure distribution for different values of nozzle inlet pressures collapse together and therefore even by considering the offsets, the pressure distribution around the cylinder appears to be independent of the nozzle inlet pressure.

8-3-1-2: The effect of cylinder offset on the pressure distribution around the cylinder

Lowering the cylinder centre with respect to the horizontal symmetry plane of the jet creates different offsets. Increasing the offset (eccentricity) at constant nozzle inlet pressure and constant spacing between nozzle and cylinder results in:

a) Stagnation point shifts towards higher rotational positions on the upper semi-cylinder. For example for e/D=0.5, θ_{st}=32° (p_{in}=20 psig, H/D=4). Variations of θ_{st} with respect to e/D for differing values of p_{in} and H/D=4,8 are exemplified in figs.(8-14) - (8-15). Referring to these figures it is obvious that the effect of offset on stagnation point angular position is less for higher spacing between cylinder and nozzle, for example for the case of e/D=0.5 and p_{in}=30 psig, θ_{st} changes from 34.4° for H/D=4 to 18.2° for H/D=8.

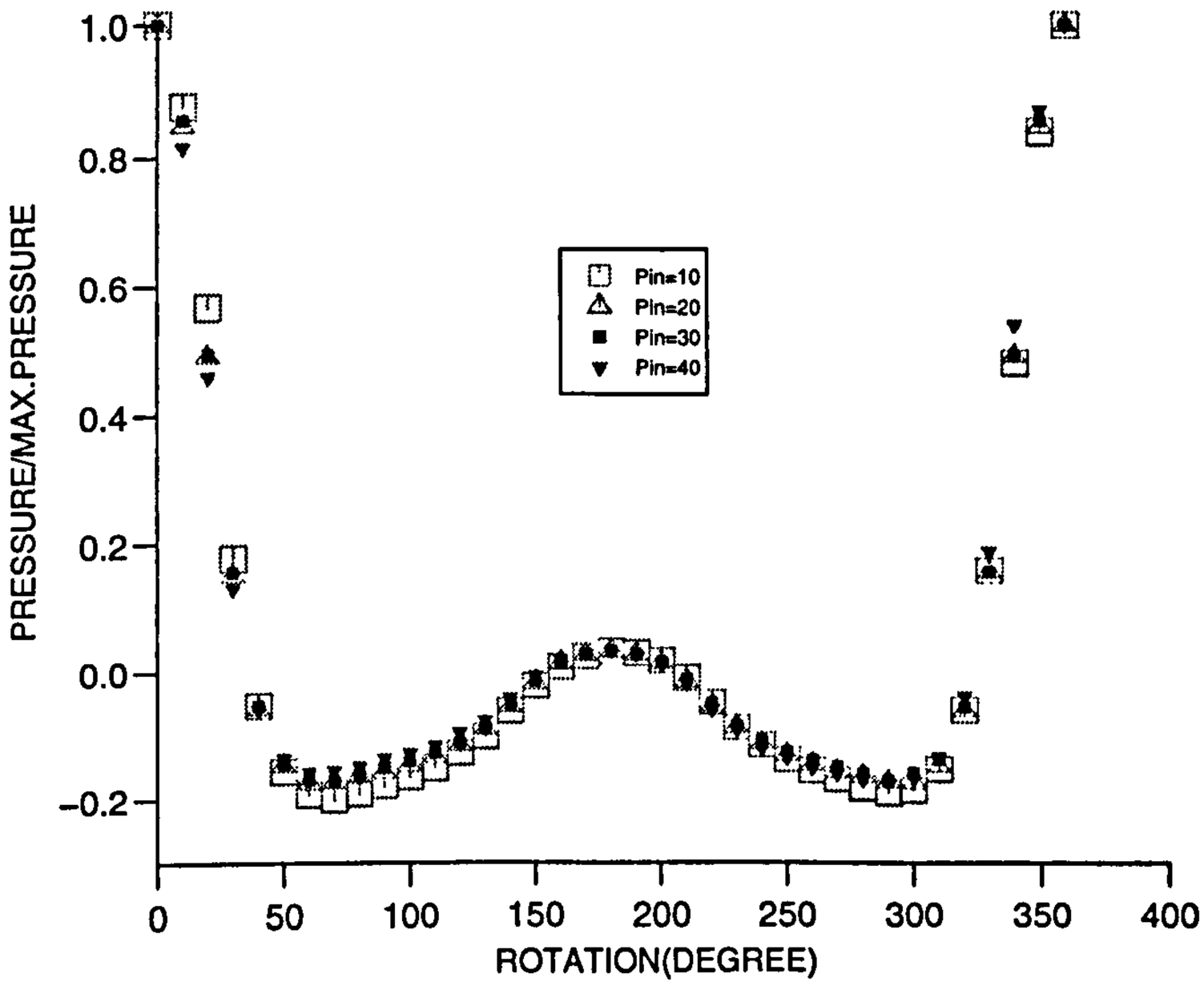

Fig.(8-7): Pressure distribution around the cylinder for different inlet pressures to the nozzle, H/D=4, e/D=0.

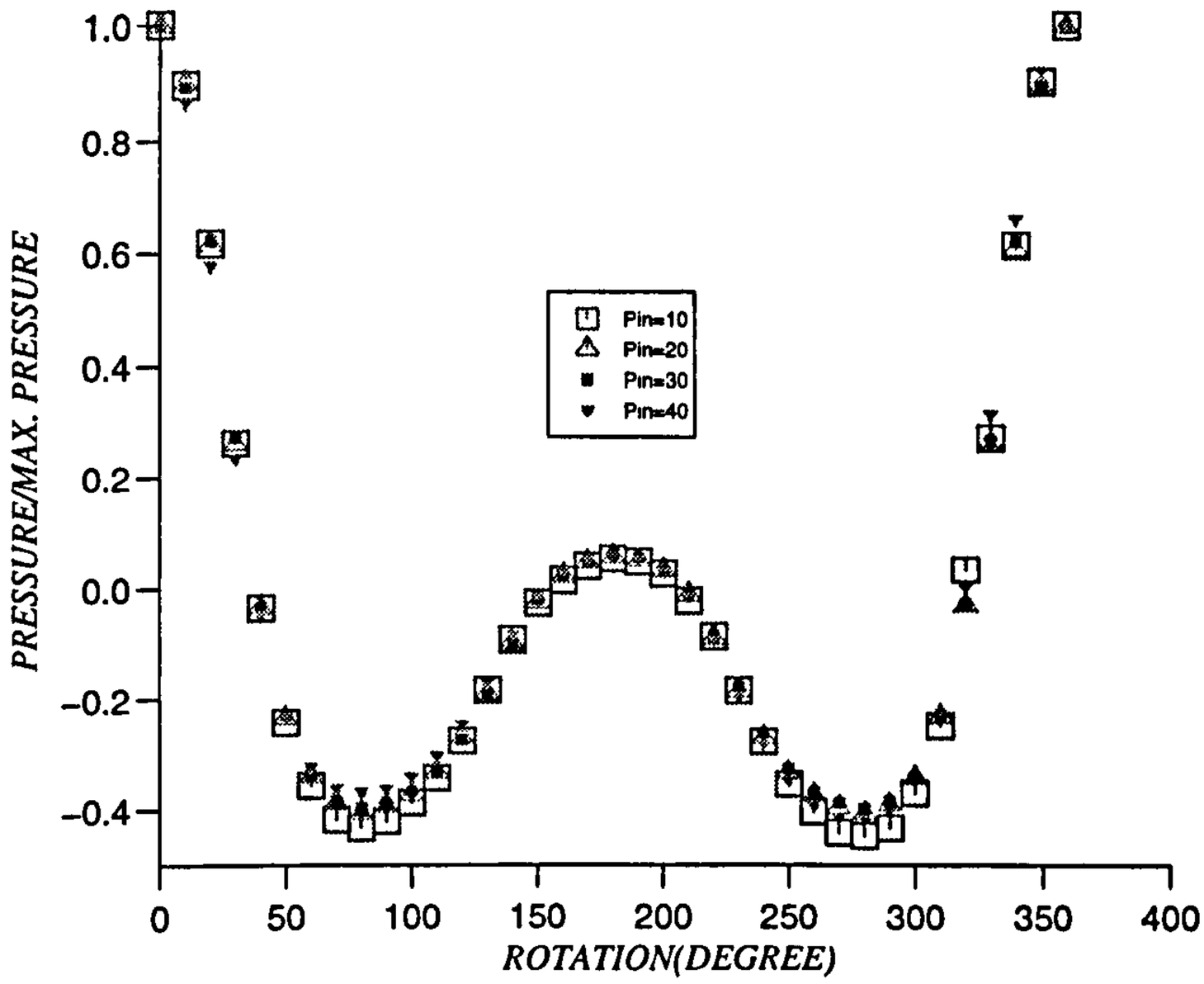

Fig.(8-8): Pressure distribution around the cylinder for different inlet pressures to the nozzle, H/D=6, e/D=0.

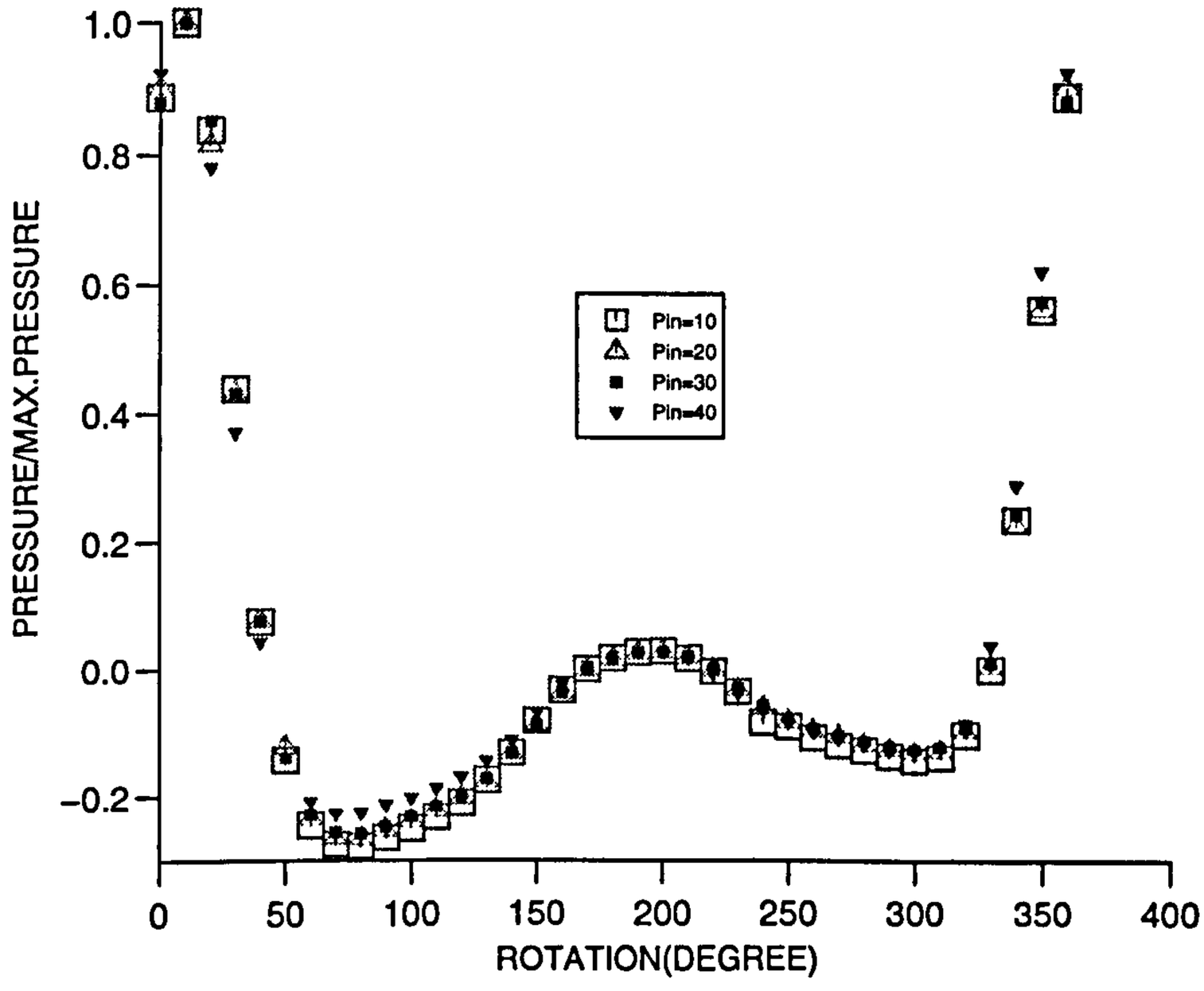

Fig.(8-9): Pressure distribution around the cylinder for different inlet pressures to the nozzle, H/D=4, e/D=0.1.

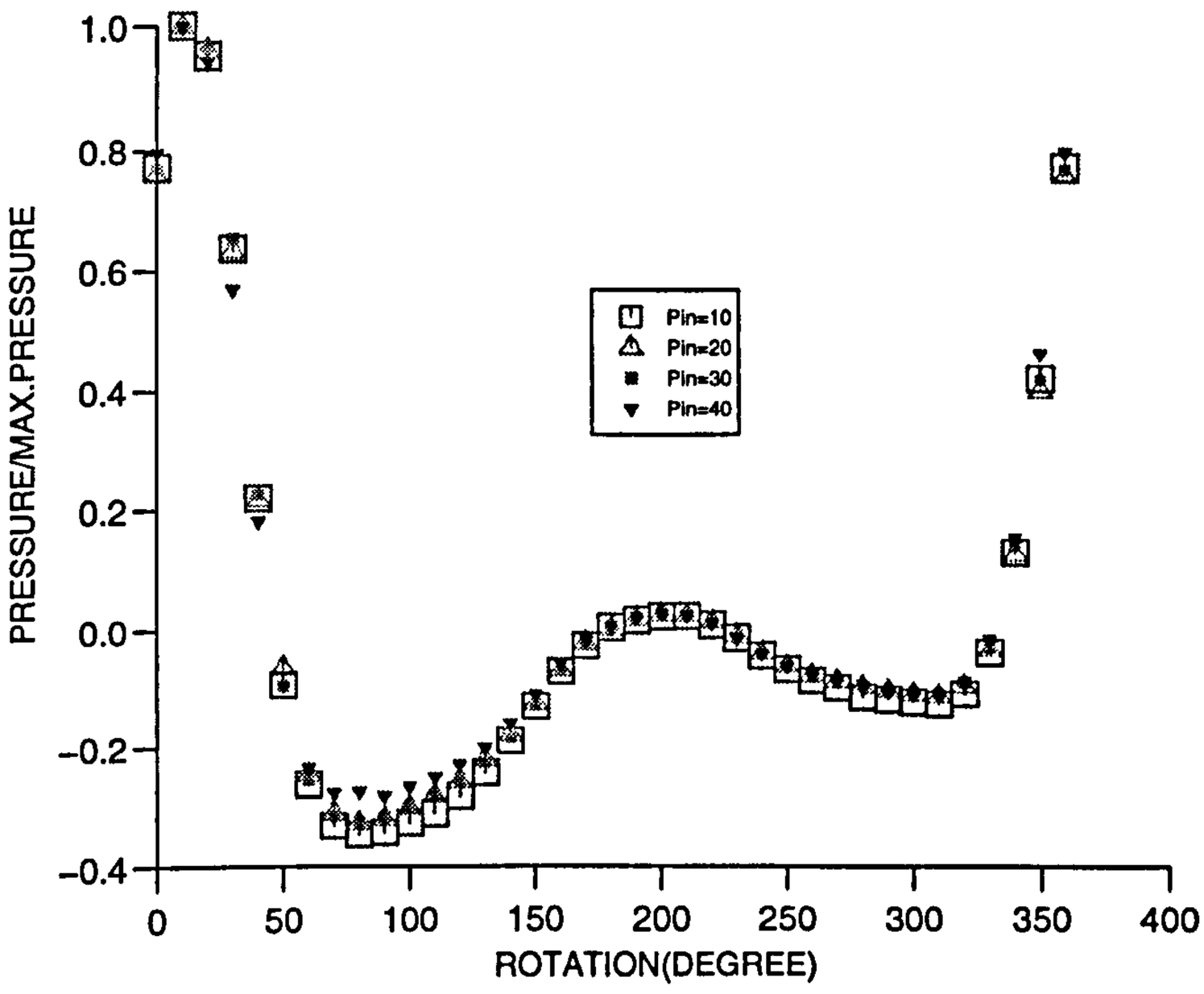

Fig.(8-10):Pressure distribution around the cylinder for different inlet pressures to the nozzle, H/D=4, e/D=0.2.

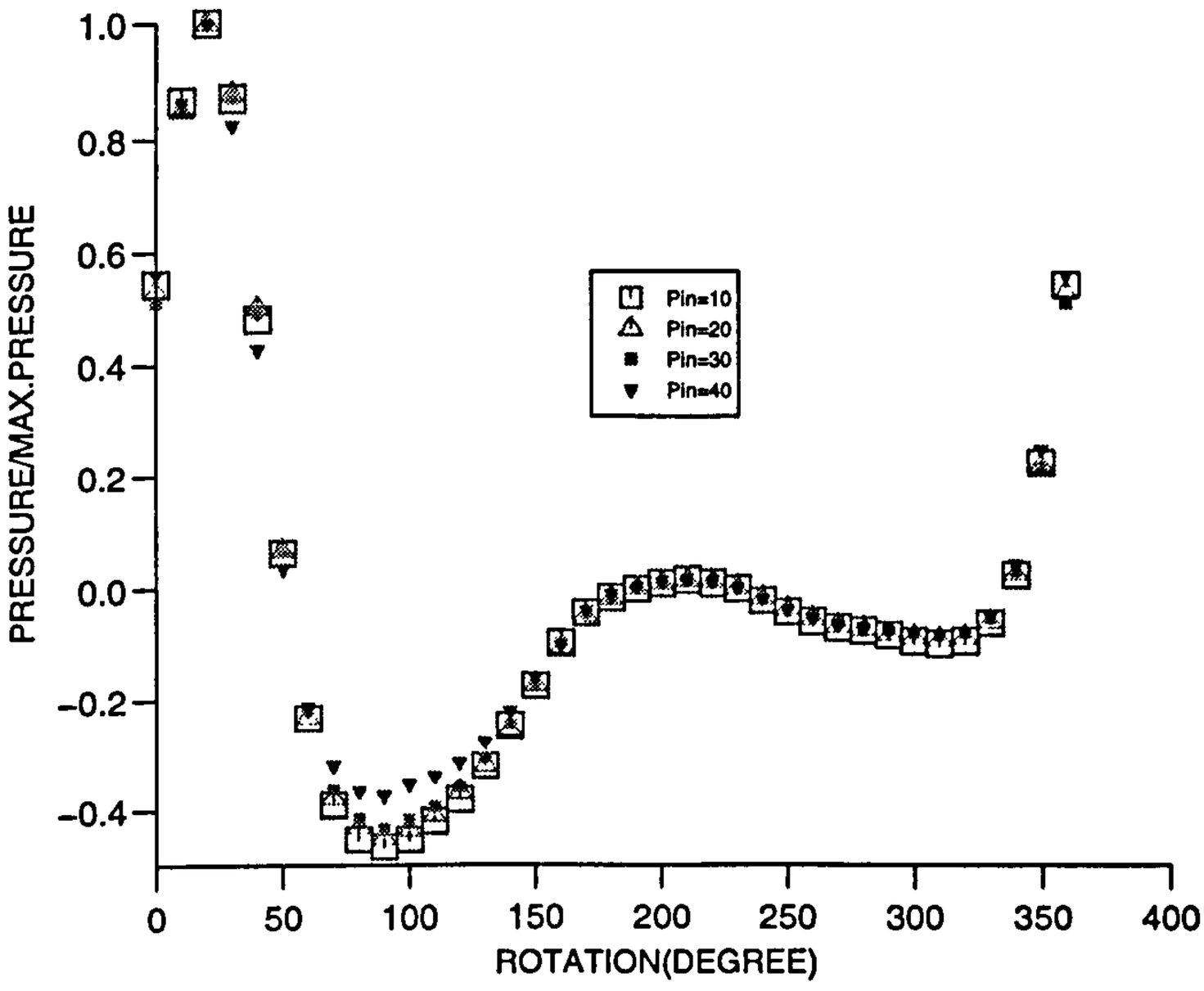

Fig.(8-11): Pressure distribution around the cylinder for different inlet pressure to the nozzle, H/D=4, e/D=0.3.

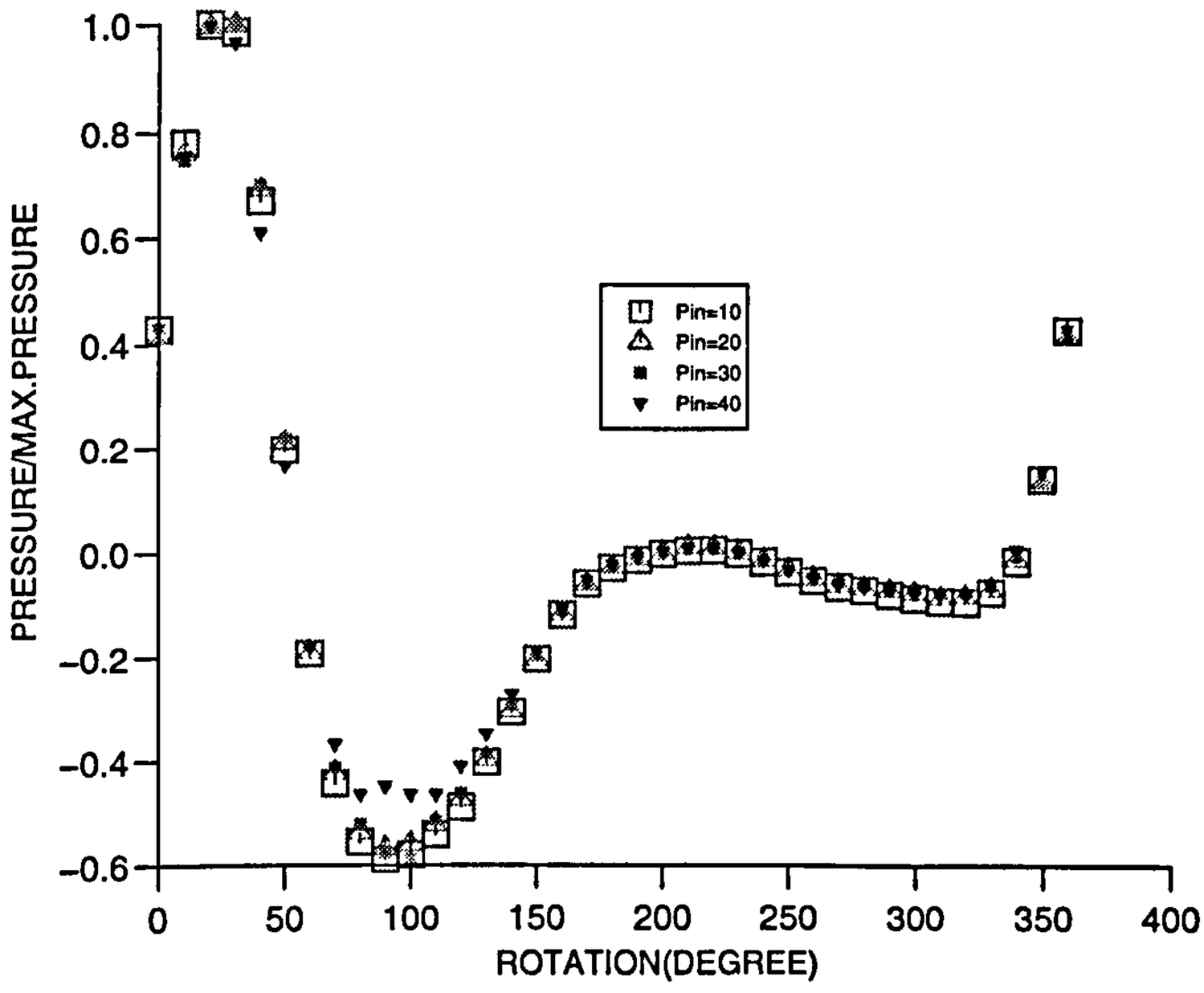

Fig.(8-12): Pressure distribution around the cylinder for different inlet pressures to the nozzle, H/D=4, e/D=0.4.

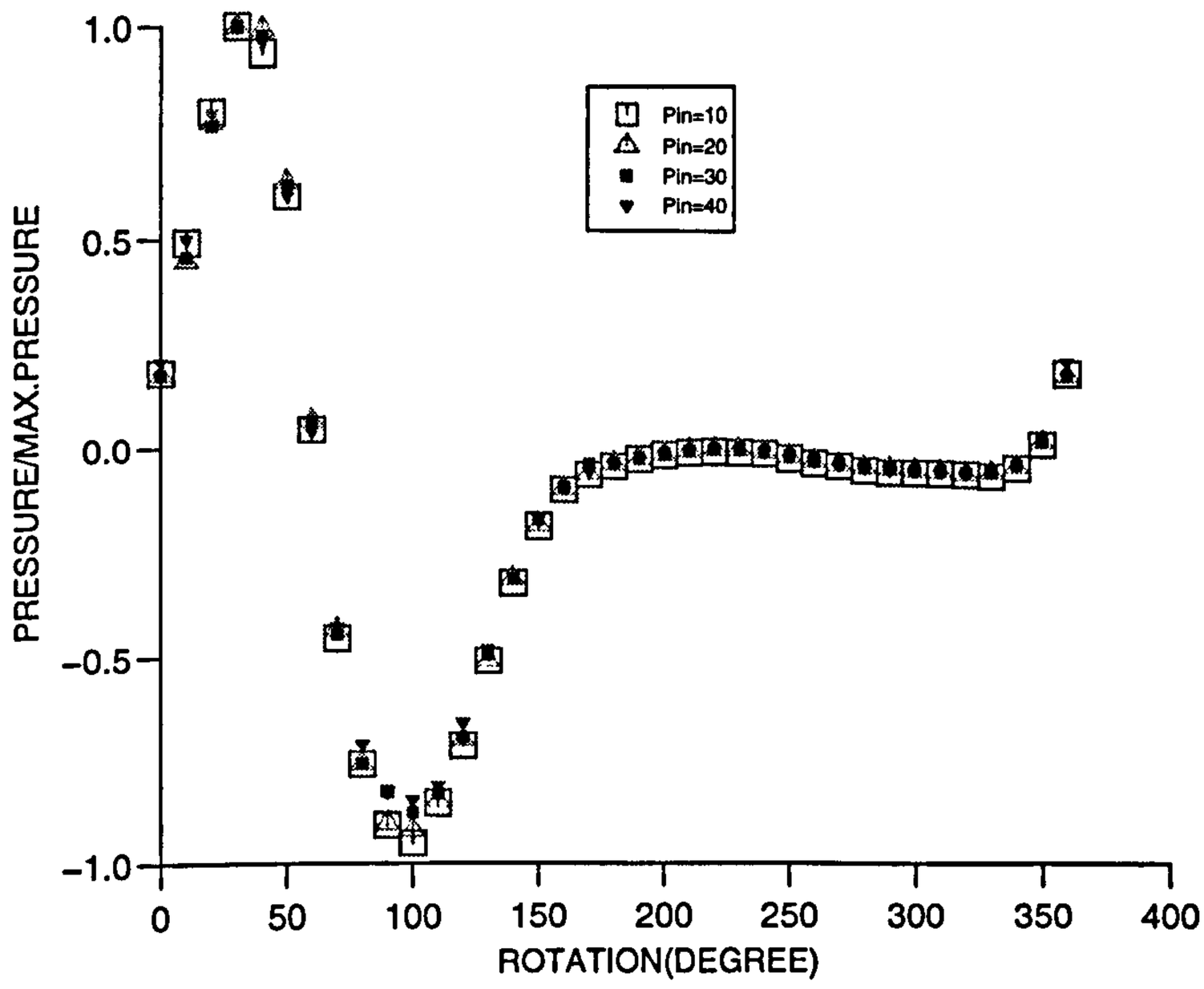

Fig.(8-13): Pressure distribution around the cylinder for different inlet pressures to the nozzle, H/D=4, e/D=0.5.

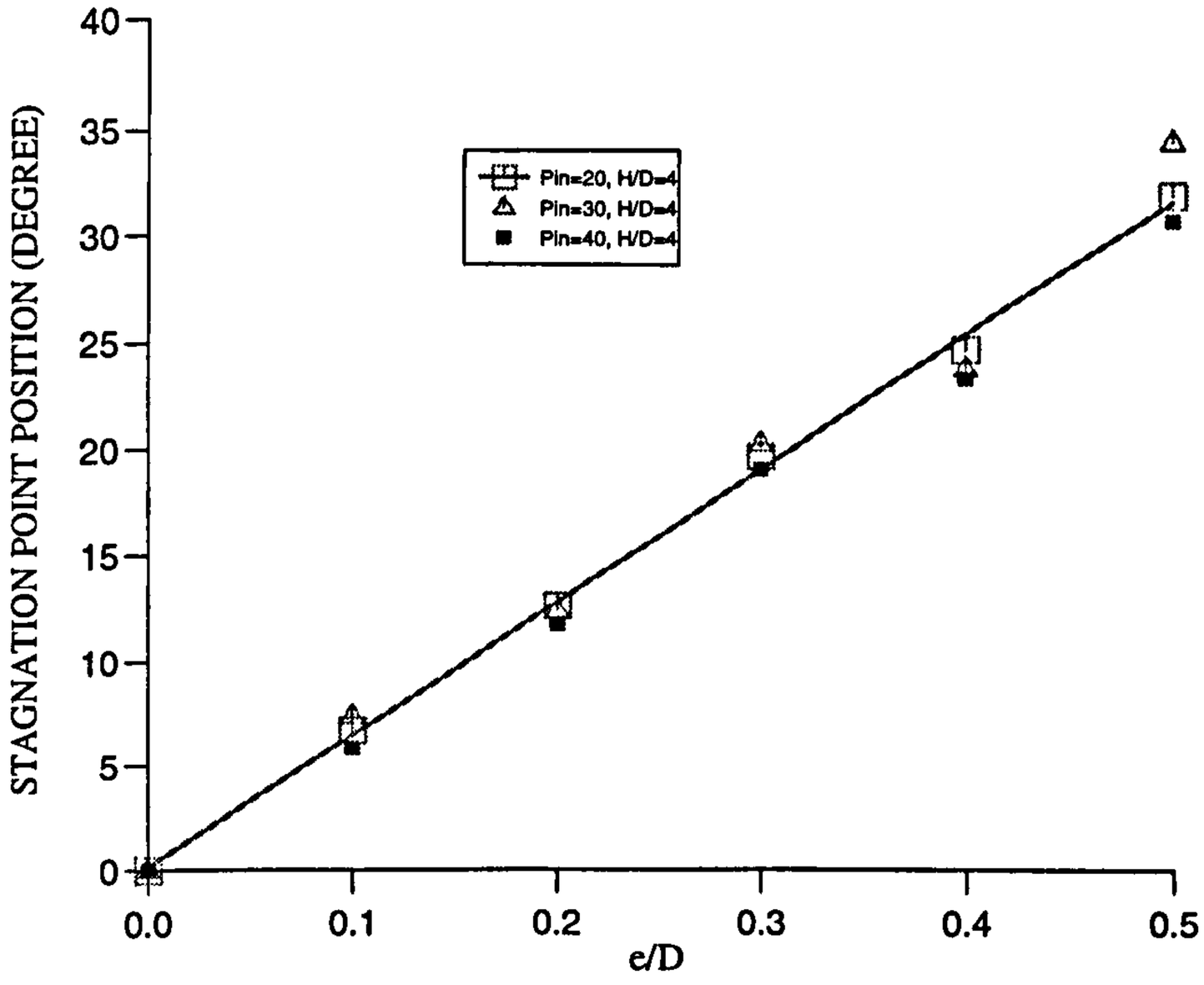

Fig.(8-14): Variation of stagnation point position angle with offset (e/D) for different values of nozzle inlet pressure and H/D=4.

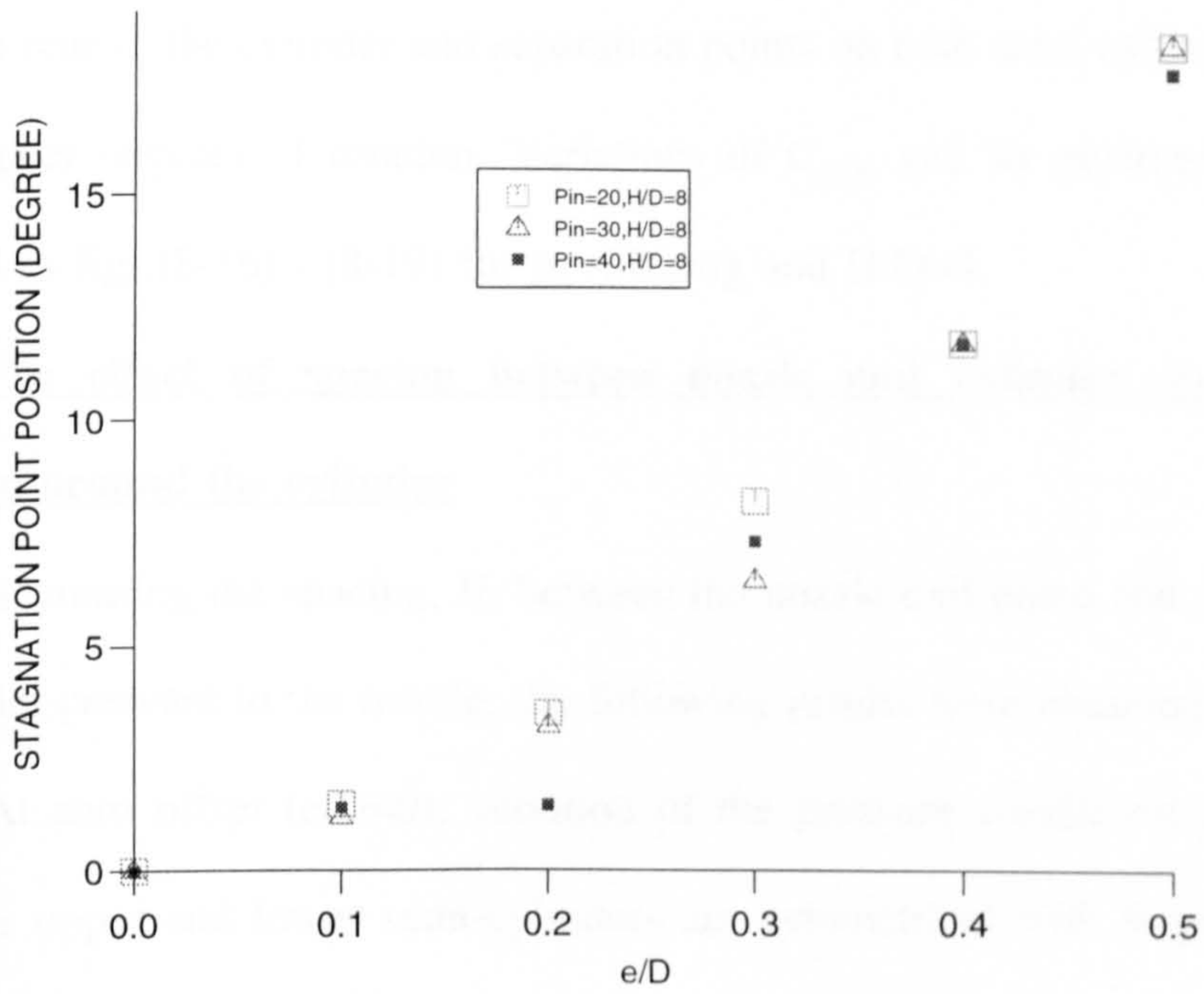

Fig.(8-15): Variation of stagnation point position angle with offset (e/D) for different values of nozzle inlet pressure and H/D=8.

b) By increasing the offset ratio e/D, the minimum pressure coefficient, C_{pmin}, on the upper semi-cylinder decreases in magnitude and its angular position moves towards higher degrees of rotation, but on the lower semi cylinder by increasing the offset ratio the minimum pressure coefficient increases in magnitude and its angular position moves towards higher degrees. By considering these variations, it is obvious that by increasing the offset ratio, the Coanda effect on the upper surface causes the jet to adhere to the cylinder surface and therefore after a rapid drop of pressure occurs from the stagnation point pressure to very low values, pressure recovery takes place at the rear of the cylinder and separation points on both semi-cylinders moves towards higher degrees of rotation. Variations of C_{pmin} and its position angle are represented in figs.(8-16) - (8-19) for p_{in}=30 psig and H/D=4.

8-3-1-3: The effect of spacing between nozzle and cylinder on pressure distribution around the cylinder

By increasing the spacing, H, between the nozzle exit plane and cylinder, at constant inlet pressure to the nozzle, the following results were obtained:

a) At zero offset (e/D=0), variation of the pressure coefficient around the cylinder for upper and lower semi-cylinders are symmetrical with larger pressure drops from stagnation point pressure to lower values at far distances. By increasing the distance, the width of separation region at the rear of the cylinder decreases and separation points on both semi-cylinders move towards the rear stagnation point. This result indicates that the well known Coanda effect is more effective at higher values of H/D, fig.(8-20).

b) In offset conditions the upper semi cylinder pressure drops from the stagnation point pressure to lower values and the jet adheres to the cylinder surface due to

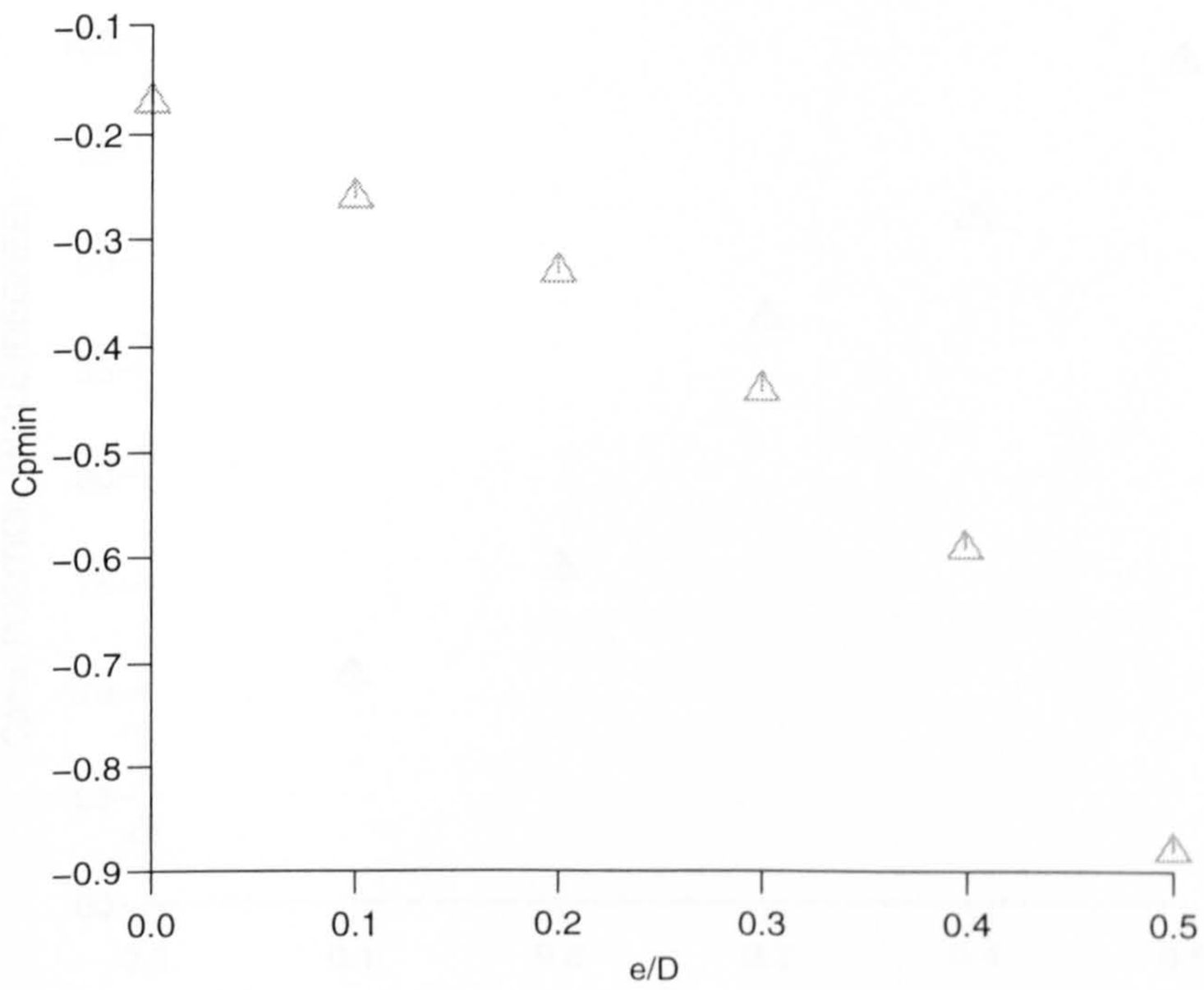

Fig.(8-16): Variation of C_{pmin} with e/D on the upper semi-cylinder for p_{in}=30 psig and H/D=4.

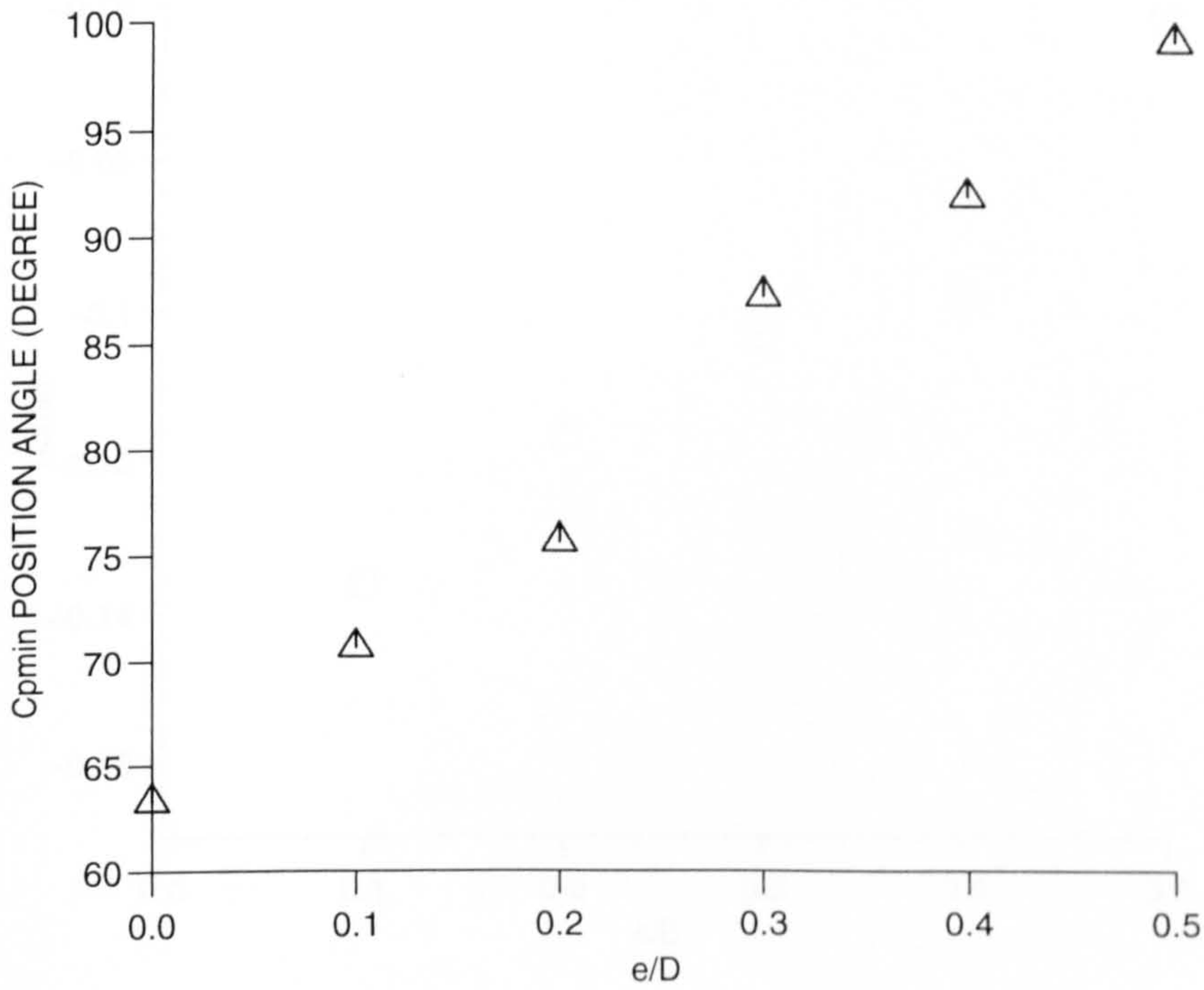

Fig.(8-17): Variation of θ_{Cpmin} with e/D on upper semi-cylinder for p_{in}=30 psig and H/D=4.

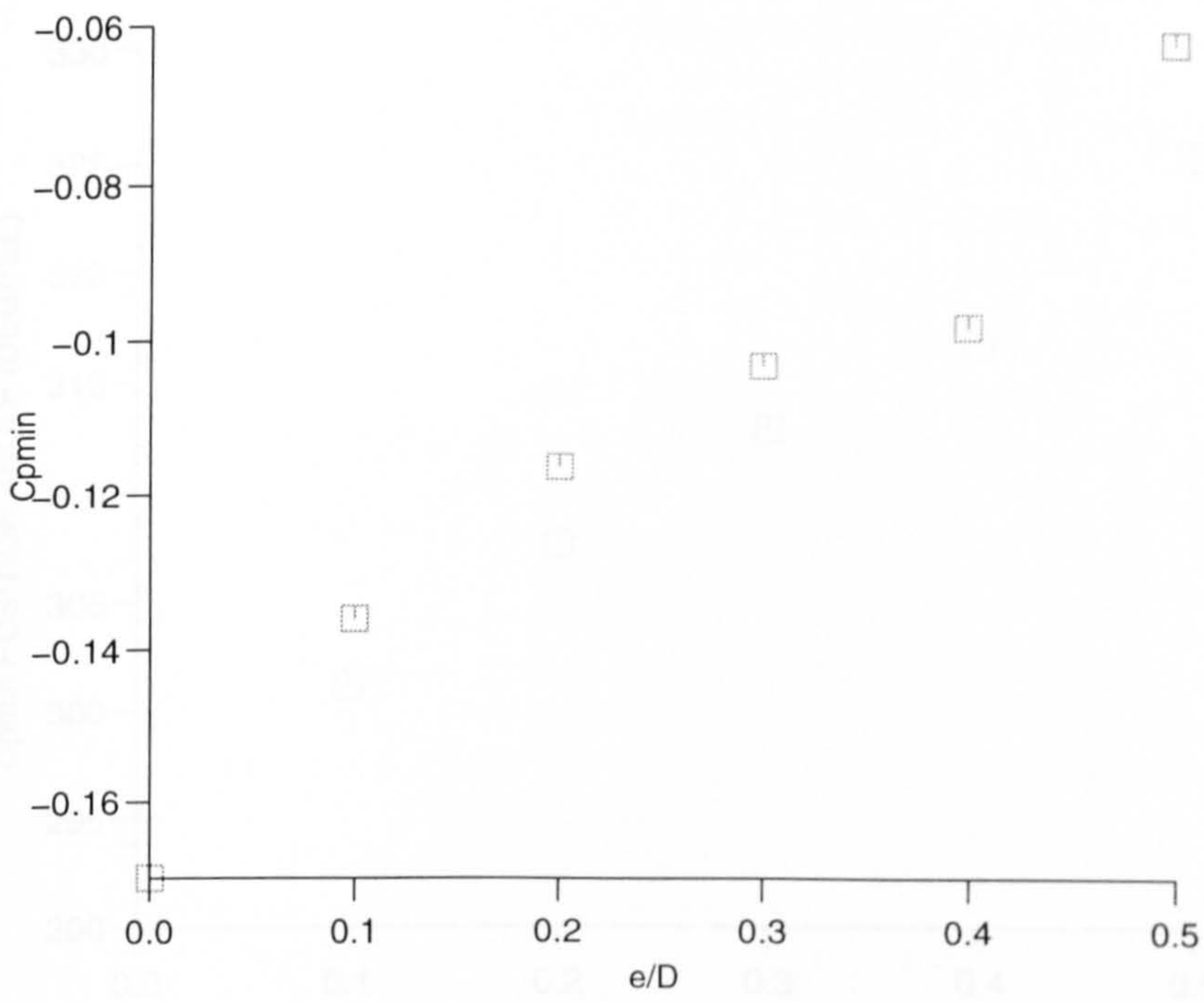

Fig.(8-18): Variation of C_{pmin} with e/D on lower semi-cylinder for p_{in}=30 psig and H/D=4.

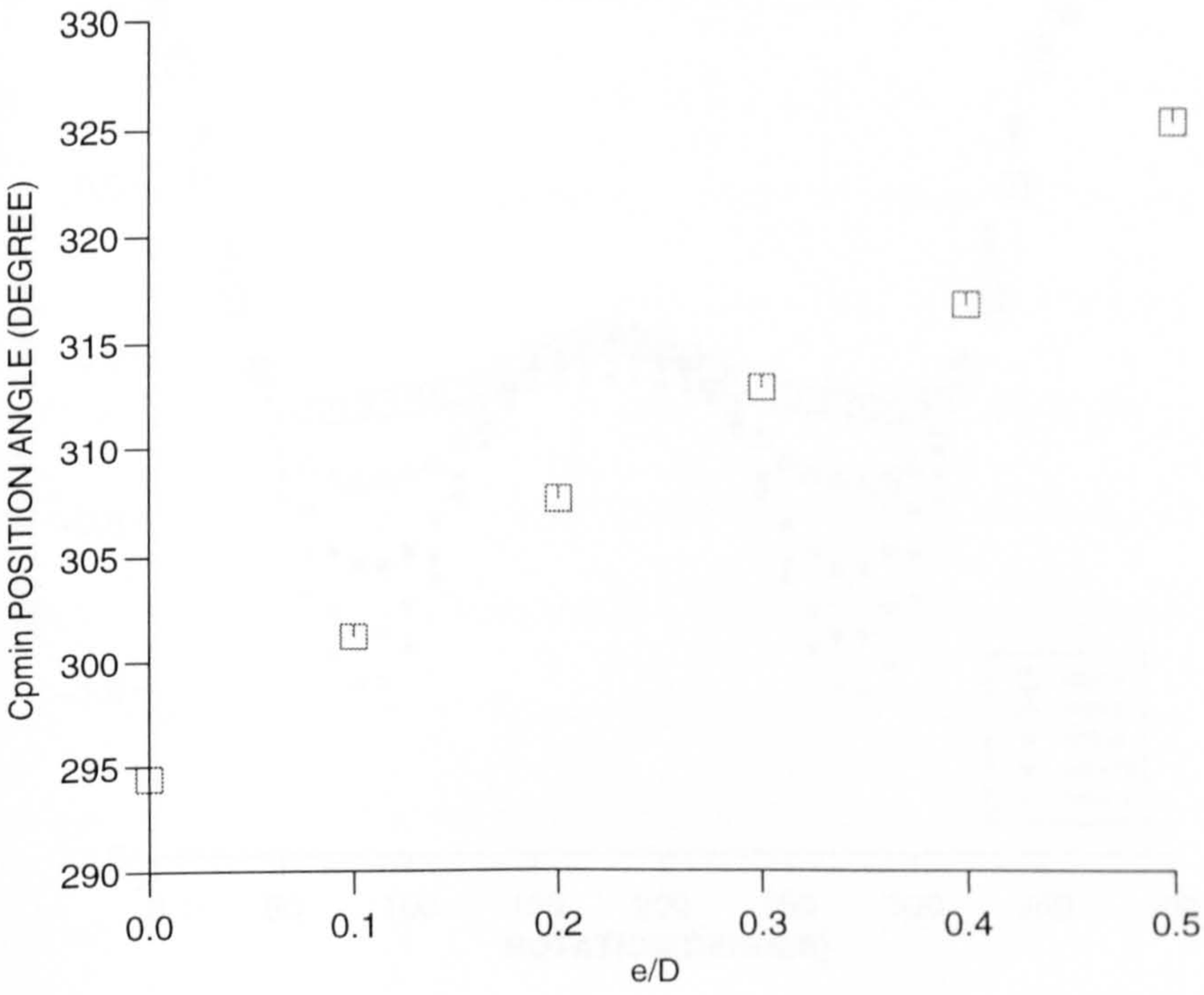

Fig.(8-19): Variation of θ_{Cpmin} with e/D on lower semi-cylinder for p_{in}=30 psig and H/D=4.

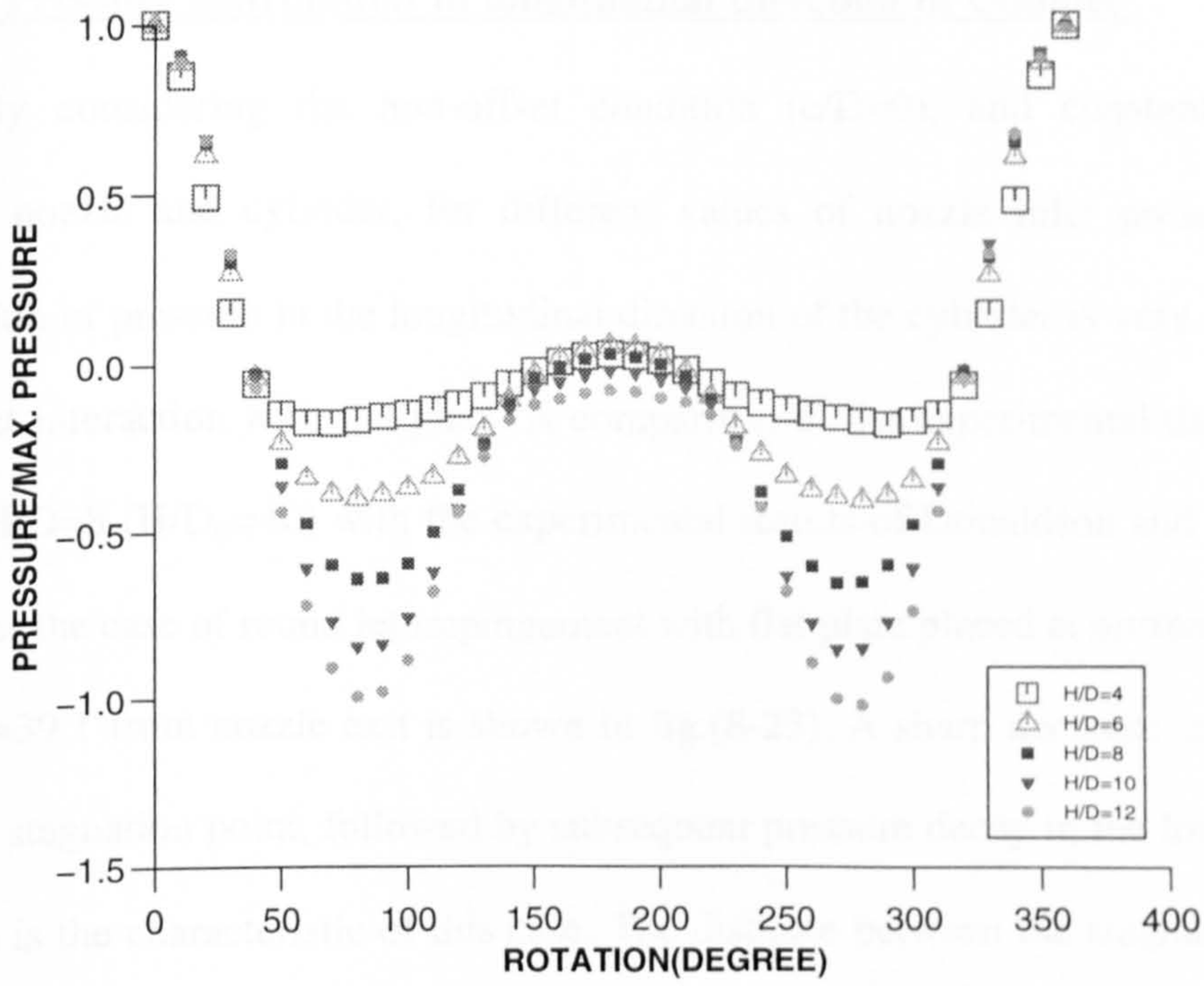

Fig.(8-20):Variation of C_p with degree of rotation for p_{in}=30 psig and e/D=0.

the Coanda effect, and pressure recovery takes place at the rear of the cylinder. For constant inlet pressure to the nozzle and constant offset, the effect of offset on pressure distribution relatively diminishes for far distances, fig.(8-21).

c) In offset conditions, for constant nozzle inlet pressure and constant offset, the position of the stagnation point is a function of H/D and by increasing the distance this point moves towards the zero degree position and therefore reduces the effect of offset on pressure distribution, figs.(8-21) - (8-22).

8-3-1-4: Pressure distribution in longitudinal direction of cylinder

By considering the non-offset condition (e/D=0), and constant spacing between nozzle and cylinder, for different values of nozzle inlet pressures, the distribution of pressure in the longitudinal direction of the cylinder is very similar to that of jet interaction with flat plate. A comparison of the experimental data for the case of H/D=8 (H/D_N=40) with the experimental results of Donaldson and Snedeker (1971) for the case of round jet impingement with flat plate placed at normal distance of H/D_N=39.1 from nozzle exit is shown in fig.(8-23). A sharp decrease in pressure from the stagnation point, followed by subsequent pressure decay in the longitudinal direction is the characteristic of this case. The distance between the stagnation point and the point where the pressure reaches ambient conditions, on the position related to θ=0 degrees of rotation, is in agreement with those obtained from surface flow visualisation by the aid of the oil-lampblack technique. By increasing the spacing between nozzle and cylinder, the pressure drop from the stagnation point pressure to lower values takes place more slowly, figs.(8-24) - (8-26).

8-3-2: Free jet and slot jet impingement onto a circular cylinder

The experimental set up consisted of a subsonic wind tunnel, two specially

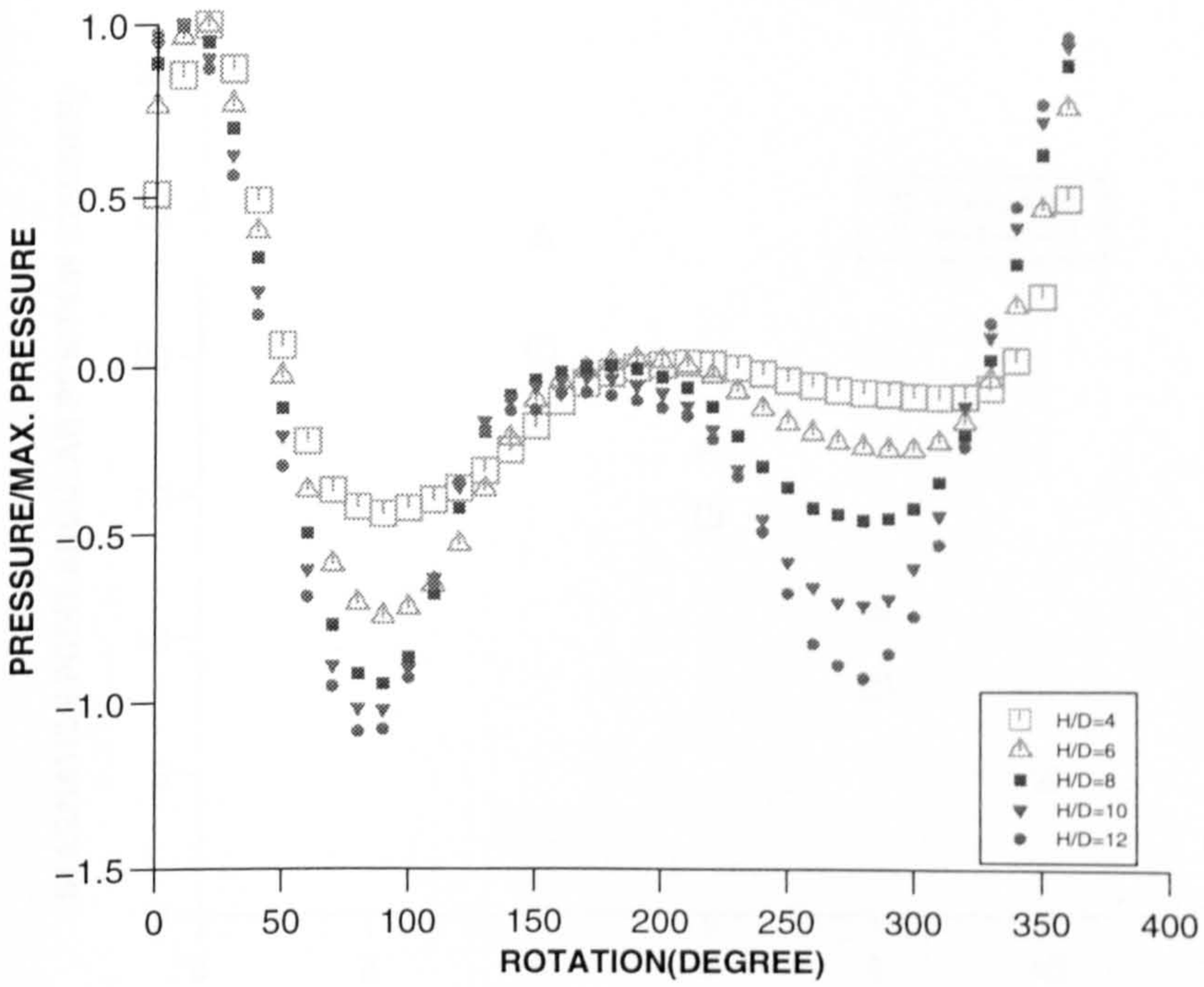

Fig.(8-21): Variation of c_p with degree of rotation for p_{in}=30 psig. and e/D=0.3.

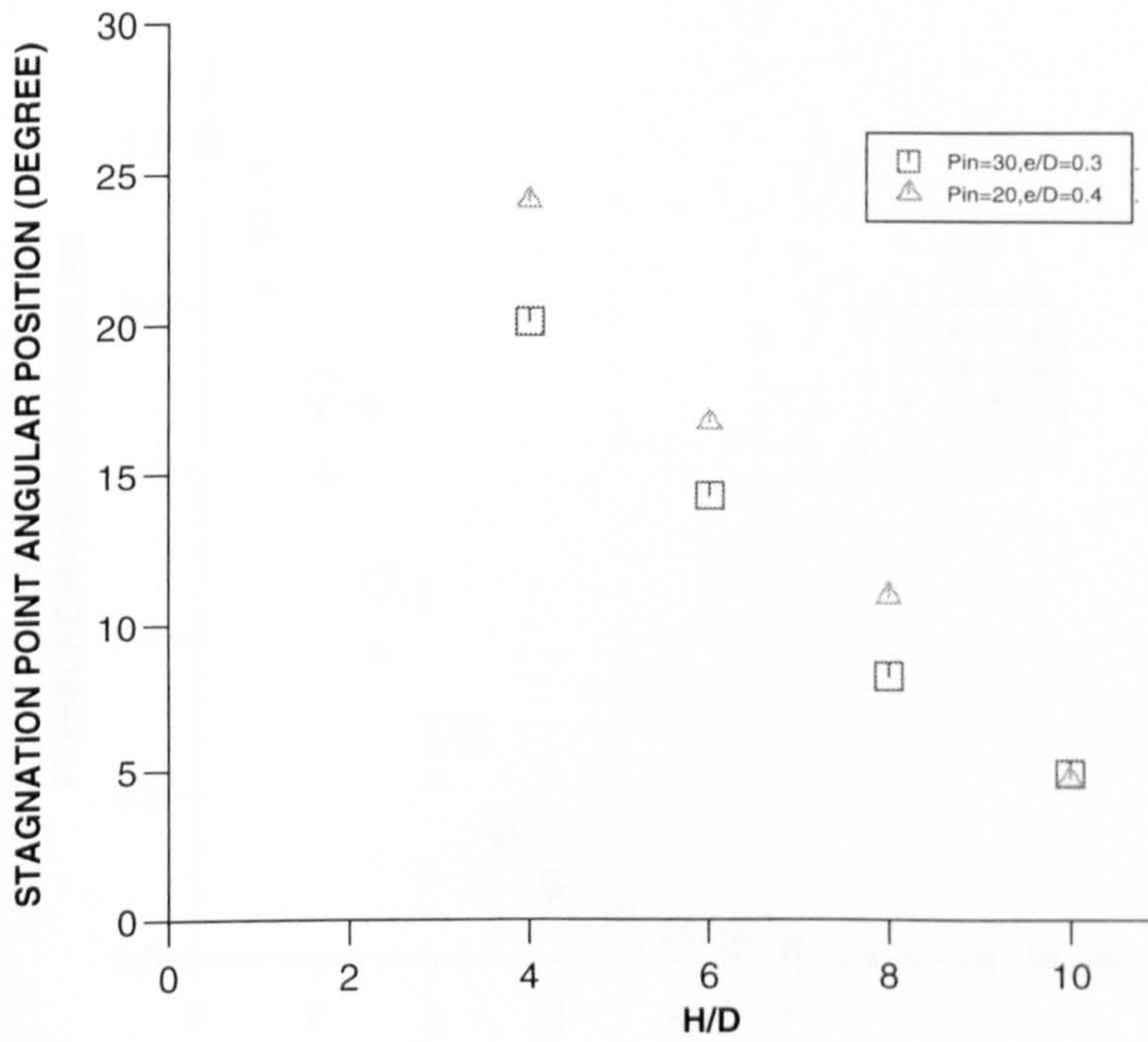

Fig.(8-22): Variation of stagnation point angular position with spacing between nozzle and cylinder.

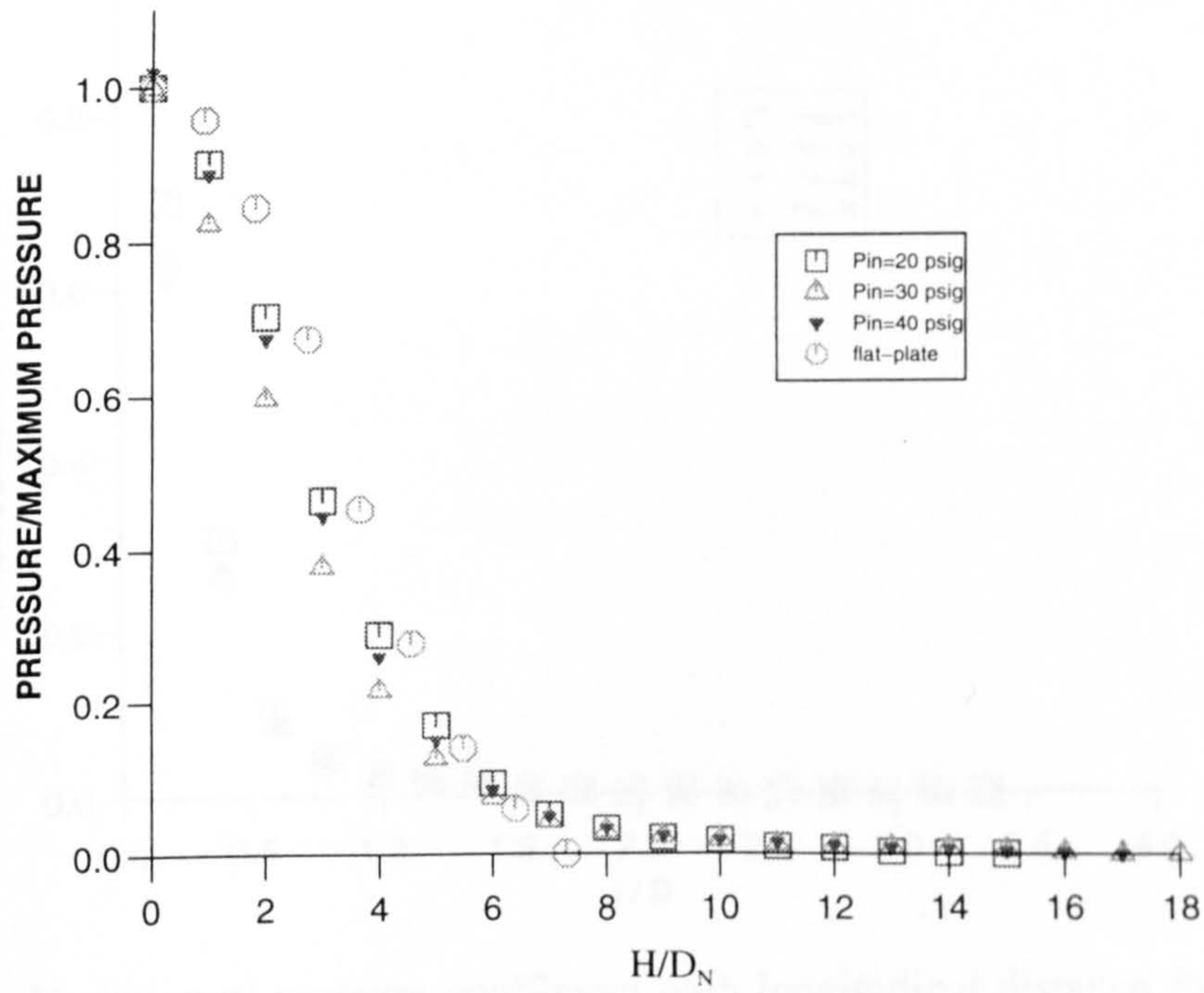

Fig.(8-23): Comparison of pressure distribution in longitudinal direction of a cylinder for H/D_N=40 with pressure distribution on flat plate for H/D_N=39.1, both due to an interaction of turbulent axisymmetric jet.

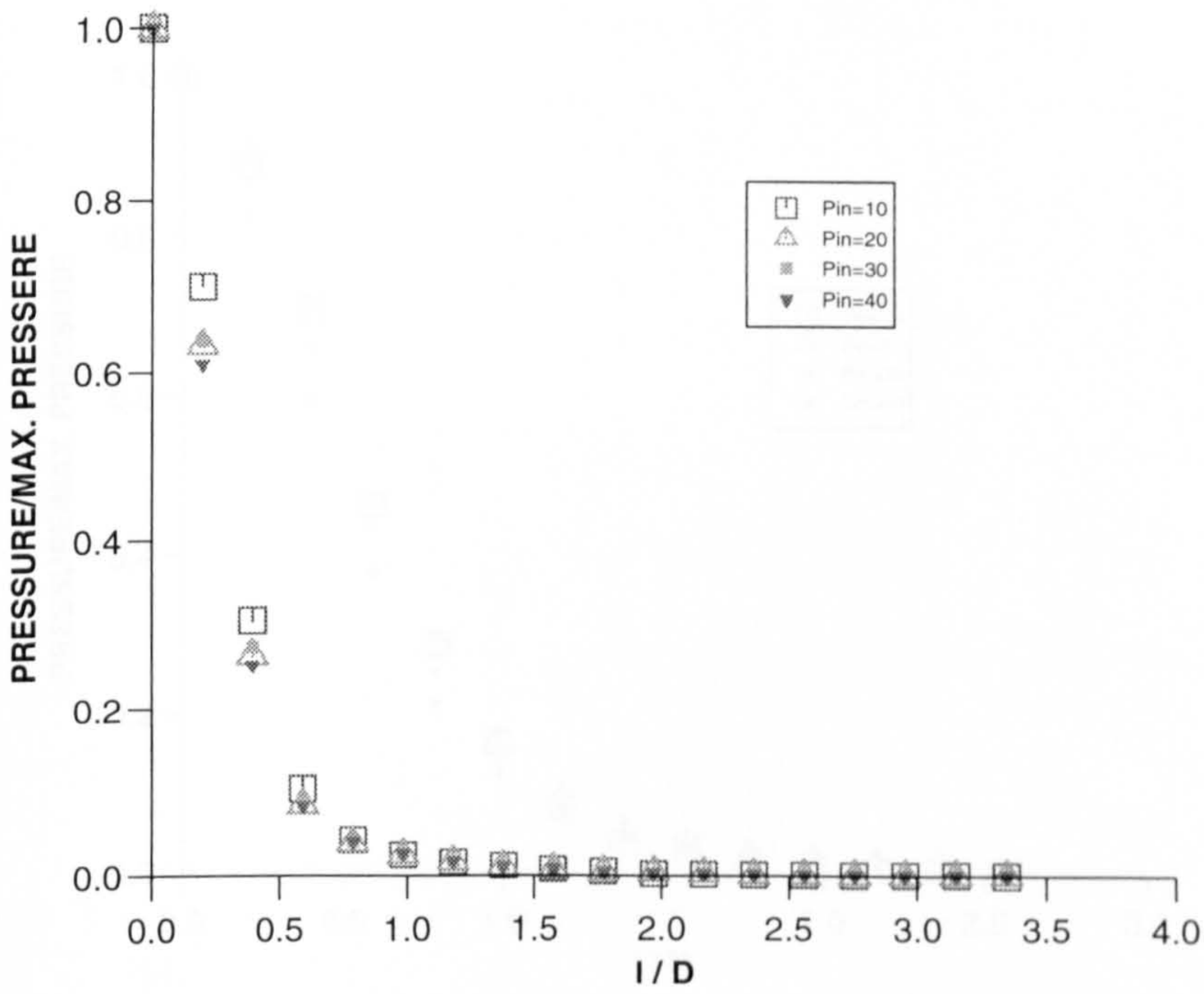

Fig.(8-24): Variation of pressure coefficient with longitudinal distance for H/D=4 and e/D=0.0.

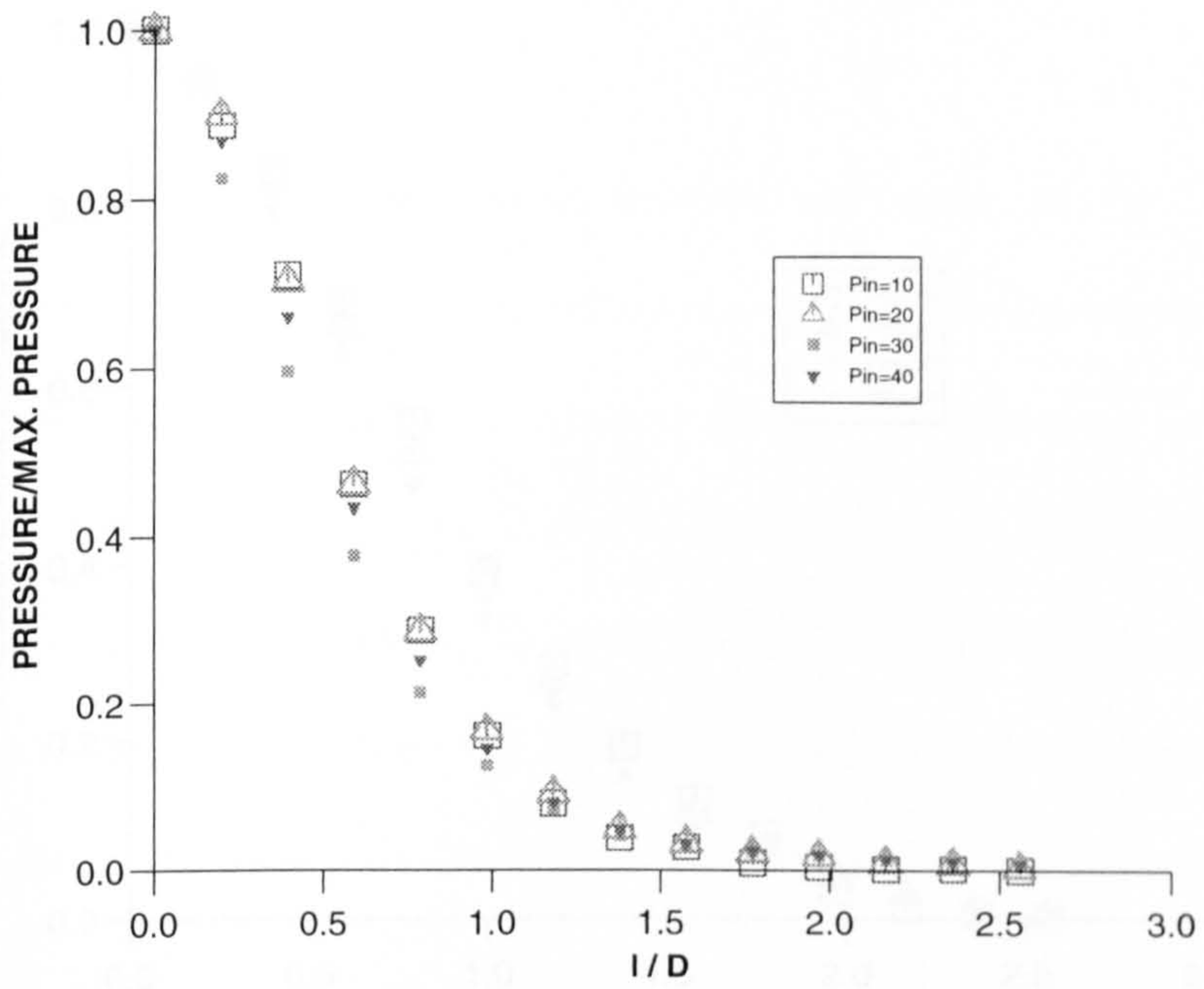

Fig.(8-25): Variation of pressure coefficient with longitudinal distance for H/D=8, e/D=0.0.

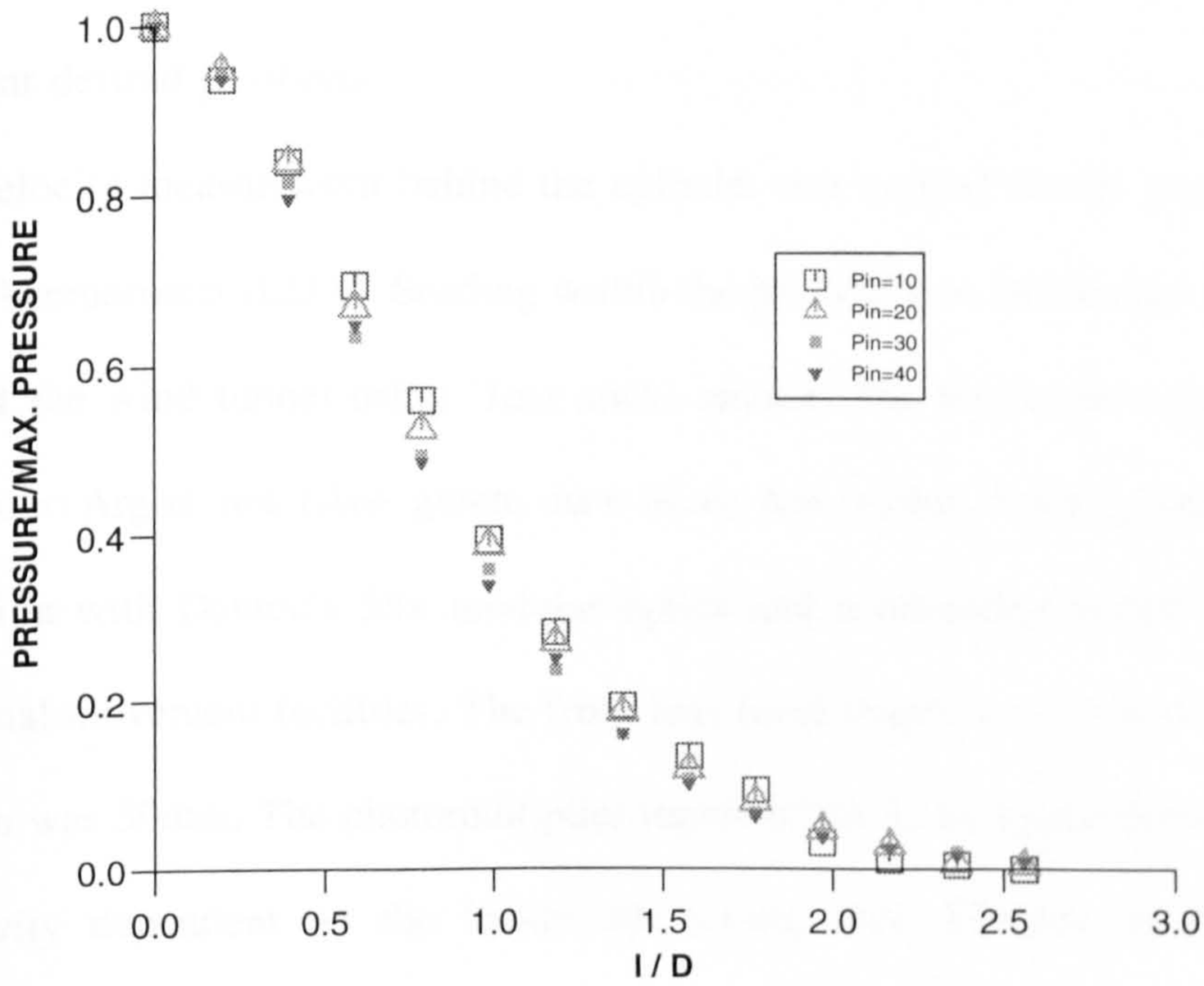

Fig.(8-26): Variation of pressure coefficient with longitudinal distance for H/D=12, e/D=0.0.

shaped wooden pieces attached to the exit end of a wind tunnel to form a slot of width 1.5" (≈38.1mm), a circular cylinder, a Laser Doppler Anemometer (LDA) and a multitube manometer. The cylinder had an outside diameter of 3" (≈76.2mm) and included pressure tappings inserted inside 36 equally spaced radially drilled holes of diameter 2mm in mid-section. These tappings were connected to a multitube manometer for measurement of the wall static pressure distribution. Two ends of the cylinder were fastened and connected to the front section of the wind tunnel by means of two variable supports at each end, in order to be able to set up the cylinder in different desired positions.

Velocity measurement behind the cylinder was carried out by using a Laser Doppler Anemometer (LDA). Seeding within the jet flow was introduced at the inlet section of the wind tunnel using 'Joss stick' smoke. The hardware consisted of a three colour Argon ion (Ar+ green, Ar+ blue, Ar+ violet) laser system used in combination with Dantec's 55x modular optics and a mounting bench with three dimensional movement facilities. The front lens focal length was 310mm and beam separation was 30mm. The photomultiplier inputs of the LDA signal processor have a sensitivity dependent on the bandwidth setting. Six different bandwidth are available and must be set to optimize the data rate and accepted percentage. It can be checked by looking at the histogram display from the data acquisition. The range of velocities encountered has to be fully contained in the histogram. However to reduce the noise, the bandwidth should be set to minimum value where this is attained. The processor is used with a Bragg cell that produces an optical frequency shift of 40MHZ.

The data acquisition provides on-line histograms of the velocity which builds

up as the data arrives. When starting the data acquisition a Direct Memory Access (DMA) transfer of data from the processor is enabled and the data is directly transferred to computer RAM memory. Under program control the RAM data in memory is validated, saved on disc and added to the on-line histogram. However, it should be noted that for velocity measurement across the jet flow and especially behind the cylinder, where the flow was observed by using a laser sheet, the flow was highly unsteady. The sampling rate of the LDA system is not fixed, but fluctuates in time and is strongly correlated with the local flow field and particle arrival statistics from the flow which transport them. Random errors present in the measurements may simply be due to the difficulty in maintaining a stable flow for the long periods of time required for the LDA measurements. Also by considering automatic movement for the mounting bench in the vertical direction, specifying a suitable bandwidth for each measurement of velocities which have high variations in that direction, is nearly impossible. The range of bandwidths were selected to cover the maximum possible range of velocities.

A theoretical base of the velocity measurements by using the LDA system will be reviewed in an appendix. The schematic representation of the slot and cylinder arrangements as well as experimental set up are represented in figs.(8-27) - (8-28).

8-3-2-1: Free jet velocity distribution

After setting up the experimental apparatus, the first set of experiments measured the velocity in a free slot jet issued from a slot of width 1.5" (≈38.1mm). Due to large differences between the axial velocity, u and the velocity in a perpendicular direction to the jet symmetrical axis, v, measurement of u and v have

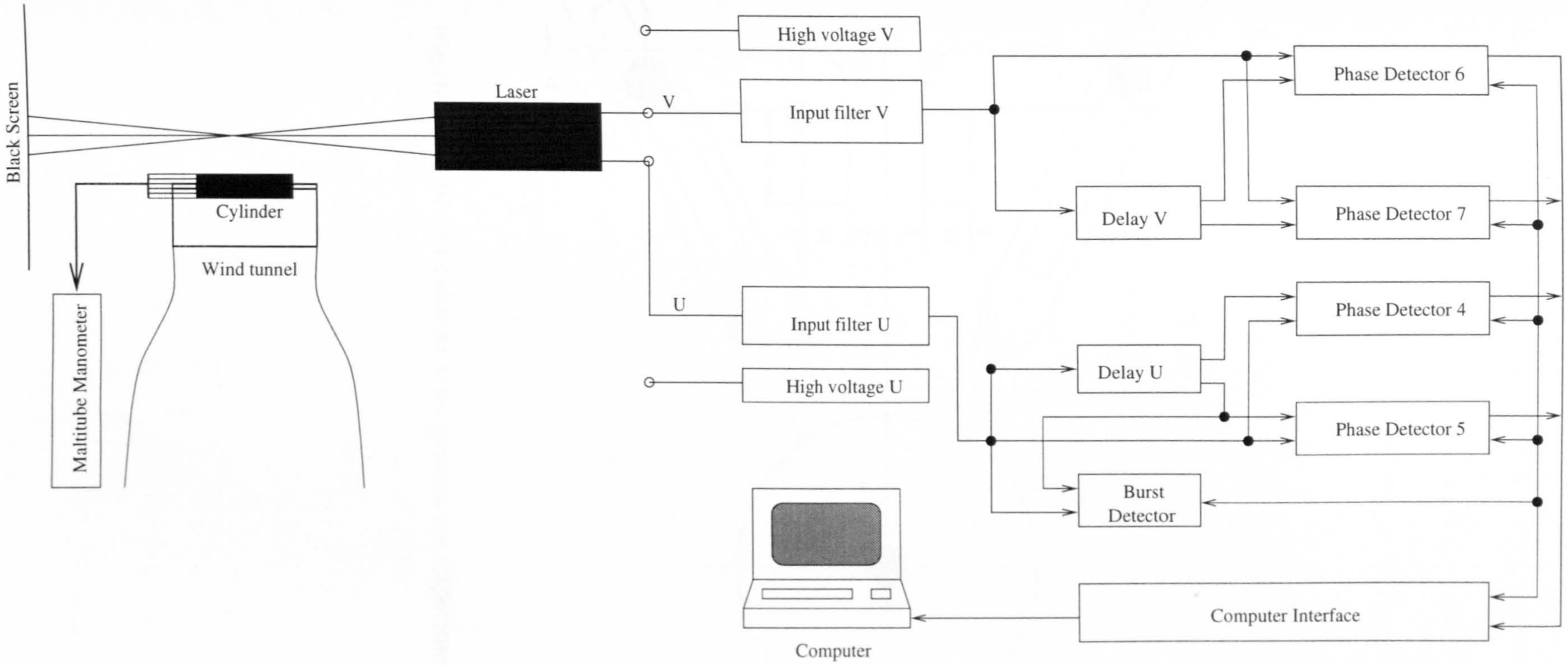

Fig(8-27): Schematic diagram of experimental set up

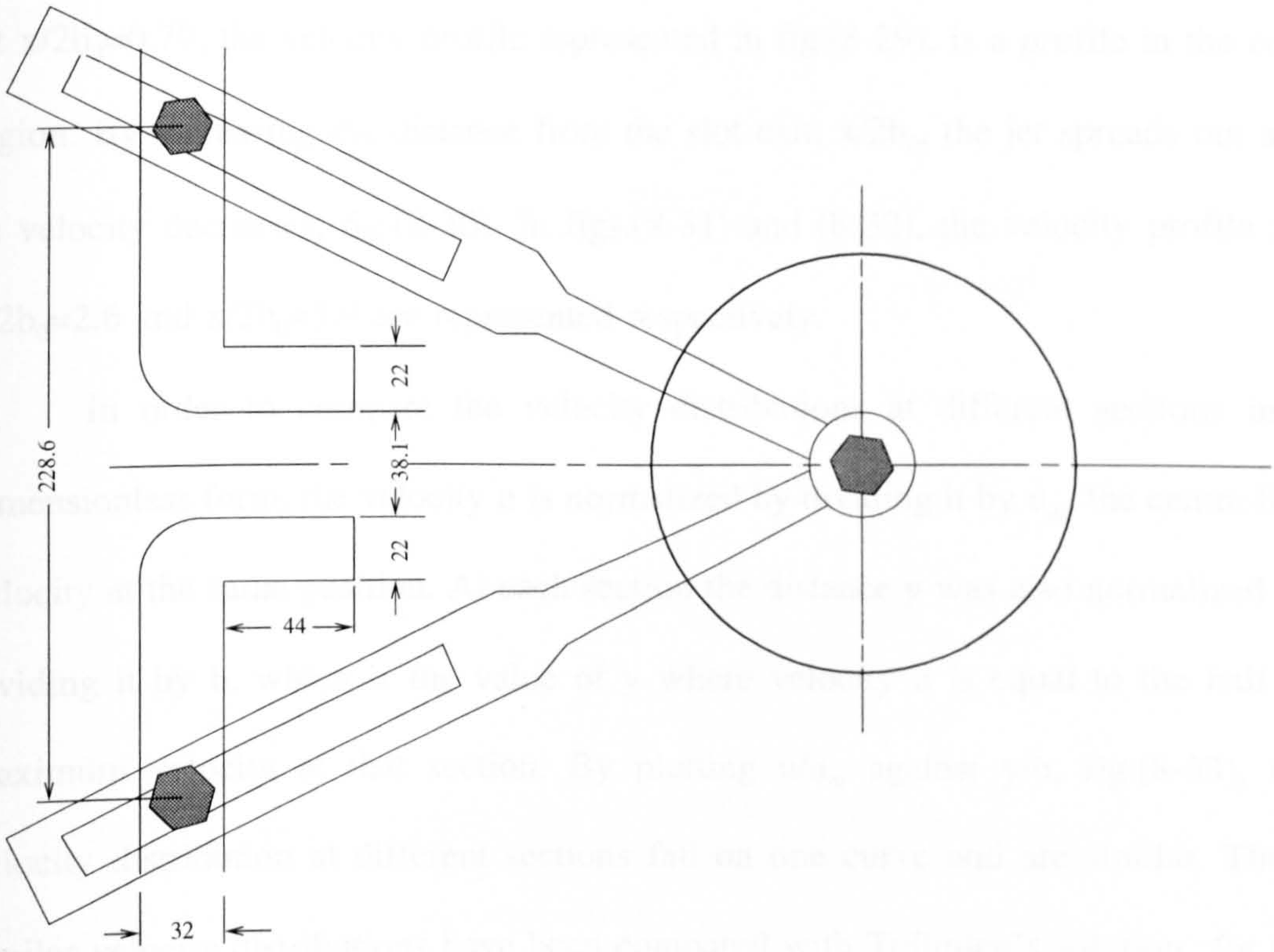

Fig.(8-28): Slot and cylinder arrangement for experimental set up.

of the optional assembly about its centre line for v measurements. Velocity measurements for each case have been carried out in the vertical plane passing through the mid position of the slot, at different axial distances from slot exit, at different vertical positions with a step of 5mm and by taking 1000 samples at a time limit of 5 minutes for each measurement.

The mean velocity at the exit from the slot in its mid position was 38 m/sec. At $x/2b_0$=0.79, the velocity profile represented in fig.(8-29), is a profile in the core region. By increasing the distance from the slot exit, $x/2b_0$, the jet spreads out and its velocity decreases, fig.(8-30). In figs.(8-31) and (8-32), the velocity profile for $x/2b_0$=2.6 and $x/2b_0$=3.9 are represented respectively.

In order to compare the velocity distributions at different sections in a dimensionless form, the velocity u is normalized by dividing it by u_m, the centre line velocity at the same position. At each section the distance y was also normalized by dividing it by b, which is the value of y where velocity u is equal to the half of maximum velocity at that section. By plotting u/u_m against y/b, fig.(8-33), the velocity distribution at different sections fall on one curve and are similar. These similar velocity distributions have been compared with Tollmien's solution for the velocity distribution in the plane turbulent free jet adopted from Abramovich (1963).

8-3-2-2: Slot jet impingement onto a circular cylinder

A cylinder of diameter 3" (≈76.2 mm) was placed in front of the slot by its adjustable supports. The ratio of slot width to the cylinder diameter was $2b_0/D$=0.5, the normalized distance between cylinder and slot was H/D=1.31. By adjusting the supports it was possible to position the cylinder in different offsets with respect to the horizontal plane passing through the slot centre. The alignment of the cylinder

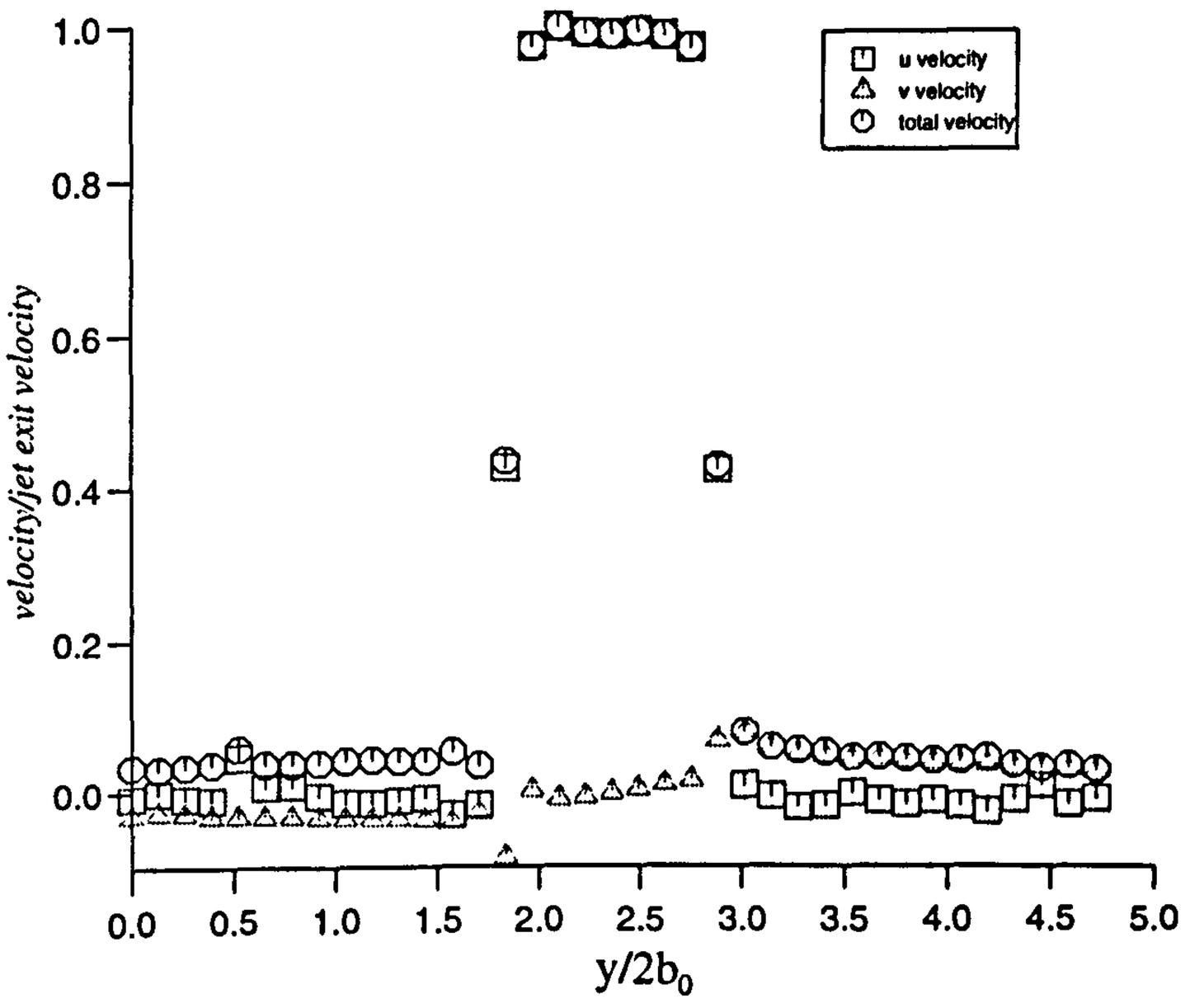

Fig.(8-29): Free jet velocity profile for axial distance of $x/2b_0$=0.79.

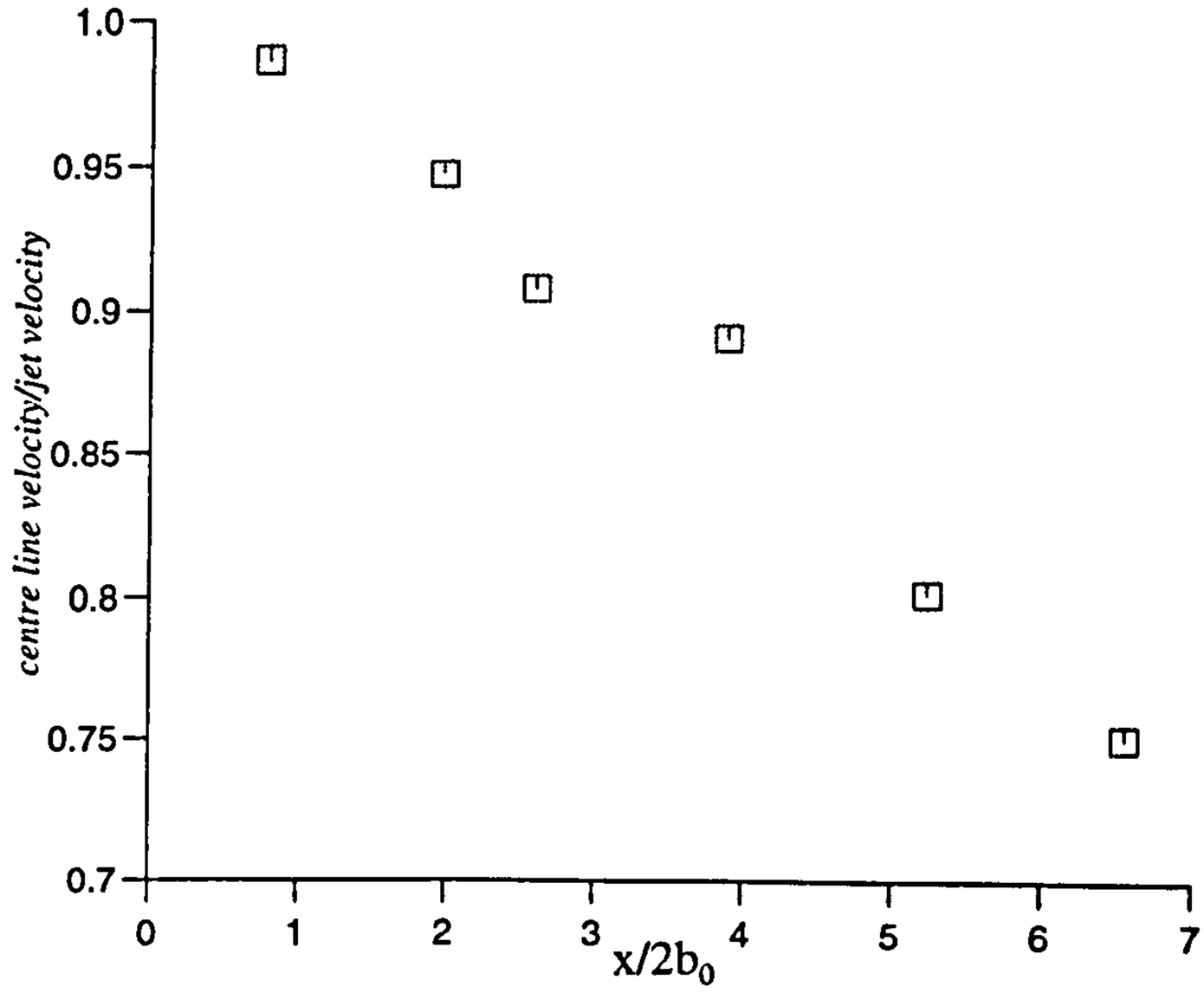

Fig.(8-30): Centre line velocity decay for free jet.

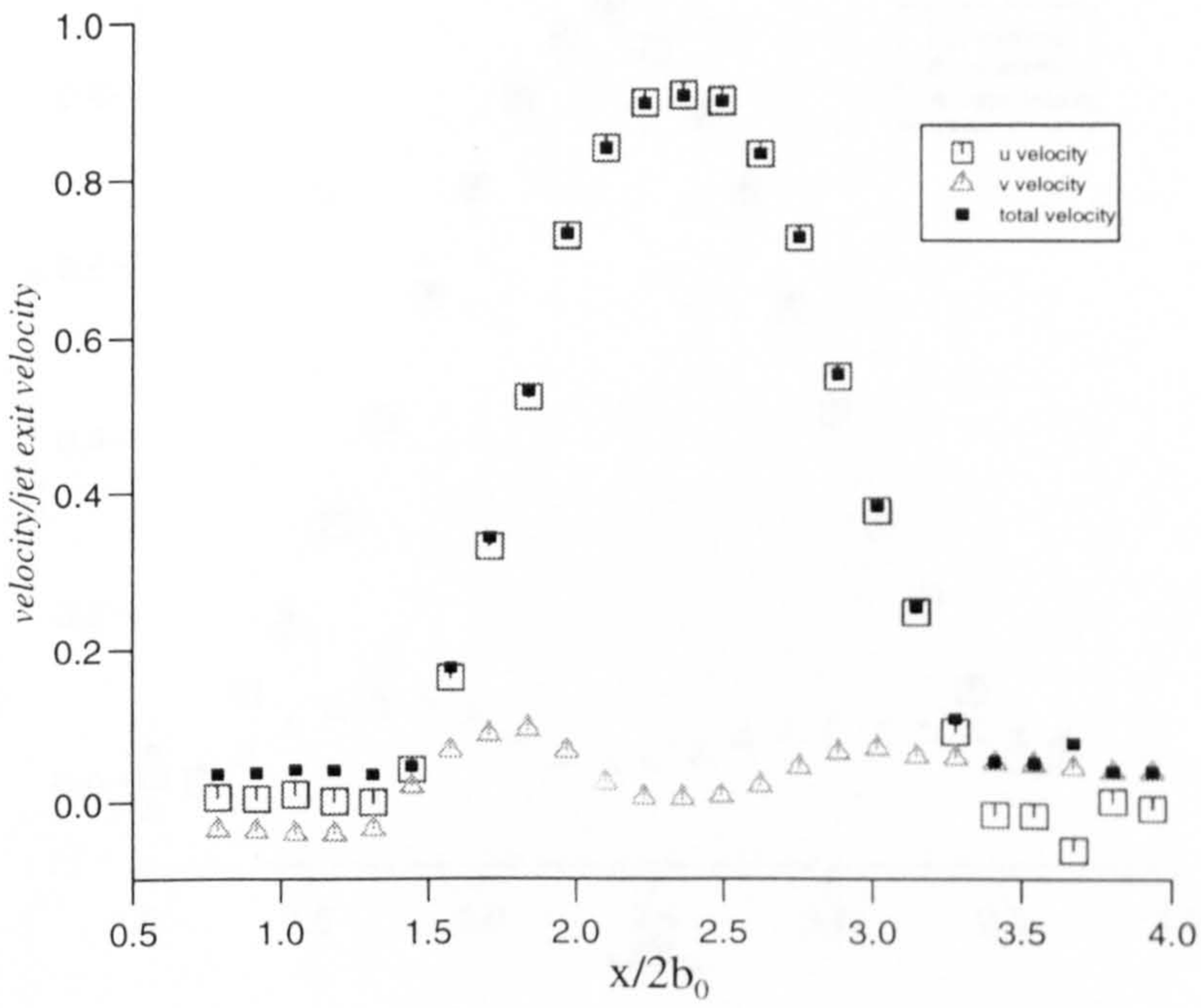

Fig.(8-31): Free jet velocity profile for axial distance $x/2b_0$=2.6.

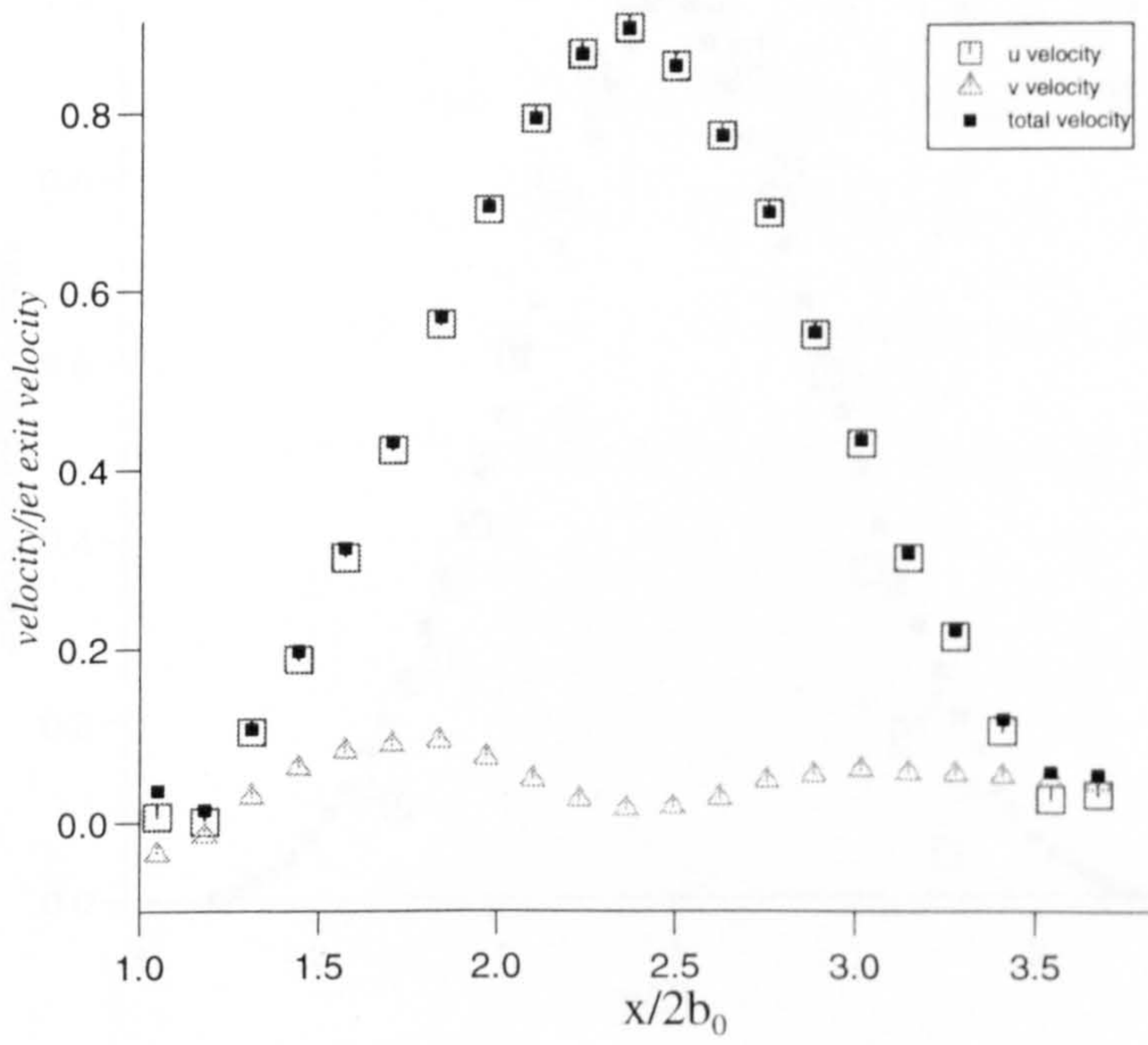

Fig.(8-32): Free jet velocity profile for axial distance $x/2b_0$=3.9.

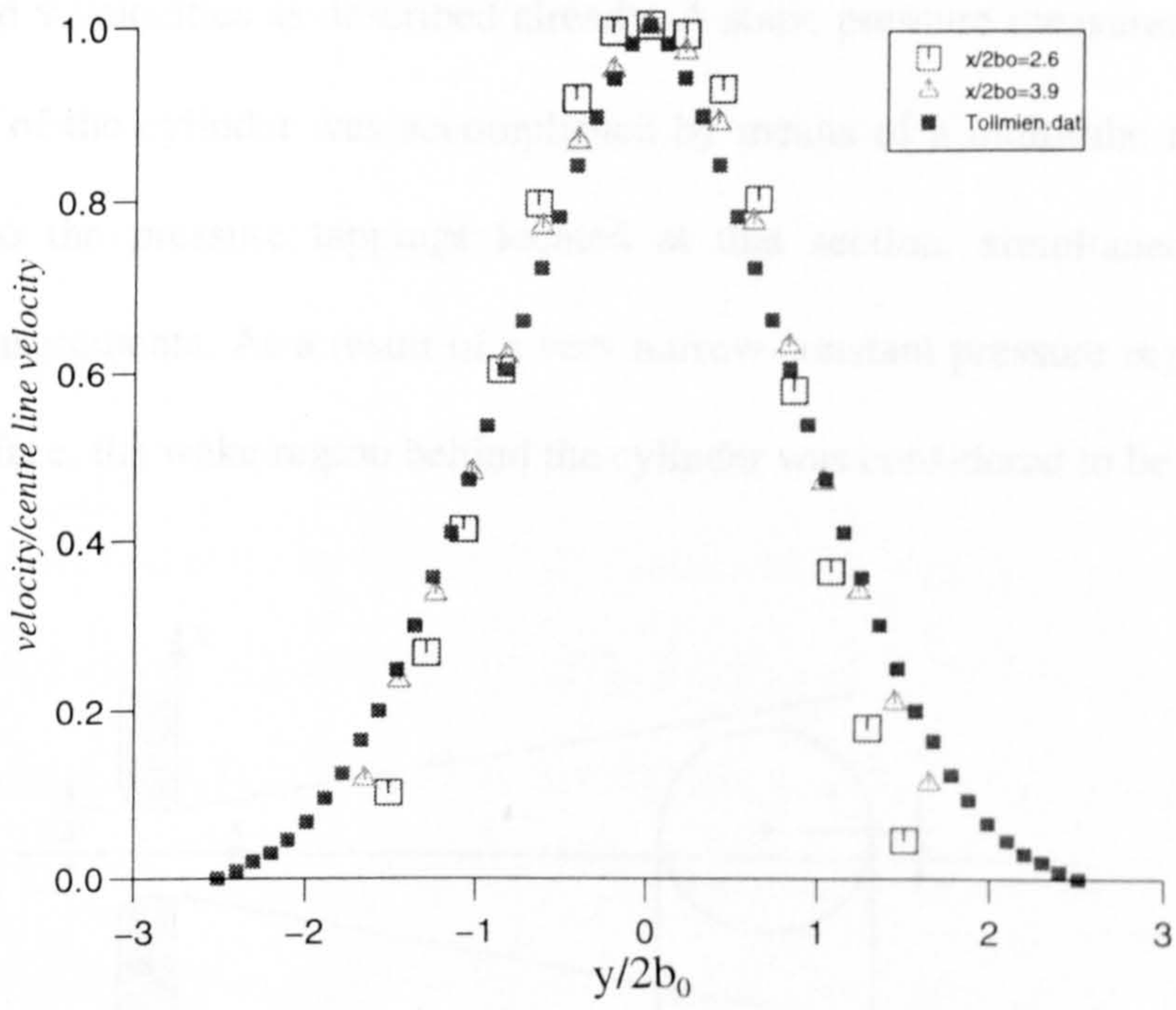

Fig.(8-33): Similar velocity profiles for free jet.

been taken separately by the same channel and by applying a 90 degrees of rotation was checked with the help of a spirit level. This arrangement is shown in fig.(8-34). It should be noted that two confining plates A and B, which define the shape of the slot, give rise to entrainment inwards to the jet surface, which will subsequently affect the jet development.

The Reynolds number of the jet flow with respect to the slot width was 99439, so that the jet flow was turbulent. The velocity measurements were carried out for u and v velocities as described already. A static pressure measurement at the mid-section of the cylinder was accomplished by means of a multitube manometer connected to the pressure tappings located at that section, simultaneously with velocity measurements. As a result of a very narrow constant pressure region on the cylinder surface, the wake region behind the cylinder was considered to be small and

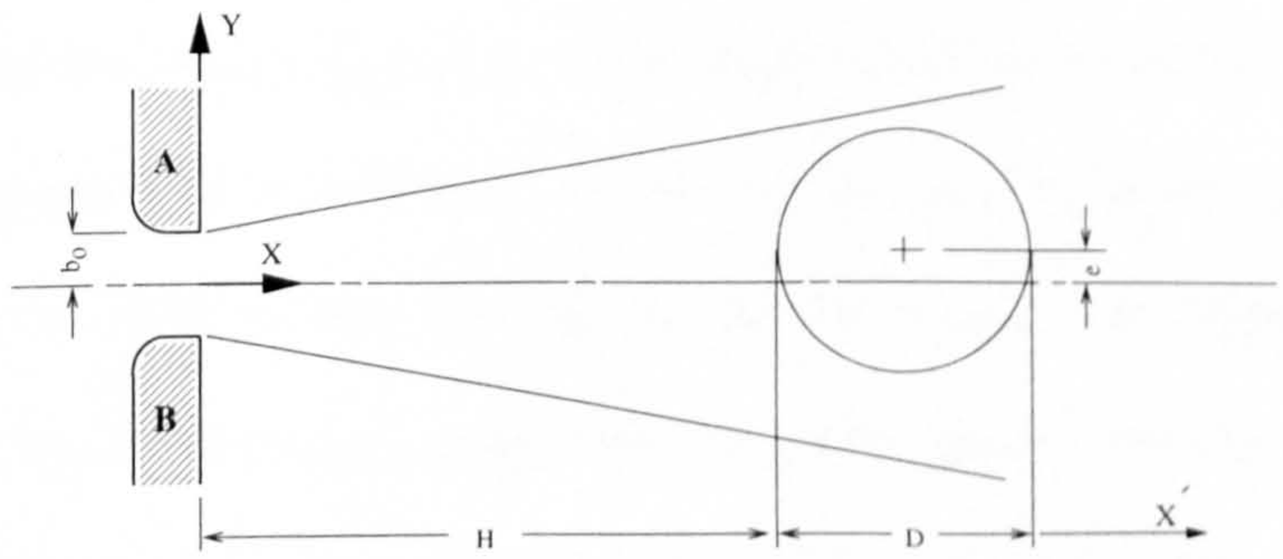

Fig.(8-34): Schematic representation of cylinder location with respect to slot.

separation points were very close to the rear stagnation point. Axial velocity measurements behind the cylinder show that at a very short distance behind the cylinder (x´/D=0.656), a normal shape of a jet velocity profile appears. Velocity profiles for distances x´/D=0.328 and x´/D=0.656 from the rear stagnation point as

well as the pressure distribution around the cylinder are presented in figs.(8-35) -(8-37).

8-3-2-2-1: Effect of cylinder offset on velocity profile behind the cylinder

Different offsets to the cylinder with respect to the horizontal plane through the centre of the slot, are achieved by moving the cylinder in an upward direction, in this case the velocity profiles behind the cylinder are not be symmetrical. Behind the lower semi-cylinder the velocity increases, whereas behind the upper semi-cylinder it decreases. For the case of $x'/D=0.33$ behind the cylinder and $e/D=0.2$ the lower peak velocity position in y-direction is nearly at $y_1/D=1.3$ below the slot centre. At the same section, by increasing the offset to $e/D=0.4$ the position of lower peak moves upward and its new position is $y_1/D=0.066$ above the slot centre, so at higher offsets jet flow passing around the lower semi-cylinder will have more deflection upwards due to the influence of Coanda effect, figs.(8-38) and (8-39).

Similar behaviour exists for $x'/D=0.66$. For the case of $e/D=0.2$ the lower side peak velocity position is $y_1/D=1.57$ below the slot centre, so by comparison with $x'/D=0.33$ it is obvious that for $e/D=0.2$ by increasing the distance behind the cylinder, on the lower side, the peak velocity moves away from the slot centre-line, figs.(8-40) and (8-41). By increasing the offset, $e/D=0.4$, at the same position ($x'/D=0.66$) only one maximum velocity behind the cylinder is recognizable and located at $y_1/D=1.57$ above the slot centre-line. A comparison between two different offsets ($e/D=0.2$, 0.4) for $x'/D=0.66$ shows that by increasing the offset, the flow deflects upwards due to the Coanda effect, fig.(8-42).

For the case of $e/D=0.4$, by increasing the distance behind the cylinder the flow will have only one maximum, its value decreases by increasing the distance but

its vertical distance from slot centre-line increases, fig.(8-43).

8-3-2-2-2: Effect of cylinder offset on the pressure distribution around the cylinder

The pressure distribution around the circular cylinder due to the interaction of a slot jet onto the cylinder have been represented in fig.(8-37). By applying an offset to the cylinder with respect to the horizontal symmetry plane of slot, variation of static pressure around the cylinder will not be symmetrical. For the case of e/D=0.2 there is a nearly constant pressure region from 180° to 310 degrees of rotation measured from the stagnation point, on the lower semi-cylinder. This constant pressure region, fig.(8-44), shows that the wake flow is deflected which agrees with the previously observed results obtained from velocity measurement for this case.

For the case of e/D=0.4 the behaviour of the pressure distribution curve changes completely. In comparison with the non-offset case, for the upper semi-cylinder the minimum pressure coefficient increases while on the lower semi-cylinder it decreases. The behaviour of pressure coefficient variation is in agreement with the results obtained from velocity measurement and show that for the jet flow over the lower semi-cylinder, the separation point moves forward (towards the position of 180°) and flow attaches to this convex solid surface due to the Coanda effect and therefore deflects upwards, fig.(8-45).

***

The overall discussion of the results together with the results obtained from numerical solution will be represented in chapter 10. The numerical solution of the problem is the subject of next chapter.

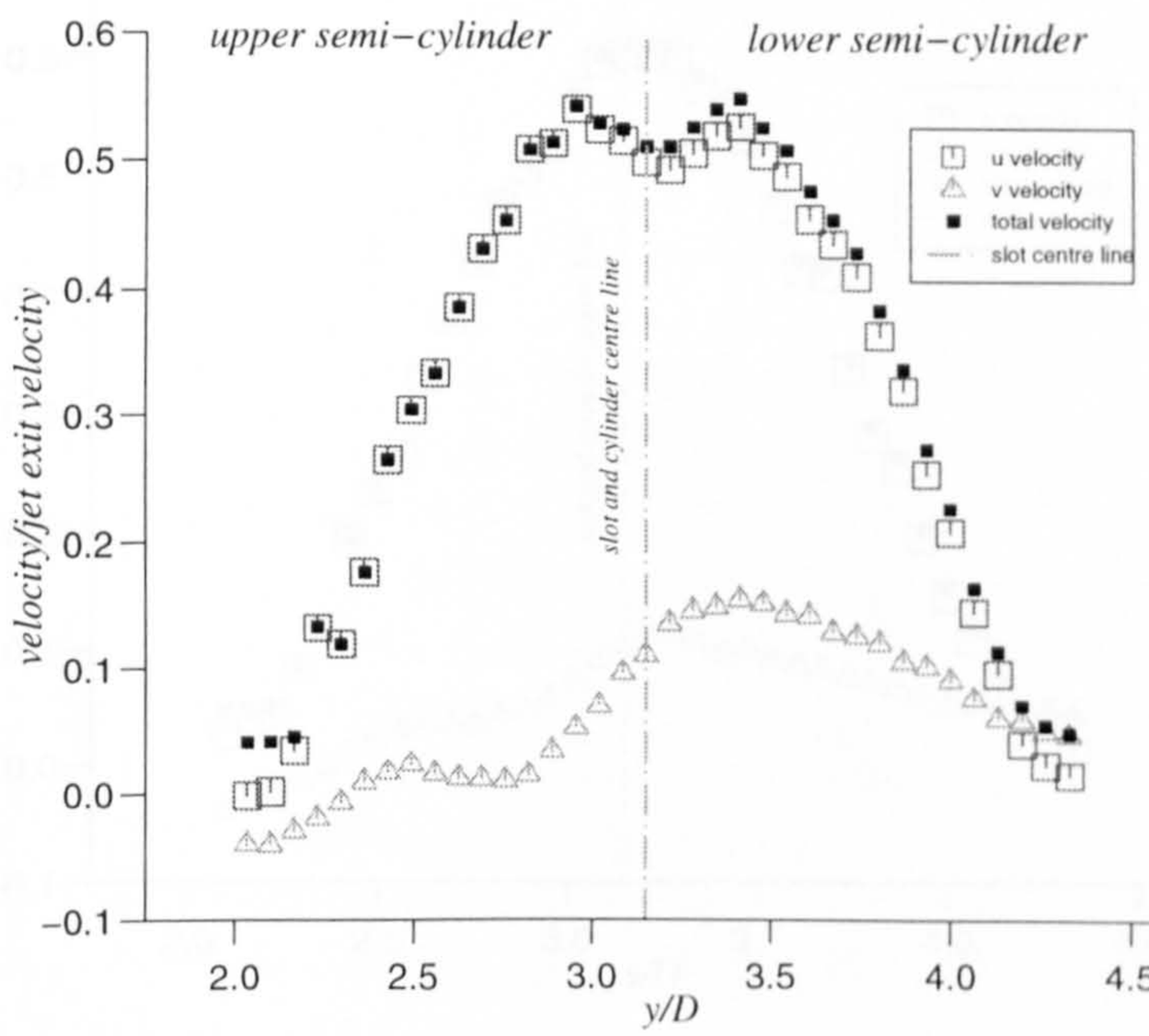

Fig.(8-35): Normalized velocity variation in vertical direction behind the cylinder for e/D=0.0 and x´/D=0.33.

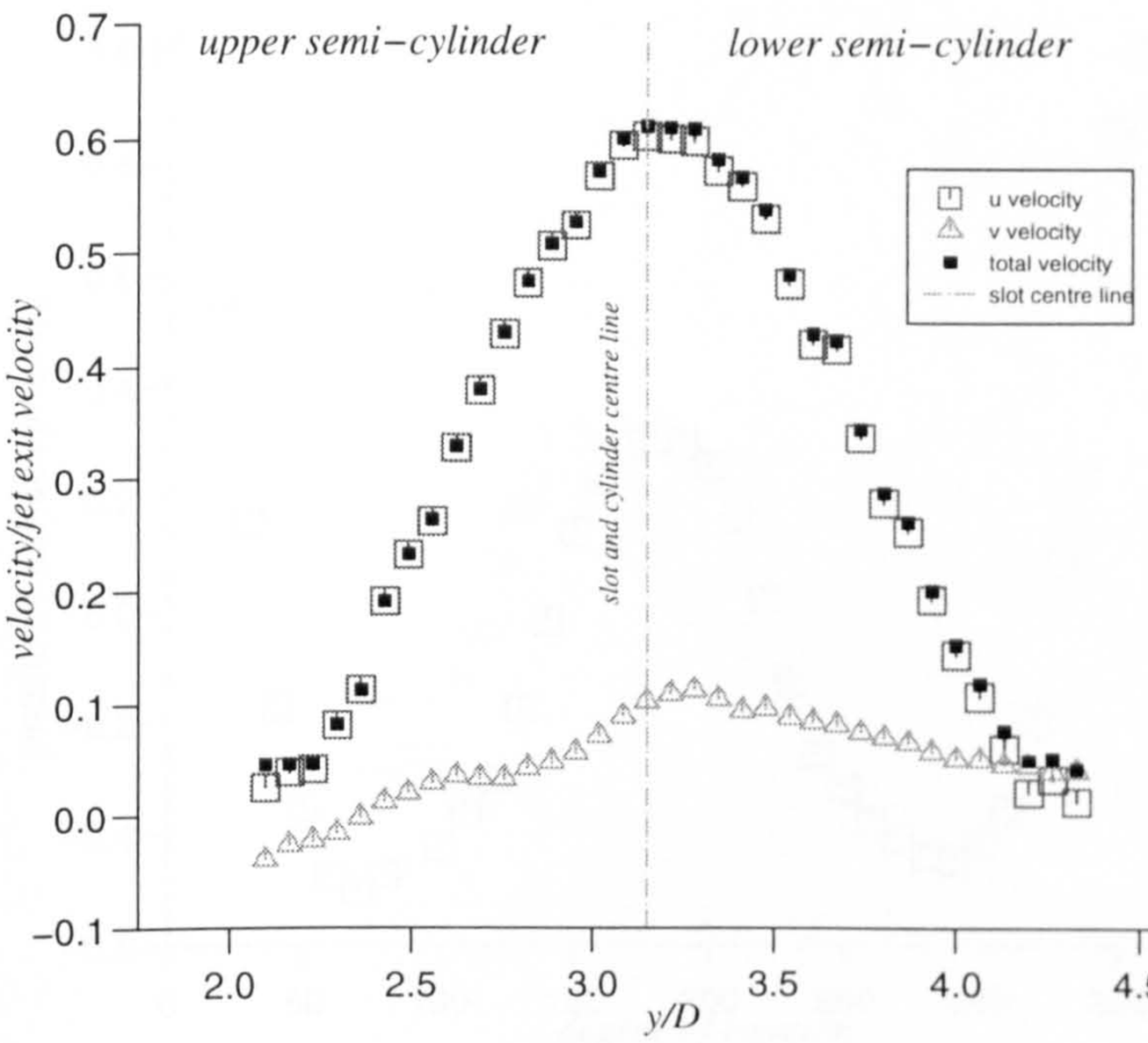

Fig.(8-36): Normalized velocity variation in vertical direction behind the cylinder for e/D=0.0 and x´/D=0.66.

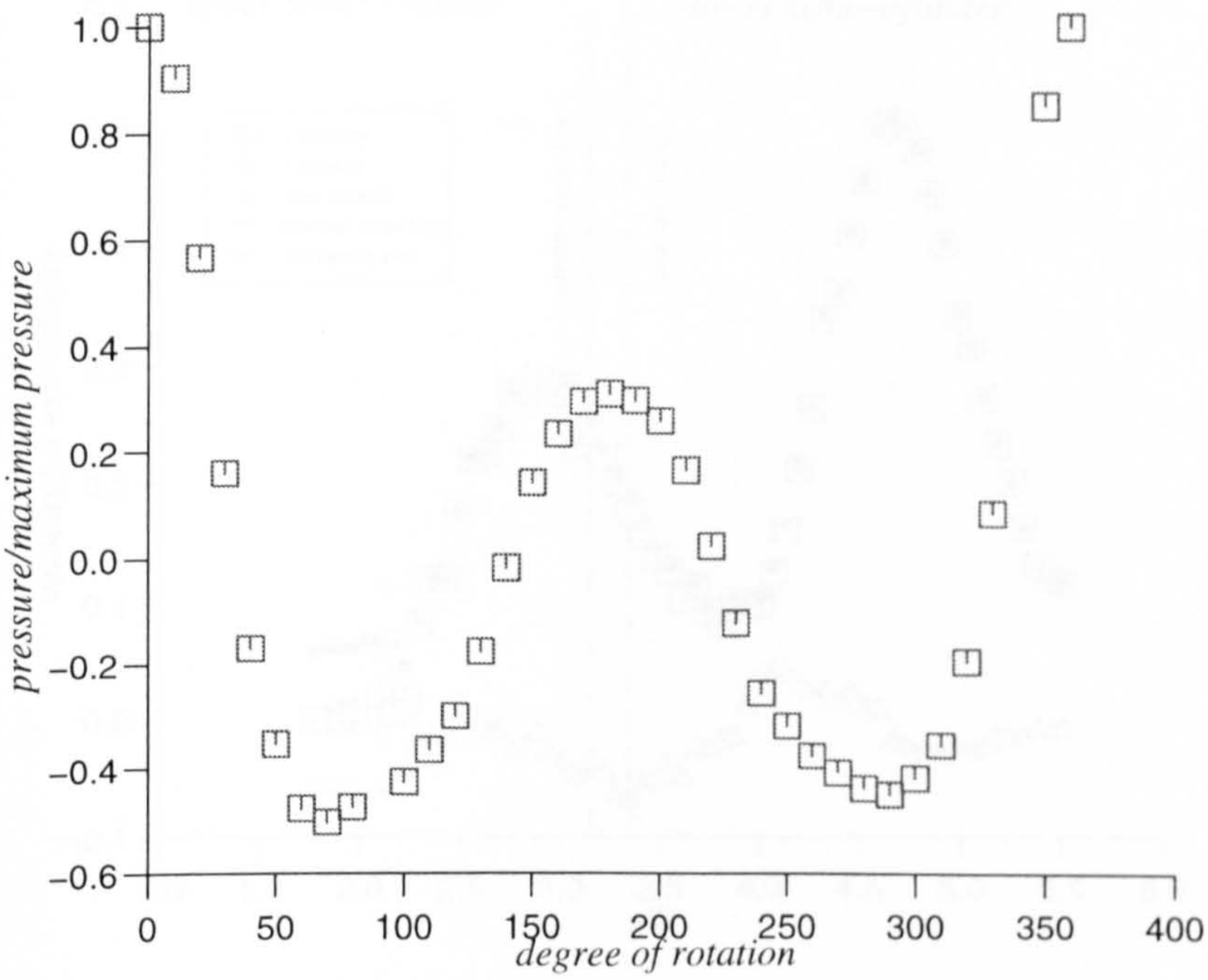

Fig.(8-37): Variation of pressure coefficient versus degree of rotation for e/D=0.0 and H/D=1.31.

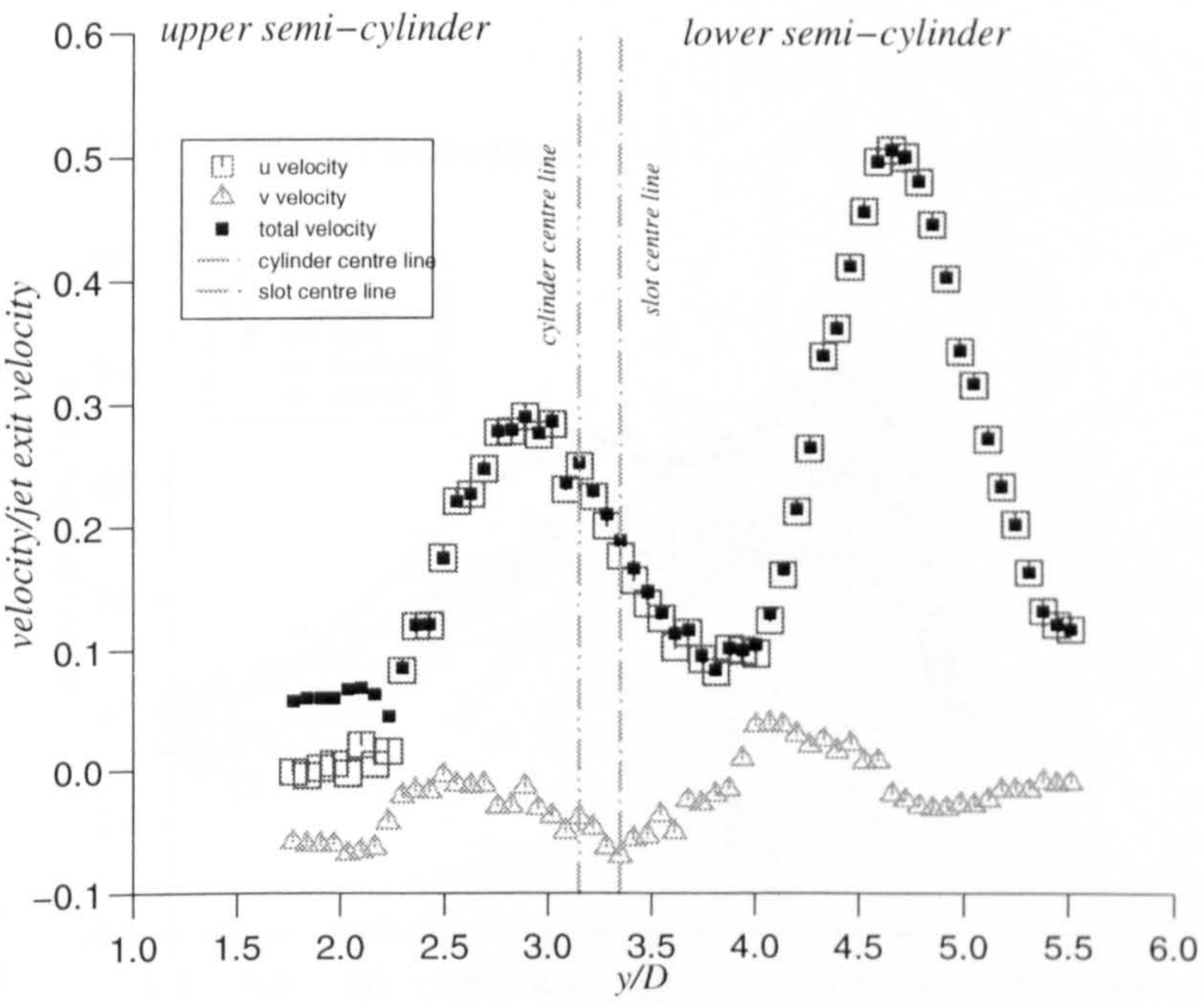

Fig.(8-38): Normalized velocity variation in vertical direction behind the cylinder for e/D=0.2 and x´/D=0.33.

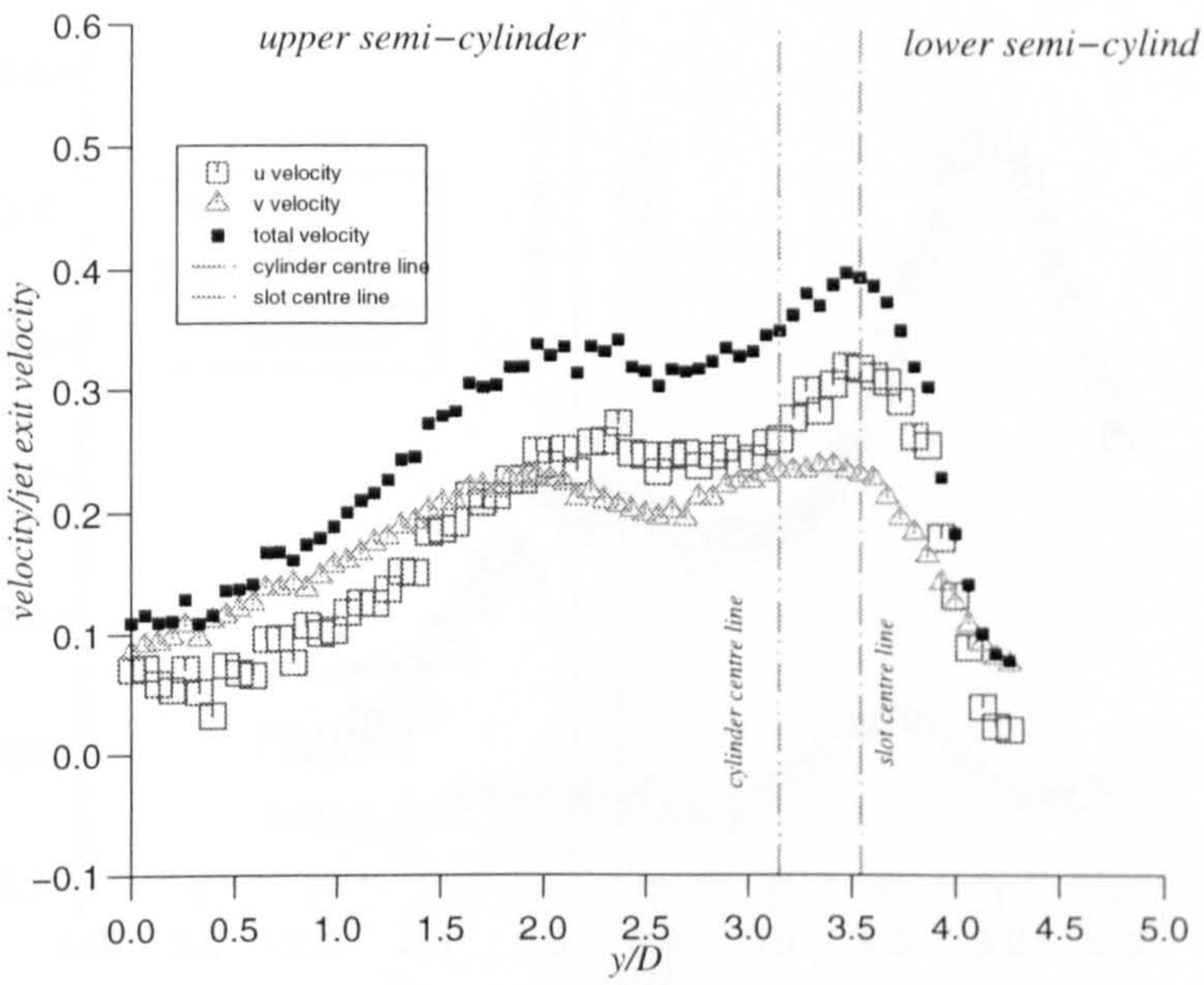

Fig.(8-39): Normalized velocity variation in vertical direction behind the cylinder for e/D=0.4 and x′/D=0.33.

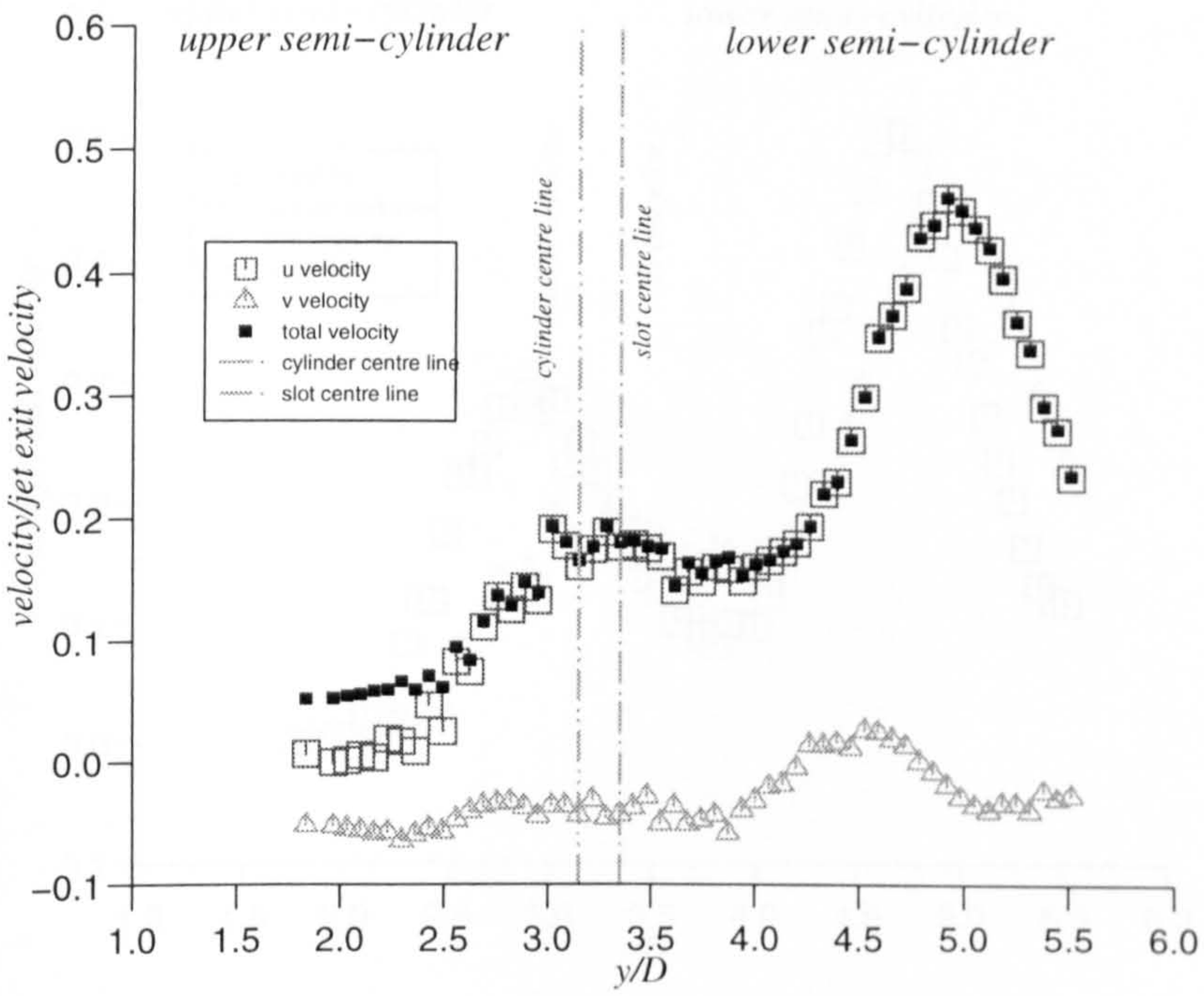

Fig.(8-40): Normalized velocity variation in vertical direction behind the cylinder for e/D=0.2 and x´/D=0.66.

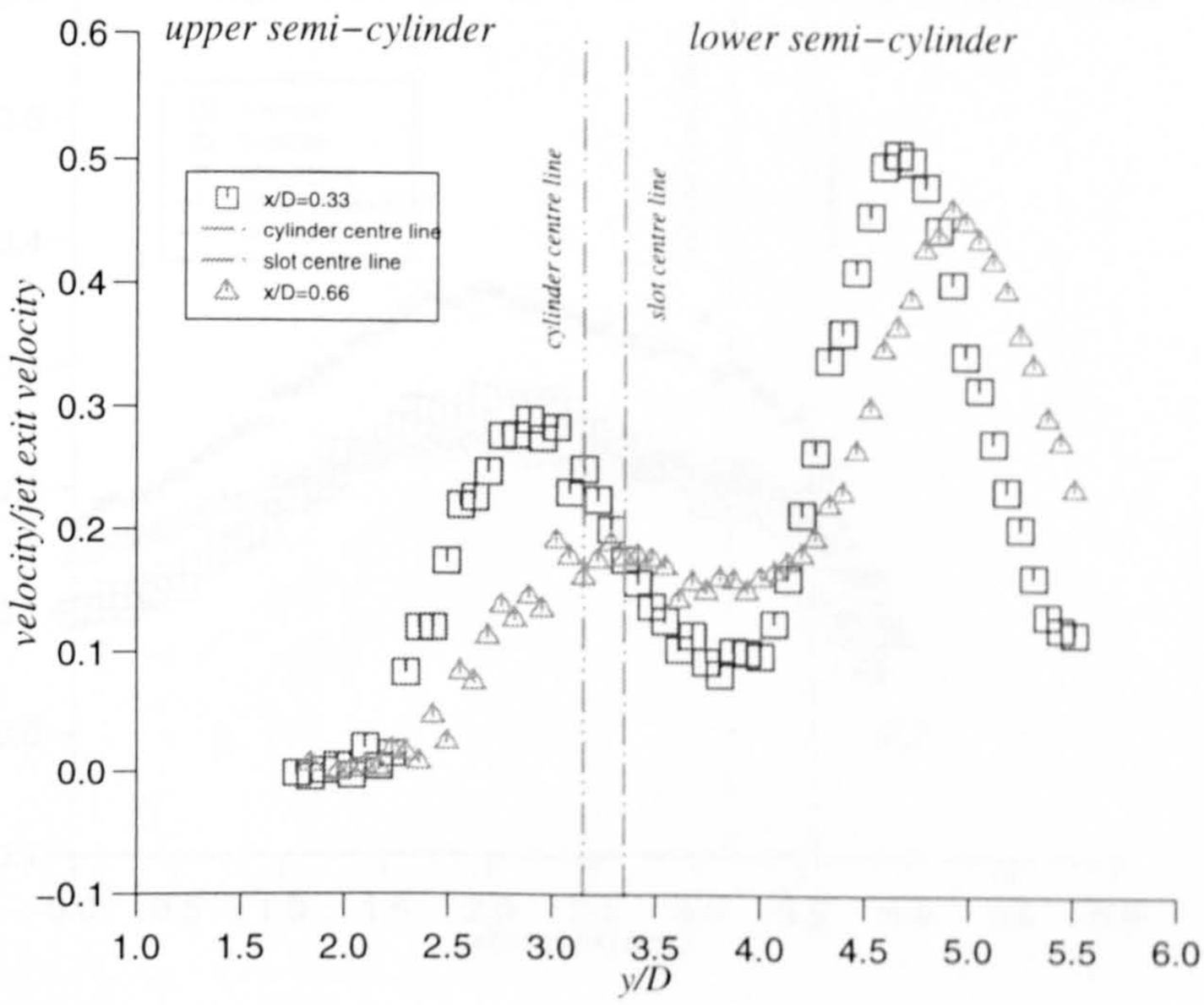

Fig.(8-41): Comparison between u velocity profiles for e/D=0.2 and x/D=0.33 with e/D=0.2 and x´/D=0.66.

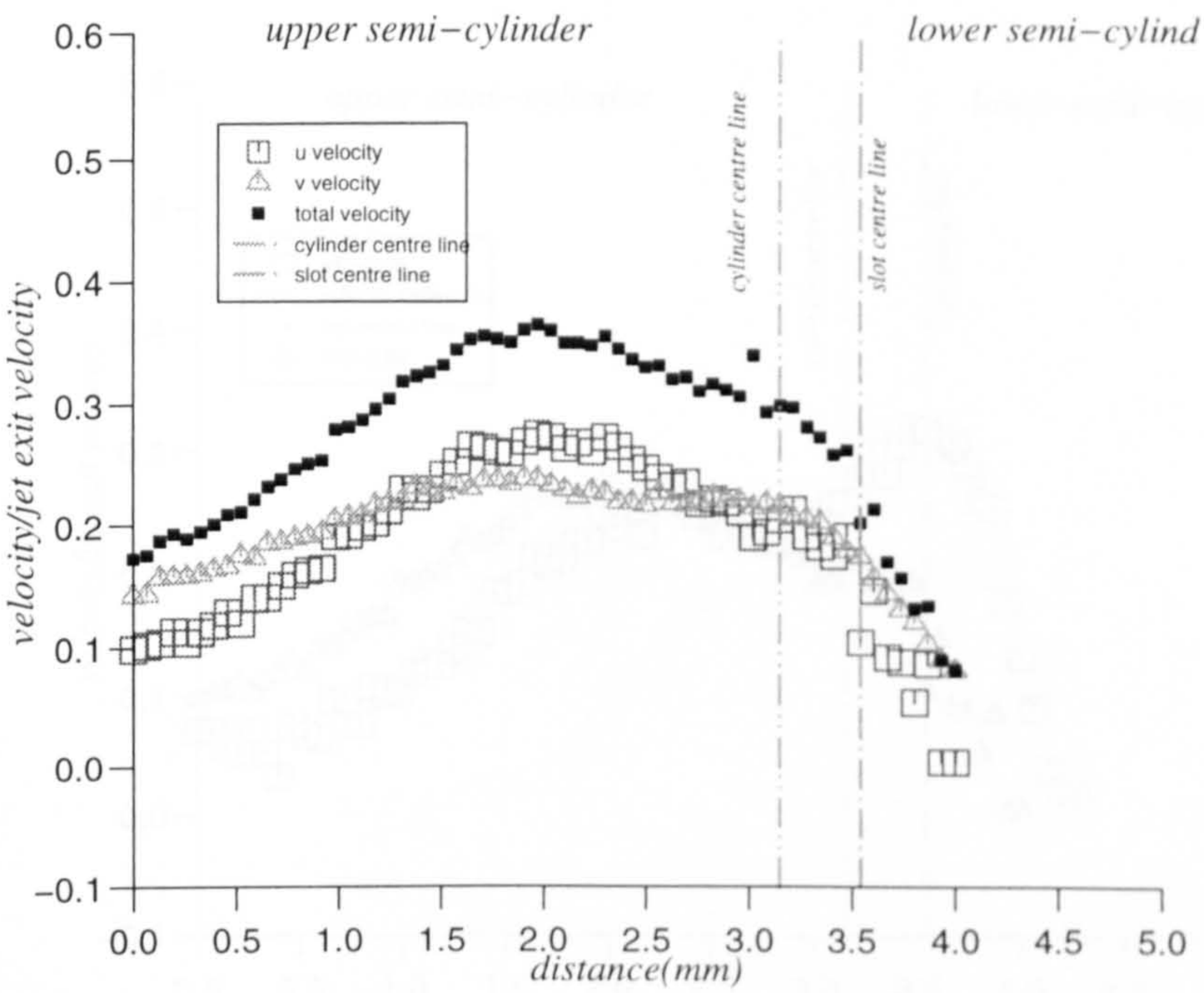

Fig.(8-42): Normalized velocity variation in vertical direction behind the cylinder for e/D=0.4 and x´/D=0.66.

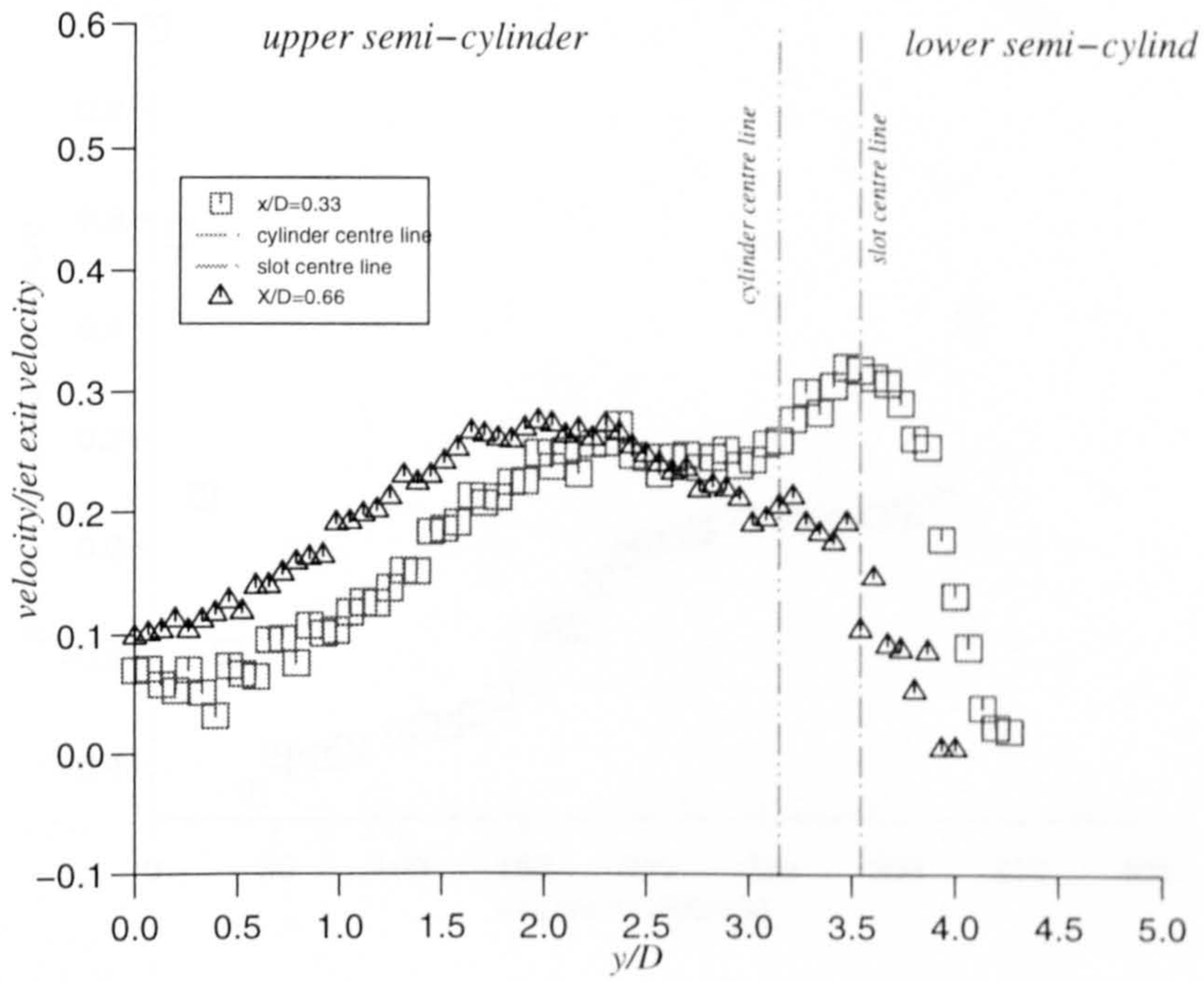

Fig.(8-43): Comparison between u velocity profiles for e/D=0.4 and x´/D=0.33 with e/D=0.4 and x´/D=0.66.

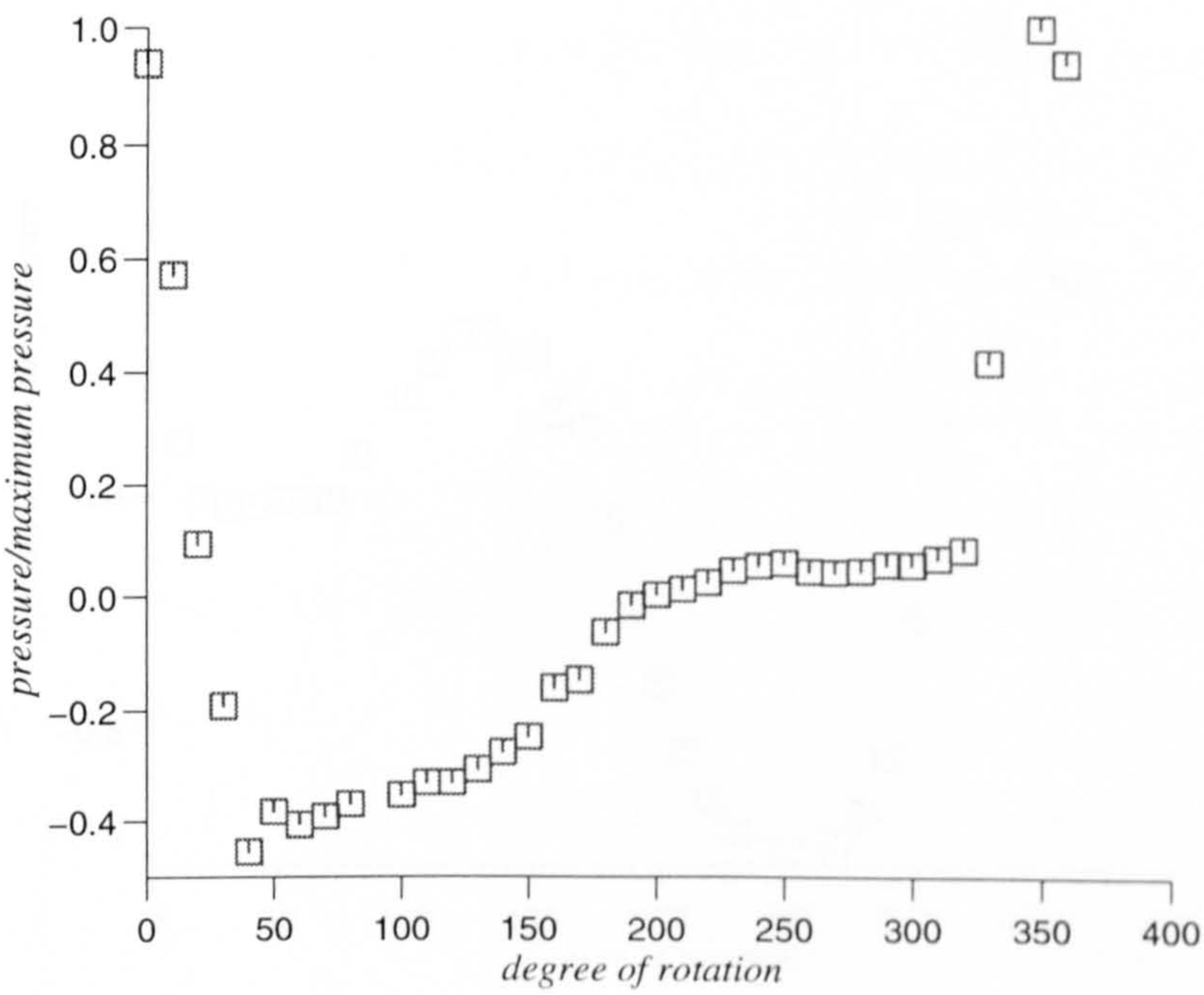

Fig.(8-44): Variation of pressure coefficient versus degree of rotation for e/D=0.2 and H/D=1.31.

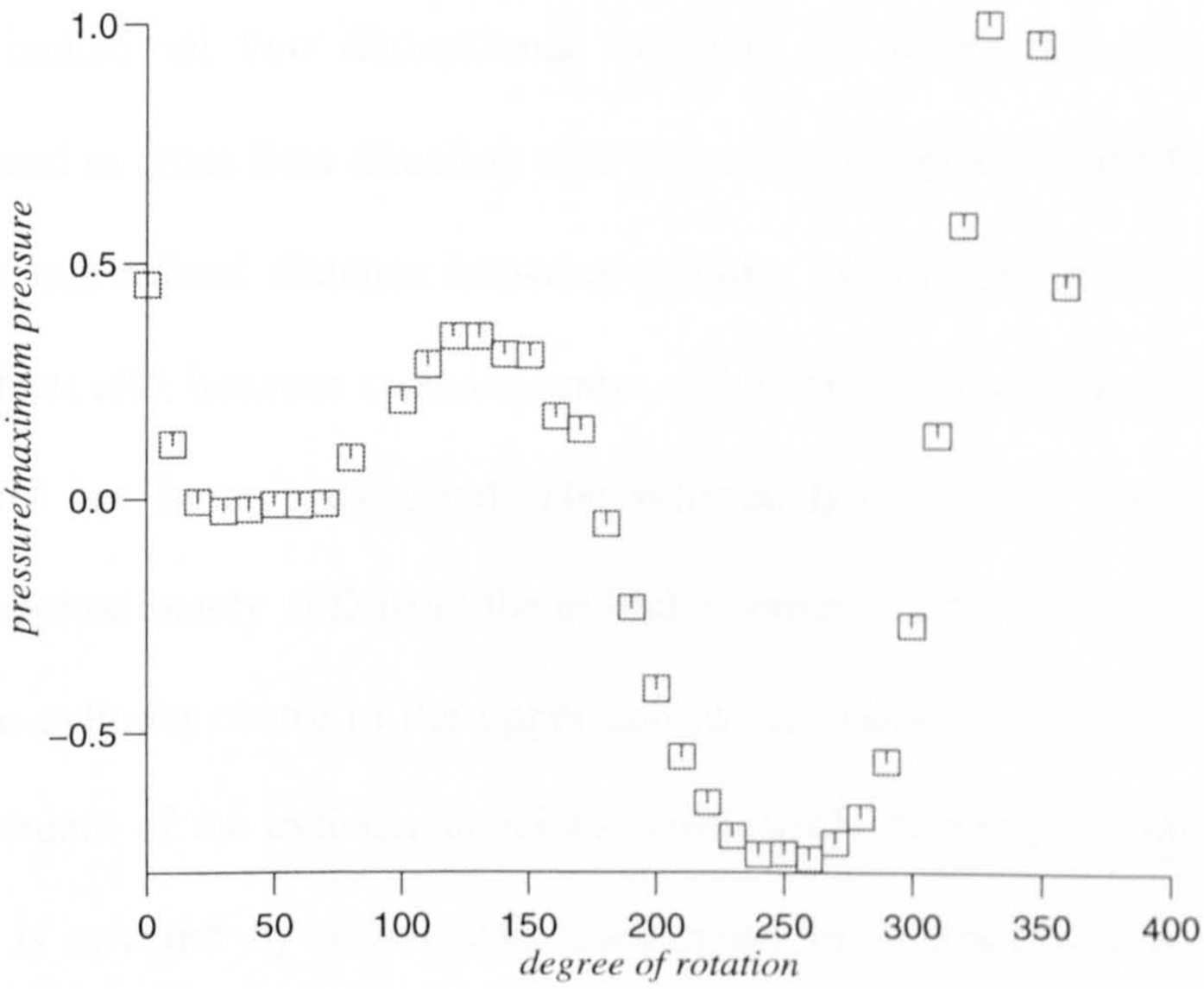

Fig.(8-45): Variation of pressure coefficient versus degree of rotation for e/D=0.4 and H/D=1.31.

CHAPTER

9

NUMERICAL STUDY OF SLOT JET IMPINGEMENT ONTO A CIRCULAR CYLINDER

9-1: Problem description

An isothermal two dimensional turbulent jet impinging onto a circular cylinder placed in cross-flow direction with respect to the jet axis for different values of h/D (the normalized distance between cylinder centre line and slot exit), and different offsets e/D, between cylinder centre and horizontal plane passed through the centre of slot has been investigated. The solution field for the case of h/D=1.81 extends to approximately 10D from the cylinder centre to the outflow boundary, and 5D from the cylinder centre to the upper and lower boundaries. In this case the jet flow downstream of the cylinder develops sufficiently to obtain complete velocity profiles. It is covered by a 301×255 node mesh to achieve a grid independent solution; the variation in axial velocity values by moving from a 301× 255 mesh to a 326×264 mesh being less than 2%. The extension of the flow domain for slot to cylinder distances of h/D=2.51 and 3.496 is the same as that for h/D=1.81, but each of them is covered by a 320×255 and a 344×255 node mesh, respectively. A uniform grid in both directions is obtained by fixing grid points on internal lines using linear interpolation and is generated by means of a grid generation program. A typical shape of this grid is represented in fig.(9-1).

Air at 15°C issuing from a slot ($2b_0$=12.73mm) at 120 m/sec, 0.5% turbulence

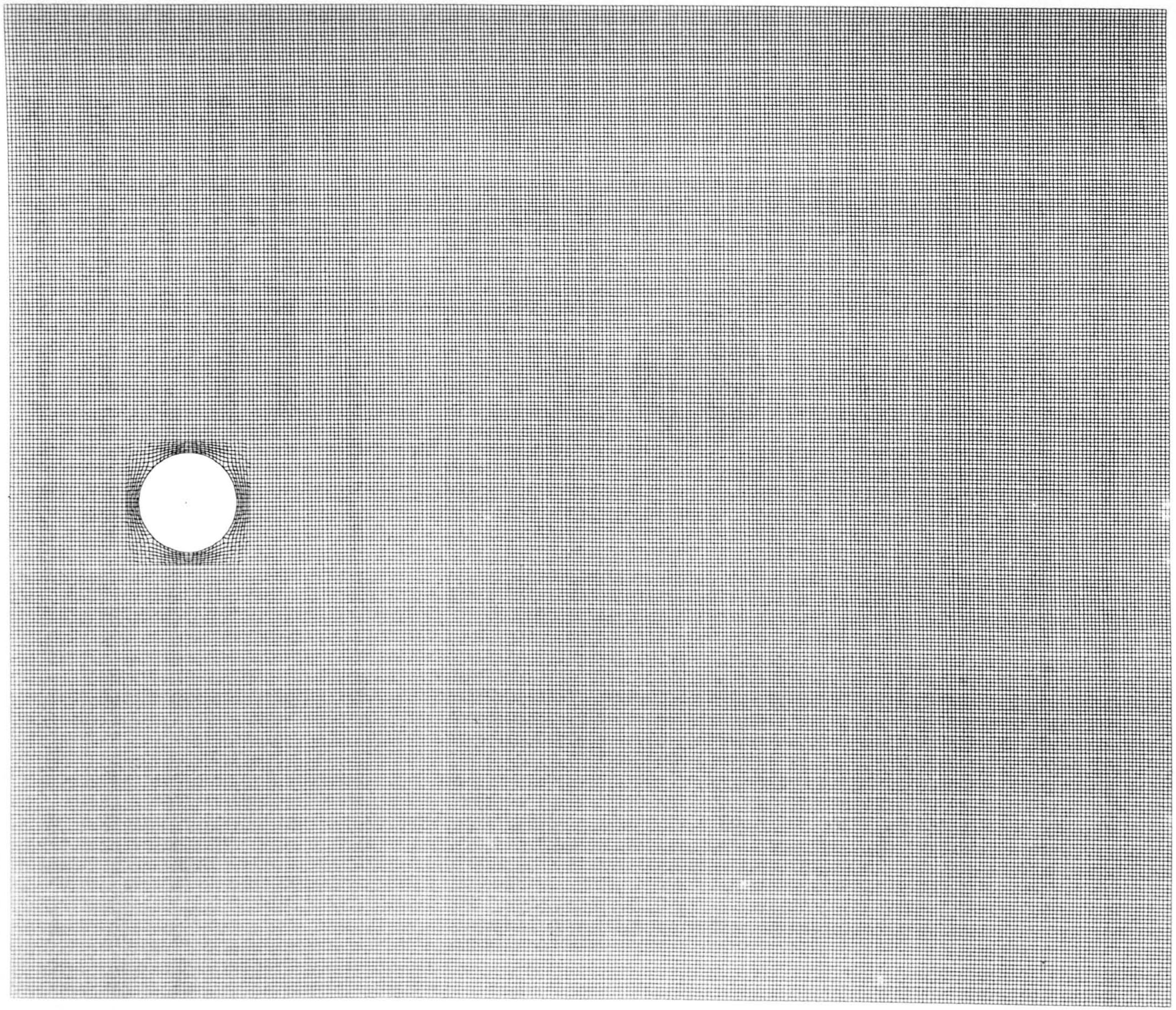

Fig.(9-1): Grid generated for h/D=1.81

intensity and $R_{ej}=1.05\times10^5$, impinges onto a cylinder of diameter $D=4b_0$ located horizontally in the cross flow direction with respect to the jet axis, at three different distances from the slot exit, h/D=1.81, 2.51 and 3.5. The boundary conditions for numerical calculations have already been mentioned in chapter 4. The calculation domain is divided into four different zones around the cylinder, fig.(9-2), and numerical calculations carried out by the procedure described in chapter 5.

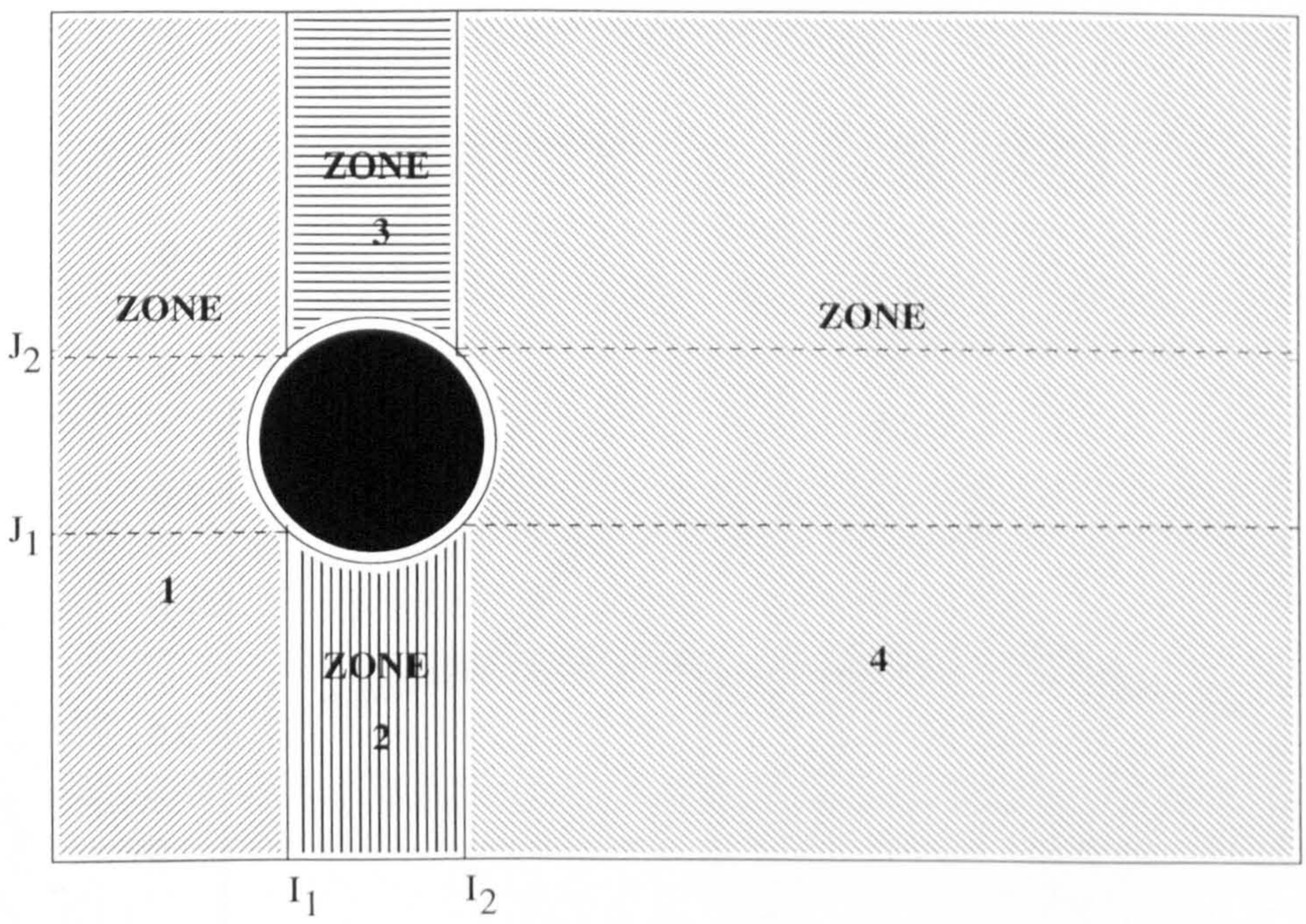

Fig.(9-2): Schematic representation of calculation zones.

9-2:Results and discussions

9-2-1: Non-offset conditions

Variation of axial velocity in a direction normal to the jet centre line and at different distances behind the cylinder, fig.(9-3), shows that an enclosed region between stream-lines through the separation points (s_1 and s_2), and the rear side of the cylinder between two separation points is formed, and includes two sets of concentrated vortices. In the free stream behind the cylinder the existence of a

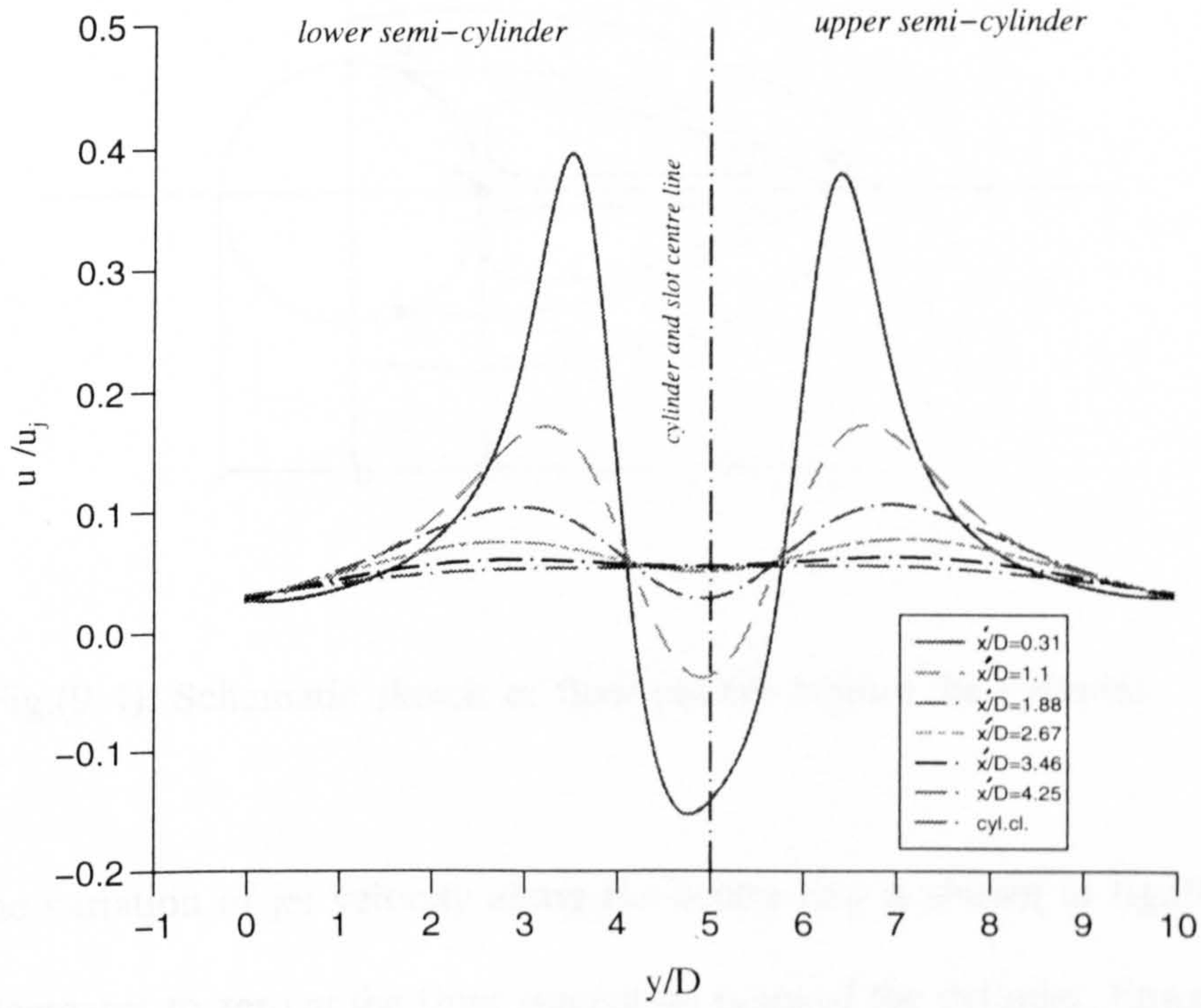

Fig.(9-3): Axial velocity variation in normal direction to jet centre line and at different axial distances from cylinder for h/D=1.81 and e/D=0.0.

stagnation point (s_4), which coincides with the junction of two stream-lines through two separation points, and characterised by zero centre-line velocity behind the cylinder is confirmed. The position of this stagnation point, referring to figs.(9-4) and (9-5), is $x'/D=1.4$, which is in the range of data obtained for parallel flow past a circular cylinder. A schematic diagram of the flow pattern behind the cylinder is represented in fig.(9-4).

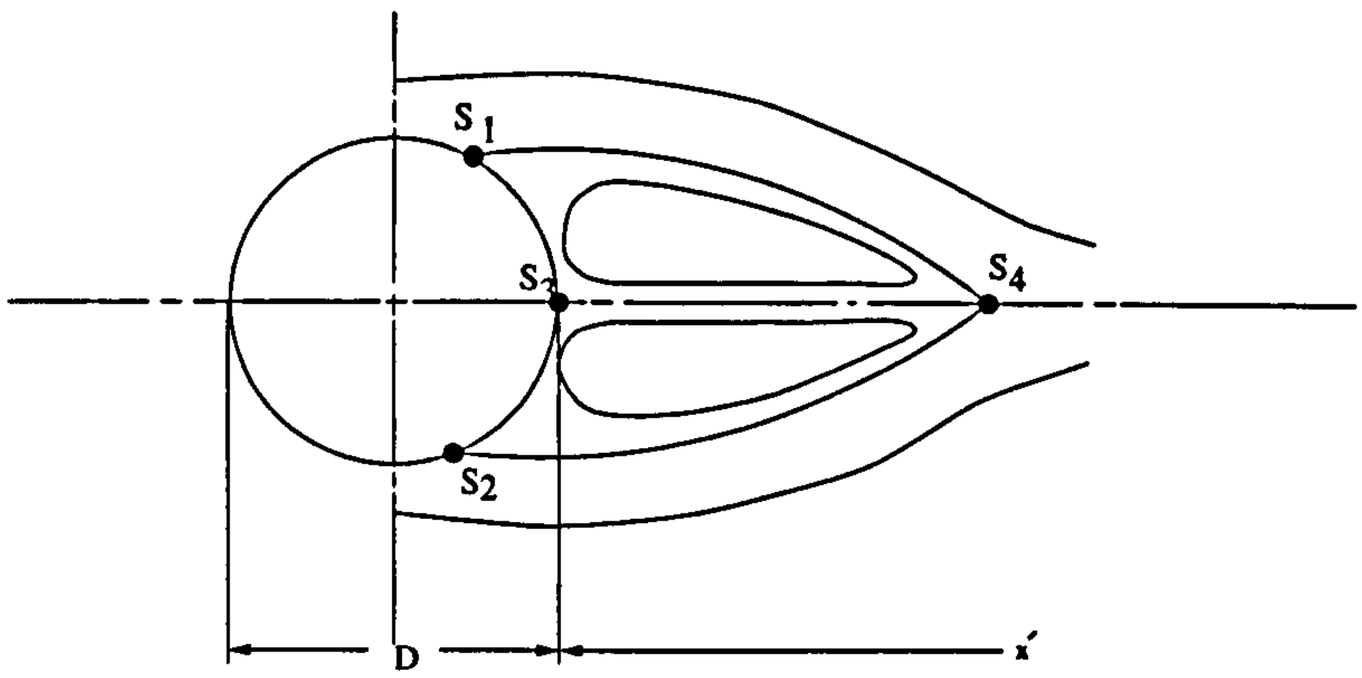

Fig.(9-4): Schematic sketch of flow pattern behind the cylinder.

The variation of jet velocity along the centre line is shown in fig.(9-5). The velocity decreases to zero at the front stagnation point of the cylinder. From the rear stagnation point on the cylinder surface (s_3) velocity decreases from zero and then increases towards zero at the end of wake region (s_4), which corresponds to $x'/D=1.4$. The velocity then increases and reaches to a maximum at $x'/D=3.95$, in agreement with the results obtained from the velocity diagram, fig.(9-3), and after this position it has the normal shape of a fully developed jet velocity profile and begins to decay gradually.

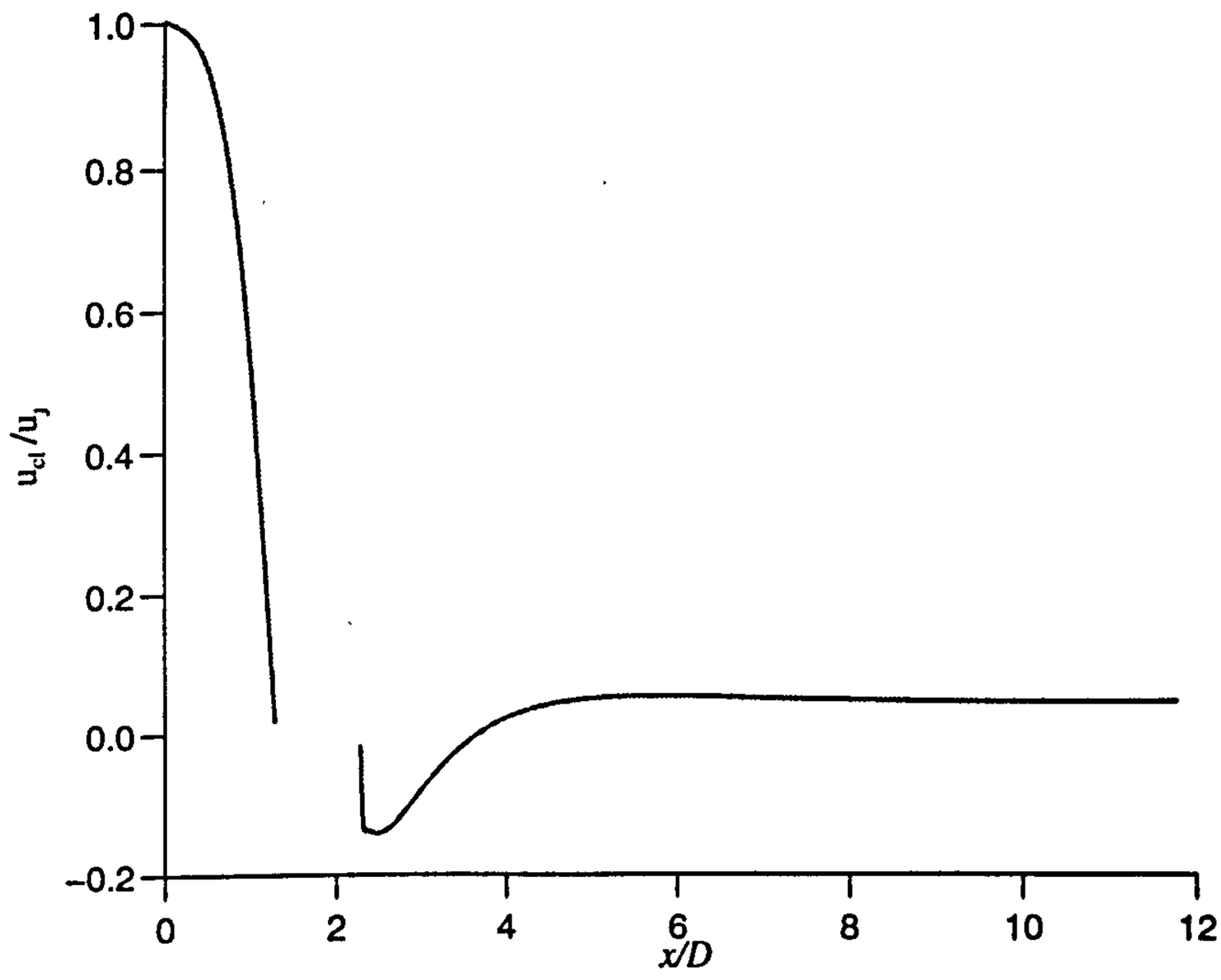

Fig.(9-5): Variation of jet centre line velocity for h/D=1.81 and e/D=0.0.

The pressure distribution, plotted as the variation of pressure coefficient (c_p=gauge pressure/ stagnation point gauge pressure) with the angular position on the cylinder surface is shown in fig.(9-6). The angular position of minimum pressure coefficient is ±50° from frontal stagnation point. This position is related to the angular position of maximum shear stress. Referring to fig.(9-7) for the variation of shear stress coefficient with angular position, the angular position of maximum shear stress is very close to the position of minimum pressure coefficient, and the small difference between these two is related to the turbulent conditions of the jet flow. The angular position of separation points on the cylinder surface are the points where shear stress vanishes. Referring to fig.(9-7) the related positions of these points for the upper semi-cylinder is 83° and for the lower semi-cylinder is 276°, measured from the front stagnation point. The difference between these two positions is related to the deviation of the jet centre line from its geometrical position. Transferring these two points to fig.(9-6), shows that the approximate locations of the separation points are the two ends of the nearly-constant pressure region on the cylinder surface which determines the beginning of wake region behind the cylinder.

Axial velocity profiles for h/D=2.51 and 3.5 are shown in figs.(9-8)-(9-9) respectively. Considering these two figures, it is obvious that by increasing the spacing between slot and cylinder, the enclosed region behind the cylinder still exists. Referring to the variation of centre line velocities for each case, fig.(9-10) for h/D=2.51 and fig.(9-11) for h/D=3.5 show that the length of the wake region reduces by increasing the spacing between slot and cylinder, from x′/D=1.4 for h/D=1.81 falls to x′/D=0.9647 for h/D=2.51 and x′/D=0.6316 for h/D=3.5. From the end of this region velocity increases and reaches to a maximum. The position of this

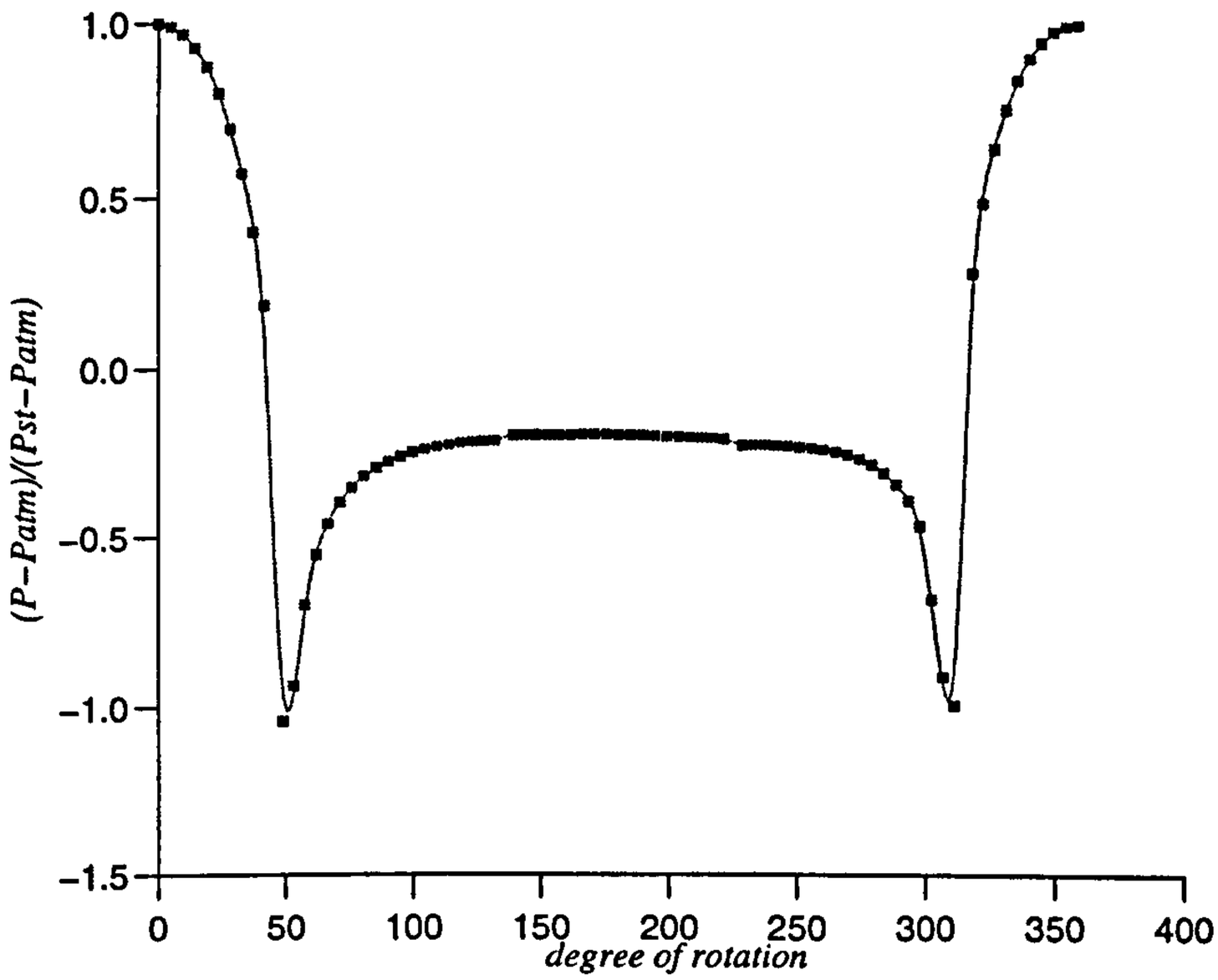

Fig.(9-6): Variation of pressure coefficient on cylinder surface for h/D=1.81 and e/D=0.0.

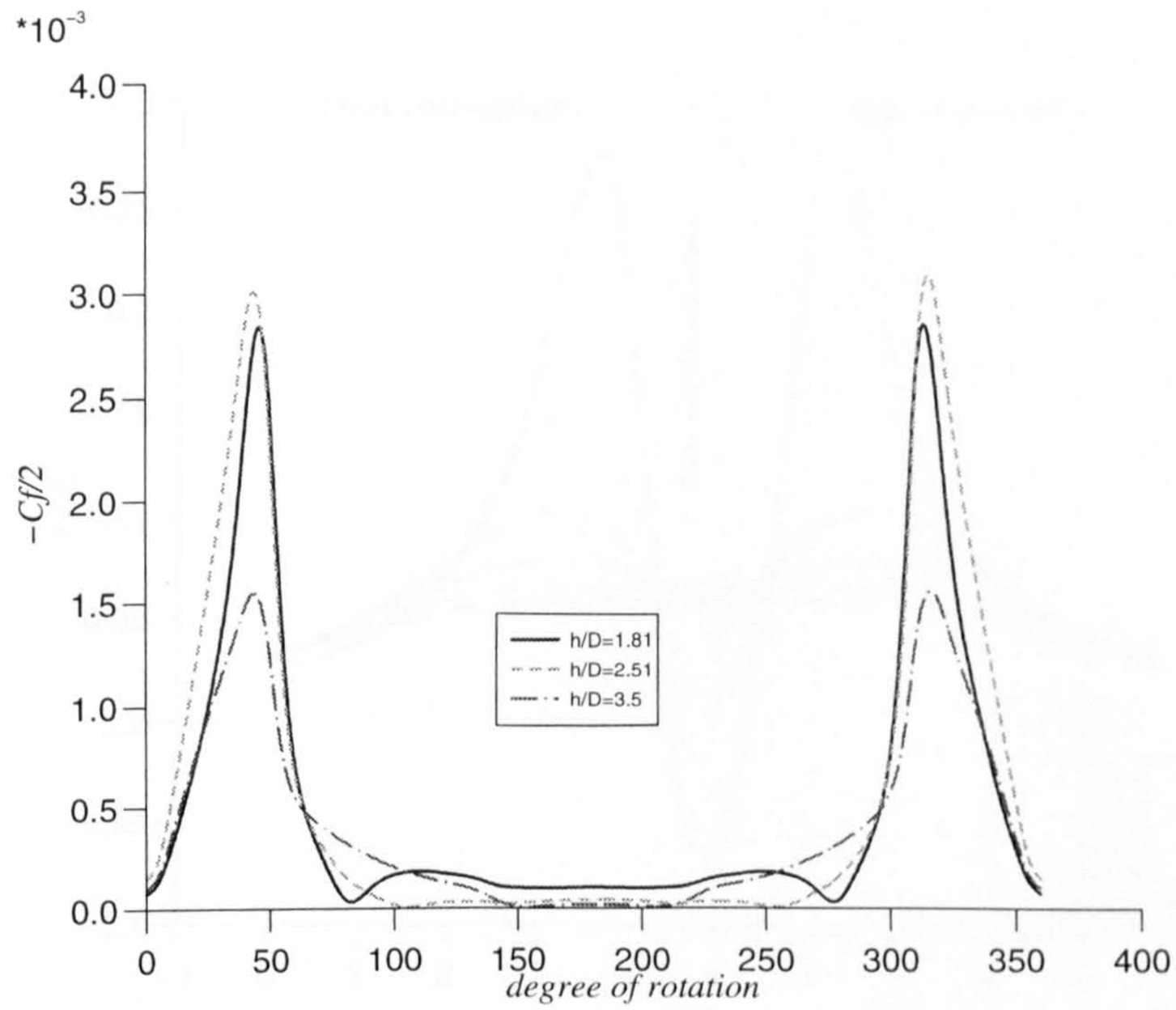

Fig.(9-7): Variation of stress coefficient on cylinder surface for e/D=0.0 and different spacings between slot and cylinder.

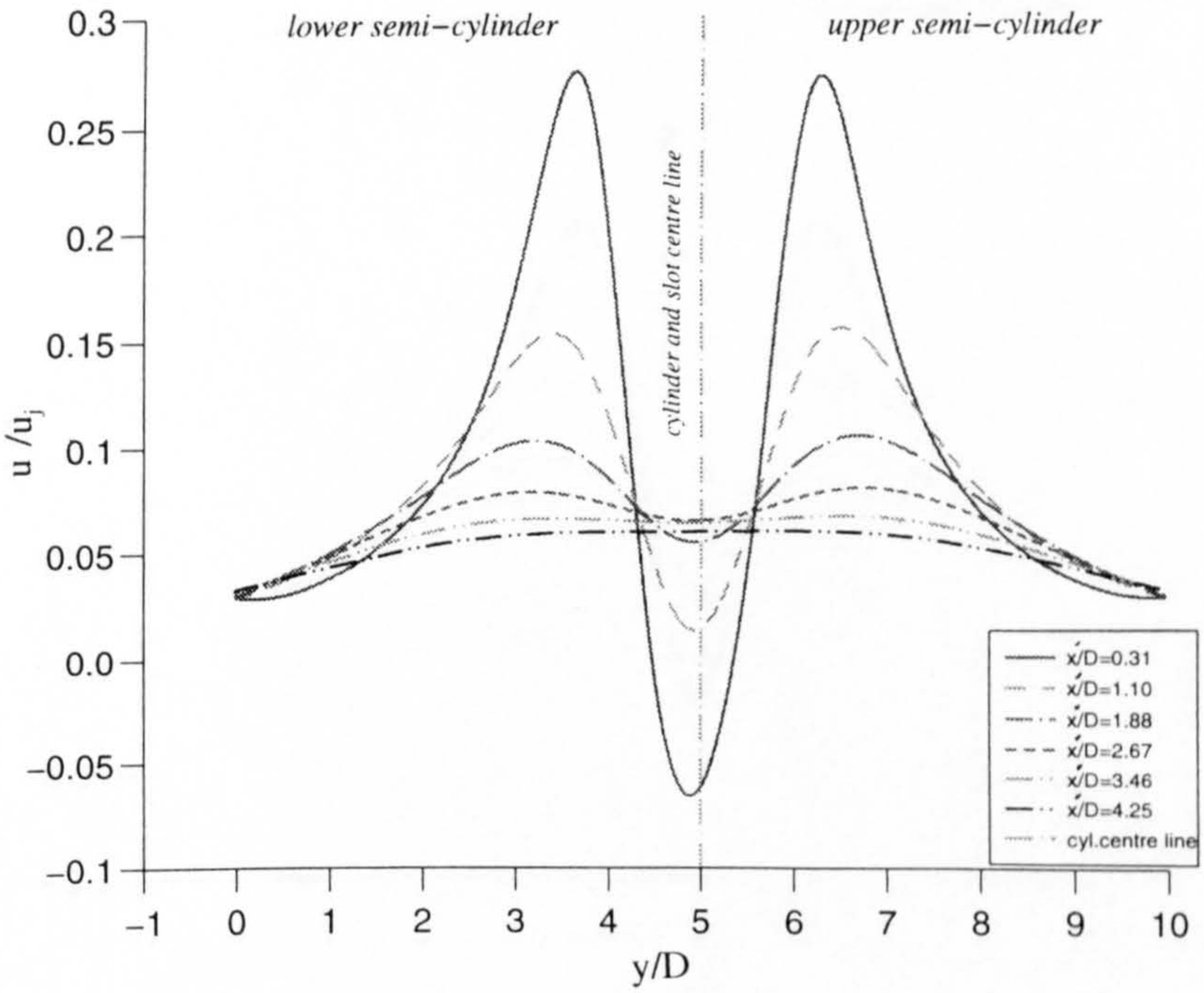

Fig.(9-8): Axial velocity profiles behind the cylinder at different distances from cylinder for h/D=2.51 and e/D=0.0.

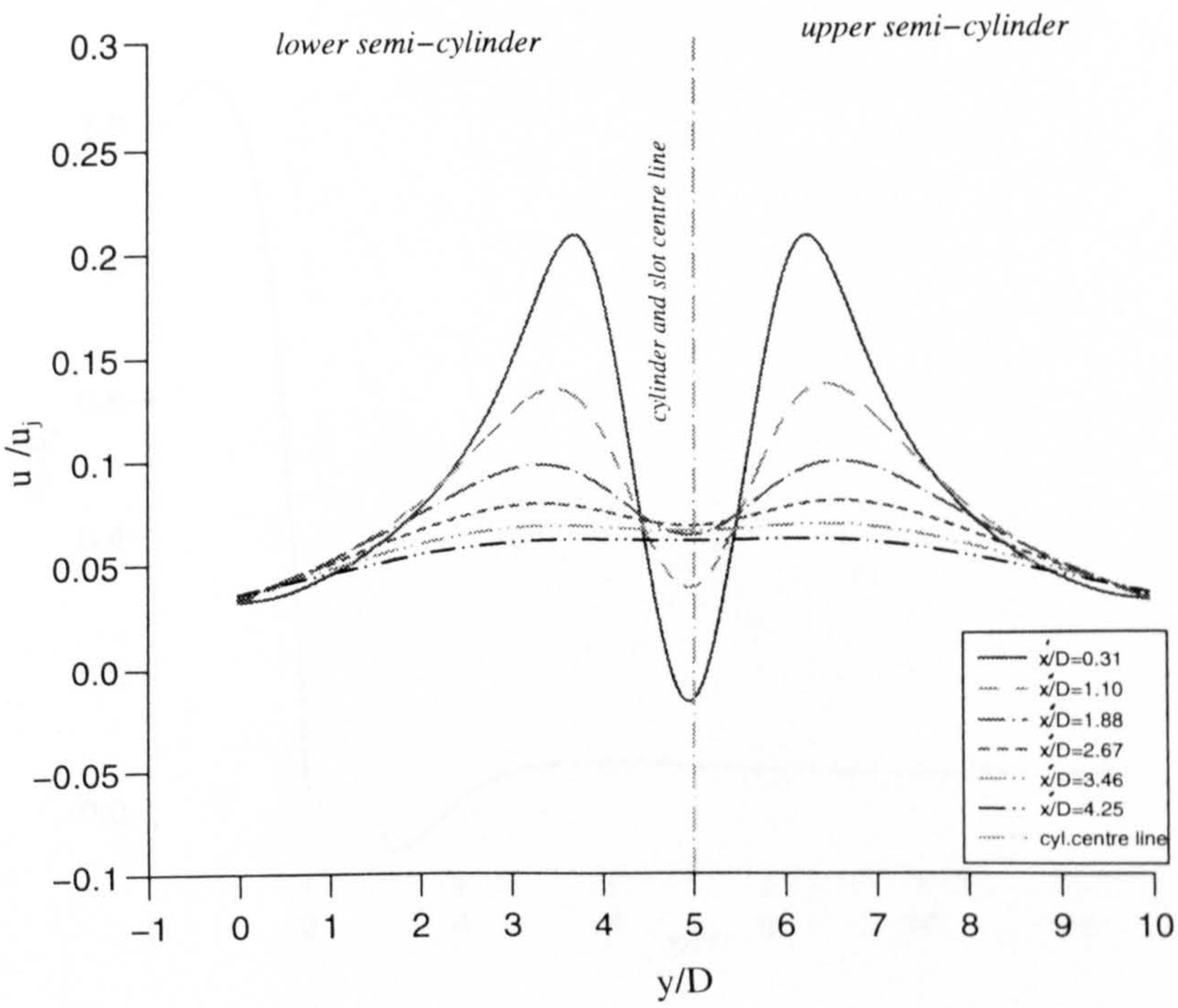

Fig.(9-9): Axial velocity profiles behind the cylinder for different distances from the cylinder, h/D=3.5 and e/D=0.0.

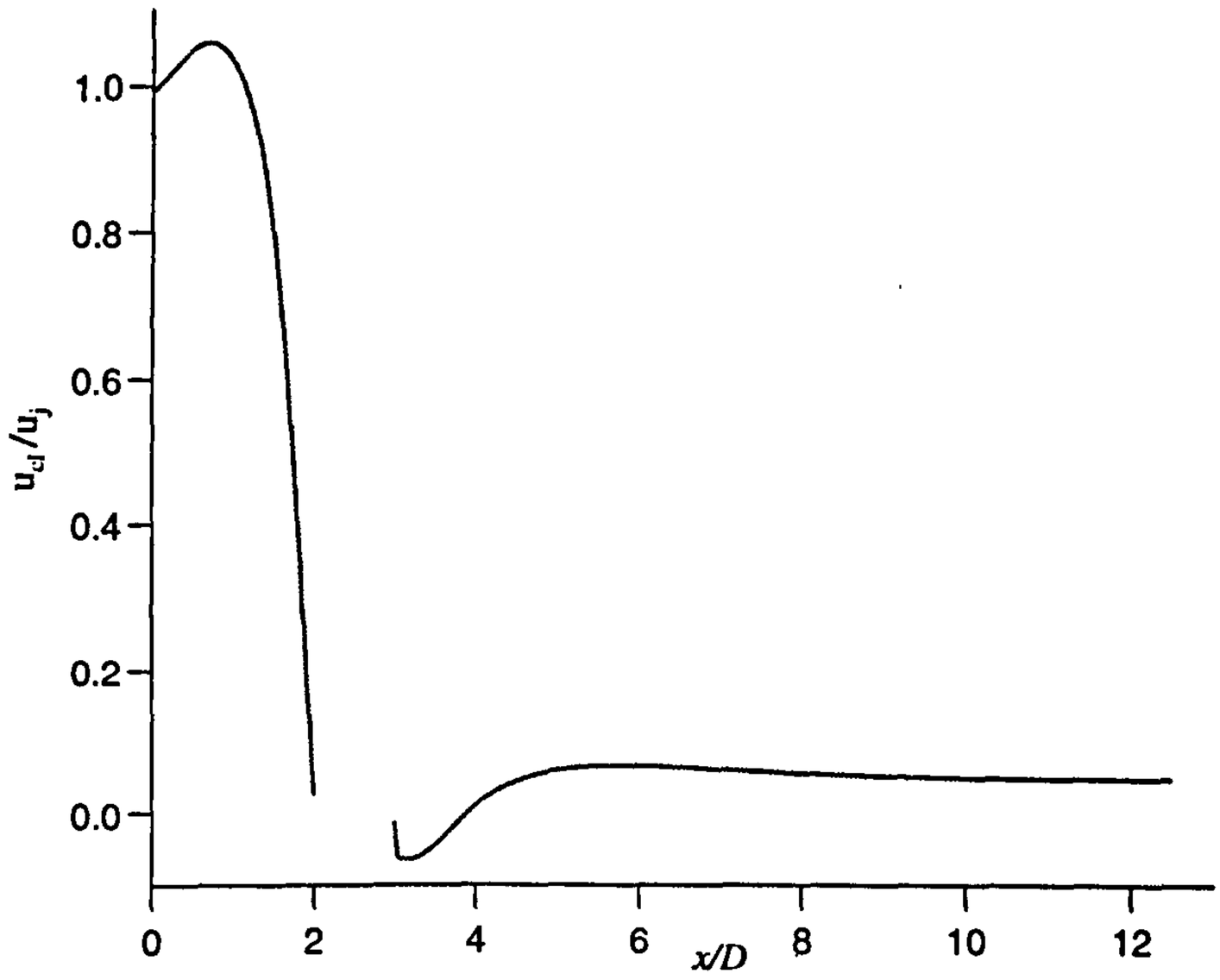

Fig.(9-10): Variation of jet centre line velocity for h/D=2.51 and e/D=0.0.

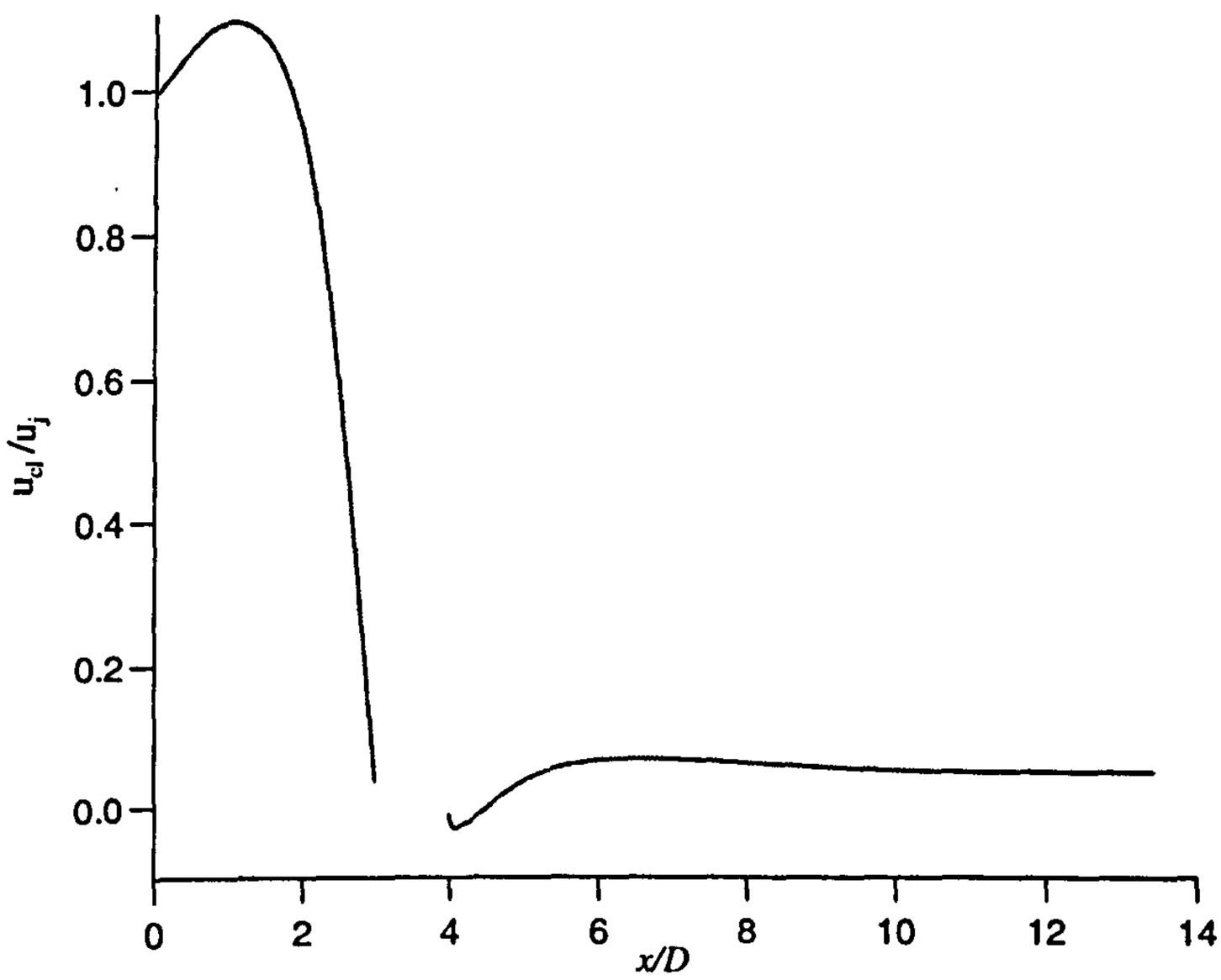

Fig.(9-11): Variation of jet centre line velocity for h/D=3.5 and e/D=0.0.

maximum centre line velocity from the rear end of the cylinder is decreased with increased spacing between the slot and cylinder and falls from x´/D=3.95 to 2.87 and then 2.675 related to h/D=1.81, 2.51 and 3.5 respectively.

Referring again to fig.(9-7) for the approximate position of separation points, taken as the vanishing point of shear stress on cylinder surface is shown in table (9-1):

Table(9-1): Position of separation points for different spacing between slot and cylinder

h/D	S_1	S_2
1.81	83	276
2.51	107	252
3.5	153	207

The data shows that by increasing the distance between cylinder and slot, the separation point moves towards the rear stagnation point which causes the width of the wake region to decrease, and consequently by considering the previously mentioned variation in the length of this region, the enclosed wake region is smaller.

Comparing the maximum shear stress on the cylinder surface for different spacings shows that the angular position of maximum shear stress is nearly constant and it is in the range of 43°-45°for the upper semi-cylinder and 314°-317° for lower semi-cylinder. By increasing the spacing from h/D=1.81 to 2.51 there is a slight rise in magnitude of the shear stress coefficient within about 5%, but further increase of the spacing to h/D=3.5 causes the maximum shear stress to reduce by about 50%. So, for cleaning purposes of a single cylinder the optimum spacing between slot and cylinder is up to 2.51 times of cylinder diameter.

Comparing the centre line velocity variations for different spacings between

cylinder and slot show that the velocity at the exit from the slot for h/D=1.81, fig.(9-5), decreases continuously towards zero velocity at the stagnation point, but by increasing the distance between slot and cylinder, for h/D=2.51 and 3.5, figs.(9-10) and (9-11), there is a slight rise in velocity at the exit from the slot followed by a subsequent decease to zero at the stagnation point. The position and magnitude of this maximum velocity increases by increasing the spacing and for h/D=2.51, x/D=0.67 and u/u_j=1.06, which increases for h/D=3.5 to x/D=1.07 and u/u_j=1.093. This increase, which has been reported also by Kang and Greif (1992) for R_e=100, in agreement with the results of Townsend (1956), is due to the formation of an under-pressure region between slot and cylinder.

Variation of static pressure on the cylinder surface for h/D=2.51 and 3.5 are shown in figs.(9-12) and (9-13) respectively. The position of minimum pressure coefficients are the same as h/D=1.81 and located at ±50°, which is in agreement with the results obtained from shear stress coefficient variations and, as mentioned already, the difference between these two is related to the turbulence of the fluid flow. By transferring the position of separation points obtained from shear stress coefficient variations to the pressure variations curve, it is found again that their positions are related to the two ends of the constant pressure region on the pressure variation curve, but identifying solely through the pressure curve is difficult, and stress variation helps give a better criterion for their positions.

Fig.(9-13) shows that at positions related to ±37° there is a sudden slight jump on the pressure curve which might be related to the forming of a small separation bubble on the cylinder surface in these two positions.

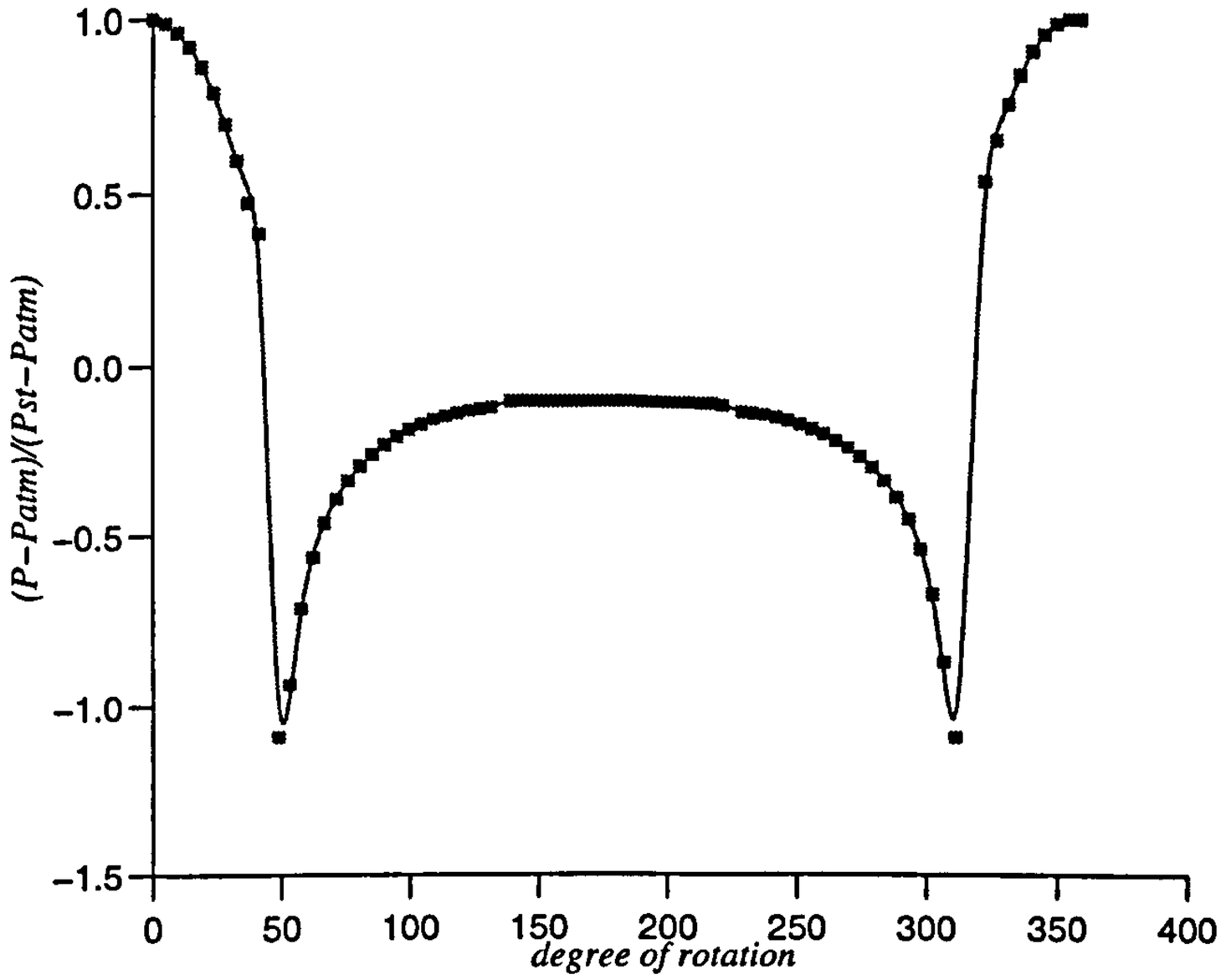

Fig.(9-12):Variation of pressure coefficient on cylinder surface for h/D=2.51 and e/D=0.0.

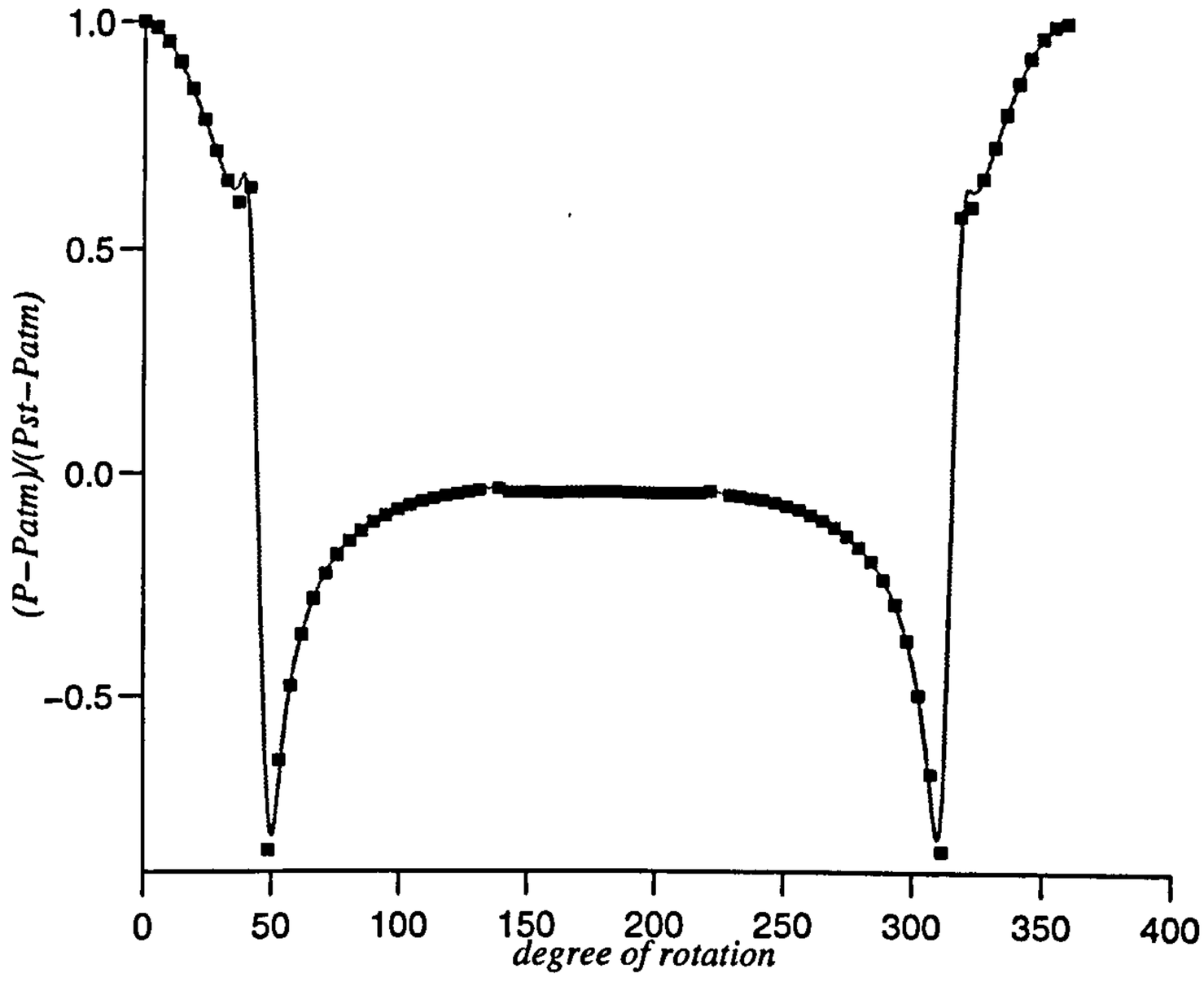

Fig.(9-13): Variation of pressure coefficient on cylinder surface for h/D=3.5 and e/D=3.5.

9-2-2: Offset conditions

Different offsets between horizontal planes passing through the centre of the slot and the centre of the cylinder is created by lowering the slot position and keeping constant spacing between the cylinder and slot.

Four different offsets of e/D=0.039, 0.0786, 0.196 and 0.393 were created. Velocity profiles obtained for these four cases are represented in figs.(9-14)-(9-17), and show that in all cases by applying an offset, velocity behind the cylinder increases on the lower side of the cylinder and decreases on the upper side. The increase of the velocity on the lower side is about 10%, 19%, 39% and 54% respectively with respect to the non-offset case. The same measurement for the upper side shows that the velocity decreases on this side by about 10%, 20%, 44% and 67% respectively from the non-offset case.

Considering the normal position of the peak velocity behind the lower side of the cylinder with respect to the cylinder horizontal centre line shows that by increasing the offset, the distance between peak velocity and cylinder centre line decreases, table(9-2) and as a result of it the flow shows more tendency to adhere to the cylinder surface due to the Coanda effect.

Table(9-2): Positions of peak velocity behind lower side of cylinder from cylinder centre line by changing offset and for x´/D=0.31

e/D	0.0	0.039	0.0786	0.196	0.393
y_2 /D	1.513	1.48	1.41	1.31	1.22

For the velocity profile behind the upper side of the cylinder, by increasing the offset, there is only a slight rise in the distance of peak velocity from the cylinder horizontal centre line and it changes from y_2 /D=6.4 for e/D=0, to y_2 /D=6.5 for

e/D=0.393, for constant horizontal distance of x´/D=0.31. By increasing the horizontal distance behind the cylinder, this difference will increase slightly, for example for x´/D=1.1, y/D changes from 6.67 for e/D=0 to 6.87 for e/D=0.393. So for the offset cases the Coanda effect will be effective only on the offset side with respect to the cylinder centre line.

Considering the velocity profiles behind the cylinder and at different distances from cylinder rear end x´/D, shows that the position of peak velocity behind the lower side of the cylinder with respect to the horizontal centre line of the cylinder, y_2/D, increases with increasing x´/D, and finally reaches a nearly constant value with a slight decrease towards the cylinder centre line. For example for the case of e/D=0.393, fig.(9-17), its variation is tabulated in table(9-3).

Table(9-3): Variation of peak velocity position behind the lower side of the cylinder at different horizontal distances and for e/D=0.393

x´/D	0.31	1.1	1.88	2.67	3.47	4.25
y_2/D	1.22	1.27	1.4	1.52	1.59	1.56

It should be noted that increasing the offset in the lower side of the cylinder causes the peak velocity on the upper side of the cylinder to decrease rapidly and disappear at a certain horizontal distance from the rear end of cylinder.

The variation of pressure coefficient on the cylinder surface, fig.(9-18), shows that by increasing the offset, on the upper semi-cylinder, the minimum pressure coefficient increases while on the lower semi - cylinder its value decreases, but the positions of minimum pressure coefficient on both semi-cylinders remain nearly unchanged with respect to the non-offset case. These positions give a rough estimation of the angular positions of maximum shear stress on the cylinder surface.

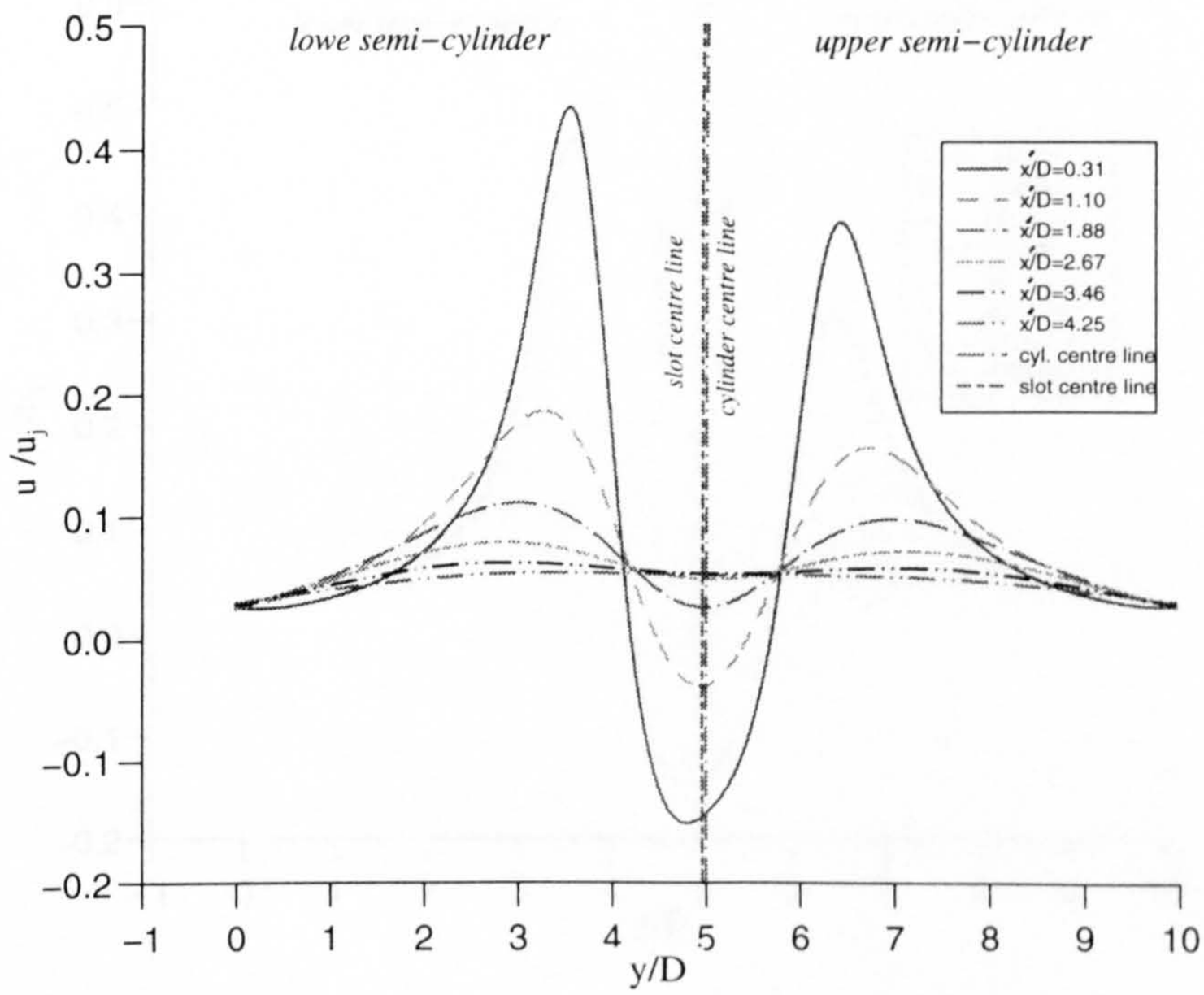

Fig.(9-14): Axial velocity profiles behind the cylinder at different distances from cylinder for h/D=1.81 and e/D=0.039.

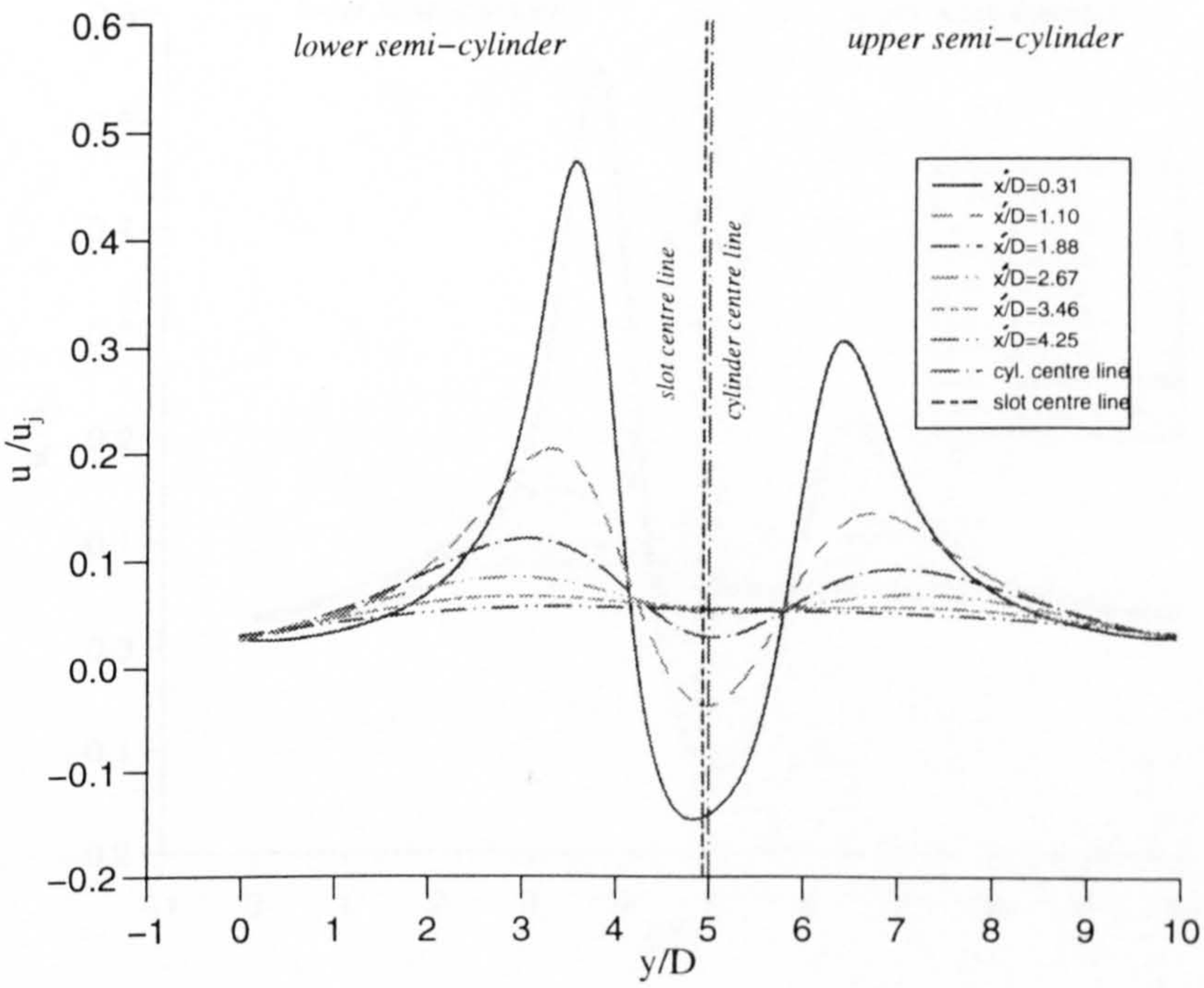

Fig.(9-15): Axial velocity profiles behind the cylinder at different distances from cylinder for h/D=1.81 and e/D=0.0786.

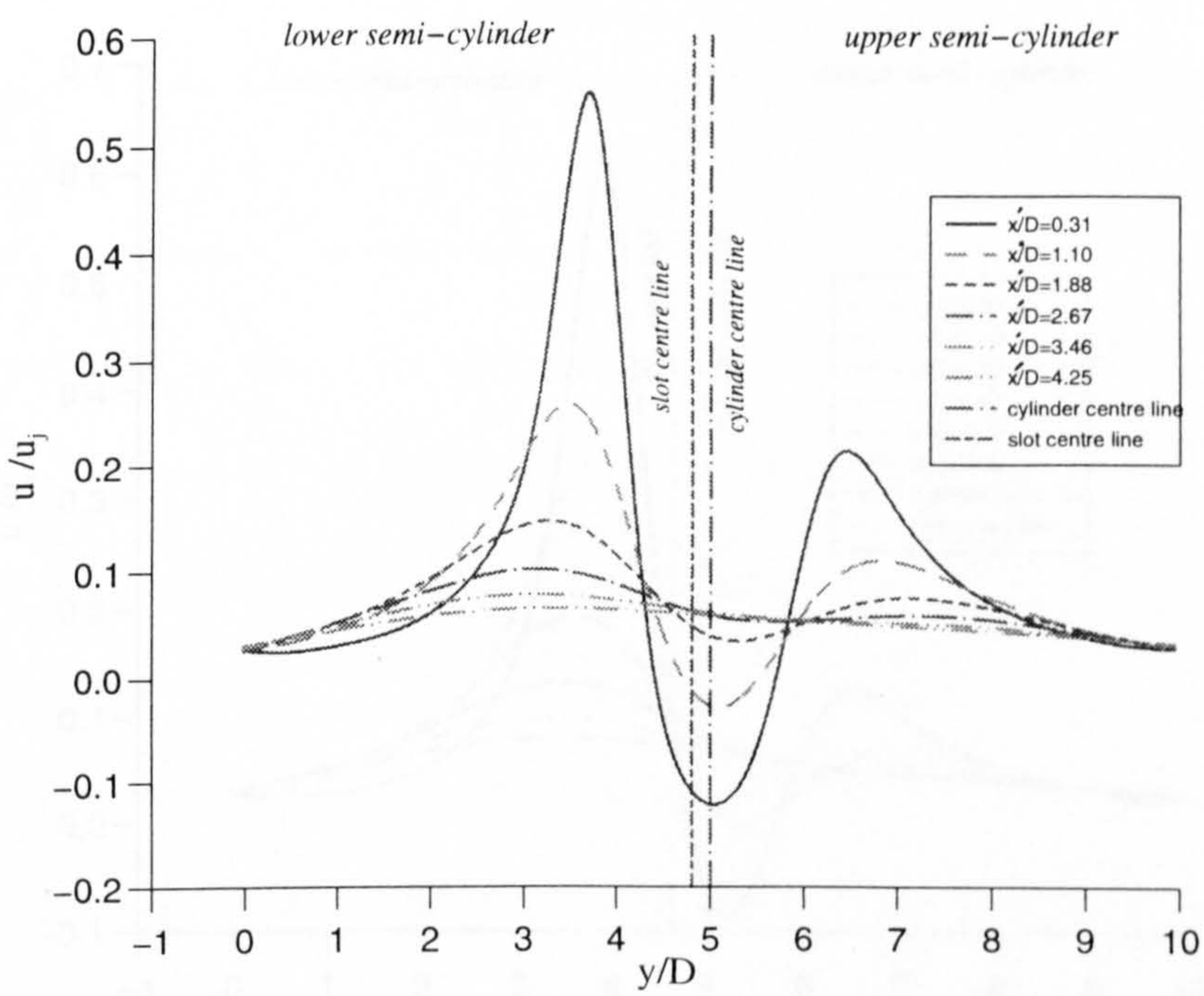

Fig.(9-16): Axial velocity profiles behind the cylinder at different distances from cylinder for h/D=1.81 and e/D=0.196.

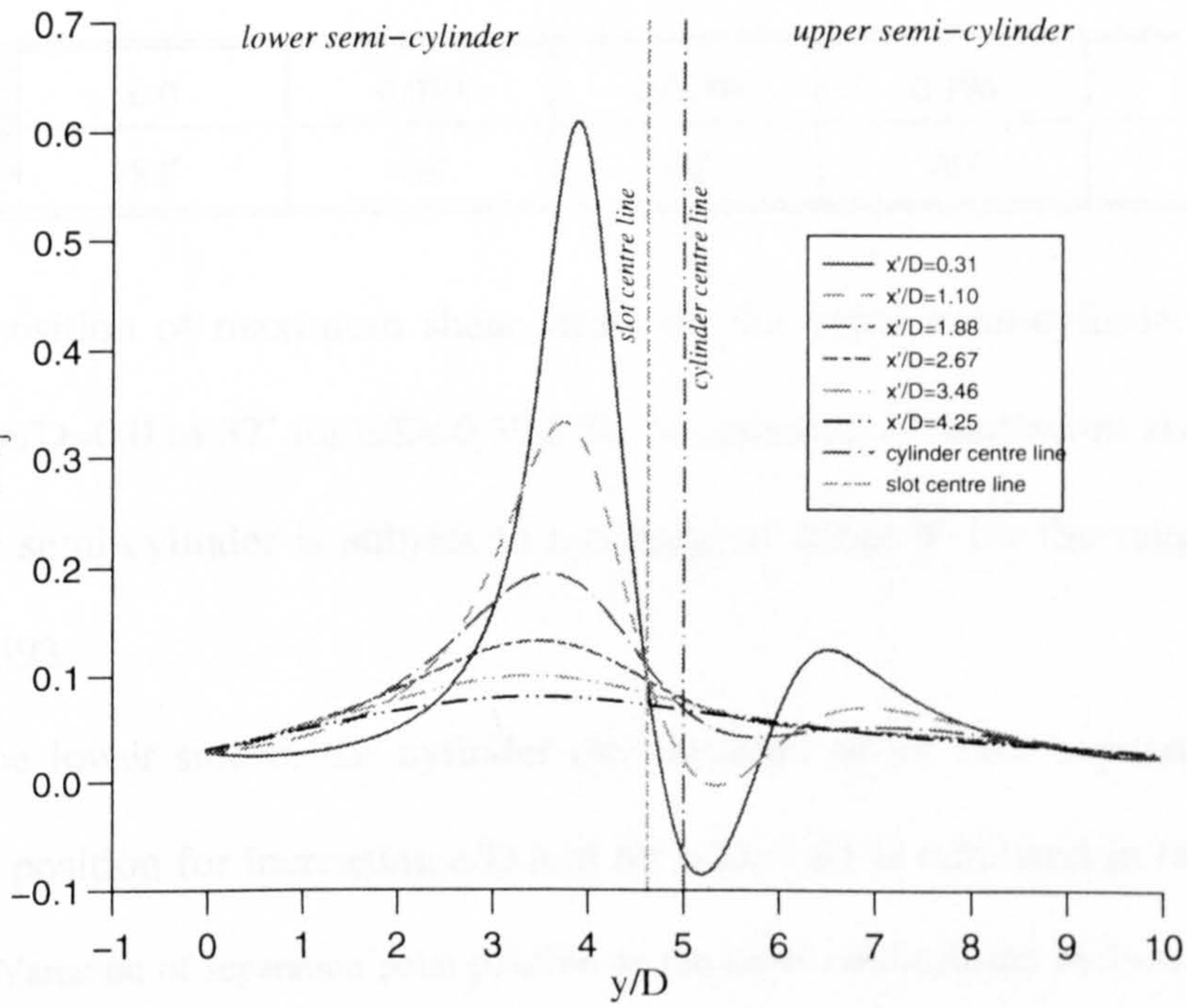

Fig.(9-17): Axial velocity profiles behind the cylinder at different distances from cylinder for h/D=1.81 and e/D=0.393.

The variation of shear stress coefficient with respect to angular position on cylinder surface and for different values of offsets are shown in fig.(9-19) for h/D=1.81. Again by considering the shear stress vanishing point on each semi-cylinder to be the approximate position of the separation points, referring to fig.(9-19), on the upper semi-cylinder, the position of separation point changes according to table (9- 4).

Table(9-4): Variation of separation point position on the upper semi-cylinder by increasing the offset.

e/D	0.0	0.039	0.0786	0.196	0.393
θ_{s1}	83°	76°	69°	60°	56°

The position of maximum shear stress on the upper semi-cylinder changes from 46° for e/D=0.0 to 37° for e/D=0.393. So the position of maximum shear stress on the upper semi-cylinder is subject to a change of about 9° for the range of e/D from 0 to 0.393.

On the lower side of the cylinder the variation of jet flow separation point with angular position for increasing e/D and for h/D=1.81 is tabulated in table (9-5).

Table(9-5): Variation of separation point position on the lower semi-cylinder by increasing the offset.

e/D	0.0	0.039	0.0786	0.196	0.393
θ_{S2}	276	285	275	245	204

Considering tables (9-4) and (9-5) shows that by increasing the offset on the lower semi-cylinder (offset side) the flow adheres to the cylinder surface due to the Coanda effect and the separation point moves towards the rear stagnation point,

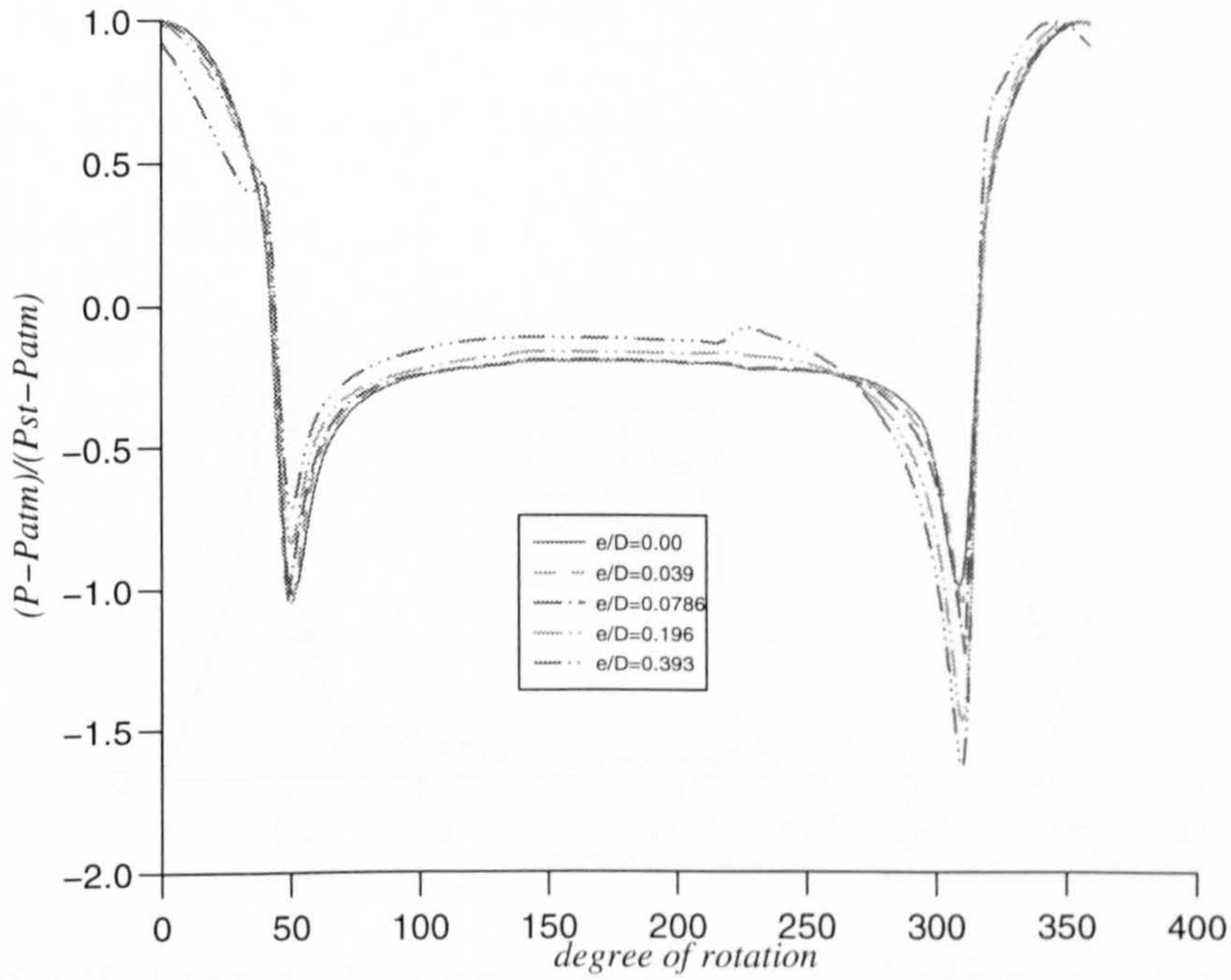

Fig.(9-18): Variation of pressure coefficient on cylinder surface for different offsets.

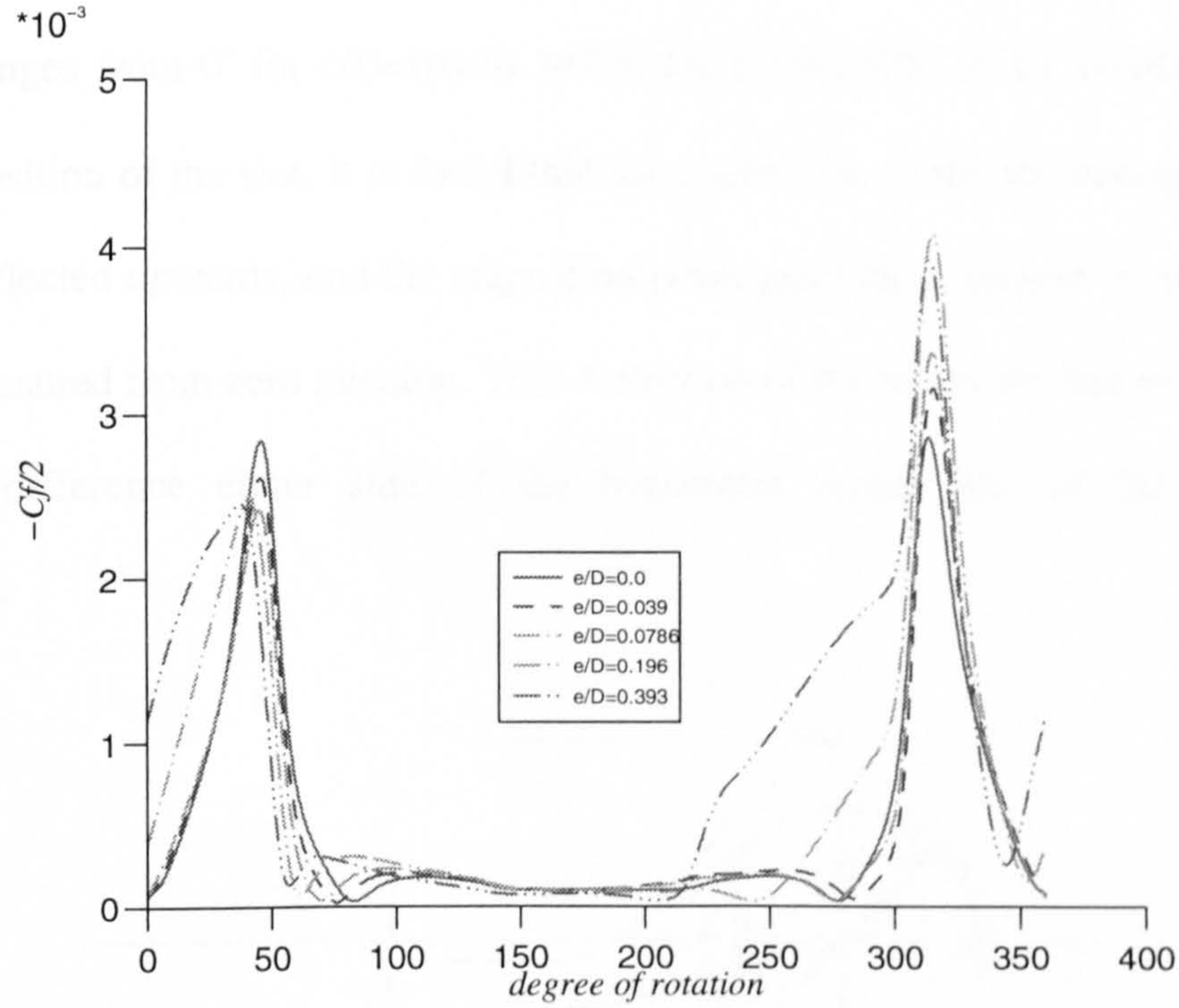

Fig.(9-19): Variation of shear stress coefficient on cylinder surface for different offsets.

but on the upper semi cylinder the flow separates from the cylinder surface at lower angular positions.

An inspection of the variation of stress coefficient on the lower semi-cylinder shows that in spite of appreciable increase in shear stress coefficient, by increasing the offset, the angular position of maximum shear stress coefficient remains nearly constant and at the same value of the non-offset case.

Variations of shear stress coefficient shows that the position of stagnation point changes from 0° for e/D=0.0 to 344.5° for e/D=0.393. So by considering the central position of the slot, it is found that the centre line of the jet issuing from the slot is deflected upwards, and the stagnation point position is subject to an angle of -15.5° measured from zero position. This deflection of the jet centre line is due to the pressure difference either side of the horizontal centre line of the cylinder, fig.(9-20).

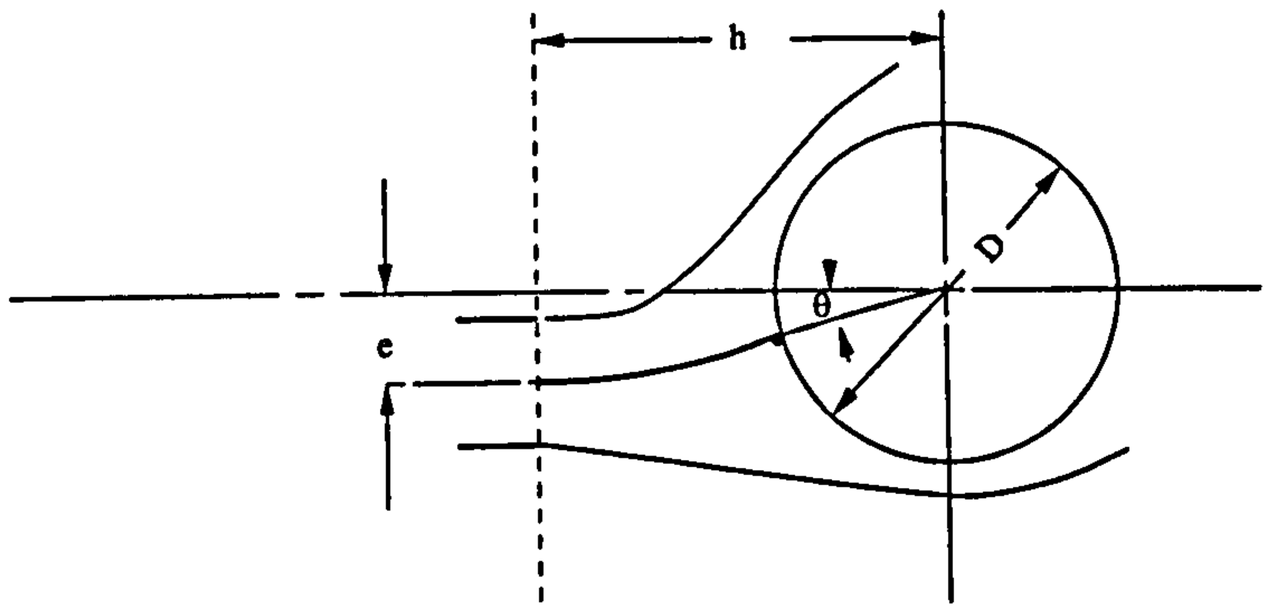

Fig.(9-20): Schematic sketch of jet centre line deflection.

On the upper semi-cylinder the area affected by shear stress for e/D=0.0 extends from θ=0° to θ=83° so the total affected area is contained by $\Delta\theta_1$=83°. Due to the effect of the offset, this area reduces and for e/D=0.393 it extends from θ=0° to θ=57° and for this case the total area is contained within $\Delta\theta_2$=57°. For the lower

semi-cylinder, for e/D=0, the area affected by the shear stress extends from the angular position of 276° to 360° and the whole affected area is contained within $\Delta\theta_3$=84°. For an offset equal to e/D=0.393 the affected area is enclosed between θ_1=204° and θ_2=344° and subjected to $\Delta\theta_4$=139°, which shows that because of the offset, the area affected by the shear stresses increases on the lower semi-cylinder (offset side) and decreases on the upper semi-cylinder, fig.(9-21).

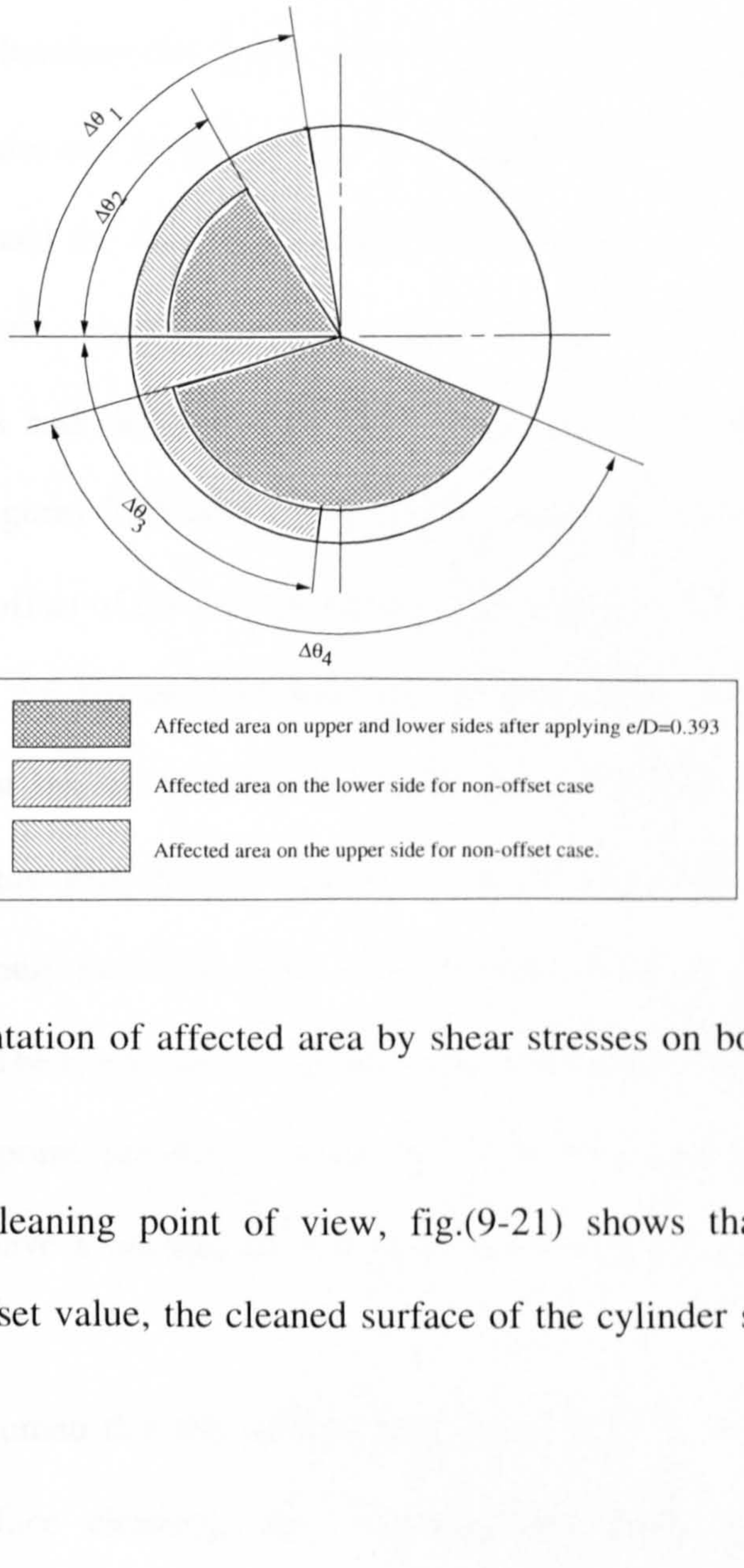

Fig.(9-21): Presentation of affected area by shear stresses on both side of cylinder.

From a cleaning point of view, fig.(9-21) shows that by applying and increasing the offset value, the cleaned surface of the cylinder should be greater on the offset side.

CHAPTER

10

DISCUSSION

The objective of the present study has been to investigate the interaction of a turbulent jet with a circular cylinder, with particular reference to clarifying the effect of spacing between the nozzle and the cylinder as well as the effect of offset between the cylinder and the jet axis on the pressure, shear stress distributions on the cylinder surface, and the flow field behind the cylinder.

Experimental measurements of the surface pressure distribution for axisymmetric jets and slot jets show that symmetry is maintained for non-offset conditions, c.f. figures 7, 8 and 37 of chapter eight and figures 6, 12 and 13 of chapter nine. An offset of the jet axis gives rise to minimum pressure on the opposite side to the offset, c.f. figures 9-13 and 45 of chapter eight and figure 18 of chapter nine. Of particular interest for both the offset and non-offset conditions is that the normalized pressure distributions appears to be independent of the jet Reynolds number, and are only functions of the spacing between the jet and cylinder and the offset condition. These pressure distributions give a broad indication of the position of the stagnation point, position of maximum shear stress and separation points. All these quantities have a bearing on the potential use of a jet as a surface cleaning device.

If it is assumed that the surface shear stress will be an important parameter in assessing surface cleaning, then a numerical model is required since the

measurement of surface shear stress is difficult. Thus the experimental studies have been more important as a means of validating the computer code as opposed to directly assessing cleaning.

Within the limits of the experimental methods available, four major points of comparison between a model and experiment can be made.

(i) Stagnation point position on the cylinder;

(ii) Position of maximum shear stress;

(iii) Position of separation points;

(iv) Velocity profiles downstream of the cylinder.

Although some data has been obtained for an axisymmetric jet, most of the work, both theoretical and experimental is centred on the interaction of a two dimensional jet with a circular cylinder.

For the non offset case, and under constant spacing conditions the pressure has its maximum value at the stagnation point. As the angular position (measured from the stagnation point) increases the pressure decreases and reaches a minimum value which may be interpreted as the angular position of the maximum shear stress, c.f. figures 6 and 7 of chapter nine. The decreasing of pressure and increasing of shear stress up to this position arises through the rapid acceleration of the flow. Downstream of the maximum position, the velocity decreases due to viscous dissipation and as a result of it the pressure increases and shear stress decreases. The angular position on cylinder surface where the shear stress is zero, specifies the position of separation point. From theoretical calculations the separation point is 83° which is much less than the experimental value of 170° obtained in the present study, fig.(8-37). The reason for the difference between experimental and theoretical

predictions of separation point position may be due to a number of factors. A major influence may be related to the turbulence level of about 4% on the jet centreline at nozzle exit for the experimental case. Evidence for this is shown in fig.(10-1) where turbulence measurements using the LDA system very close to the jet exit show marked increases in turbulence level specially those associated with the axial velocity.This turned out to be higher than comparable experiments of Tani and Kumatsu (1966) and Bradshaw and Love (1959) who typically recorded turbulence intensity of about 0.5%. Out of interest turbulence intensities at larger distances from the nozzle are shown in fig.(10-2), together with an indication of the jet boundary inferred from mean velocity measurements in fig.(8-29). In the centre of the jet maximum turbulence levels of about 4% have been recorded. The experiments also show that large velocity fluctuations near the edge of the jet are found. This is partly due to low values of $\bar{u}$ in this region but unsteadiness in the jet and the location of the jet exit in a plane surface may give rise to complex entrainment. In contrast, the experiments of Tsuchiya et al. (1993) who used an oil-film method to locate the separations, was found to be nearly 83° which compares very well with the present theory. This suggest that the Coanda effect was less pronounced in these experiments and may be due to the large jet diameter to cylinder diameter.

Equally important is the expected shortcoming of the k~ε method, Craft et al. (1993), which is known to be inadequate for predicting flow in regions of high shear layer close to the wall.

Further comparison of the theory and experiment can be made by observing the velocity distributions downstream of the cylinder. A major difference lies in the structure of the wake region immediately down stream of the cylinder. From the

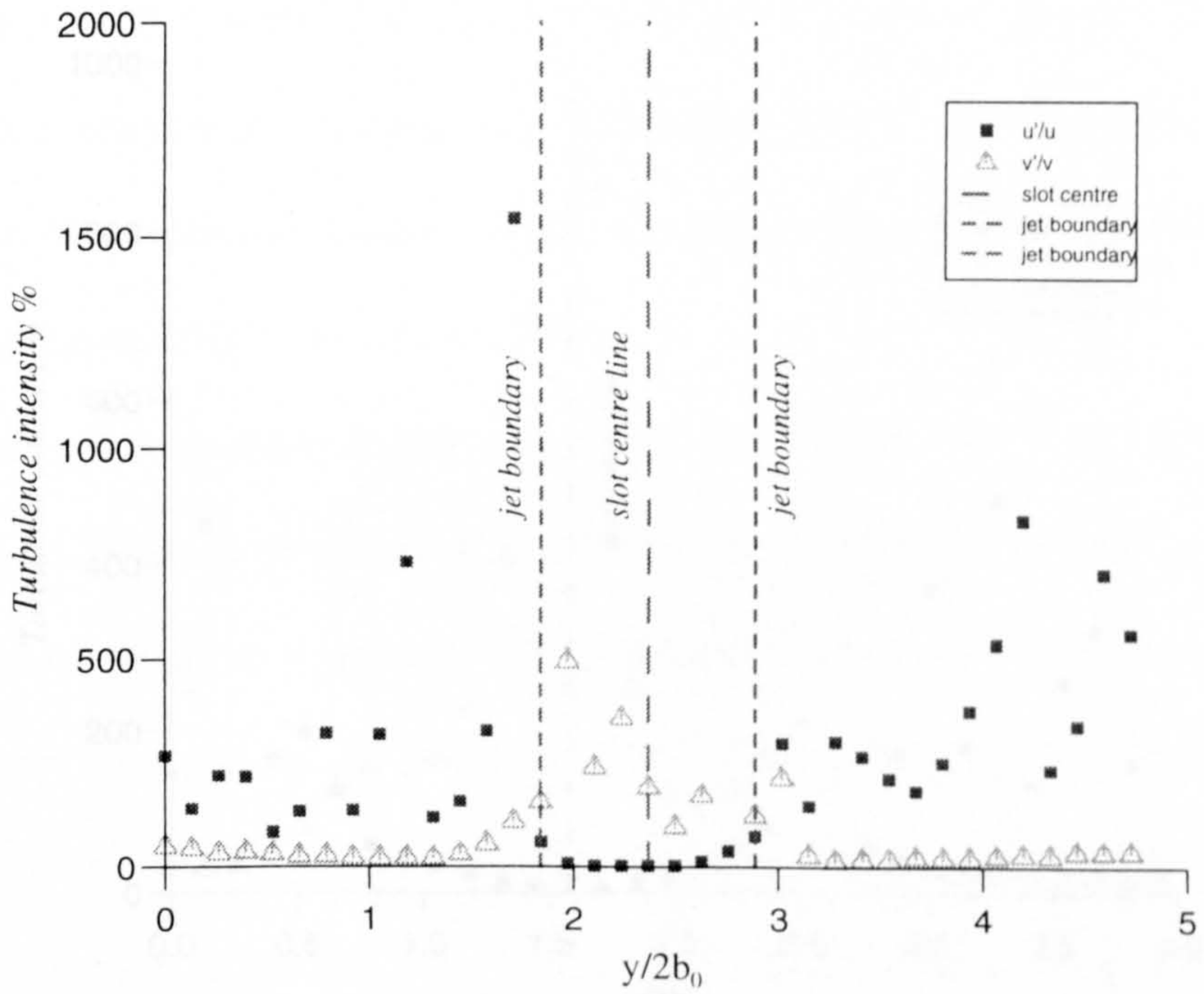

Fig.(10-1): Turbulence intensity profiles for free jet and for axial distance of $x/2b_0=0.79$.

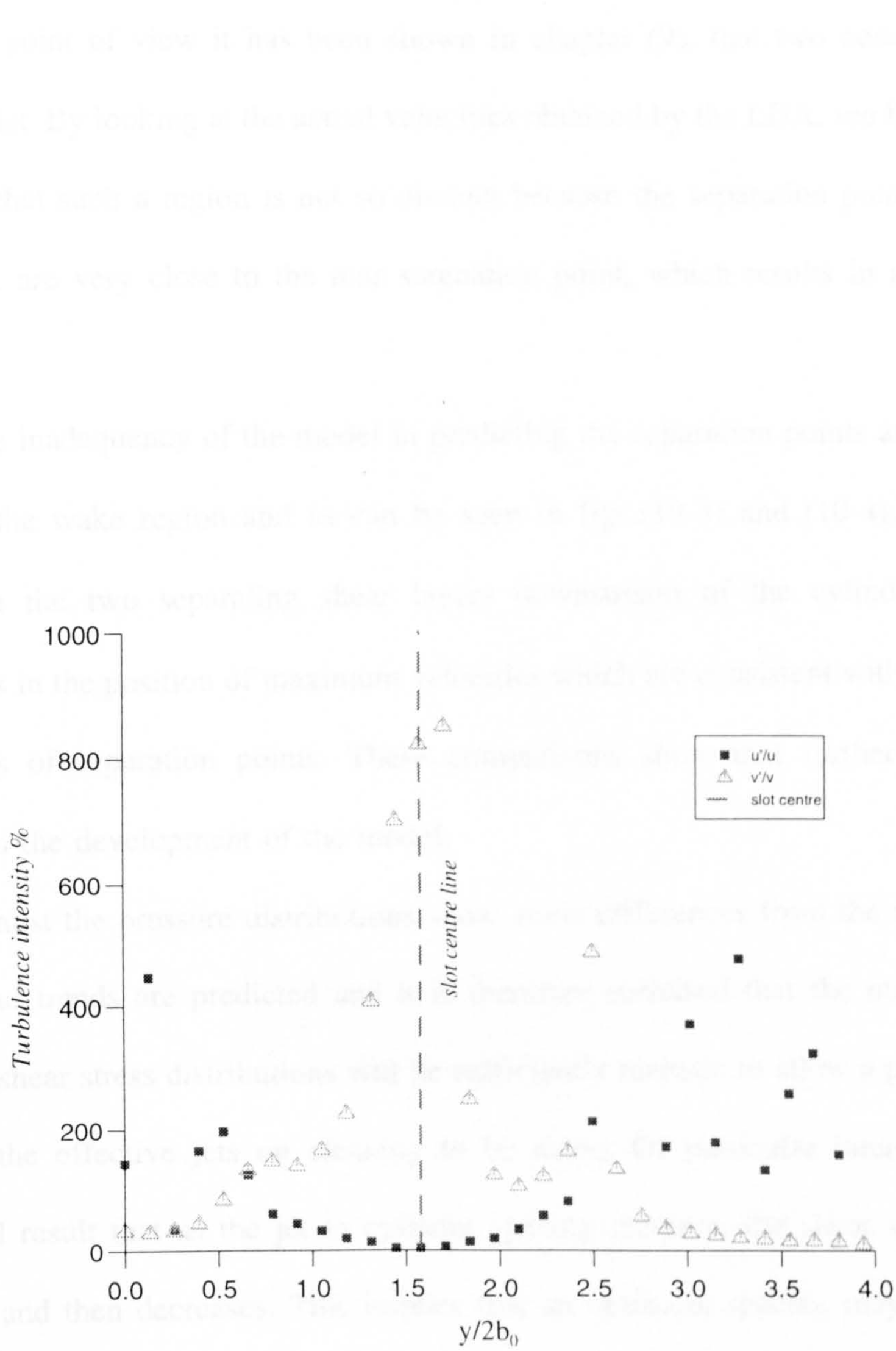

Fig.(10-2): Turbulent intensity profiles for free jet and for axial distance of $x/2b_0=2.6$.

theoretical point of view it has been shown in chapter (9), that two concentrated vortices exist. By looking at the actual velocities obtained by the LDA, see fig(8-35), it is clear that such a region is not so distinct because the separation points in the experiment are very close to the rear stagnation point, which results in a smaller region.

The inadequency of the model in predicting the separation points affects the whole of the wake region and as can be seen in figs.(10-3) and (10-4), velocity profiles in the two separating shear layers downstream of the cylinder, show differences in the position of maximum velocities which are consistent with the poor predictions of separation points. These comparisons show that further work is required in the development of the model.

Whilst the pressure distributions show some differences from the numerical work broad trends are predicted and it is therefore surmised that the numerically predicted shear stress distributions will be sufficiently realistic to allow a parametric study of the effective jets on cleaning to be made. Of particular interest is the theoretical result that as the jet to cylinder spacing increase, the shear stress first increases and then decreases. This implies that an optimum spacing may exist for maximum cleaning. The theoretical results also show that the separation points, located at the point where shear stress is zero, tends to move aft as the spacing between the jet and cylinder increases, table (9-1). This suggests that the Coanda effect becomes more effective at higher jet to cylinder spacing.

Applying an offset between the horizontal symmetrical lines of the cylinder and slot causes the front stagnation point to move away from the zero degree position (the position of the stagnation point for non-offset case). Its new position will be

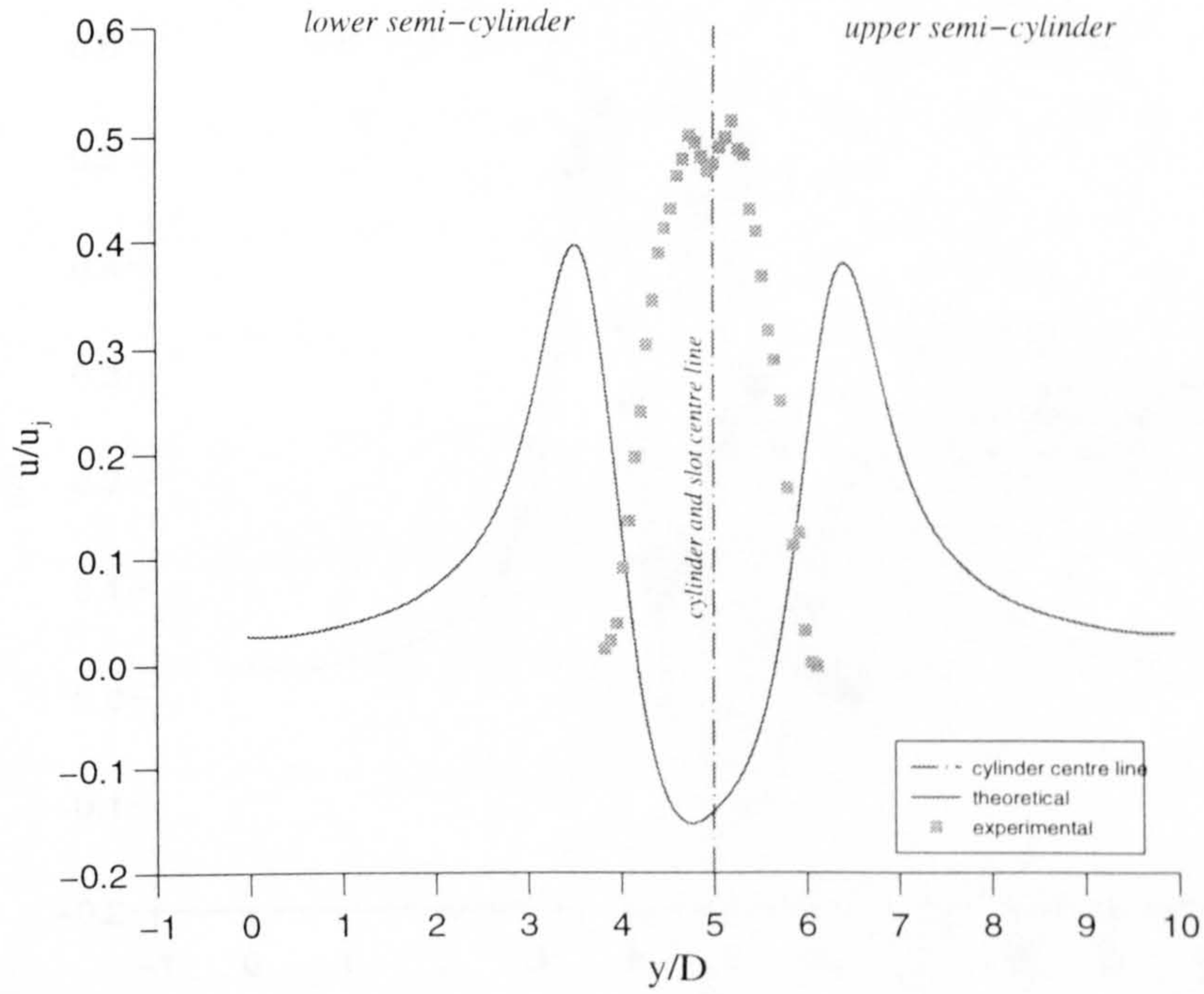

Fig.(10-3): Comparison between theoretical and experimental results for velocity profile behind the cylinder at x´/D=0.31, h/D=1.81 and e/D=0.0.

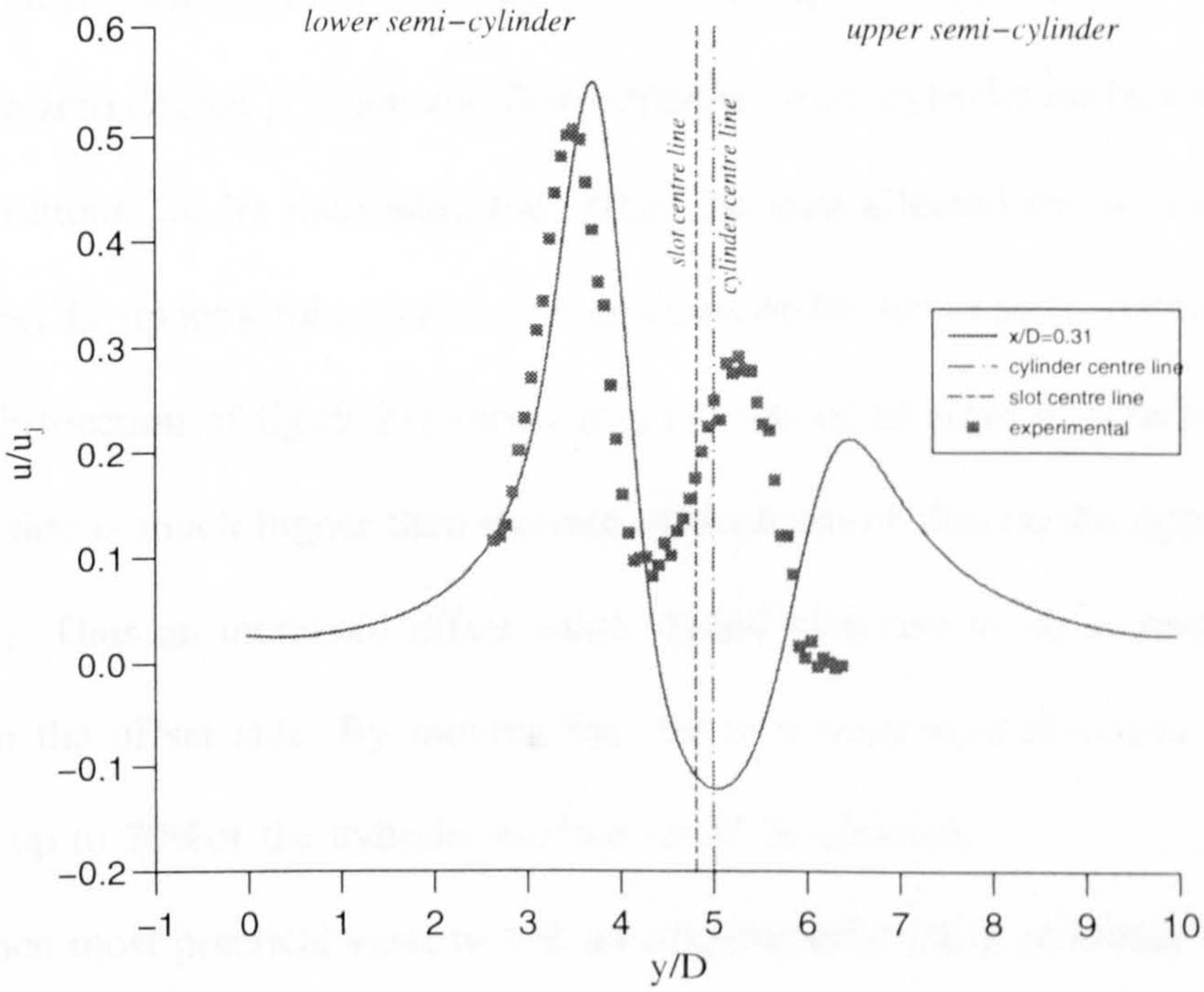

Fig.(10-4): Comparison between theoretical and experimental results for a velocity distribution behind the cylinder at x´/D=0.31, h/D=1.81 and e/D≈0.2.

somewhere between zero and the intersection point of the geometrical symmetry axis of the jet with the cylinder. This deflection of the jet centreline is due to the pressure difference either side of the horizontal centreline of the cylinder, fig.(9-20). Figure (10-5) shows the variation of the stagnation point position as a function of e/D, and for this point of comparison the model is quite good.

By increasing the offset, the separation point position on the offset side of the cylinder surface moves towards the rear stagnation point due to the Coanda effect. On the opposite side by increasing the offset, the separation point position moves towards the zero degree position and flow separates from cylinder surface at smaller angular positions. So by increasing the offset, the area affected by the shear stress decreases on the upper semi-cylinder and increases on the lower semi-cylinder (offset side). An inspection of fig.(9-21) shows that the rate of increase of affected area at the offset side is much higher than the rate of decrease of that on the opposite side of cylinder. Thus an increased offset value should give rise to an increase in area cleaned on the offset side. By moving the slot in a transverse direction to the jet centreline up to 70%of the cylinder surface could be cleaned.

Since most practical systems use an axisymmetric jet, it is useful to make a comparison of the slot jet and axisymmetric jet cases in order to judge the value of two dimensional calculations to predict the cleaning. A comparison of the pressure distribution for a round jet and a slot jet impacting on a cylinder, fig.(10-6), at the same spacing shows that for the case of the round jet, flow separates earlier than the slot jet. This is due to side losses in the longitudinal direction of the cylinder of an axisymmetric jet. The slot jet can transfer more momentum in the circumferential direction of the cylinder than can a round jet. As the main aim of this study is related

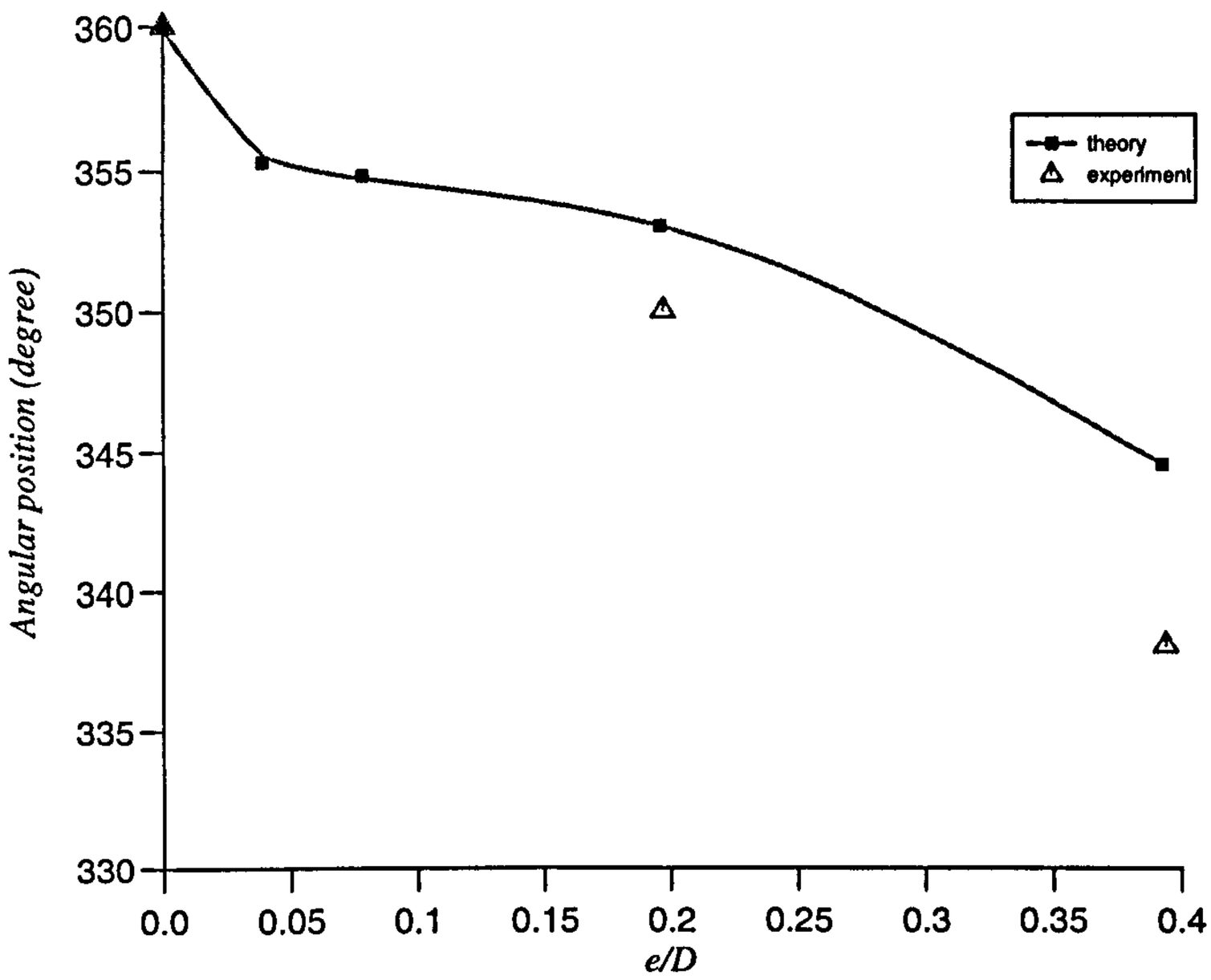

Fig(10-5): Variation of the stagnation point position as a function of e/D

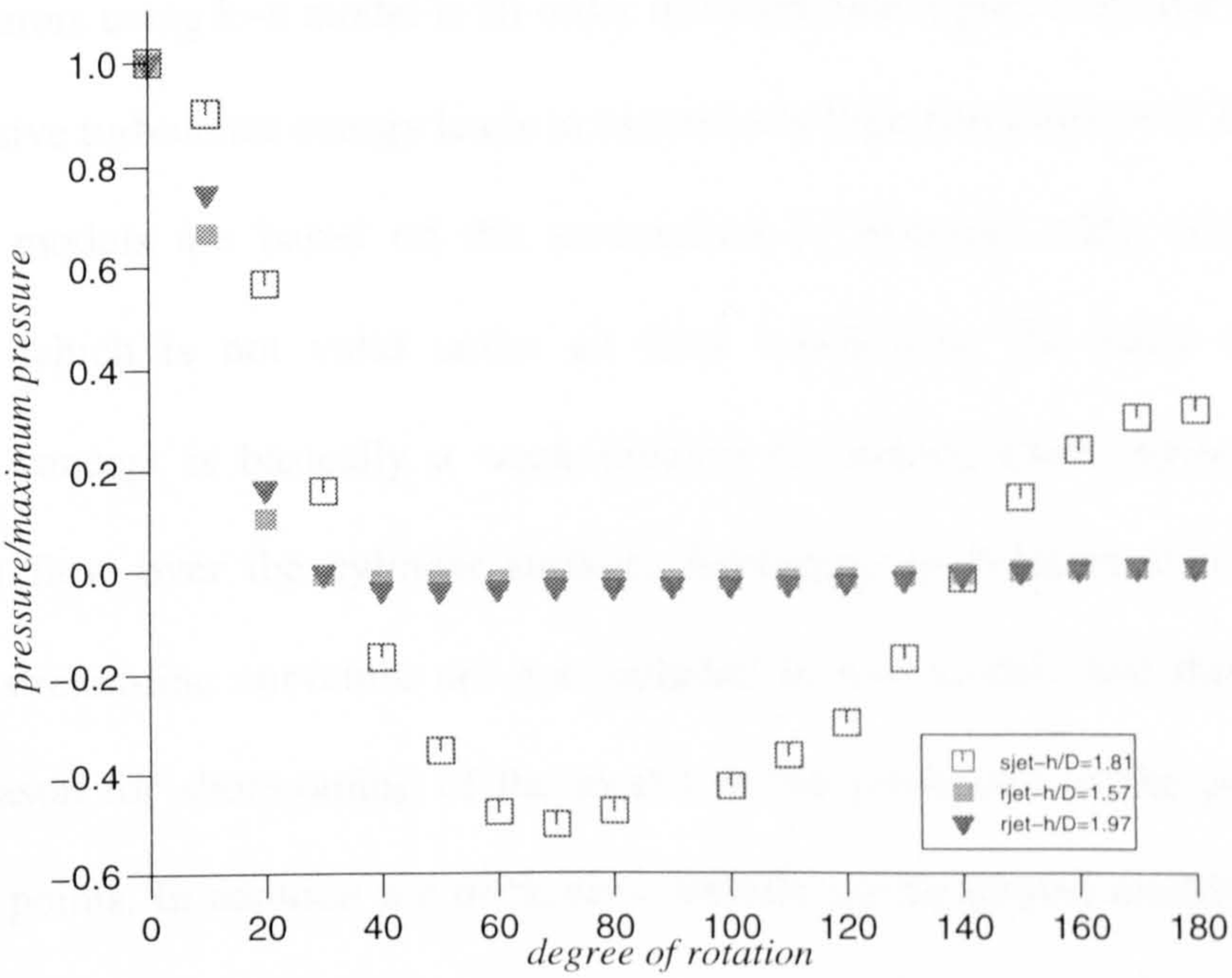

Fig.(10-6): A comparison between round jet and slot jet interaction onto a circular cylinder referring to pressure distribution on the cylinder

to the cleaning of cylindrical tubes, the above observation suggests that at the same conditions a slot jet will be more efficient than a round jet.

As discussed already much of the disagreement between experiment and theory appears to be associated with the failure of the high Reynolds version of k~ε model to predict the separation points. This in turn alters the velocity profiles downstream of the cylinder. According to Cooper et al. (1993), for jet impingement problems, the level of turbulence energy (k) near the stagnation point computed by six contributors using k~ε model is an order of magnitude higher than that measured. This excessive turbulence energy leads to excessively high entrainment of free stream fluid. k~ε models are based on the assumption of isotropic eddy viscosity and diffusivity which is not valid under all flow conditions. The eddy viscosity / diffusivity concept is basically a weak relation for impingement regions and for subsequent flow over the cylinder surface. According to Polat et al. (1989), the effects of stream-line curvature are not included in k~ε models and this could be another reason for shortcoming of the model in the prediction of the positions of separation points. In addition the turbulence models are developed mainly for flows parallel to the wall and for the case of impingement flows the standard k~ε model is subject to a failure in the radial wall jet region which is related to abnormally high levels of length scale near a wall. Studies by Malin (1988) and Bradshaw (1973) suggest that these high levels of length scale are related to lateral divergence of flow in the radial case. Perhaps use of the low-Reynolds version of k~ε model in which the calculations can be carried out right to the wall, without the use of wall functions, can resolve some of the problems, but still some modifications will be required for using it over the curved surfaces.

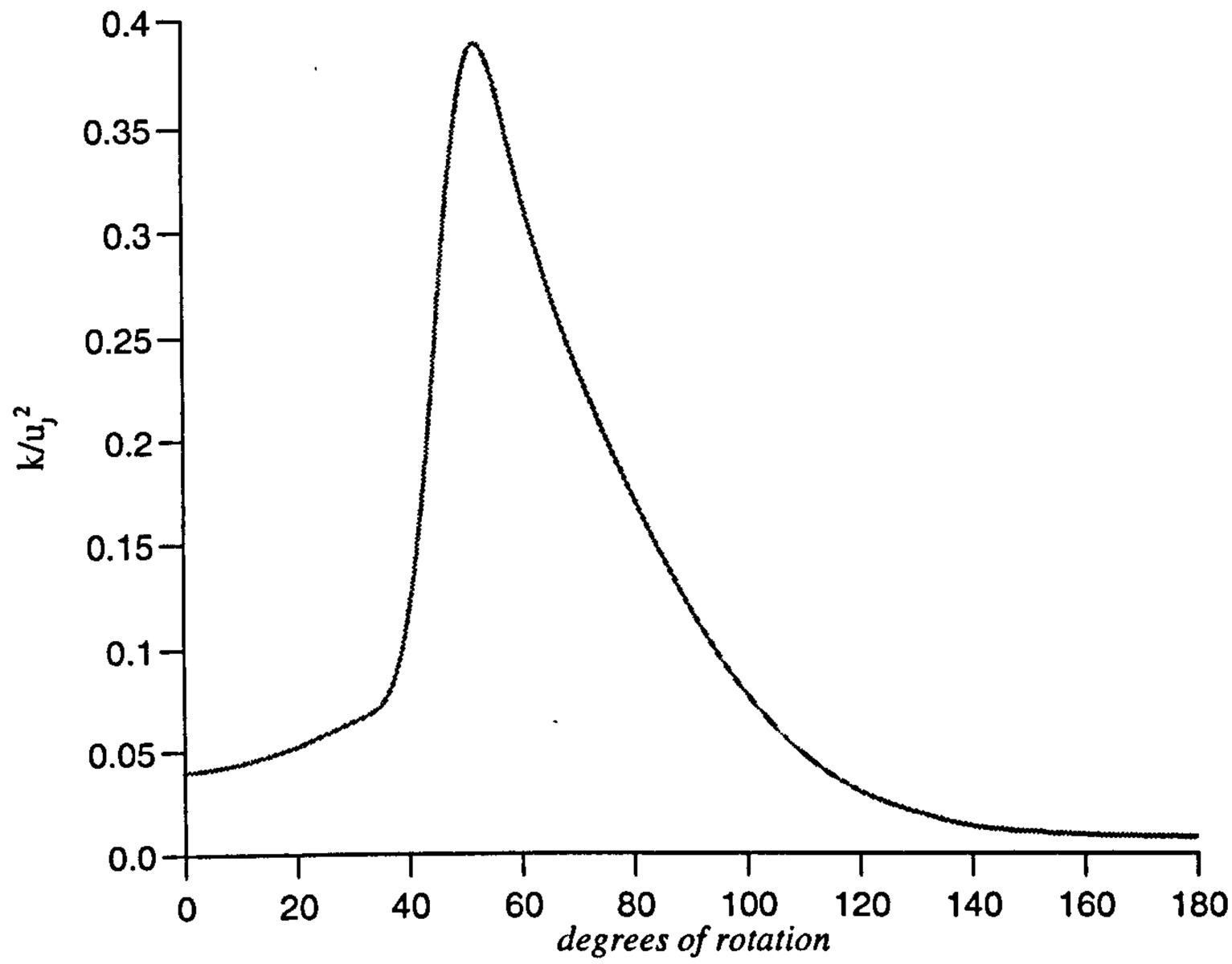

Fig.(10-7): Variation of turbulent kinetic energy on circular cylinder for h/D=1.81 and e/D=0.0

Finally, referring to the variation of turbulence energy (k) close to the cylinder surface, fig.(10-7), shows that there is a sharp increase in turbulence energy (k) from the 36° angular position to a maximum value at nearly 52°. It subsequently rapidly decrease and reaches to 10% of its maximum value at an angular position of 120°. Due to this sharp increase and rapid decrease of turbulence energy, the pressure coefficient changes more rapidly at the point of minimum pressure than observed in the experimental measurements.

In summary the present work has provided new experimental data relating to the pressure distribution and the velocity distribution in the wake region around the cylinder due to the impingement of round and slot jets for a range of offsets and spacings between the slot and the cylinder. This has been complemented by numerical simulation which has not been previously reported. Whilst some additional effort is required to improve the model it was felt that the data was of sufficient value to provide estimates of the surface area that could be cleaned by a jet.

CHAPTER

11

CONCLUSIONS - FUTURE RECOMMENDATIONS

By considering that the shear stress is the more probable controlling parameter of surface cleaning, the main conclusions of this study are:

1) Slot jets are more effective than round jets for cleaning purposes.

2) By increasing the spacing between cylinder and slot, the maximum shear stress on the cylinder surface increases slightly until a certain spacing (h/D=2.51). By further increasing the spacing the maximum shear stress decreases rapidly. This gives an optimum spacing between slot and cylinder for the cleaning of cylindrical tubes.

3) By applying the offset, on the offset side the area affected by shear stresses increased when the offset was increased, so from the cleaning point of view, more area will be cleaned on the offset side.

By considering that 80% of the area affected by shear stresses on the cylinder surface will be cleaned, moving the slot from e/D=+0.4 to e/D=-0.4 with respect to the cylinder centre line, causes 68% of the symmetrical surface of the cylinder to be cleaned ($\Delta\Theta=123^{\circ}$ on each side) and 32% of it remains fouled at the rear of the cylinder. This area can also be cleaned by giving an inclining the angle ($\pm 57^{\circ}$) of the slot after completion of the first period of cleaning.

Future recommendations:

1) Jet interaction with single cylinder:

1-1: For the case of slot jet interaction with a single cylinder, the effect of a

horizontal flat plate at different normal distances from the top and bottom of the cylinder could be investigated.

1-2: Numerical solution of a round jet interacting with a cylindrical surface should include 3D effects.

2) Jet interaction with matrix of tubes:

2-1: Interaction of a slot jet with two successive horizontally placed cylindrical tubes considering the effect of the gap between cylinders on the flow field.

2-2: Interaction of a slot jet with two horizontal cylinder with the same spacing from the slot and considering the effect of the normal gap between cylinders on the flow field.

2-3: Interaction of slot jet with a matrix of tubes.

3) Modelling:

Accurate modifications of the k~ε turbulence models for the impingement region and the wall jet case on cylindrical surfaces, to obtain closer agreement between numerical calculations and experiment are required.

* * *

In summary the results of this work provide a basic part in the understanding of the cleaning of cylindrical tubes in heat exchangers by the interaction of a high speed compressible turbulent air jet, and can be used as a basis for, or in support of future works.

REFERENCES

ABRAMOVICH, G.N. ; "The Theory of Turbulent Jets" M. I. T. Press. Cambridge, Massachusetts, 1963.

AGRAWAL, R.K. and BOWER, W.W. ; "Navier- Stokes Computations of Turbulent Compressible Two-Dimensional Impinging Jet Flow Fields", AIAA, J., vol. 20, no. 5, p. 577, 1982.

ALBERTSON, M.L. , DAI, Y.B. , JENSEN, R.A. and ROUSE, H. ; "Diffusion of Submerged Jets", ASCE Trans., vol. 115, p. 639, 1950.

AMANO, R.S. ; "Turbulence Effect on the Impinging Jet on a Flat Plate", Bulletin of the JSME, vol. 26, no. 221, p. 1891, 1983.

AMANO, R. S. and BRANDT, H. ; "Numerical Study of Turbulent Axisymmetric Jets Impinging on a Flat Plate and Flowing into an Axisymmetric Cavity", Trans. ASME, J. of Fluid Eng., vol. 106, p. 410, 1984.

AMANO, R.S. and JENSEN, M.K. ; "Turbulent Heat Transfer of Impinging Jet on a Flat Plate", ASME paper, NO. 82-WA/HT-55, 1982.

AMANO, R.S. and SUGIYAMA, S. ; "An Investigation on Turbulent Heat Transfer of an Axisymmetric Jet Impinging on a Flat Plate", Bulletin of JSME, vol. 28, no. 235, p. 74, 1985.

BAKKE, P. ; "An Experimental Investigation of a Wall Jet", J. Fluid Mech., vol. 2, Pt. 5, p. 467, 1957.

BELTAOS, S. and RAJARATNAM, N. ; "Plane Turbulent Impinging Jets", J.of Hydraulic Research, vol. 11, no. 1, p. 29, 1973.

BIRCH, N.S. ; "Jet Interaction with Heat Exchangers", Ph.D. Thesis, University of Liverpool, 1992.

BRADBURY, L. J. S. ; "The Structure of Self-Preserving Turbulent Plane Jet", J. Fluid Mech. vol. 23, p. 31, 1965.

BRADSHAW, P. ; "Effects of Streamline Curvature on Turbulent Flow" AGARDograph, no. 169, 1973.

BRADSHAW, P. and LOVE, E.M. ; "The Normal Impingement of a Circular Air Jet on a Flat Surface" ARCR. and M., no. 3205, 1959.

BRAHMA, R.K., FARUQUE, O. and ARORA, R.C. ; "Experimental Investigation of Mean Flow Characteristics of Slot Jet Impingement on a Cylinder", Wärme-und Stoffübertragung, vol. 26, p. 257, 1991.

BROWN, T.D. ; " The Deposition of Sodium Sulphate from Combustion Gases", J. Inst. Fuel , vol. 39, p. 378, 1966.

CHENOWETH, J. M. ; " Final Report of the HTRI/TEMA Joint Committee to Review the Fouling Section of the TEMA Standards", J. of ASME, Heat Transfer Engineering, vol. 11, no. 1, p. 73, 1990.

CHIENG, C.C. and LAUNDER, B.E. ; "On the Calculation of Turbulent Heat Transport Downstream from an Abrupt Pipe Expansion", Numerical Heat Transfer, vol. 3, p. 189, 1980.

CHIOU, C.C. and LEE, S.L. ; "Forced Convection on a Rotating Cylinder with an

Incident Air Jet", Int. J. Heat Mass Transfer, vol. 36, no. 15, p. 3840, 1993.

COOPER, D., JACKSON, D.C., LAUNDER, B.E. and LIAO, G.X. ; "Impinging Jet Studies for Turbulent Model Assessment-1. Flow Field Experiments", Int. J. Heat Mass Transfer vol. 36, p. 2675, 1993.

CRAFT, T.J. , GRAHAM, L.J. and LAUNDER, B.E. ; "Impinging Jet Studies for Turbulence Model Assessment-2. An Examination of the Performance of Four Turbulence Models", Int. J. Heat Mass Transfer, vol 36, no. 10, p. 2685, 1993.

Di CARLO, J.T. ; "Guidelines Aid in Application, Operation of Soot Blowers", Oil and Gas J., vol. 77, no. 19, p. 88, 1972.

DONALDSON, C.D. and SNEDEKER, R.S. ; "A Study of Free Jet Impingement. Part 1. Mean Properties of Free and Impinging Jets", J.Fluid Mech., vol. 45, Pt.2, p. 281, 1971.

ECKERT, E.R.G. and DRAKE, R.M.(Jr.), ; "Heat and Mass Transfer", 2nd ed., Mc Graw-Hill , New York, 1959.

EMMONS, H.W. ; "Shear Flow Turbulence", Proc. 2nd. U. S. National Congress App. Mech. ASME, 1954.

EPSTEIN, N. ; "Fouling in Heat Exchangers", Heat Transfer, vol. 6, p. 235 , Hemisphere, New York, 1978.

EPSTEIN, N. ; "Fouling: Technical Aspects (Afterword to Fouling in Heat Exchangers)", in Fouling of Heat Transfer Equipment, ed. E. F. C. Somerscales and J. G. Knudsen, p 31, Hemisphere, Washington, 1981.

FÖRTHMANN, E. ; "Turbulent Jet Expansion", NACA TM 789, 1936. (see Abramovich [1]).

GARDON, R. and AKFIRAT,J.C. ; "The Role of Turbulence in Determining the

Heat Transfer Characteristics of Impinging Jets", Int. J. Heat Mass Transfer, vol. 8, p. 1261, 1965.

GAUNTNER, J.W. and LIVINGOOD, N.B. ; "Survey of Literature on Flow Characteristics of a Single Turbulent Jet", Rep.ASA TN D-5652, 1970.

GARETTO, L.S. , GOSMAN, A.D. , PATANKAR, S.V. and SPALDING, D.B. ; "Two Calculation Procedures for Steady Three Dimensional Flows with Recirculation", Proc. 3rd. Int. Conf. Num. Methods Fluid Dyn., vol. 11, p. 60, 1972.

GIBSON, M.M. and SPALDING, D.B. ; " A Two-Equation Model of Turbulence Applied to the Prediction of Heat Transfer in Wall Boundary Layer", ASME Paper 72/HT/15, 1972.

GLAUERT, M.B. ; "The Wall Jet", J. Fluid Mech. , vol. 1, Pt. 6, p. 625, 1956.

GOERTLER, H. ; see Gauntner et. al. [36].

GOLDSTEIN, R.J. and FRANCHETT, M.E. ; "Heat Transfer from a Flat Surface to an Oblique Impinging Jet", ASME, J. Heat Transfer, no. 110, p. 84, 1988.

GUO, C.Y. and MAXWELL, W.H.C. ; "Numerical Modeling of Normal Turbulent Plane Jet Impingement on a Solid Wall", J. Eng. Mech., vol. 110, no. 10, p. 1498, 1984.

GUTMARK, E., WOLFSHTEIN, M., and WYGNANSKI, I. ; "The Plane Turbulent Impinging Jet", J. Fluid Mech., vol. 88, Pt. 4, p. 737, 1978.

HANJALIC, K. ; "Two Dimensional Asymmetrical Turbulent Flow in Ducts", Ph.D. Thesis, University of London, 1970.

HANJALIC, K. and LAUNDER, B.E. ; "A Reynolds Stress Model of Turbulence and its Application to Asymmetric Shear Flows", J.Fluid Mech., vol. 52, p. 609,

1972.

HARLOW, F.H. and NAKAYAMA, P.I. ; "Transport of Turbulence Energy Decay Rate" Los Alamos, Sci. Lab. Rep., LA 3854, 1968.

HASSAN, D. ; "Heat Exchanger Fouling", Chem. Eng. Res. Group, Council for Sci. and Ind. Res., CSIR Report, CENF 339, 1980.

HUANG, G.P. , MUJUMDAR, A.S. and DOUGLAS, J.M. ; "Numerical Prediction of Fluid Flow and Heat Transfer Under a Turbulent Impinging Slot Jet with Surface Motion and Cross Flow", ASME Paper #84-WA/HT-33, 1984.

HUANG, G.P. , MUJUMDAR, A.S. and DOUGLAS, W.J.M. ; "Prediction of Heat Transfer Under a Plane Turbulent Impinging Jet Including Effects of Cross Flow and Wall Motion", Drying, ed. A. S. Mujumdar, Hemisphere, 1982.

JAMBUNATHAN, K. , LAI, E. , MOSS, M.A. and BUTTON, B.L. ; " A Review of Heat Transfer Data for Single Circular Jet Impingement", Int. J. Heat Fluid Flow, no. 13, p. 106, 1992.

JONES, W.P. and LAUNDER, B.E. ; "The Calculation of Low-Reynolds-Number Phenomena with a Two-Equation Model of Turbulence", Int. J. Heat Mass Transfer, vol. 16, p. 1119, 1973.

JONES, W.P. and LAUNDER, B.E. ; "The Prediction of Laminarization with a Two-Equation Model of Turbulence", Int. J. Heat Mass Transfer, vol. 15, p. 301, 1972.

KANG, S.H. and GREIF, R. ; "Flow and Heat Transfer to a Circular Cylinder with a Hot Impinging Air Jet", Int. J. Heat Mass Transfer, vol. 35, no. 9, p. 2173, 1992.

KOTANSKY, D.R. and BOWER, W.W. ; "A Basic Study of the VTOL Ground Effect Problem for Plannar Flow", J. Aircraft, vol. 15, no. 4, 1978.

KOTSOVINOS, N.E. ; "A Note on the Spreading Rate and Virtual Origin of a Plane Turbulent Jet", J. Fluid Mech., vol. 77, p. 305, 1976.

KUMADA, M. and MABUCHI, I. ; "Studies on the Heat Transfer of Impinging Jet (1st Report, Mass Transfer for Two-Dimensional Jet of Air Impinging Normally on a Flat Plate)", Bull. JSME, vol. 13, p. 77, 1970.

LAMPINEN, M.J. ; "Application of Turbulence Theory to the Determination of Heat Transfer Coefficients in an Aerofoil Dryer", Drying Technology, vol. 3, no. 2, p. 171, 1985.

LAUNDER, B.E. , MORSE, A. , RODI, W. and SPALDING, D.B. ;"The Prediction of Free Shear Flows - A Comparison of the Performance of Six Turbulence Models", Imperial College, Mechanical Engineering Department Report TM/TN/A/19, 1972.

LAUNDER, B.E. , REECE, G.J. and RODI, W. ; "Progress in the Development of a Reynolds-Stress Turbulence Closur", J. Fluid Mech., vol. 68, Pt. 3,p. 537, 1975.

LAUNDER, B.E. and SPALDING, D.B. ; "The Numerical Computation of Turbulent Flows", Computer methods in Applied Mechanics and Engineering, vol. 3, p. 269, 1974.

LJUBOJA, M. and RODI, W. ; "Calculation of Turbulent Wall Jets with an Algebraic Stress Model", Proc. Symp. on Turbulent Boundary Layers, Forced, Incompressible, non-reacting, ed. H.E.Weber, p. 131, 1979.

LOONEY, M.K. and WALSH, J.J. ; "Mean - Flow and Turbulent Characteristics of Free and Impinging Jet Flows", J. Fluid Mech., vol. 147, p. 397, 1984.

LOVE, E.S. , GRIGSBY, C.E. , LEE, L.P. and WOODLING, M.J. ; "Experimental and Theoretical studies of Axisymmetrical Free Jets", NASA TR/R-6,

1959.

MALIN, M.R. ; "Prediction of Radially Spreading Turbulent Jets", AIAA J., vol. 26, p. 750, 1988.

MARTIN, H. ; "Heat and Mass Transfer between Impinging Gas Jets and Solid Surfaces", Advances in Heat Transfer, vol. 13, 1977.

MARNER, W.J. and SUITOR, J.W. ; "A Survey of Gas Side Fouling in Industrial Heat Transfer Equipment", JPL Publications, Pasadena, Calif., 1983.

MATHEWS, L. and WHITELAW, J.H. ; "The Prediction of Film Cooling in the Presence of Recirculating Flows with a 2-Equation Model of Turbulence", Imperial College, Mechanical Engineering Department Report, EHT/TN/A/35, 1971.

Mc NAUGHTON, K.J. and SINCLAIR, C.G. ; " Submerged Jets in Short Cylindrical Flow Vessels", J. Fluid Mech., vol. 25, no. 2, p. 367, 1966.

NG, K.H. and SPALDING, D.B. ; "Predictions of Two Dimensional Boundary Layers on Smooth Walls with a 2-Equation Model of Turbulence", Imperial College, Mechanical Engineering Department Report, BL/TN/A/25, 1970.

NG, K.H. and SPALDING, D.B. ; "Some Applications of a Model of Turbulence to Boundary Layers Near Walls", Phys. Fluids, vol. 15, p. 20, 1972.

PAI, S. ; "Fluid Dynamics of Jets", D. van Nostrand Co., Inc., 1954.

PAMADI, B.N. ; "On The Impingement of Supersonic Jet on a Normal Flat surface", Aeronautical Quarterly, p. 199, 1981.

PATANKAR, S.V. and SPALDING, D.B. ; "A Calculation Procedure for Heat, Mass and Momentum Transfer in Three - Dimensional Parabolic Flows", Int. J. Heat Mass transfer, vol 15, p. 1787, 1972.

PATANKAR, S.V. ; "Numerical Heat Transfer and Fluid Flow", Mc Graw-Hill,

1980.

PATANKAR, S.V. and SPALDING, D.B. ; "Heat and Mass Transfer in Boundary Layers", 2nd. edition, Intertext books, London, 1970.

POLAT, S., HUANG, B. , MUJUMDAR, A.S. and DOUGLAS, W.J.M. ; "Numerical Flow and Heat Transfer Under Impinging Jets : A Review", Annual Review of Numerical Fluid Mechanics and Heat Transfer, edited by Tien, C.L. and Chawla, T.C., Chapter 4, Hemisphere Publishing Co. 1989.

POLAT, S., MUJUMDAR, A.S. and DOUGLAS, W.J.M. ; "Heat Transfer Distribution under a Turbulent Impinging Jet - A Numerical Study", Drying Technology, vol. 3, no. 1, p. 15, 1985.

POREH, M. and CERMAK, J.E. ; "Flow Characteristics of a Circular Submerged Jet Impinging Normally on a Smooth Boundary", Sixth Midwestern Conference on Fluid Mechanics, Univ. Texas, p. 198, 1959.

POREH, M., TSUEI, Y.G. and CERMAK, J.E. ; "Investigation of a Turbulent Radial Wall Jet", J. Appl. Mech., vol. 34, no. 2, p. 457, 1967.

RAJARATNAM, N. ; "Turbulent Jets", Elsevier Scientific Publishing Co.. New York, 1976.

REICHARDT, H. ; See Gauntner et al.[36].

RODI, W. ; "The Prediction of Free Turbulent Boundary Layers by use of a 2-Equation Model of Turbulence", Ph.D. thesis, University of London, 1972.

RODI, W. and SPALDING D.B. ; "A Two Parameter Model of Turbulence and its Application to Free Jets", Wärme und Stoffübertragung, vol. 3, p. 85, 1970.

RUSSEL, P.J. and HATTON, A.P. ; "Turbulent Flow Characteristics of an Impinging Jet", Proc. Instn. Mech. Engrs., vol. 186, no. 52, p. 635, 1972.

SAAD, N.R. ; "Flow and Heat Transfer for Multiple Turbulent Impinging slot Jets", Ph.D. thesis, Mc Gill University, 1981.

SCHAUER, J.J. and EUSTIS, R.H. ; "Flow Development and Heat Transfer Characteristics of Plane Turbulent Impinging Jets", Tech. Rep. 3, Dept. Mech. Eng., Stanford University, 1963.

SCHLICHTING, H. ;"Boundary - Layer Theory", 6th edition, McGraw-Hill Book Co., New York, 1968.

SCHWARZ, W.H. and COSART, W.P. ; "Two-Dimensional Turbulent Wall Jet", J. Fluid Mech., vol. 10, p. 481, 1961.

SOMERSCALES, E.F.C. ; "Fouling of Heat Transfer Equipment", Hemisphere Publishing Corp., 1981.

SPALDING, D.B. ; "The Prediction of Two- Dimensional Steady Turbulent Flows", Imperial College, Heat Transfer Section Report, EF/TN/A/16, 1969.

SPALDING, D.B. ; "Concentration Fluctuations in a Round Jet", J. Chemical Engineering Science, vol. 26, p. 95, 1971.

SPALDING, D.B. ; "The k~w Model of Turbulence", Imperial College, Mech. Eng. Dept. Report, TM/TN/A/16, 1972.

SPALDING, D.B. ; "Monograph on Turbulent Boundary Layers", Imperial College, Mech. Eng. Dept. Report, TWF/TN/33, 1967.

SPALDING, D.B. ; "A Novel Finite Difference Formulation for Differential Experssions Involving Both First and Second Derivatives", Int. J. Num. Methods Eng., vol. 4, p. 551, 1972.

SPARROW, E.M. and ALHOMOUD, A. ; "Impingement Heat Transfer at a Circular Cylinder due to an Offset or Non-Offset Slot Jet", J. Heat Mass Transfer,

vol. 27, no. 12, p. 2297, 1984.

TANI, I. and KOMATSU, Y. ; "Impingement of a Round Jet on a Flat Surface", The International Congress of Applied Mechanics, p. 672, 1966.

TOLLMIEN, W. ; "Calculation of Turbulent Expansion Processes", NACA TM-1085, 1945.

TOWNSEND, A.A. ; "The Structure of Turbulent Shear Flow" , Cambridge Univ. Press, 1956.

TRENTACOSTE, N. and SFORZA, P.M. ; "An Experimental Investigation of Three-Dimensional Free Mixing in Incompressible, Turbulent, Free Jets", Rep. P1BAL-871, Polytechnic Inst. of Brooklyn, 1966.

TRUPEL ; see Abramovich[1].

TSUCHIYA, Y., UEDA, C., ALAHAKOON, A.V.B. and IKEDA, J. ; "On the Impingement Flow of a Turbulent Jet to a Circular Cylinder Near a Flat Plate", Near Wall Turbulent Flows, R.M.C. So, C.G. Speziale and B.E. Launder (Editors), Elsevier, Since Publishers, p. 803, 1993.

van DRIEST, E.R. ; "On Turbulent Flow Near a Wall", J. Aero. Sci., vol. 23, 1956.

van HEININGEN, A.R.P. ; "Heat Transfer under an Impinging Slot Jet", Ph.D. thesis, Mc Gill Univ., 1982.

VICKERS, J.M.F. ; "Heat Transfer Coefficients Between Fluid Jets and Normal Surfaces", Ind. Eng. Chem., vol. 5, no. 8, p. 967, 1959.

WOLFSHTEIN, M. ; "Convection Processes in Turbulent Impinging Jets", Ph.D. thesis, Imperial College, London, 1967.

WOLFSHTEIN, M. ; "The Velocity and Temperature Distribution in One-Dimensional Flow with Turbulence Augmentation and Pressure Gradient", Int. J.

Heat Mass Transfer, vol. 12, p. 301,1969.

ZIJNEN, B.G. ; "Measurements of the Velocity Distribution in a Plane Turbulent Jet of Air", Appl. Sci. Res., Sect. A, vol. 7, p. 256, 1958.

APPENDIX

Laser doppler anemometry

The basic theory of laser doppler anemometry is presented in this appendix. In order to explain the operating principles of LDA system, a simple fringe model is chosen. The output of a laser is separated into two parallel beams which pass through a spherical lens and bisects each other at the focal point of this lens. A set of plane parallel interference fringes, with a spacing dependent on laser wavelength and the angle between two beams, is produced in the crossing region, fig.(A-1).

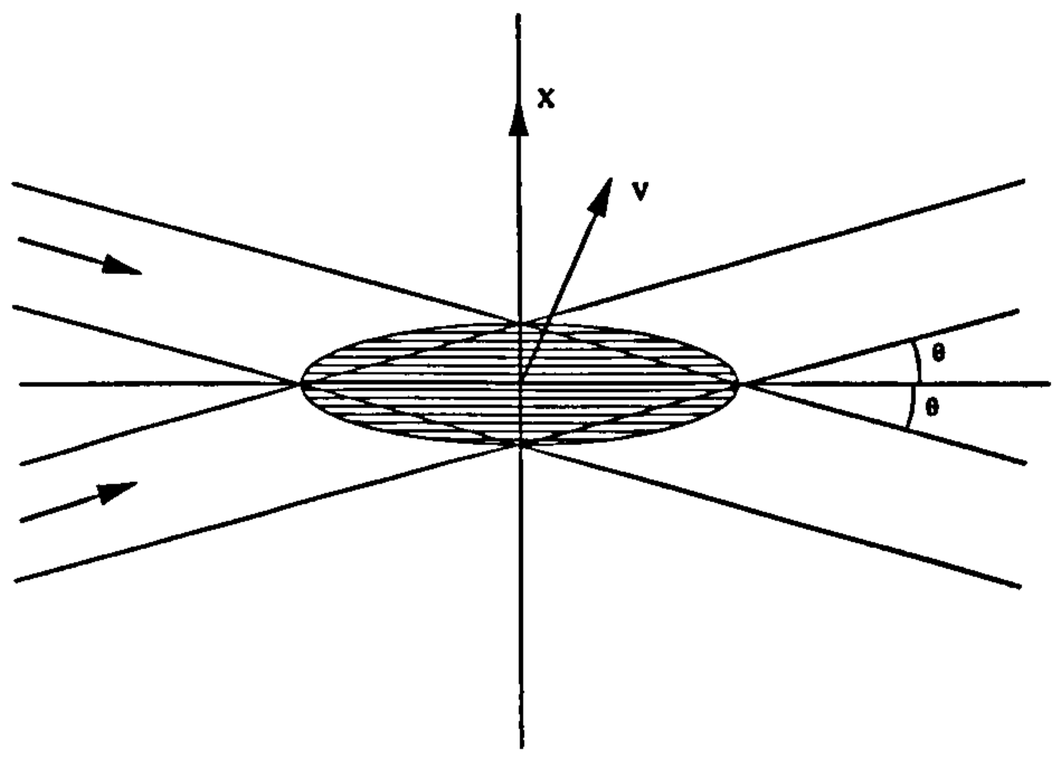

Fig.(A-1): Interference of two coherent waves producing fringes in the sampling volume.

Particles passing through this crossing region (sampling volume) with a certain velocity will alternately cover and uncover bright and dark fringes. When such a particle is observed from any direction, it will be seen to produce sinusoidal intensity fluctuations, the frequency of which will be proportional to the fringe spacing and the component of velocity v_x normal to the fringes.

To calculate the fringe spacing, consider two plane waves A and B incident onto a plane x. If the angles of incidence are θ_1 and θ_2 respectively,

$$A=a\ \exp(-ikx\sin\theta_1)$$

$$B=b\ \exp(-ikx\sin\theta_2)$$

where a and b are amplitudes of the two waves and k is their wave number and is equal to:

$$|k|=\frac{2\Pi}{\lambda}$$

and λ is the wavelength.

The intensity of distribution I(x) is therefore:

$$I(x)=(A+B)^2=a^2+b^2+2ab\cos\gamma x$$

where

$$\gamma=k\ (\sin\theta_2-\sin\theta_1)\ .$$

The fringe spacing d is given by

$$\gamma d=2\Pi$$

or

$$d=\frac{2\Pi}{k(\sin\theta_2-\sin\theta_1)}$$

$$d=\frac{\lambda}{2\ \cos(\frac{\theta_2+\theta_1}{2})\ \sin(\frac{\theta_2-\theta_1}{2})}$$

for small angles $\sin\theta=\theta$ and so

$$d=\frac{\lambda}{\theta_2-\theta_1}\ .$$

If x-direction to be normal to the bisector of the angle between two beams that is $\theta_1=-\theta_2=\theta$, the fringe spacing becomes:

$$d=\frac{\lambda}{2\sin\theta}$$

where 2θ is now the angle between two beams.

The time T taken to travel the distance d is:

$$T=\frac{d}{v_x}$$

so the frequency of the signal is:

$$\frac{1}{T}=\omega_D=\frac{2v_x}{\lambda}\sin\theta\ .$$

From this expression it is obvious that the frequency ϖ_D is independent of the direction of observation. This frequency carries no information of the sign of velocity of particle. To determine the sign of velocity a frequency shift is introduced in the transmitting optics to one of the crossing laser beams. Subsequently the fringe pattern can not remain stationary and moves in a direction normal to the fringe plane such that the light intensity at any point is modulated at the shift frequency. In this case the moving particle will scatter the light such that the difference between the modulation frequency and the shift frequency is proportional to the velocity. Thus moving in the opposite direction of the fringe movement increases the frequency, while moving in the same direction reduces it. This shift is produced by a Bragg cell.